DOCTOR OF PHILOSOPHY

Novel Tools for Interventional Magnetic Resonance Imaging

Rube, Martin

Award date:
2014

DOCTOR OF PHILOSOPHY

Novel Tools for Interventional Magnetic Resonance Imaging

Martin Rube

2014

University of Dundee

Novel Tools for Interventional Magnetic Resonance Imaging

Martin Alexander Rube

A Dissertation Submitted
in Partial Fulfillment of the
Requirements for the Degree
of Doctor of Philosophy
University of Dundee
August 2014

Contents

List of Figures vii

List of Tables ix

Abbreviations xi

Physical Constants xvii

Symbols xix

Acknowledgements xxi

Declaration of Authorship xxiii

Statement by Supervisors xxiv

Abstract xxv

1 Introduction 1
- 1.1 Background and Motivation . . . 2
- 1.2 Current iMRI Challenges . . . 3
- 1.3 Experimental Models for iMRI . . . 6
- 1.4 Thesis Outline . . . 7

2 Magnetic Resonance Imaging 15
- 2.1 Spin and Relaxation . . . 16
  - 2.1.1 Nuclear Magnetic Resonance Phenomenon . . . 16
  - 2.1.2 Magnetic Susceptibility . . . 17
  - 2.1.3 Excitation . . . 19
  - 2.1.4 Relaxation . . . 19
- 2.2 Image Formation . . . 22
  - 2.2.1 Slice Selection . . . 22
  - 2.2.2 Frequency Encoding . . . 23
  - 2.2.3 Phase Encoding . . . 23
  - 2.2.4 Reconstruction . . . 24
- 2.3 Implementation for Clinical Imaging . . . 25

2.4 Interventional Application of MRI 30
2.4.1 Fast Pulse Sequences for Interventions 31
2.4.2 Percutaneous Interventions 34
2.4.3 Endovascular Interventions 35
2.4.4 Interventional Devices 36
2.4.5 Device Visualisation 38

3 Novel Solutions for MRI Visualisation of Interventional Devices 45
3.1 Introduction 46
3.2 Materials and Methods 46
3.2.1 Device Design 46
3.2.2 MRI Setup and Protocol 51
3.2.3 In Vitro Experiments in Tissue Mimicking Phantoms 51
3.2.4 Ex Vivo Experiments in Thiel Embalmed Human Cadavers . 57
3.3 Results 58
3.3.1 In Vitro Evaluation of Developed Devices 59
3.3.2 Ex Vivo Evaluation of Developed Devices 66
3.4 Discussion 69
3.5 Concluding Remarks 73

4 Mobile Technology to Improve iMRI Workflow 75
4.1 Introduction 76
4.2 Materials and Methods 77
4.2.1 Interventional MRI Setup and Modifications 77
4.2.2 Acceptance Testing 80
4.2.3 Techniques for MRI-Guided Interventions 81
4.2.4 In Vitro Evaluation in Tissue Mimicking Phantoms 82
4.2.5 Ex Vivo Evaluation in Thiel Embalmed Human Cadavers . . 83
4.3 Results 83
4.3.1 Acceptance Testing 84
4.3.2 In Vitro Studies in Tissue Mimicking Phantoms 85
4.3.3 Ex Vivo Studies in Thiel Embalmed Human Cadavers 87
4.4 Discussion 88
4.4.1 Interventional MRI Workflow 90
4.4.2 In Vitro and Ex Vivo Studies 92
4.5 Concluding Remarks 93

5 Wireless Tracking of Interventional Devices 95
5.1 Introduction 96
5.2 Theory 97
5.3 Materials and Methods 99
5.3.1 Tracking Pulse Sequence 99
5.3.2 Interleaved Imaging Pulse Sequences 100
5.3.3 Real-Time MRI Implementation 102
5.3.4 In Vitro Experiments in Perfused Arterial Phantoms 102

5.3.5 Ex Vivo Experiments in Thiel Embalmed Human Cadavers . 104
5.4 Results 104
5.4.1 In Vitro Evaluation in Perfused Arterial Phantoms 104
5.4.2 Ex Vivo Evaluation in Thiel Embalmed Human Cadavers . . 108
5.5 Discussion 110
5.6 Concluding Remarks 113

6 Applications to Specific Interventions: Pre-clinical Iliac Angioplasty 115
6.1 Rational for Cardiovascular iMRI 116
6.2 Materials and Methods 116
6.2.1 Interventional Devices 116
6.2.2 In Vitro Studies in Perfused Arterial Phantoms 117
6.2.3 In Vivo Validation in a Porcine Model 124
6.3 Results 127
6.3.1 In Vitro Studies in Perfused Arterial Phantoms 127
6.3.2 In Vivo Validation in a Porcine Model 131
6.4 Discussion 132
6.4.1 Interventional Devices 133
6.4.2 iMRI Setup 134
6.4.3 Protocol and Workflow 135
6.5 Conclusions 137

7 Applications to Specific Interventions: Pre-clinical Endovascular Recanalisation in Acute Ischemic Stroke 139
7.1 Motivation 140
7.2 Materials and Methods 142
7.2.1 Interventional Devices 142
7.2.2 In Vitro Studies in Perfused Arterial Phantoms 142
7.2.3 Ex Vivo Studies in Thiel Embalmed Human Cadavers 144
7.2.4 Preliminary In Vivo Validation in a Porcine Model 145
7.3 Results 146
7.3.1 In Vitro Studies in Perfused Arterial Phantoms 146
7.3.2 Ex Vivo Studies in Thiel Embalmed Human Cadavers 148
7.3.3 Preliminary In Vivo Validation Experiments 149
7.4 Discussion 150
7.4.1 Interventional Devices 153
7.4.2 Device Tracking and Navigation 154
7.5 Conclusions 154

8 Summary and Outlook 157
8.1 Summary 158
8.2 Open Issues and Future Work 160
8.3 Potential Directions of Future Research 163

A Publications Arising From This Thesis **167**

Bibliography **171**

List of Figures

1.1 MRI of a Ventilated Thiel Soft-Embalmed Human Cadaver 8

2.1 Precessing Spins and Discrete States for Hydrogen 18
2.2 Spin Excitation and Relaxation 20
2.3 Free Induction Decay 21
2.4 Relaxation Times 21
2.5 Tissue Dependent Relaxation Times and Contrast Weightings . . . 22
2.6 k-Space 24
2.7 MRI Scanner Hardware 26
2.8 Spin Echo - Pulse Sequence Diagram 27
2.9 Gradient Recalled Echo - Pulse Sequence Diagram 28
2.10 RF Excitation for GRE 29
2.11 Balanced Steady State Free Precession - Pulse Sequence Diagram . 32
2.12 Approach to Steady State 33
2.13 Fast k-Space Trajectories 33
2.14 Passive Device Visualisation in MRI 39
2.15 Dipole-Dipole Susceptibility Artefact 40
2.16 Inductive Signal Coupling for a Resonant Marker 44

3.1 Illustration of MRI-Safe PEEK-Based Guidewire 47
3.2 Various Coil Designs for wRCs 49
3.3 Catheters for iMRI Visualisation 50
3.4 iMRI Setup at IMSaT in Dundee, UK 53
3.5 Signal Void of a Passive Marker 54
3.6 MRI Visualisation of the MRI-Safe Guidewire 60
3.7 Flip Angle Maps of wRCs with Different Coil Configurations 61
3.8 MRI of Catheters with a Single wRC in a Phantom 62
3.9 MRI of a Balloon Catheter with wRCs in a Phantom 62
3.10 Signal Intensities of wRCs as a Function of the Flip Angle 63
3.11 MRI of a Sidewinder Catheter with Five wRCs 63
3.12 MRI of a Catheter with One wRC and FePt nPs Markers 64
3.13 rtMRI Navigation of a Catheter with wRC and FePt nPs Markers . 65
3.14 3T MRI of a Cobra Catheter with One wRC and FePt nPs Markers 65
3.15 MRI of a Micro Catheter with One Passive Marker 66
3.16 Background Suppression and Positive Contrast of a Passive Marker 67
3.17 Temperature Measurements (acc. ASTM F2182-09) for a wRC . . . 67

3.18 Guidewire Navigation into the Vena Cava of a Thiel Cadaver 68
3.19 Straight Catheter Advanced into Iliac Artery of a Thiel Cadaver . . 69
3.20 Balloon Catheter Navigated into Iliac Artery of a Thiel Cadaver . . 69

4.1 Floor Plan of IMSaT Setup for iMRI 78
4.2 Web-based User Interface for iMRI 79
4.3 Thiel Cadaver Setup for iMRI 84
4.4 iMRI from a Tablet PC 86
4.5 MRI-Guided Needle Biopsy - In Vitro 87
4.6 MRI-Guided Needle Biopsy - Ex Vivo 88
4.7 MRI-Guided Needle Biopsy Using a Tablet PC - Ex Vivo 89
4.8 Needle Position Verification - Ex Vivo 89

5.1 Pulse Sequence Diagram for wRC Position Detection 99
5.2 Block Diagram of the Tracking and Imaging Pulse Sequences 101
5.3 Balloon Angioplasty in a Clinical MRI Scanner 103
5.4 Tracking Signal Plots - In Vitro 105
5.5 Best Tracking Signal Plot - In Vitro 105
5.6 Tracking Errors Shown as Frequency Histogram 106
5.7 In Vitro Balloon Angioplasty of the Iliac Artery 107
5.8 Wireless Device Tracking in 2D and 3D 108
5.9 Tracking Signal Plots - Ex Vivo 109
5.10 rtMRI Catheter Navigation - Ex Vivo 110

6.1 Multi-Modality Setup at IMSaT with rtMRI Modifications 117
6.2 In-Room iMRI Display and Control Setup 118
6.3 Arterial Phantom Setup for Cardiovascular Interventions 120
6.4 Flow Diagram for Iliac Angioplasty Protocol 121
6.5 Multi-Modality Setup at Goethe University Hospital Frankfurt . . . 125
6.6 Procedure Times for Iliac Angioplasties - In Vitro 127
6.7 Iliac Angioplasty - Product rtMRI Interface 129
6.8 Iliac Angioplasty - Research rtMRI Interface 130
6.9 Flow/Velocity Examination of the Iliac Artery 130
6.10 MRI-Guided Iliac Angioplasty - In Vivo 132
6.11 rtMRI Device Navigation into the Aorta - In Vivo 133

7.1 Photographs of the In Vitro Setup for Mechanical Thrombolysis . . 143
7.2 Device Navigation into the M1 - In Vitro 147
7.3 Micro Catheter Navigation into the M1 - In Vitro 148
7.4 MRI Examination of the Brain State - Ex Vivo 149
7.5 Device Navigation into the MCA - Ex Vivo 150
7.6 Balloon Angioplasty of the Carotid Artery - In Vivo 151
7.7 Balloon Inflation in the Carotid Artery - In Vivo 151
7.8 In Vivo Assessment of Balloon Dilatation 152

8.1 Combined Active and Wireless Tracking for Robotic Interventions . 164

List of Tables

2.1 Spin Echo - Parameter Combinations 28
2.2 Gradient Recalled Echo - Parameter Combinations 29

3.1 Catheters for iMRI Visualisation 52
3.2 MRI Parameters for the Guidewire Experiments 54
3.3 MRI Parameters for the Catheter Experiments 55
3.4 Susceptibility Artefact Sizes of the Guidewire Markers 61

4.1 Needle Targeting Accuracy 86

5.1 MRI Parameters for the Tracking Study 101

6.1 MRI Parameters for the In Vitro Study - Product Protocol 123
6.2 MRI Parameters for the In Vitro Study - Research Protocol 124
6.3 MRI Parameters for the In Vivo Study 126

7.1 MRI Parameters for the Mechanical Thrombolysis Experiments . . 144

Abbreviations

1D	One dimensional
2D	Two dimensional
3D	Three dimensional
ASTM	**A**merican **S**ociety for **T**esting and **M**aterials
BPM	**B**eats **P**er **M**inute
BW	**B**and **W**idth
C4	**C**arotid artery segment from petrolingual ligament to prox. dural ring
CAHID	**C**entre for **A**natomy and **H**uman **ID**entification
CE marking	Symbol for conformity to EU directives & free EEA marketability
CFK	**C**arbon **F**ibre-Enhanced Plastics
ch	**ch**annel
CNR	**C**ontrast-to-**N**oise **R**atio
$\mathbf{CS_{MRI}}$	**MRI** Scanner **C**oordinate **S**ystem [Cartesian, right-handed]
$\mathbf{CS_{Patient}}$	**Patient C**oordinate **S**ystem [Cartesian, right-handed]
CSS	**C**ascading **S**tyle **S**heets
CT	**C**omputer **T**omography
DAM	**D**ouble **A**ngle **M**ethod
dB	**d**eci**B**el
DFT	**D**iscrete **F**ourier **T**ransform
DICOM	**D**igital **I**maging and **C**ommunications in **M**edicine
DSA	**D**igital **S**ubtraction **A**ngiography
DWI	**D**iffusion-**W**eighted **I**maging
EEA	**E**uropean **E**conomic **A**rea
EM	**E**lectro **M**agnetic

ETL	**E**cho **T**rain **L**ength
F	**F**rench
FA	**F**lip **A**ngle
FDA	**F**ood and **D**rug **A**dministration
FeO	Iron (**Fe**) **O**xide
FFT	**F**ast **F**ourier **T**ransform
FID	**F**ree **I**nduction **D**ecay
fps	**f**rames **p**er **s**econd
FePt	Iron (**Fe**) Platinum (**Pt**) alloy
FoV	**F**ield **o**f **V**iew
FT	**F**ourier **T**ransform
GE	**G**eneral **E**lectric
Gd	**Gad**olinium
HIFU	**H**igh-**I**ntensity **F**ocused **U**ltrasound
HTML	**H**yper **T**ext **M**arkup **L**anguage
HR	**H**adamard modulated **R**eadout
IA	**I**ntra**A**terial
IEC	**I**nternational **E**lectrotechnical **C**ommission
iMRI	**i**nterventional **M**agnetic **R**esonance **I**maging
IMS	**I**nterventional **M**anagement of **S**troke
IMSaT	**I**nstitute for **M**edical **S**cience **a**nd **T**echnology (Dundee, UK)
IRB	**I**nstitutional **R**eview **B**oard
ISO	**I**nternational **S**tandards **O**rganization
IP	**I**nterent **P**rotocol
IV	**I**ntra**V**enous
LCD	**L**iquid **C**rystal **D**isplay
LE	**L**ower **E**xtremity
M1	**M**CA segment from origin to bi- / trifurcation
M2	**M**CA segment from bi- / trifurcation to origin of cortical branches
MCA	**M**iddle **C**erebral **A**rtery
MR	**M**agnetic **R**esonance

MRA	**M**agnetic **R**esonance **A**ngiography
MRI	**M**agnetic **R**esonance **I**maging
MRgFUS	**M**agnetic **R**esonance-**g**uided **F**ocused **U**ltrasound **S**urgery
NaCl	Sodium (**Na**) chloride (**Cl**)
NMR	**N**uclear **M**agnetic **R**esonance
nPs	**n**ano **P**article**s**
PAA	**P**oly **A**crylic **A**cid partial sodium salt
PC	**P**ersonal **C**omputer
PD	**P**roton **D**ensity
PEBAX	**P**oly**E**ther **B**lock **A**mide
PEEK	**P**olyether **E**th**E**r **K**etone
PNR	**P**eak to **N**oise **R**atio
ppm	**p**arts **p**er **m**illion
PRS	**P**lanar **R**ectangular **S**piral
PWI	**P**erfusion-**W**eighted **I**maging
$\mathbf{r_2}$	Spin-Spin (T_2) **r**elaxivity
RF	**R**adio **F**requency
RMS	**R**oot **M**ean **S**quared
ROI	**R**egion **O**f **I**nterest
rtMRI	Near **r**eal-**t**ime **M**agnetic **R**esonance **I**maging
SAR	**S**pecific **A**bsorption **R**ate
SI	**S**ignal **I**ntensity
SMD	**S**urface **M**ounted **D**evice
SNR	**S**ignal-to-**N**oise **R**atio
SPIO	**S**uper**P**aramagnetic **I**ron **O**xide
SSID	**S**ervice **S**et **ID**entifier
SSL	**S**ecure **S**ockets **L**ayer
$\mathbf{T_1}$	Spin-Lattice Relaxation Time
$\mathbf{T_2}$	Spin-Spin Relaxation Time
TCP	**T**ransmission **C**ontrol **P**rotocol
TE	**E**cho **T**ime

TR	**R**epetition **T**ime
ToF	**T**ime **o**f **F**light
UI	**U**ser **I**nterface
USB	**U**niversal **S**erial **B**us
VNC	**V**irtual **N**etwork **C**omputing
WLAN	**W**ireless **L**ocal **A**rea **N**etwork
WMI	**W**hite **M**arker **I**maging
WPAN	**W**ireless **P**ersonal **A**rea **N**etwork
wRC	**w**ireless **R**esonant **C**ircuit

Abbreviations - MRI Pulse Sequences

bSSFP[1]	**b**alanced **S**teady **S**tate **F**ree **P**recession
FGRE	**F**ast **G**radient **R**ecalled **E**cho
FLASH[2]	**F**ast **L**ow **A**ngle **SH**ot
FISP[3]	**F**ast **I**maging with **S**teady State **P**recession
FSE[4]	**F**ast **S**pin **E**cho
FSPGR[5]	**F**ast **SP**oiled **G**radient **R**ecalled Echo
GRE[6]	**G**radient **R**ecalled **E**cho
HASTE[7]	**H**alf Fourier **A**cquisition **S**ingle Shot **T**urbo **S**pin Echo
PSIF	time reversed FISP
rtFLOW	**r**eal-**t**ime **FLOW** sensitive phase contrast
SE	**S**pin **E**cho
SPGR[5]	**SP**oiled **G**radient **E**cho
spGRE	**sp**iral **G**radient **R**ecalled **E**cho
SSFP[3]	**S**teady **S**tate **F**ree **P**recession
SSFSE[7]	**S**ingle **S**hot **F**ast **S**pin **E**cho
VIBE[8]	**V**olumetric **I**nterpolated **B**reath-hold **E**xamination

[1]This is called trueFISP on Siemens, FIESTA on GE and b-FFE on Philips scanners.
[2]This is called FLASH on Siemens, SPGR on GE and T1FFE on Philips scanners.
[3]This is called FISP on Siemens, GRASS on GE and FFE on Philips scanners.
[4]This is called FSE on GE and TSE on Siemens and Philips scanners.
[5]This is called TurboFLASH on Siemens, FSPGR on GE and TFE on Philips scanners.
[6]This is called GRE on GE and Siemens and FFE on Philips scanners.
[7]This is called HASTE on Siemens, SSFSE on GE and Single shot TSE on Philips scanners.
[8]This is called VIBE on Siemens, LAVA on GE and THRIVE on Philips scanners.

Physical Constants

Speed of Light	c_0	=	$2.997\ 924\ 58 \times 10^{8}$ m s^{-1}
Bolzmann Constant	k_B	=	1.38×10^{-23} m^2 kg s^{-2} K^{-1}
Local Gravity Factor (Dundee, UK)	g	=	9.816050 m s^{-2}
Planck's Constant	h	=	$6.626\ 069\ 57 \times 10^{-34}$ J s
Copper Conductivity (at 293 K)	σ_{Cu}	=	$59.6\ \times 10^{6}$ S m^{-1}
Permeability of Free Space	μ_0	=	$4\ \pi\ \times 10^{-7}$ H m^{-1}
Permittivity of Free Space	ϵ_0	=	$8.854\ 187 \times 10^{-12}$ F m
Gyromagnetic Ratio for ^1H	γ	=	42.576×10^{6} H T^{-1}

Symbols

A	Area	$[\mathrm{m}^2]$
B	Magnetic Field Strength	[T]
C	Capacitance	[F]
E	Energy	[J]
F	Force	[N]
f	Frequency	[Hz]
Δf	Bandwidth	[Hz]
G	Field Gradient	
${}^1H$	Hydrogen	
h	Height	[m]
I	Current	[A]
J	Quantized Angular Momentum	$[\mathrm{A} \cdot \mathrm{T} \cdot \mathrm{m}^2 \cdot \mathrm{Hz}^{-1}]$
L	Inductance	[H]
l	Length	[m]
m	Magnetic Moment	$[\mathrm{A} \cdot \mathrm{m}^2]$
M	Magnetisation	$[\mathrm{A} \cdot \mathrm{m}]$
m_z	Magnetic Quantum Number	
N	Number of Windings	
n	Number or Sample Size	
N_{EX}	Number of Excitations	
N_{PE}	Number of Phase Encoding Steps	
N_{FE}	Number of Frequency Encoding Steps	
P	Plane	
P_i	Peak Position for RF Excitation Number i	

Q	Quality Factor	
R	Electrical Resistance	$[\Omega]$
s	Signal	
T	Temperature	[K]
t	Time	[s]
T_m	Torque	$[\mathrm{N} \cdot \mathrm{m}]$
V	Volume	$[\mathrm{m}^3]$
w	Width	[m]
α	Flip Angle	[deg]
Δ	Difference	
λ	Wavelength	[m]
μ	Permeability	$[\mathrm{H} \cdot \mathrm{m}^{-1}]$
σ	Electrical Conductivity	$[\mathrm{S} \cdot \mathrm{m}^{-1}]$
χ	Magnetic Susceptibility	
ω	Angular Frequency	$[\mathrm{rads}^{-1}]$
$\varnothing$	Diameter	[m]
$\#$	Quantity	

Acknowledgements

There is a long list of people that I would like to acknowledge throughout this exiting project. The research and this thesis would not have been possible without the collaborations across industry and academia and I am grateful for the funding that I received from the European Communitys Seventh Framework Programme (FP7/2007-2013) under grant agreement number 238802 (IIIOS project).

First, I would like to thank my first supervisor, Andreas Melzer, for giving me this opportunity three and a half years ago. He always supported me and gave me the freedom to pursue research in different fields while focusing on this dissertation project. I am very grateful for his after working hours and weekend crash courses in human anatomy and interventional skills.

Next, I would like to express my gratitude to my second supervisor, Graeme Houston as well as Richard White and Razvan Buciuc who gave me crucial advice and guidance from a clinical perspective. It was a great pleasure to work with each of the interventional radiologists and invaluable to get their feedback throughout this project.

I sincerely acknowledge the fellow students and staff at the Institute for Medical Science and Technology (IMSaT). Especially, I would like to thank Ben Cox, who became a close friend, always assisted me and provided excellent input throughout his time at IMSaT. I am also very grateful for his never-ending patience while reviewing my scientific writing. Thanks also to Fabiola Fernandez-Gutierrez, it was a great pleasure to work with her and to have endless discussions about work and non-work related topics. Special thanks to Stratos Kokkalis, Remco Stam and Stuart Coleman on whom I could always count on and share my passion for mountaineering, which contributed to make my time in Scotland so enjoyable. Special thanks also to Alex and Osnat Volovyk for introducing me to Israel.

Another person whose input was very valuable is Andrew Holbrook. He became a very good friend during our collaboration and I am in debt for his almost 24/7 support with RTHawk debugging. His knowledge and patience significantly

helped to get me up to speed in real-time Magnetic Resonance Imaging and to implement many of my ideas.

In particular I want to thank Florian Steinmeyer for his positive attitude, the valuable discussions as well as his encouragement, mentorship and friendship over the past five years. Working with him was always a great pleasure and I am looking forward to rewarding discussions in the future.

Further, I want to thank Juan Santos, Joelle Barral and William Overall for helpful input and discussions. Also, I thank Leonard Fass and John Ferrut as well as Tom Breslin and Gabor Mizsei for their friendly and helpful support. I am in particular thankful for the help and input from Labonny Biswas. In addition, I am very grateful for crucial advice and hints from Charles Dumoulin and Martin Graves.

My thanks also to Erwin Immel, Stephan Zangos, Alf Theisen and Thomas Vogl who made the animal experiments possible. Moreover, I am very grateful to Mandy Kaiser, Patricia Seifert and Praveen Ashok for fruitful collaborations.

I also want to acknowledge my dearest friends Thomas Fricke, Felix Horn, Thomas Katzenberger, Andreas Dietzel, and my cousin Glenn Schabert who were always there when I needed them most.

Lastly, I would not have been able to follow my dreams without the remarkable support of my wonderful family. I feel the infinite gratitude to my parents, Liesel and Hartwig Rube, who always believed in me, encouraged me to follow my own way and provided help when I needed it. Thank you. Special thanks to my amazing sisters, Ulrike and Claudia Rube, who have travelled to all corners of the world to visit me and have always been a great support. I also thank my grandparents, Hans-Peter and Hannelore Schabert for being so interested in my work and for their guidance and support. I have been blessed to have such a wonderful wife, Manuela. Your love, understanding and incredible support made this dissertation possible. At the very end of the last year you made me the best present in the world with our little baby boy Lukas. This thesis is for both of you.

Declaration of Authorship

I, Martin Alexander Rube, declare that this thesis titled, 'Novel Tools For Interventional Magnetic Resonance Imaging' and the work presented in it are my own. I confirm that:

- I am the author of the thesis.
- Unless otherwise stated, all references cited have been consulted by myself.
- The work of which the thesis is a record has been done by myself.
- The work has not been previously accepted for a higher degree.

Signed: 

Date: 15 May 2014

Statement by Supervisors

I, Andreas Melzer, have read this thesis titled, 'Novel Tools For Interventional Magnetic Resonance Imaging' and certify that the conditions of the relevant Ordinance and Regulations have been fulfilled.

Signed: 

Date: 11 May 2014

Andreas Melzer, First Supervisor

I, John Graeme Houston, have read this thesis titled, 'Novel Tools For Interventional Magnetic Resonance Imaging' and certify that the conditions of the relevant Ordinance and Regulations have been fulfilled.

Signed: 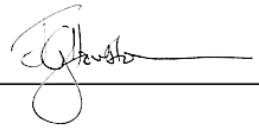

Date: 01/05/14

John Graeme Houston, Second Supervisor

UNIVERSITY OF DUNDEE

Abstract

Institute for Medical Science and Technology (IMSaT)
College of Medicine, Dentistry & Nursing

Doctor of Philosophy (Ph.D)

Novel Tools For Interventional Magnetic Resonance Imaging

by Martin Alexander Rube

Magnetic Resonance Imaging (MRI) provides unique advantages such as superior soft tissue contrast, true multiplanar imaging, variable contrast mechanisms, measurement of temperature changes, perfusion and diffusion, and no ionizing radiation. Despite considerable research efforts in the field of interventional MRI, numerous challenges remain including restricted access to the patient, high acoustic noise and a shortage of MRI-safe devices.

Novel methods and devices are presented in this thesis with the primary objective of enabling effective MRI-guided interventions, particularly abdominal needle and common catheter-based endovascular interventions. Firstly, a set of MRI-safe devices (guidewires, micro guidewires, catheters and micro catheters) were developed with passive or inductively coupling resonant markers for MRI visualisation. Secondly, a method was implemented for wireless tracking and dynamic guidance of instruments. Thirdly, a framework of technologies was developed for in-room display, wireless MRI remote control and multi-user communication along with a dedicated user interface and imaging protocol.

These implementations were assessed in regards to MRI-safety, performance and usability and evaluated for MRI-guided liver biopsies, balloon angioplasty procedures and also for mechanical thrombolysis. Flow phantoms, Thiel soft-embalmed human cadavers with partially re-established perfusion and a porcine model were used for *in vitro*, *ex vivo* and *in vivo* validation, respectively.

The results demonstrate that these interventions are experimentally feasible and practical when using the presented developments: automated device tracking and equipment designed for MRI-guided interventions streamlined procedural workflow. Specifically, it was shown that fast and accurate needle placements along complex trajectories were feasible using a wireless interactive display and control device with a dedicated user interface for interventions. Moreover, safe and efficacious balloon angioplasties of the iliac artery were practical using the described framework of technologies along with a dedicated MRI protocol. Finally, it was demonstrated that these developments could be adapted and applied to MRI-guided endovascular mechanical thrombolysis of the middle cerebral artery.

The technologies, described in this thesis have been shown to overcome many of the present limitations and should therefore be useful for enabling MRI-guided interventions while not further constraining the operating physician in an already complex environment. Nevertheless, it is acknowledged that many crucial issues remain to be solved in the field of iMRI and in the context of the presented research. In particular further device optimisations, improvements of the tracking implementation along with further *in vivo* evaluations are required before moving towards clinical evaluation. This thesis sets the groundwork for moving ahead with the eventual clinical realisation of optimised MRI-guided interventions.

Chapter 1

Introduction

Advances in modern medicine, including the development of minimal access surgery [1], have aimed to minimise the invasiveness of medical treatments. This is a substantial achievement because pain, discomfort, and disability, or other morbidity as a consequence of a medical procedure is more frequently related to trauma involved to approach a target area rather than the procedure itself [2]. However, minimizing the invasiveness of procedures can lead to a significant increase in procedural complexity [3, 4] and technology required. Comprehensive information beyond the skin is indispensable if minimal access techniques are conducted. Medical imaging can provide this crucial information and has revolutionised medicine since the discovery of X-Rays by W. C. Roentgen in 1895 [5]. Since then, many imaging technologies such as X-Ray, Ultrasound, Computer Tomography (CT), Magnetic Resonance Imaging (MRI) or nuclear imaging have evolved for diagnosis and treatment of disease [6].

1.1 Background and Motivation

With the first *in vitro* images using nuclear magnetic resonance (NMR) in 1974 [7], MRI is considered as one of the most significant advances of the last century in the field of medical technology [8]. MRI is non-invasive, does not use ionizing radiation and provides contrast between normal and abnormal soft tissues superior to any other imaging modality [9]. Magnetic Resonance (MR) can provide true multi-planar imaging capabilities with variable contrast mechanisms and allows to measure perfusion [10], diffusion [11], temperature changes [12] and also biochemical and biophysical tissue characteristics (i.e. chemical tissue composition [13], neural connectivity and neural activity [14]).

Moreover, MRI can be used intra-operatively in neurosurgery [15] and i.e. to guide minimally invasive procedures [16]. Despite the broad spectrum of MRI-guided therapeutic applications, MRI was conventionally developed for diagnostic imaging and efficient patient throughput [17]. For more than two decades [18], extensive research has been attributed to interventional MRI (iMRI) applications and technologies. However, iMRI has primarily been performed in academic and

research centres [19] due to numerous remaining challenges. These include a restricted access to the patient [15], high acoustic noise levels [20], the need for MRI-safe devices [21, 22] and high costs [23] related to MRI.

The aim of this thesis is to incorporate the advantages of high field MRI ($\geq$ 1.5 T) for endovascular and percutaneous interventions while providing the interventionalist with the safety, confidence and efficacy that they are used to from other imaging modalities such as X-Ray fluoroscopy, CT or ultrasound. It should also be beneficial by reducing ionizing radiation exposure to clinical staff, paediatric or pregnant patients and in minimally invasive procedures with long intervention times.

1.2 Current iMRI Challenges

Significant developments in the field of MRI have contributed to make iMRI faster and safer [24, 25] and the patient access has significantly improved with modern open or short and wide bore MRI systems [24]. However, the following key challenges have not been fully addressed in the past, yet are critical for successful implementation of iMRI:

(i) Device Visualisation and Tracking

Most commercially available interventional devices, such as needles, catheters, guidewires or implants, are not designed with MRI compatibility [21, 22] in mind and can interact with the different electromagnetic (EM) fields of MRI scanners [21, 26]. One of the largest hurdle to overcome is the shortage of MRI-safe devices in particular in the context of endovascular interventions [23, 27]. Novel approaches for material selection as well as innovative strategies are required for developing devices for iMRI. Safe and versatile device visualisation is crucial in this regard because conventional MRI-safe device materials [28] do not contribute to the MR signal [4], may cause imaging artefacts [9, 29, 30] or create safety risks for the patient [31–36].

(ii) Real-Time Guidance

Instant image display, similar to X-Ray fluoroscopy or ultrasound-guided procedures, is a necessity for any image-guided procedure and also a key requirement for iMRI. However, as Michael Lustig stated: "MRI is burdened by an inherently slow data acquisition process" [37]. Image acquisition time has been considerably reduced in MRI over the past decades and temporal resolutions comparable to X-Ray fluoroscopy can be achieved using ultra-fast pulse sequences [38] in combination with improved computer performance and advanced reconstruction techniques such as parallel imaging [39, 40] or compressed sensing [37]. Closed-loop control of MR image acquisition and in-room display opens a new dimension [41] for interactive near real-time MRI (rtMRI). Generally, scanner manufacturers provide product (i/Drive Pro Plus [42], GE Healthcare, Waukesha, WI, USA) or work in progress user interfaces (Interactive Front End [43] (Siemens, Erlangen, Germany) and eXTernal Control [44] (Philips Healthcare, Best, the Netherlands)) that allow continuous data acquisition and image display. These applications, however, allow a very limited selection of pulse sequences and only basic modifications of parameters during imaging. On the contrary, a more versatile research platform [45] (RTHawk, HeartVista, Palo Alto, CA, USA) has been proposed that allows for fundamental changes of the image acquisition scheme during MRI scanning. To date, this research framework has not received regulatory approval (U.S. Food and Drug Administration (FDA) / CE marking). Major shortcomings of all currently available user interfaces are that these are not tailored to specific interventional applications and are limited to a single MRI scanner manufacturer and cannot be used across multiple platforms i.e. on partner sites with a different MRI scanner and software.

(iii) Interactive MRI Remote Control

The EU directive 2004/40/EC has set fixed limits for occupational exposure to EM fields, which were based on guidelines of the International Commission for Non-ionizing Radiation Protection (ICNIRP). Commissioned studies [46, 47] demonstrated that these exposure limits, would adversely impact several aspects of diagnostic and interventional MRI within the EU [48]. As result the implementation of the directive was postponed to allow for substantive revisions [4, 48]. The directive 2004/40/EC has recently been replaced by the directive 2013/35/EU, in which MRI is treated as a special case with an exemption (or derogation) from exposure limits [49].

An integral part of iMRI procedures is that the operating physician manipulates interventional devices (in the scanner room) and the scanner operator (in the control room) adjusts the scan acquisition to identify the device and its manipulations. However, adjustments can require multiple gestures, intense discussion between operator and physician (if a communication system is in place) or may necessitate the operator stopping or pausing the scan to enter the scanner room. This can cause significant workflow interruptions and delays. Moreover, if a major change to the current scan acquisition (e.g. change of pulse sequence) is required, the current scan must be aborted and a new scan started, including adjustment of parameters, orientation, pulse sequence download and pre-scanning processes, resulting in additional delays. Thus, the physician in the scan room needs table side controls to operate [23] and adjust the scan acquisition without delay.

(iv) Communication

The fast switching gradient fields (in the kHz range) of current MRI scanners result in significant noise levels and noise protection is required during scanner operation in contrary to silent imaging technologies such as X-Ray, ultrasound or CT. Previous studies [50–52] have demonstrated that this gradient noise (ranging between 70 and 110 dB [53]) obstructs communication between operating physician, assisting staff, patient and scanner operator. Preceding experiments in Dundee

[54] have also identified that this created a major workflow challenge, resulting in a significant increase in intervention time and safety concerns.

(v) Workflow

Although MRI has previously widely been used for guiding and monitoring a variety of interventions in the research domain, most studies focused on challenging procedures including stem cell therapy [55], cardiac electrophysiology mapping [56, 57] and heart valve repairs and replacements [58]. However, the iMRI workflow is still greatly compromised by complex MRI operation, limited access to and communication with the patient and the requirement to ensure MRI safety throughout a procedure [21]. At present, iMRI is well established in the field of breast biopsy but other application such as local injections, tumour ablations or solid tumour biopsies are primarily limited to research centres [19]. Dedicated training facilities and programs are available at very few centres only (i.e. Dundee or organised by MR:Comp GmbH (Gelsenkirchen, Germany)). Previous studies have identified that interventionalists experience and appropriate training would significantly influence the success and procedure time of MRI-guided interventions [59]. As a consequence, MRI has not been widely accepted for guiding interventions in clinical routine.

1.3 Experimental Models for iMRI

Device developments, evaluations and practical training on *in vitro*, *ex vivo* and *in vivo* models are essential in interventional radiology as the complexity of procedures and devices is continuously increasing [60]. In the context of this thesis tissue mimicking phantoms were used to assess the performance of developed devices and applications, in particular during initial development stages. These *in vitro* models mimic one or several tissue properties such as dielectric properties, density, viscosity and relaxation properties for MRI. Additionally anatomically correct polymer-based models were used in the context of this thesis that resemble parts of the human vasculature and its pathologies. Moreover, perfusion pumps

can be connected to these vessel replica models to simulate blood flow under normal physiologic or diseased conditions [61].

Vessel replica models depict the correct anatomy of interest in great detail. However, these models are mainly polymer-based and cannot mimic biologic tissue effects. Fresh or frozen human cadavers represent anatomically correct *ex vivo* models with organic variances but have a limited shelf life time [61]. The embalming protocol, developed by Professor Thiel of the University of Graz, Austria, represents a cadaver preservation technique that maintains full flexibility of the limbs [62]. Thiel soft-embalmed cadavers, opposed to formalin fixed ones, retain their natural colours and flexibility, features that are of considerable interest in interventional procedures. Although, this embalming method has originally been developed for dissections, the Thiel cadaver model has successfully been used for laparoscopic surgery [63], neurosurgery [64], and oral surgery [65]. Thiel soft-embalmed cadavers present a feasible model for ultrasound-based regional anaesthesia [66] and are also suitable for MRI [67]. Moreover, Thiel embalmed cadavers were used for micro-vascular exercise because of the excellent condition of fine anatomical structures [68]. Thiel embalmed cadavers have been further developed in Dundee as a model for iMRI research and training with re-established respiratory motion (see Figure 1.1) and partial re-perfusion [61, 69].

A major limitation of human cadavers is that, at present, correct physiological conditions cannot be re-established and that potential complications cannot be simulated. Thus, *in vivo* models are required before clinical application of novel developments. The domestic swine is a frequently used animal model for interventional research due to the numerous similarities between human and porcine anatomy [60, 70] and was therefore also used in the context of this thesis.

1.4 Thesis Outline

In this thesis methods and related devices are described that have been developed to enable dynamic MRI control and rtMRI guidance for percutaneous and endovascular interventions. This thesis is structured in several blocks as follows:

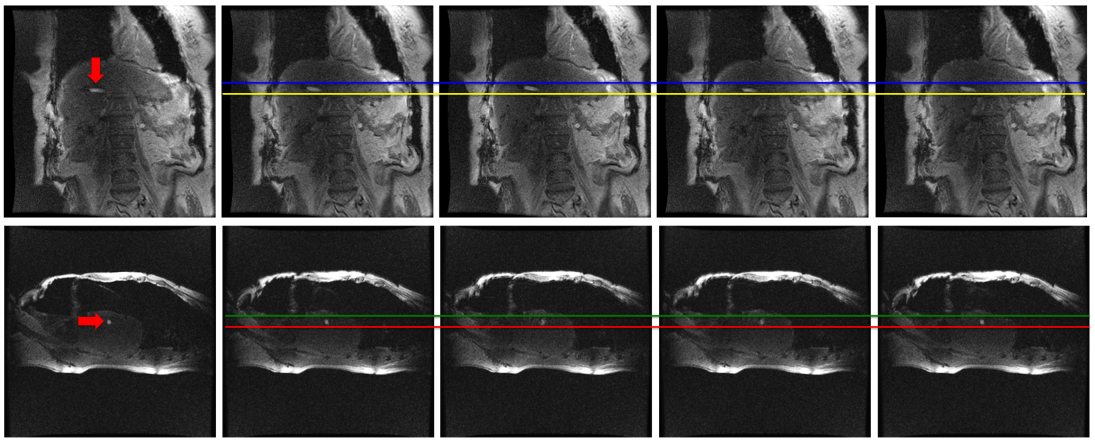

FIGURE 1.1: Sequential MR images (top: coronal / bottom: axial) of a Thiel soft-embalmed human cadaver with mechanical ventilation - The images were obtained with a sequential multiphase acquisition ($B_0 = 1.5$ T, FIESTA, TE/TR = 5.2 / 10.9 ms, FA = 60°, FOV = 40 cm x 40 cm, Matrix = 256 x 256, Slice thickness = 5 mm, phases = 30). The red arrow indicates a balloon catheter (filled with 1:100 Gadolinium doped saline solution) inserted in the right quadrant of the liver.

Firstly, lead-in materials (Chapters 1 and 2), secondly, a block with technical developments (Chapters 3 through 5) and thirdly, a block with pre-clinical validation studies (Chapters 6 and 7). The final chapter (Chapter 8) summarizes the main findings, limitations and potential future research directions. A brief summary of each chapter is provided in the following section.

Chapter 2: Magnetic Resonance Imaging

This thesis like "any novel work rests on an accumulation of previous and current literature" [71]. This chapter reviews the basic principles, key concepts and acquisition methods for MRI. The NMR phenomenon, spin excitation and image formation based on tissue specific relaxation effects and practical implementations are presented. Specific aspects and considerations for interventional applications are also described in this chapter.

Chapter 3: Visualisation of MRI Safe Interventional Devices - (Challenge [i])

In this chapter device visualisation methods for guidewires and catheters are presented. Polymer-based guidewires were developed in collaboration with EPFlex

Feinwerktechnik GmbH (Dettingen/Erms, Germany). Passive MRI visualisation was accomplished using superparamagnetic iron-oxide (SPIO) or iron-platinum alloy (FePt) nanoparticles (nPs) incorporated under the final coating. Additionally, a set of catheters was prepared with different marker configurations according to the head shape of a catheter. Phantom and Thiel soft-embalmed human cadaver experiments are presented demonstrating the capability of these devices for MRI-guided endovascular interventions.

Visualisation of the (head) shape and orientation of catheters was feasible using multiple wirelessly connected resonant circuits (wRC) or a single wRC on the tip and passive FePt nPs markers along the shaft. A single wRC on the tip was found satisfactory for uncomplicated catheter navigation during MRI with low and intermediate flip angle (FA) (<45°). The quality factor (Q) of a wRC significantly affected the signal characteristics in MRI and during very low FA (<5°) imaging, signals were mainly detected in close proximity of the wRC while background signals were suppressed. This information can be used for automated device tracking and will be described in Chapter 5.

Although susceptibility-based visualisation was more difficult to depict in MRI, it was found acceptable for device navigation in the current study. The induced susceptibility artefacts were manipulated by changing imaging parameters (mainly the echo time (TE)) or the concentration of the nPs. Dedicated pulse sequences [72, 73] enabled positive contrast of FePt and SPIO nPs markers while the background was suppressed. However, automated tracking similar to [74] was neither achieved for SPIO nor FePt nPs.

All visualisation techniques in this study did not require a connection between device and MRI scanner, thereby simplifying instrument handling and avoiding elongated electrically conductive structures, which are the major source of instrument heating in MRI [75]. Heating experiments according to ASTM F2182-09 [36] confirmed that no significant radio frequency (RF) induced heating (<0.6 °C) occurred for the wRC with the highest Q ($\approx$ 65). Both nPs markers were found negligible for guidewire handling and mechanical performance. On the contrary, the wRCs applied to the surface resulted in a significant increase in diameter and

stiffness of catheters. Further studies are required to achieve a miniaturised wRCs design and to fully assess the mechanical performance in particular during more complex device manipulations.

Chapter 4: Mobile Technology to Improve Workflow of iMRI - (Challenges [ii - iv])

In this chapter a wireless interactive display and control device combined with a platform independent web-based User Interface (UI) was developed and evaluated for improving workflow of iMRI. The novel iMRI-UI provides image acquisition of up to three independent slices of various pulse sequences with different contrast weightings. Pulse sequence, scan geometry and important parameters can be changed on the fly via the iMRI-UI on a tablet computer for improved lesion detection and interventional device targeting.

The components and setup were tested and found conditionally MRI-safe to use according to current ASTM standards. Despite minor temporary touchscreen interferences at a close distance (<20 cm) no other mal functions, degraded MRI quality or imaging artefacts were observed.

The iMRI-UI was validated for core biopsies in a liver phantom (n = 40) and Thiel soft-embalmed human cadavers (n = 24) with mechanical ventilation. The 3D root-mean-square distance error was 2.8 ± 1.0 (phantom) / 2.9 ± 0.8 mm (cadaver) and overall procedure times ranged between 12 - 22 minutes (phantom) / 20 - 55 minutes (cadaver). The wireless MRI control setup enabled fast and accurate interventional biopsy needle placements along complex trajectories and improved the workflow for percutaneous interventions using MRI guidance in a pre-clinical trial.

Chapter 5: Wireless Tracking of Interventional Devices - (Challenge [i])

In this chapter a robust method for wireless tracking and dynamic guidance of interventional devices equipped with a wRC is presented. Device tracking is crucial for iMRI because conventional device materials do not contribute to the MR signal,

may cause susceptibility artefacts and are generally invisible if moved out of the scan plane.

The proposed method uses a weak spatially-selective excitation pulse with very low FA, a Hadamard multiplexed tracking scheme and also employs phase-field dithering. This method results in reduced background signal intensities while maintaining a local signal enhancement resulting from the point-source marker. Device tracking was interleaved with various user-selectable fast pulse sequences receiving a geometry update from the tracking kernel in less than 30 ms. The phase-field dithering has significantly improved our tracking robustness for catheters with small diameters (4-6 French (F)). The volume root mean square distance error was 2.81 mm (standard deviation: 1.31 mm).

This wireless device tracking approach provides a feedback loop, intuitive iMRI scanner interaction, does not constrain the physician and delivers very low specific absorption rates (SAR). Devices with wRC can be exchanged during a procedure without modifications to the setup or the pulse sequence. Balloon angioplasties of the iliac artery are presented in flow phantom and Thiel soft-embalmed human cadaver experiments, demonstrating the capability of this technique for iMRI. Position information for a single tracking coil was satisfactory for balloon angioplasties of the iliac artery but further studies are required for more complex navigation and catheter shapes before animal trials and clinical application.

Chapter 6: Applications to Specific Interventions: Pre-clinical Iliac Angioplasty - (Challenges [i-v])

In this chapter an improved framework of technologies (Chapters 3 through 5) for in-room image display, control, communication and techniques for MRI-guided vascular interventions was extended and validated for safe, fast and efficient MRI-guided angioplasty of the iliac arteries. MRI was used for interactive real-time imaging during endovascular utilisation of novel or modified devices such as guidewires and catheters and also for pre-, intra- and post-procedural visualisation and measurement of vascular morphology and flow. A detailed analysis and comparison of

the X-Ray angiography workflow was conducted[1] and applied to solely MRI-guided balloon angioplasty of the common iliac artery in perfused arterial phantom (n = 39) and *in vivo* experiments (n = 6) in a porcine model.

MRI-guided iliac angioplasty procedures (39 procedures in 6 sessions) were successfully performed *in vitro* using a conventional closed bore (60 cm) 1.5 T MRI scanner (located in a research centre) with progressive adaptation of the technique and workflow. Safe and efficacious solely MRI-guided endovascular interventions were found to be feasible and practical using an improved framework of technologies along with an optimised workflow. In particular the real-time flow analysis was found to be helpful for pre- and post-interventional assessments. The novel setup and protocol enabled a reduction in table time for the MRI-guided procedures to a minimum of 6 minutes and 33 seconds with a mean procedure time of 9 minutes and 2 seconds, which is comparable to the mean procedure time of 8 minutes and 42 seconds for the standard X-Ray-guided procedure.

The presented *in vivo* experiments (6 procedures in 3 pigs) confirmed that MRI-guided iliac angioplasty procedures were feasible (mean procedure time: 25 minutes and 42 seconds) but the workflow was constrained because only parts of the developed framework could be applied to the wide (70 cm) and short (120 cm) bore 1.5 T MRI scanner located in a clinical centre (excluding modifications to pulse sequences).

The results of this study illustrate the feasibility of endovascular interventions such as common iliac angioplasty, solely using MRI guidance and a novel framework of technologies. It was shown that dedicated equipment designed for interventions and a streamlined iMRI workflow improved the procedural efficacy. However, design optimisation of the MRI-safe catheters and further *in vivo* experiments, in particular using the entire framework of technologies, are required before clinical evaluation.

[1]Please note, the workflow analysis was not scope of this thesis but will be published in the associated Ph.D thesis "Workflow analysis, modelling and simulation for improving conventional and MRI-guided vascular interventions" by F. Fernandez-Gutierrez.

Chapter 7: Applications to Specific Interventions: Pre-clinical Endovascular Recanalisation in Acute Ischemic Stroke - (Challenges [i-v])

Although many methods and technologies are introduced in Chapters 3 through 6, this chapter will demonstrate how these can be applied to MRI-guided endovascular mechanical thrombolysis (clot retrieval). There are three key motives for this study: Firstly, performing diagnosis and treatment in the same imaging modality can save crucial time to initiate treatment (i.e. caused by preparation, patient handling and transfer), which is considered the primary disadvantage of endovascular stroke therapy [76]. Secondly, using MRI avoids ionising radiation and nephrotoxic and allergenic iodine-based contrast media [77]. Thirdly, MRI is the only imaging modality that can visualise the blood vessels and the state of the brain parenchyma facilitating critical decision making during a procedure as the viability of brain tissues can be evaluated and tissues at risk for irreversible infarction can be detected [78].

A set of customised micro guidewires and catheters was prepared for iMRI visualisation with passive susceptibility markers or wRCs. Experiments were conducted in a perfused vascular phantom (recanalisation of the middle cerebral artery (MCA)), Thiel soft-embalmed human cadavers (recanalisation of the MCA) and a living pig (angioplasty of the right carotid artery) to assess the feasibility of MRI-guided recanalisation. The *in vitro* and *ex vivo* experiments were performed in a conventional closed bore 1.5 T MRI scanner using a pulsatile flow pump and artificial blood clots, which were inserted into the MCA (M1 or M2 segment) in case of the phantoms.

To the authors' knowledge, this is the first time that re-perfusion of a brain in a Thiel soft-fixed cadaver has been established. Optimisations of the setup and protocol are required because MR angiography (MRA) revealed that perfusion of the brain resulted in considerable extravasation and thus loss of discernible brain structure. Therefore, all subsequent cadaver experiments were performed without perfusion. Instead a diluted Thiel solution doped (1:100) with Gadolinium (Gd) was injected. MRA enabled generating 3D roadmaps, which were used during device navigation. *In vivo* experiments (single case study) were performed in a

porcine model using a short and wide bore 1.5 T scanner located in a clinical centre. Therefore, only minor modifications to the setup and no modifications to pulse sequences were permitted, which excluded device tracking and generating 3D roadmaps for the animal study.

Solely MRI-guided recanalisations of the MCA were found to be feasible in the flow phantom (n = 9/9) and Thiel soft-embalmed human cadavers (n = 7/9). Automated device tracking was possible during the initial stages of each intervention but manual scan plane alignments were required above the C4 segment of the internal carotid artery due to the catheter diameter at the location of the wRC. The initial animal experiments validated the devices for interventions such as balloon angioplasty of the carotid artery (n = 2/2) using MRI guidance. Manual scan plane alignments to localise a particular device were feasible but generally time consuming.

The results of this study demonstrate that MRI-guided endovascular mechanical thrombolysis using rtMRI guidance is experimentally feasible. However, much research is required before MRI becomes a feasible imaging modality for guiding interventions in acute ischemic stroke. In particular device, protocol and cadaver model optimisations along with further animal experiments, are required to validate successful blood clot removals before clinical evaluation. However, it is hoped that this preliminary study can set the stage for further research in the field of MRI-guided stroke therapy.

Chapter 8: Summary and Outlook

This chapter gives a summary of the main findings presented in this thesis, put in a broader context, and proposes potential directions of future research in the field of iMRI.

Chapter 2

Magnetic Resonance Imaging

2.1 Spin and Relaxation

This section reviews the NMR phenomenon, the basic principles of spin excitation and tissue dependent relaxation mechanisms.

2.1.1 Nuclear Magnetic Resonance Phenomenon

All atoms with odd number of protons and/or neutrons have a spin correlating with an intrinsic magnetic moment m that is directly proportional to the quantised angular momentum J.

$$m = \gamma \cdot J = \gamma \cdot \hbar \cdot m_z \tag{2.1}$$

The gyromagnetic ratio γ is a proportionality constant and characteristic for each nucleus. m_z is the spin angular momentum quantum number and $\hbar$ is Planck's constant h divided by 2π. If a nucleus is affected by an external magnetic field B_0, the moment m experiences a torque T_m and precesses about the field direction of B_0. The angular precession frequency ω_0 is proportional to the external field strength and can be expressed by the Lamor Equation 2.2.

$$\omega_0 = \gamma \cdot B_0 \tag{2.2}$$

Nuclei possess only discrete energy levels according to quantum mechanics[1] and these are termed states. A nucleus affected by a magnetic field B_0 has $2 \cdot m_z + 1$ possible values for the angular momentum J. In the human body Hydrogen (^1H) predominates, as living tissue contains about 60 - 80 percent water (H_2O) [79] and hydrocarbons as well as proteins with Hydrogen content. According to quantum mechanics, the proton has only two possible states (Figure 2.1) with the values $m_z = \pm\frac{1}{2}$ and the two energy states, parallel $\uparrow$ or anti-parallel $\downarrow$ in respect to B_0, depend on the internal energy E [80]. In thermal equilibrium and without external magnetic field, the numbers of protons in each state of energy are evenly

[1] Generally, quantum mechanics is required to describe the NMR phenomenon but in the context of this thesis classical mechanics is consulted as intuitive representation and is mostly sufficient once an ensemble of spins according to Niels Bohr's "principle of correspondence" is considered (see Figure 2.1) and their average behaviour can be measured [26].

distributed. The energy gap ΔE (see Figure 2.1) between those two discrete energy bands E_- and E_+ (or $E\uparrow$ and $E\downarrow$) can be expressed by Equation 2.3.

$$\Delta E := E_+ - E_- = \gamma \cdot \hbar \cdot B_0 = \hbar \cdot \omega_0 \tag{2.3}$$

The ratio between the number of spins in the energetic preferred state lower $n\uparrow$ and upper energy state $n\downarrow$ can be described by the Boltzmanns distribution 2.4.

$$\frac{n\uparrow}{n\downarrow} = e^{-\frac{\Delta E}{k_B \cdot T}} \tag{2.4}$$

Whereas, k_B is the Boltzmann constant and T represents the absolute temperature. The difference between the spins in the upper and lower state creates a net magnetisation M_0, which is a vector field representing the density of induced magnetic moments m and is generally expressed by Equation 2.5 per unit volume (the proton density PD represents the number of Hydrogen atoms in a particular volume [26]).

$$M_0 = \frac{PD \cdot \gamma^2 \cdot \hbar^2 \cdot B_0}{4 \cdot k_B \cdot T} \tag{2.5}$$

2.1.2 Magnetic Susceptibility

The magnetic susceptibility χ is a quantitative measure, specific for each tissue and defines by how much a substance becomes temporarily magnetised when an external magnetic field B_0 is applied [26]. Generally, the susceptibility is dependent on the temperature. However, with few exceptions (i.e. during interventional thermal treatments) the tissues relevant for MRI can be considered at constant temperature and, thus, χ may ordinarily be taken to be a scalar and isothermal quantity. For most substances (without initial magnetisation), the magnetisation M is a function of the applied field [81] B_0 and can be written as following:

$$M = \chi \cdot \frac{B_0}{\mu} \tag{2.6}$$

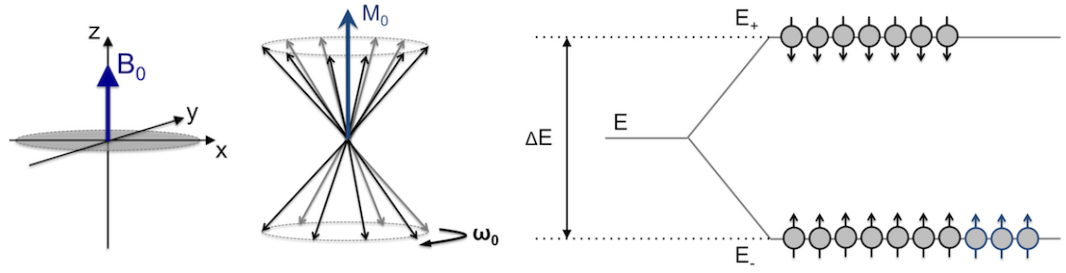

(a) External field B_0 (b) Spin ensemble (c) Energy states for Hydrogen

FIGURE 2.1: Schematic representation of precessing spins and discrete states for Hydrogen - **(a)** An external magnetic field B_0 determines the z-axis of the MRI coordinate system (CS_{MRI}). Each nucleus experiences a torque and precesses with the Lamor frequency about the axis of B_0. The proton has only two discrete states, E_- and E_+ and a small surplus of spins **(b)** is aligned in the in the favoured lower energetic state E_-. This statistical distribution is determined by Equation 2.4 and creates a net magnetisation M_0, which can be used for MRI. Figure **(c)** illustrates the two discrete energy bands E_- and E_+. The energy gap ΔE between is directly proportional to B_0 and the transition between E_- and E_+ is also determined by Equation 2.2 [26].

μ represents the magnetic permeability that is determined by $\mu = \mu_0 \cdot \mu_r$ with the permeability of free space μ_0 and the material dependent term μ_r. The permeability and the susceptibility are related by the following equation:

$$\mu = \mu_0(1 + \chi) \tag{2.7}$$

Most human body tissues are diamagnetic (generally $\chi < 10^{-5}$), for instance, the susceptibility of air and dense bone is close to zero, while iron-containing molecules such as haemoglobin and blood breakdown products have the highest susceptibility [26]. Although the susceptibility χ of tissues is small, the differences between various tissues and air are sufficient to set up substantial local magnetic field gradients G that show up in MRI [26]. If an object with volume V and magnetic susceptibility χ is positioned in a static magnetic field B_0, it will experience the magnetic force F_m in direction of the strongest field gradient G. This is described by Equation 2.8.

$$F_m = \frac{\chi}{\mu_0} \cdot B_0 \cdot \frac{dB_0}{dr} \tag{2.8}$$

Whereas, the field gradient G at the position of the object is defined by $\frac{dB_0}{dr}$.

2.1.3 Excitation

The sections 2.1.1 and 2.1.2 explained that an external magnetic field B_0 creates a net magnetisation M_0 in a large ensemble of protons. However, this is not directly measurable if M_0 is aligned in parallel to the external magnetic field B_0 because this magnetisation is very small (in the order of μT [26]) compared to B_0 (0.2 - 7 T for full body scanners).

A second EM field B_1 is required that can rotate the magnetisation M_0 into the transverse plane where a sensitive receiver can detect a measurable signal $s(t)$. This radio frequency (RF) field is produced by a transmit coil that is orientated perpendicular to B_0. The Maxwell equations [82] form the basis for EM considerations and, thus, the basis of the field distribution of this oscillating B_1 field. The RF waveform is produced either linearly or circularly polarised [8, 26] and requires a carrier frequency f_1 that fulfils the resonance condition $f_1 = \frac{\omega_0}{2\pi}$.

This RF waveform can be used to rotate M_0 away from the longitudinal direction (z-axis) by a certain, so called flip angle (FA). This angle α is the angle between the main field B_0 and the magnetisation vector M immediately after the excitation pulse has terminated [8]. Typically a FA $\alpha = 90°$ or lower is applied to tip the magnetisation vector into the transverse plane (P_{xy}). The kinetics of the magnetisation M in the clockwise rotating reference frame (the precession of the spins appears stopped at $\omega = -\omega_0$ and M becomes a stationary vector [8]) is given by Equation 2.9.

$$(\frac{dM}{dt})_{rot} = \gamma M \times (B_0 + \frac{\omega}{\gamma} + B_1) \overset{(\omega=-\omega_0)}{=} \gamma M \times B_1 \tag{2.9}$$

2.1.4 Relaxation

An RF pulse transfers protons from the lower energy state E_- to the high energy state E_+ (see Figure 2.1). The state E_+ is also stable for the proton and an external field is required to return to E_-. Once the B_1 field has been switched off, however, the magnetisation M relaxes back to equilibrium (longitudinal axis) because neighbouring protons, other nuclei or molecules also possess intrinsic magnetic moments [26], which stimulate this so called spin-lattice or T_1 relaxation effect.

Additionally, a second relaxation effect in the transverse plane (P_{xy}) occurs as soon as the initial magnetisation M_0 is tipped away from the longitudinal axis. This transverse T_2 relaxation arises from energy exchange between spins and is called spin-spin relaxation. This decay of transverse magnetisation is a result of the loss of phase coherence between spins, which arises from either intrinsic or extrinsic magnetic field inhomogeneities [26].

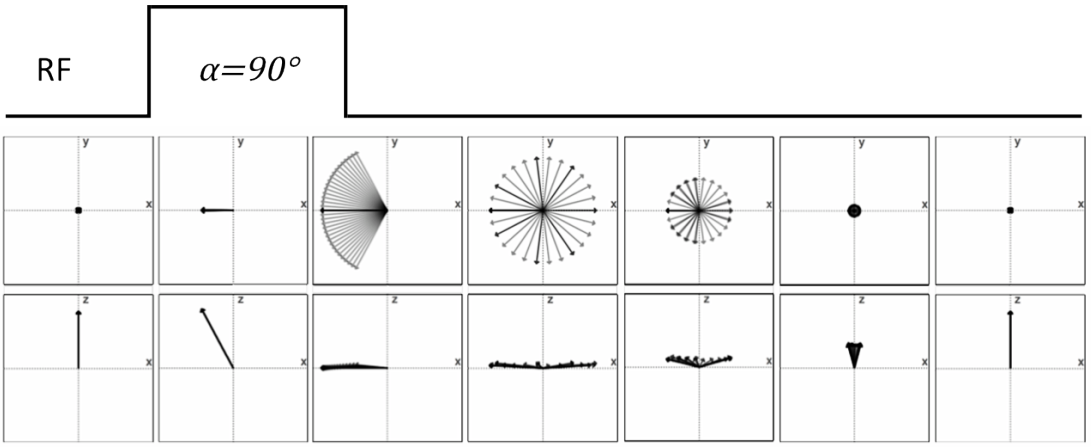

FIGURE 2.2: Spin excitation and relaxation - The top row illustrates the transverse plane (P_{xy}) and the bottom row illustrates the plane P_{xz} with the z-axis from bottom to top. A hard RF pulse with FA $\alpha = 90°$ rotates the spins into the transverse plane (P_{xy}). The RF pulse is then switched off and the spins start to dephase in the transverse plane (top) and to recover towards the longitudinal axis (bottom). Note, the first and the last image show the net magnetisation M_0 in equilibrium. Please also note, individual spins are not diminishing in size but the net magnetisation is.

Figure 2.2 illustrates these relaxation processes. Initially, an RF excitation pulse with a FA $\alpha = 90°$ is used to rotate the magnetisation M_0 into the transverse plane. The spins simultaneously start to recover along the z-axis (with the time constant T_1) and to dephase in the transverse plane (with the time constant T_2).

Figure 2.3 illustrates the oscillating decaying signal in the transverse plane after an RF excitation pulse. This signal is described as free induction decay (FID) and induces a corresponding oscillating voltage in a receive coil, which is sensitive to magnetisation perpendicular to B_0. The black dotted line represents the T_2 decay and the blue dotted line represents the T_1 recovery (Figure 2.4).

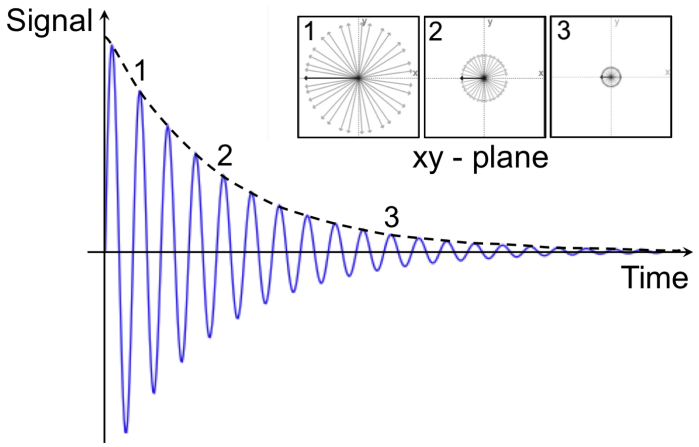

FIGURE 2.3: Free Induction Decay (FID) - The spins are exemplary shown in the transverse plane for three points in time.

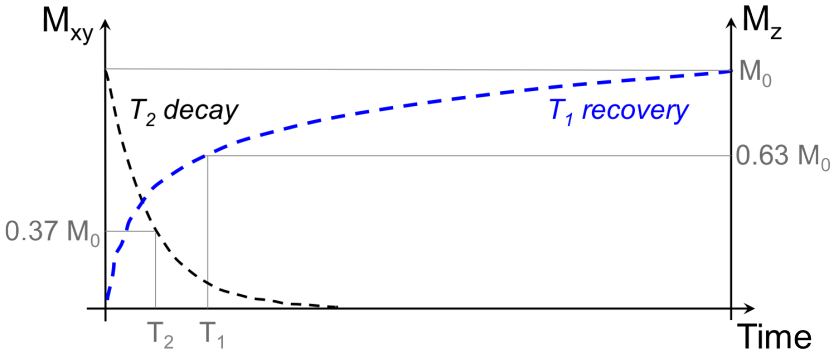

FIGURE 2.4: Relaxation times - The longitudinal magnetisation exponentially recovers with the time constant $T_1 = 0.63 \cdot M_0$ and the traverse magnetisation decays with the time constant $T_2 = 0.37 \cdot M_0$

Felix Bloch derived three differential equations (Equations 2.10) to describe the transition of magnetisation during excitation and relaxation. These equations represent the MRI signal that is detected [26] using receive coils.

$$\frac{dM}{dt} = \gamma \times B = \gamma \cdot \begin{bmatrix} (M_y B_z - M_z B_y)i \\ +(M_z B_x - M_x B_z)j \\ +(M_x B_y - M_y B_x)k \end{bmatrix} \tag{2.10}$$

The following limiting conditions can be applied to solve Equations 2.10 [26]: 1. The B_1 field can be neglected, once the RF pulse is switched off $B_1 = 0$. 2. It can be assumed that the spin system was in equilibrium ($M_x(0) = M_y(0) = 0; M_z(0) = M_0$) and the RF excitation was applied with a FA $\alpha = 90°$ along the

positive x-axis. Hence, the magnetisation immediately after the RF pulse can be expressed by $M_x(0) = M_z(0) = 0$ and $M_y(0) = M_0$. A solution of the differential equations 2.10 with limiting conditions 1 and 2 can then be expressed by Equation 2.11.

$$\begin{bmatrix} M_x \\ M_y \\ M_z \end{bmatrix} = \begin{bmatrix} M_0 \cdot sin(\omega_0 t) e^{\frac{-t}{T_2}} \\ M_0 \cdot cos(\omega_0 t) e^{\frac{-t}{T_2}} \\ M_0 \cdot (1 - e^{\frac{-t}{T_1}}) \end{bmatrix} \tag{2.11}$$

2.2 Image Formation

The signal intensity (SI) in MRI is determined by the local proton density (PD) and the tissue specific T_1 and T_2 values (Figure 2.5). However, spatial encoding is required to create two-dimensional (2D) images. Lauterbur has proposed [7] to use linear magnetic field gradients G for spatial localisation, which is discussed in the following.

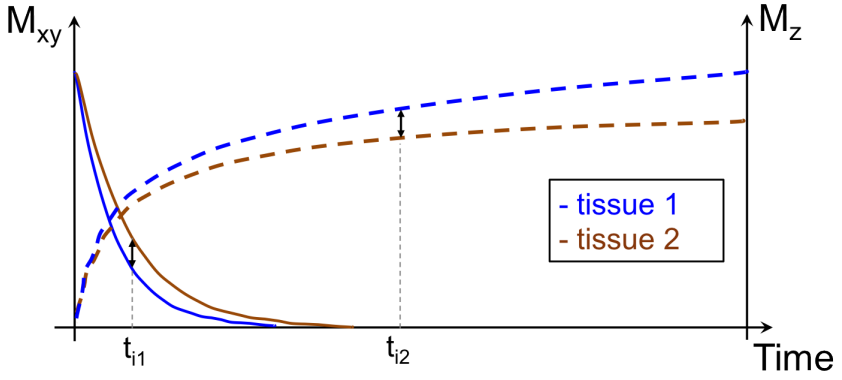

FIGURE 2.5: Tissue dependent relaxation times and contrast weightings - Relaxation curves for two different tissues - the solid lines represent the T_2 decay and the dotted lines the T_1 recovery. Two exemplary time points (t_{i1} and t_{i2}) indicate the signal difference that can be used to create image contrast in MRI.

2.2.1 Slice Selection

A linear magnetic field gradient G applied during RF excitation results in a selection of spins that precess with the Lamor frequency depending on their location in space. An RF pulse is applied with a narrow range of frequencies Δf centred about the Lamor frequency f_0. E.g. the bandwith is expressed by $\Delta f = \frac{\gamma}{2\pi} \cdot z \cdot G_z$ if

a linear magnetic field gradient G_z is applied along the z-axis to create a transverse slice with a slice thickness z.

2.2.2 Frequency Encoding

Linear magnetic field gradients can also be employed during data acquisition to make the magnetic field and thus the precession frequency a function of position. A range of frequencies can be encoded in a single repetition. For instance if a constant gradient G_x is applied along the x-axis, the magnetic field $B(x) = B_0 + G_x \cdot x$ and the precession frequency $\omega(x) = \omega_0 + \gamma \cdot G_x \cdot x$ are functions of the x-position.

2.2.3 Phase Encoding

Again, magnetic field gradients form the basis of this encoding technique. With an RF excitation pulse, spins start to dephase in the transverse plane as described in Section 2.1.4. If for instance, a linear gradient G_y is applied for phase encoding along the y-axis then the dephasing process of the spins is speed up or slow down depending on their position y along the phase encoding axis. The spins will return to their original precession frequency once the phase encoding gradient is switched off, however, the phase difference will remain encoded until the signal decays due to T_2 relaxation [26]. Other than for slice selection and frequency encoding this is a stepwise approach and multiple repetitions with different gradient amplitudes are required to encode all information that is required for a complete image. This is illustrated in Figure 2.6 for 3 different gradient amplitudes. Three-dimensional (3D) imaging can also be achieved by applying the phase encoding principle on a second axis.

The received signal $s(t)$ as sum of all contributing spins can be expressed by solving the Bloch equations 2.10 for $M_{xy} = M_x + iM_y$:

$$s(t) = \int_x \int_y \int_z M_0(x, y, z) \cdot e^{-i2\pi[kx(t)\cdot x + ky(t)\cdot y + kz(t)\cdot z]} dxdydz \tag{2.12}$$

The raw data matrix (k-space) can be filled (see Figure 2.6) line by line using a spatially selective slice excitation (I), a varying phase (II) encoding gradient

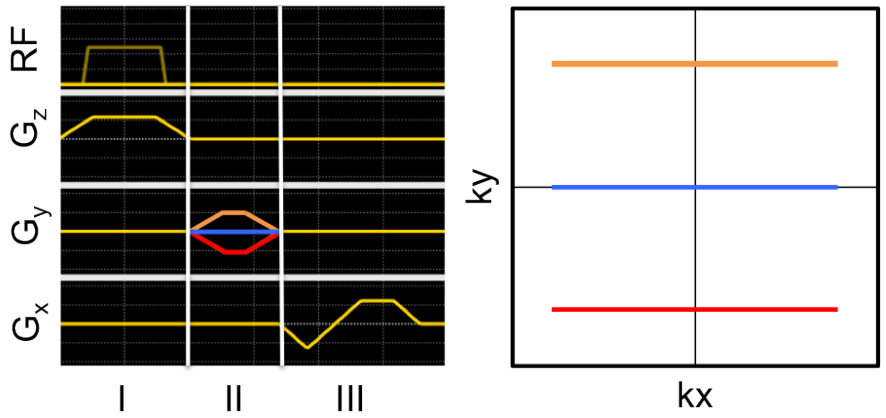

FIGURE 2.6: Pulse sequence diagram that demonstrates how k-Space is filled symmetrically with (I) a slice select gradient, (II) a phase encoding gradient and (III) a frequency encoding gradient. The three different colours for the phase encoding gradient represent a k-space line for the maximum positive, negative and zero amplitude, respectively

amplitude and frequency (III) encoding gradients to encode all required spatial frequencies.

2.2.4 Reconstruction

Images are graphical representations of the spatial distribution of the properties of an examined object [7]. The signals that are received in MRI contain a spectrum of spatial frequencies because magnetic gradient fields are applied for encoding [7]. A mathematical operation is require to generate an image with interpretative voxels from those spatial frequencies. In 1973, Lauterbur proposed to combine several projections obtained by rotating the object about an axis perpendicular to the gradient and then reconstructing the object [7] i.e. via back-projection.

The most frequently used reconstruction method in MRI is a mathematical operation known as Fourier transform (FT) and was firstly applied to MRI [83] in 1975. If a signal i.e. in time domain contains only a single oscillating frequency, then its FT will contain one single peak at this particular frequency. If a signal, however, is composed of a full spectrum of frequencies, its FT provides a histogram of that spectral content [8]. The complex FT $F(k)$ of a function $f(x)$ can be written as 2.13 with the two real variables x and k.

$$FT[f(x)] = F(k) = \int_{-\infty}^{\infty} f(x)e^{-2\pi ikx}dx \tag{2.13}$$

If $F(k)$ is known, the function $f(x)$ can be calculated by performing an inverse Fourier transform FT^{-1} according to 2.14.

$$FT^{-1}[F(k)] = f(x) = \int_{-\infty}^{\infty} F(k)e^{+2\pi ikx}dk \tag{2.14}$$

The FT can also be extended to two or more dimensions. For instance, the two dimensional FT $F(k_x, k_y)$ of a function $f(x, y)$ with the two independent variables x and y can be defined as 2.15.

$$FT[f(x,y)] = F(k_x, k_y) = \int_{-\infty}^{\infty}\int_{-\infty}^{\infty} f(x,y)e^{-2\pi ik_x x}e^{-2\pi ik_y y}dxdy \tag{2.15}$$

However, MR signals are received, sampled and digitised with a discrete (finite) number of complex data points. So instead of a FT, a discrete Fourier transform (DFT) is the practically more efficient operation [8]. The DFT can also be extended to two and more dimensions. The 2D DFT $D(k_x, k_y)$ for a rectilinear input matrix NxM of complex numbers can be written as 2.16

$$DFT[f(x,y)] = D(k_x, k_y) = \sum_{x=0}^{M-1}\sum_{x=0}^{N-1} f(x,y)e^{-2\pi i(\frac{k_x x}{M}+\frac{k_y y}{N})} \tag{2.16}$$

Because a large number of particular values are sampled in MRI [8] the computationally faster fast Fourier transform (FFT) algorithm [84] is most widely used to compute the DFT for image reconstruction in MRI.

2.3 Implementation for Clinical Imaging

In MRI, the FID is not measured directly, instead echos are created with dedicated pulse sequences. An MR pulse sequence describes the RF and gradient field activity to generate an image and can be described graphically by a pulse sequence

diagram. All imaging pulse sequences contain a means of exciting and localizing MR signals [26] and the pulse sequence diagram is illustrating basic hardware activity (see Figure 2.7) to fill k-space and collect data. The vertical axis of the pulse sequence diagram represents the gradient or RF waveforms while the horizontal axis indicates the timing. Gradient waveforms can, generally, be split up in slice selection G_S, frequency G_{FE} and phase encoding G_{PE} gradients.

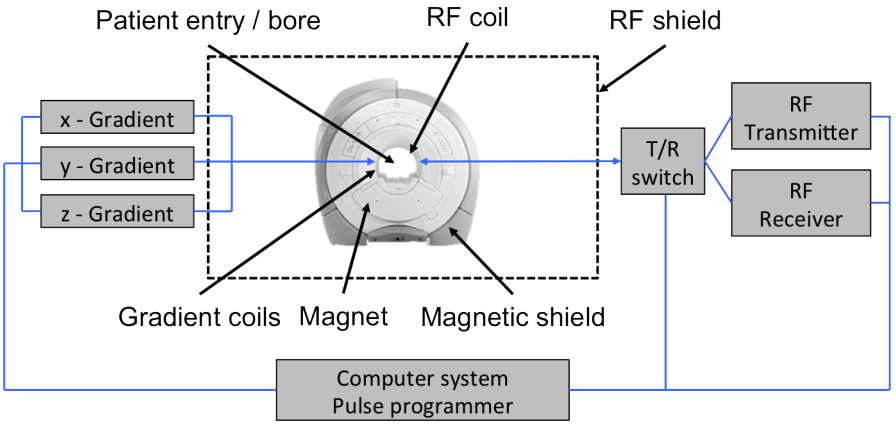

FIGURE 2.7: The basic hardware components and architecture of an MRI scanner (this figure is a modification of Figure 9.1 found in [26] on p. 168)

Pulse sequences can be split into two categories depending on the way an echo is formed: Spin Echo (SE) or Gradient Recalled Echo (GRE) pulse sequences. Both pulse sequence types begin with an RF excitation and use the two parameters echo time (TE) and repetition time (TR) for data acquisition. TE is the time between the maximum amplitude of the RF excitation and the time when an echo is formed, TR is the time between the same successive two RF excitations.

Spin Echo (SE)

The pulse sequence diagram for a single echo SE pulse sequence is illustrated in Figure 2.8. In SE sequences [85] an RF pulse with $\alpha = 90°$ flips the spins into the transverse plane (P_{xy}). The spins then dephase in the transverse plane and a refocusing RF pulse ($\alpha = 180°$) is applied to flip the spins over. This reverses their phase angles and the dephasing direction while the precession frequency is kept constant. The spins that fanned out clockwise before the RF pulse will now rephase anticlockwise and the spins that fanned out anticlockwise will now rephase

clockwise, respectively. An echo will form after the same time interval (TE/2) as between the excitation pulse and the refocusing pulse.

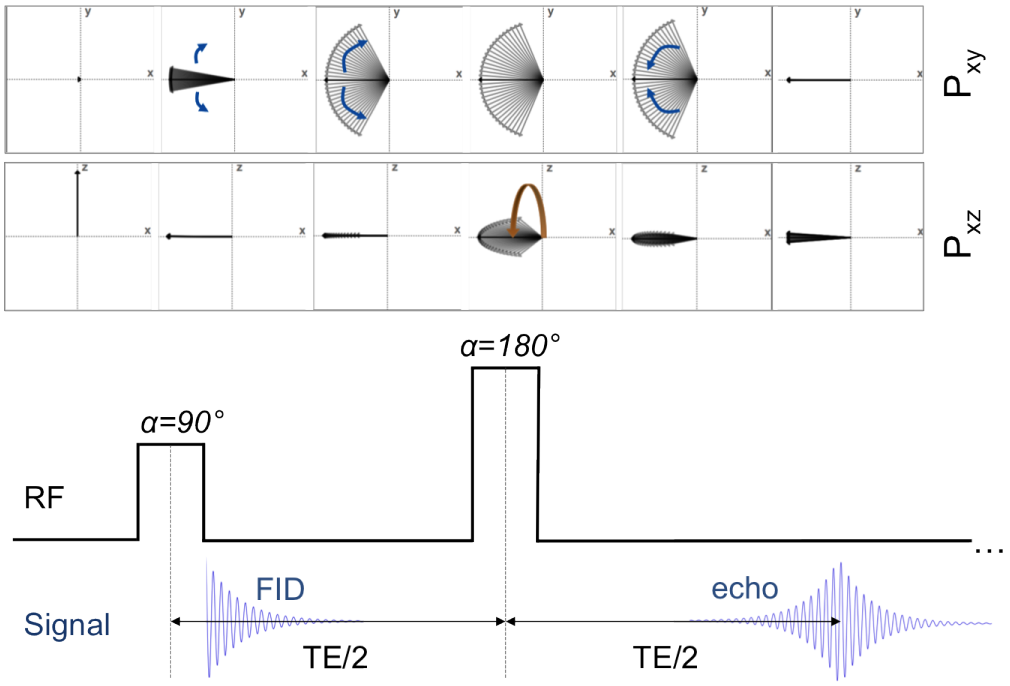

FIGURE 2.8: Spin Echo (SE) pulse sequence diagram (bottom) and spin diagrams (top) - The top row illustrates the transverse plane (P_{xy}) and the row in the middle illustrates the plane P_{xz} with the z-axis from bottom to top. Note, for simplicity no gradient activity is shown for slice selection, frequency and phase encoding.

The signal s_{SE}, considering a net magnetisation M_0 in equilibrium and neglecting T_1 relaxation during the RF excitation pulse, can be expressed [8] according to the Bloch equations 2.10 as the following:

$$s_{SE} = M_0(1 - 2e^{-\frac{TR-\frac{TE}{2}}{T_1}} + e^{\frac{-TR}{T_1}}) \cdot e^{\frac{-TE}{T_2}} \tag{2.17}$$

Hence, SE sequences can generate PD, T_1 and T_2-weighted contrasts according to the combination of the parameters TE and TR.

Gradient Recalled Echo (GRE)

GRE imaging is suitable for fast imaging [86] implementations. The pulse sequence diagram of a GRE sequence is illustrated in Figure 2.9. GRE pulse sequences use an RF excitation pulse but the longitudinal magnetisation is not inverted with

TABLE 2.1: Parameter combination to generate various contrast weightings in Spin Echo imaging [8]

Contrast Weighting	Echo time (TE)	Repetition time (TR)
T_1	Short ($\leq$20 ms)	Short ($<$700 ms)
T_2	Long ($\geq$80 ms)	Long ($>$2000 ms)
PD	Short ($\leq$20 ms)	Long ($>$2000 ms)

a refocusing RF pulse. Instead an echo [8] is generated by gradient reversal on the frequency encoding axis. Firstly, a prephasing gradient with area A causes rapid dephasing in the transverse plane (much faster than the normal FID), then a readout gradient with opposite polarity (area B + B = 2A) causes rephasing and an echo is formed (at the point where area A = B).

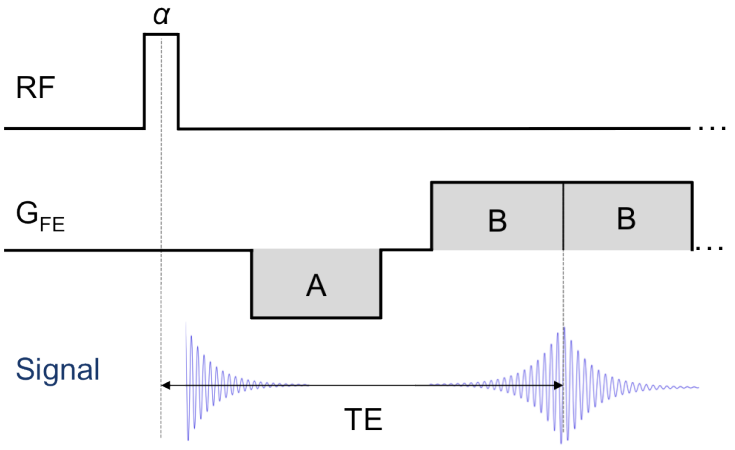

FIGURE 2.9: Gradient Recalled Echo (GRE) pulse sequence diagram. Note, for simplicity no gradient activity is shown for slice selection and phase encoding

The spins accumulate phase in the transverse plane during the entire echo time because no refocusing pulse is used and the two opposite gradients only speed up or slow down the dephasing process. Hence, local field inhomogeneities contribute to the phase evolution of the spins and the factor $e^{\frac{-TE}{T_2}}$ is replaced by $e^{\frac{-TE}{T_2^*}}$ in the signal equation for s_{GRE} in GRE images.

$$\frac{1}{T_2^*} = \frac{1}{T_2} + \frac{1}{T_2'} \tag{2.18}$$

Whereas T_2^* is related to T_2 by the parameter T_2' that is inversely proportional to the magnetic field inhomogeneity ΔB in each imaging voxel [8] $T_2' \propto 1/(\gamma \cdot \Delta B)$.

The magnetic field inhomogeneities are caused i.e. by susceptibility effects due to the imaging object in the scanner and also non-ideal imaging hardware.

Generally, excitation pulses with much smaller FA than $\alpha = 90°$ are used in GRE imaging. This enables rapid repetition and acquisition times because the lengthy T_1 recovery period is significantly reduced compared to SE imaging. The longitudinal component $M(\alpha)_z$ of the magnetisation vector after a small FA RF pulse is not zero as illustrated in Figure 2.10. However, the transverse component $M(\alpha)_{xy}$ is substantial and large enough to be used for imaging. The longitudinal component $M(\alpha)_z$ is not much smaller than the equilibrium value M_0. Hence, the T_1 recovery and full relaxation can be achieved in a very short time.

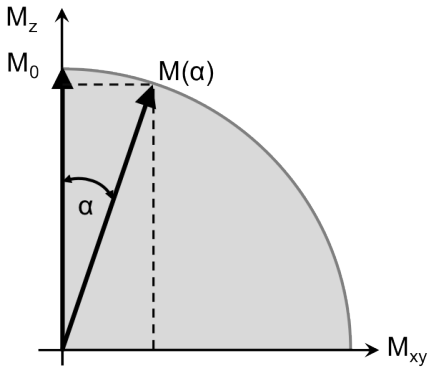

FIGURE 2.10: Response of magnetisation during small FA excitation in GRE imaging. The small FA (α) excitation pulse tips the fully relaxed magnetisation vector M_0 towards the transverse plane P_{xy}. The new magnetisation vector $\vec{M}(\alpha)$ has a large transverse component $M(\alpha)_{xy} = M_0 \cdot sin(\alpha)$ compared to the longitudinal component $M(\alpha)_z = M_0 \cdot cos(\alpha)$

TABLE 2.2: Parameter Combination to Generate Various Contrast Weightings in Gradient Recalled Echo Imaging [26]

Contrast Weighting	**Echo time (TE)**	**Flip angle (FA)** α
T_1	Short (<15 ms)	Large (> 50°)
T_2	Long (>20 ms)	Small (< 40°)
PD	Short (<15 ms)	Small (< 40°)

2.4 Interventional Application of MRI

MRI was primarily developed as diagnostic tool but has experienced a rising demand over the past three decades to be used for guiding and monitoring treatments. MRI is an appealing modality for guiding interventions as it provides contrast between normal and abnormal soft tissues more precisely than any other imaging modality [9]. Utilizing MRI for interventions can provide several benefits for the patients as well as the clinical staff due to its unique potential. MRI can achieve soft-tissue characterisation, multi-planar imaging, temperature monitoring, functional information and near real-time imaging (rtMRI) without exposure to ionizing radiation. Moreover, interventional MRI (iMRI) allows for instant evaluation of therapeutic goals throughout the intervention [4, 9]. Hence, great research efforts have been undertaken to develop new hardware, software, procedures and novel imaging suites [51] that integrate MRI into the clinical workflow of minimally invasive procedures.

Dedicated iMRI scanners have been developed, manufactured and evaluated [87, 88]. Moreover, open and low field MRI systems ($B_0 \leq 1.0$ T) have been used for non-vascular interventions using MRI guidance [89–91]. However, these systems have not developed into mainstream products [26] because the access to the patient is still significantly restricted (small vertical gap and a large distance to overcome between magnet cover and iso-centre). To date, the magnet design for high field ($\geq$1.5 T) MRI systems is restricted to cylindrical closed-bore configurations [92] and systems with a field strength of 1.5 T are used for the majority of interventional procedures due their wide availability [92] and challenges at higher field strengths [23]. These challenges include the necessity for careful shimming and adjustment of the RF frequency to avoid artefacts, increased dark banding artefacts in steady-state free precession sequences, flow artefacts, and SAR restrictions [93] as SAR is proportionally to the square of B_0 [8]. Furthermore, the higher field strength possesses larger safety hurdles to overcome for devices and equipment in the scan room.

2.4.1 Fast Pulse Sequences for Interventions

A great spectrum of MRI pulse sequences has been developed over the years. However, there is no single pulse sequence that meets all requirements for iMRI [42, 94] and a variety of pulse sequences are used during the course of a single procedure.

Interventions have high demands on acquisition speed, spatial resolution and quality of MR images [42]. Therefore, the focus of this section will be on pulse sequences that allow high frame rates and are suitable for interventional imaging. Requirements for iMRI are for instance, suitable image quality and high SNR, good tissue contrast and avoidance of artefacts. Furthermore, it may be required that a pulse sequence is sensitive or insensitive to flow and that multiple contrast weightings can be achieved during the course of an intervention.

Cartesian Pulse Sequences

Spoiled steady state sequences such as fast low-angle shot (FLASH) [86] are frequently used for iMRI as these can provide a variety of contrast weightings [42]. The FLASH pulse sequence takes advantage of small FA excitation that eliminate long waiting periods. After a small excitation interval (without data-acquisition) the spin system reaches a steady state for the longitudinal magnetisation M_z, which is dependent on the repetition time of the RF pulses, their FA, and T_1. Once the system reaches a steady state, images can be acquired without time constraints [86] and residual magnetisation in the transverse plane M_{xy} is spoiled by gradient and/or RF spoiling before the next repetition [26]. The approach to steady state by RF spoiling is illustrated in Figure 2.12.

Steady-state free precession (SSFP) [95] or fully balanced steady-state free precession (bSSFP) [96] pulse sequences are frequently used for iMRI because they can achieve T_2/T_1 contrast [95, 96] and are particular useful to distinguish vessels from surrounding tissue employing high FAs [42, 97]. The residual magnetisation in the transverse plane M_{xy} is rewound before the next repetition, i.e. by balancing or reverting the total gradient area for one or more axis to zero. In a SSFP sequence this can be achieved by adding a second gradient with the same area A

and polarity behind the readout gradient with the area = 2B in Figure 2.9. All gradients are balanced in fully balanced sequences such as bSSFP and additionally phase-alternating RF excitation pulses are used (see Figure 2.11). However, bSSFP is prone to banding artefacts due to off-resonance effects that cause oscillating MR signal from excitation to excitation [26].

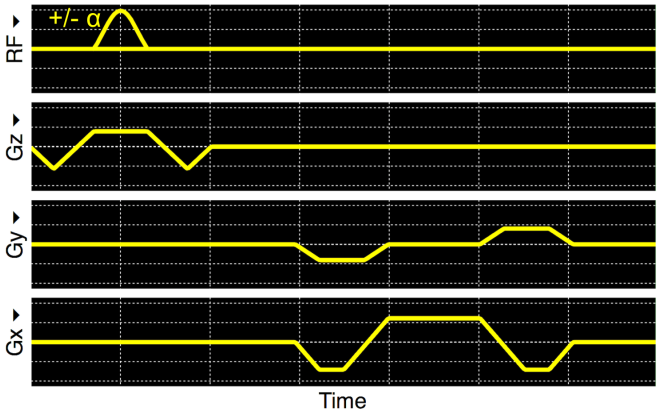

FIGURE 2.11: Pulse sequence diagram of a balanced steady state free precession (bSSFP) sequence. All gradients are balanced and phase-alternating RF excitation pulses (+ and - α) are used.

In their original implementations [86, 95, 96], the pulse sequences that were described in the last paragraph use a Cartesian readout scheme to fill k-space. The scan time is then determined by $t_{scan} = N_{EX} \cdot N_{PE} \cdot TR$. Whereas, N_{EX} is the number of excitations (or averages) and N_{PE} represents the number of phase encoding steps. Pulse sequences with Cartesian readout scheme can be accelerated by re-using specific k-space data [42] points that were acquired in another time-frame i.e. with techniques such as sliding window reconstruction or keyhole methods [98, 99] or by using interpolation methods such as zero padding. Zero padding (or zero filling) describes an effective and widely used reconstruction method for image interpolation. It does not add any information content to the raw data but can effectively increase spatial resolution without increasing the scan time [100].

Non-Cartesian Pulse Sequences

Other fast imaging techniques are based on segmented image acquisition where large parts or the whole k-space are acquired in a single TR using non-rectilinear

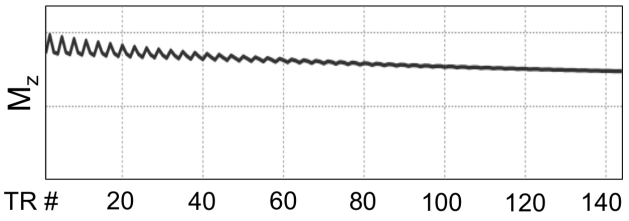

FIGURE 2.12: The longitudinal magnetisation is approaching steady state with a low excitation angle. Simulation performed in SpinBench (Version 1.3.2, HeartVista, Inc., Palo Alto, CA, USA) employing RF spoiling and following parameters: FA = 15°, TR = 5 ms, T_1 = 800 ms.

k-space trajectories (example trajectories are illustrated in Figure 2.13). To date, most clinical MRI pulse sequences use a rectilinear (Cartesian) k-space trajectory [37]. However, certain non-rectilinear trajectories, such as radial or spiral trajectories can provide many benefits for iMRI [42] for instance high temporal resolution or motion insensitivity.

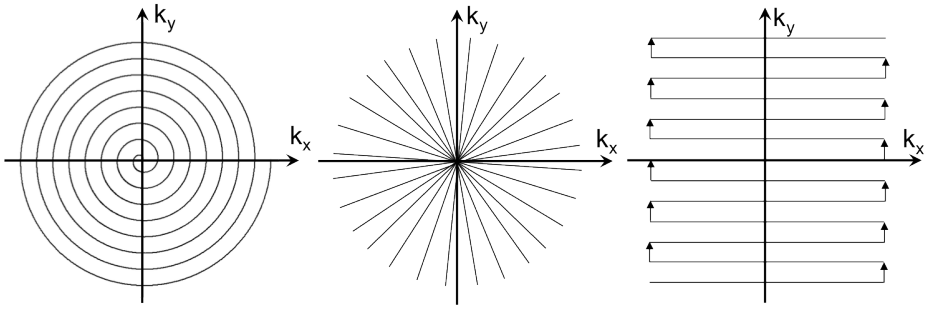

FIGURE 2.13: Three different non-rectilinear k-space trajectories: At the left side a spiral trajectory, in the middle a radial trajectory and on the right side an echo planar trajectory.

A spiral trajectory is a very efficient method of traversing k-space using oscillatory gradients [42] and is frequently used in cardiac imaging. Pulse sequences with an echo planar (EPI) trajectory can also achieve high frame-rates, but suffer from poor SNR, and reduced resolution if large ROIs are examined. Furthermore, these sequences are prone to geometrical distortions and artefacts at tissue boundaries, which make EPI sequences less favourable for abdominal [101] and interventional imaging.

Pulse sequences with a non rectilinear or a non-uniformly sampled k-space trajectory, however, cannot be directly reconstructed with FT or FFT and require advanced reconstruction techniques. A fast and frequently used method for image

reconstruction of such sequences is called gridding. Gridding is an interpolation method that re-samples the data employing a convolution function to a rectilinear k-space grid before a subsequent FFT [8].

As discussed in Section 2.3, SE pulse sequences are less prone to field inhomogeneities than GRE sequences. Hence SE sequences are well suited for imaging of susceptibility artefact prone areas and for imaging interventional devices that have paramagnetic components. The main drawback of SE sequences is that the acquisition time is generally much longer than in GRE sequences. However, a Single Shot Fast Spin Echo (SSFSE) [102] with half-Fourier acquisition can achieve sub-second temporal resolution with a single echo-train and provide excellent T_2-weighted contrast. This pulse sequence is used in a variety of clinical applications such as abdominal imaging and has also been used in percutaneous interventions performed using MRI guidance [103]. The major drawback of SSFSE imaging is that many refocussing RF pulses are required, which result in a significant accumulation of applied RF energy and SAR limitation issues (SAR is proportional to the B_1 amplitude), in particular if used for iMRI. The focus of this thesis is on percutaneous and endovascular interventions and specific considerations for these applications are described in the following.

2.4.2 Percutaneous Interventions

Percutaneous interventions under image-guidance have become an important tool for diagnosis and treatment. In particular, MRI can be valuable for guiding interventions where conventional and well established image-guidance methods such as CT or ultrasound cannot achieve the required sensitivity [24, 59, 104] in terms of lesion detection and avoids potential risks of ionizing radiation and iodine contrast agents [77]. MRI provides superior soft-tissue contrast and native visualisation of blood vessels without the need of contrast agents along with different contrast mechanisms for image acquisition. MRI provides true multi-planar imaging capabilities with arbitrary orientation and consequently allows to interactively align the scan plane according to a instrument trajectory [105]. MRI can be utilised to characterise lesions before, after and moreover during an intervention [24, 106].

MR-guided percutaneous interventions, such as bone and soft-tissue biopsies (breast, liver, kidneys, prostate), drainages, therapeutic instillations (pain therapy and embolisation) and thermal treatments such as tumour ablations [107–109] (uterine fibroids, bone, liver, prostate, breast, brain), have been reported. These were clinically demonstrated using either open low-field [110–113] or closed bore high-field MRI systems [19, 59, 114]. Moreover, robotic assisted and MRI-guided percutaneous interventions (spine and prostate) have been demonstrated [115–117] but have not made the transfer into clinical routine in virtue of remaining workflow challenges, shortage of MRI-safe devices and high costs associated with MRI (see also Section 1.2).

2.4.3 Endovascular Interventions

X-Ray fluoroscopy-guided catheter-based procedures are state of the art treatment of cardiovascular disease. X-Ray provides high temporal and spatial resolution, is cost-effective and widely available. Limitations of X-Ray are poor visualisation of soft tissues (such as those of the cardiovascular system) and the need for nephrotoxic and allergenic iodine-based contrast media [77]. Interventions can be time-consuming resulting in significant ionizing radiation dosage, which can accumulate for the patient throughout the procedure(s) [118]. Moreover, clinical staff working in an angiography suite can be exposed to radiation [118] from several procedures every day. A recent long-term study [119] concludes that an increase in cancer risk is still likely with current low-dose X-Ray technology.

Cardiovascular applications of iMRI have substantial clinical potential [23, 120] because MRI provides superior soft-tissue contrast, sufficient spatial and temporal resolution [23, 92] and multi-planar 3D reconstructions. MR angiography (MRA) can furthermore visualise the anatomy of vessels and its pathologies [23] and also assess the morphology of the vascular wall [121]. Another big advantage is that endovascular procedures are performed according to Seldinger [122] and the percutaneous access site (transfemoral access) can be located in front of the MRI scanner while the the region of interest is positioned in the iso-centre of the

MRI scanner [23]. iMRI has been demonstrated for a variety of endovascular procedures including stenting [123], filter deployments [124, 125], embolisation [126], cardiac electrophysiology mapping during catheterisation [56, 57] and heart valve repairs and replacements [58].

The following section describes the key device categories that are relevant for the research presented in this thesis and outlines distinct requirements for these devices if intended for use during MRI-guided interventions.

2.4.4 Interventional Devices

The EM fields of MRI scanners (see Section 2.3) can interact with electrically conductive interventional instruments such as needles, guidewires [22, 92, 127], metall-braided catheters [51] and implants [21, 36]. In this context, it is important that novel medical implants and devices are designed, assessed and evaluated in terms of MRI usability, performance and safety [21]. The U.S. Food and Drug Administration (FDA) and the International Standards Organization (ISO) have also recognised the need for standardised tests to address MRI safety issues for active and passive medical devices and implants [30, 36, 128–130].

The magnetic susceptibility [29, 81] (see Section 2.1.2) and the electrical conductivity of device components are important parameters for MRI safety [21] and can furthermore be responsible for imaging artefacts [22, 29, 81]. The degree of acceptable image degradation related to a device [30] has to be defined and evaluated for each interventional application [81].

2.4.4.1 Cannulae

Percutaneous needle interventions require needle visualisation relative to surrounding tissues [29] to avoid damage to critical structures such as main vessels. The freehand technique is the most frequently used method for percutaneous interventions using MRI guidance [19, 24, 59, 104, 105, 114, 131] and closely resembles the workflow typically used for CT or ultrasound-guided percutaneous procedures [19]. As rather rigid needles are employed, the most common approach is to make use of the susceptibility artefact caused by the instruments itself [29, 105]. This

approach requires manual scan plane adjustments but is generally well accepted [25, 29, 105, 111, 114] for device visualisation during MRI-guided percutaneous procedures. Thus, no further investigations were performed for cannula visualisation during percutaneous interventions in the context of this thesis.

2.4.4.2 Guidewires

Guidewires are one of the most commonly used tool in the vascular specialists workshop [132] and play a key role for endovascular interventions. The most frequently used diameters are 0.035" or 0.038" during interventions on major vessels and 0.014" or 0.016" for branches and small vessels [132]. Most commercially available guidewires for X-Ray fluoroscopy contain tapered stainless steel rods covered with fine wire spirals or nitinol [22] wire with polymer coating to achieve the required mechanical performance. These components can lead to attraction forces (if ferromagnetic), imaging artefacts and significant local RF induced tissue heating [32, 33, 133] if used during MRI operation.

To date few concepts, *in vitro* [27, 134], animal [135, 136] and first-in-man [137] studies of MRI-compatible guidewires have been published. And only recently the first MRI-safe guidewire has been approved for clinical use. This MRI-safe guidewire received the CE mark in October 2012 based on the collaboration and testing [134, 138] with the author according to ISO 13485 and is described in Section 3.2.1.1. Due to RF induced heating risks and the small diameters of guidewires, the choice of visualisation methods for iMRI is constrained. In this thesis it is therefore proposed to employ passive visualisation methods for guidewires [138]. It should be noted that passive visualisation represents one approach to the problem of visualisation of guidewires in MRI and other methods might be feasible. For instance guidewires incorporating micro receive coils for active tracking have also been proposed [133, 139, 140]. However, studies reported that locally measured temperatures [140] were significantly higher during high SAR conditions than the relevant IEC limits [141]. Moreover, the small diameter of guidewires constitutes a significant challenge for producing guidewires with incorporated micro coils and adequate mechanical properties.

2.4.4.3 Catheters

Catheters are thin and flexible tubes and are used for a variety of medical disciplines to treat disease. In this thesis catheters for endovascular procedures are considered exclusively, which can be used percutaneously using the Seldinger technique [122]. The Seldinger technique achieves access to the vascular system by inserting a catheter over a flexible guidewire through a puncture hole after withdrawal of a puncture needle [122]. A broad array of catheter choices (size, head shape, stiffness) is commercially available for endovascular procedures. Passing a guidewire into the catheter head can modify the head shape [132], which allows entering specific vessel branches. Most catheters are produced with polymeric materials such as polyethylene, polyurethane, polyamide, polytetrauorethylen, or a combination of these [132]. These materials can generally be considered MRI compatible [28]. However, most commercially available catheters are developed for X-Ray fluoroscopy and contain para- or ferromagnetic materials used as braiding in order to improve mechanical and handling performance [22]. This can compromise MRI safety and cause severe imaging artefacts.

2.4.5 Device Visualisation

Suitable visualisation techniques are required to identify and guide instruments to the intended target area. In this context, it can be distinguished between passive identification techniques [142–144], inductively coupling resonant markers [145] and active tracking techniques [146].

2.4.5.1 Passive Markers

Three mechanisms can be used to passively visualise devices in MRI (see Figure 2.14). Firstly, the displacement of water within a voxel by the device itself (absence of water protons), secondly by materials that locally affect the T_1 and T_2 relaxation properties (predominantly one or the other) of the surrounding tissue and thirdly locally induced field inhomogeneities [29] caused by materials with a severely different magnetic susceptibility χ compared to surrounding tissues.

FIGURE 2.14: Passive device visualisation in MRI - The images (B_0 = 1.5 T, FGRE, TE/TR = 3/25 ms, FA = 78°, Matrix = 224 x 224, FOV = 22 cm x 22 cm, Slice thickness = 2 mm) display a short section of a polymer catheter ($\varnothing = 2$ mm (6-F)) inserted into a phantom. Figure **(a)** shows the catheter without any marker substance while the signal void (black dot) is caused by displacement of surrounding water protons. Figure **(b)** shows the same catheter coated with a Gadolinium-based marker (similar to [147]) and **(c)** with a marker containing FePt nanoparticles (nPs) (similar to [148]).

A very high spatial resolution or devices with large diameters are required in order to use the displacement of surrounding water protons alone. If devices with a small diameter and a sufficient temporal resolution are requirements then the second and third method are superior i.e. integrating MRI contrast agents [147] or other paramagnetic substances such as dysprosium-oxide [143] or stainless steel [149] into an interventional device. The main benefit is that these markers are very simple to incorporate into small devices, do not require modifications to the MRI scanner hardware and can be used during most standard imaging pulse sequences. The drawback of paramagnetic substances is that these are relatively expensive and a relatively large volume is required for passive device visualisation.

Contrast agents i.e. containing Gadolinium (Gd) ions (Gd^{3+}) [150] make use of the T_1-shortening effect [147] of surrounding water protons due to the paramagnetic properties of Gd. The advantages of this device visualisation approach are that the visualisation is independent of the orientation with respect to the static magnetic field B_0 [144] and that Gd-based contrast agents are widely available and generally well-tolerated in most patients [150]. Gd-based contrast agents are also useful for visualisation of larger devices with multiple lumen, catheters that can be flushed (while no guidewire is present) or devices with a large fluid reservoir (such as balloon catheters).

Para- or ferromagnetic substances have a susceptibility that is significantly different from water and their appearance in MRI is beyond what is expected on the grounds of displaced water alone [29] as the material disturbs the magnetic

field beyond the voxel [151]. A very small quantity of super-paramagnetic or ferromagnetic materials, with a magnetisation $M > 10^{-4}$ T causes dipole magnetic field distortions (Figure 2.15) and intravoxel dephasing due to a significant difference in magnetic susceptibility [151] between the material and surrounding tissues in the field of view (FOV). The size and shape of these dipole artefacts are greatly dependent on the marker material [152], the imaging pulse sequence including sequence parameters [138] and the orientation in regards to the main magnetic field B_0 [153]. As a result the accuracy of passive device visualisation is limited [29]. However, passive markers made from superparamagetic nanoparticles (nPs) [138] can be realised at micro metre scales and can therefore be applied to small and delicate interventional devices such as guidewires. An additional benefit is that passive visualisation can be employed for different field strengths without modifications to the interventional device. However, the marker size in MR images varies because the susceptibility artefact is dependent on the field strength [153].

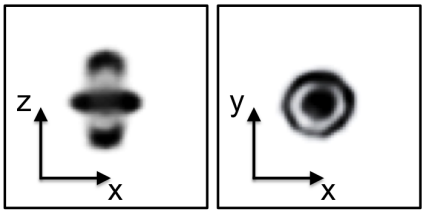

FIGURE 2.15: Dipole magnetic field distortion caused by a superparamagentic (FePt) marker (similar to [148]). MR images (left: coronal, right: axial) were acquired with a FSPGR sequence (TE/TR = 10 / 100 ms, FA = 60°, FOV = 24 cm x 24 cm, Matrix = 256 x 256, Slice thickness = 5 mm) and the background was then subtracted.

It has previously been shown [72, 153–156] that paramagnetic substances can also exploit positive contrast in dedicated pulse sequences. Positive contrast can i.e. be generated by employing dephasing gradients [156], known as the white marker phenomenon, or a method based on a SSFP sequence where gradients dephase any signal at the centred TE while local gradient fields induced by the marker substance compensate for intrinsic dephasing [72]. Another approach makes use of selective excitation [154] or selective suppression [155] using spectrally selective RF pulses. Exploiting positive contrast has also been extended for automated device tracking using a single paramagnetic ring marker attached to a guidewire

[149]. A dedicated tracking pulse sequence employing echo-dephased projections along all three physical axes was used to localise this paramagnetic marker [149]. The drawback is that the susceptibility artefact due to the stainless steel marker was reported relatively large ($\varnothing$ = 20 mm) compared to the guidewire ($\varnothing$ = 0.89 mm) and might mask relevant anatomy. Furthermore, off-resonances and other field inhomogeneities in the body could potentially affect the robustness of this device tracking approach and modifications to the pulse sequence are required if different marker materials are employed [74].

2.4.5.2 Micro Receive Coils

Active tracking was initially proposed by Dumoulin *et al.* [146] and employs one or several small receive coil(s) attached or incorporated into an interventional device. Each micro coil requires an electrical connection to a receiver channel of the MRI scanner. A dedicated tracking pulse sequence, employing one-dimensional (1D) projection readouts, is used for localisation (X,Y,Z) of each micro coil in space. A sharp peak corresponding to the position of a micro coil is measured along the readout axis because the micro coil is sensitive to a very small region only. This tracking technique allows for fast, reliable and highly accurate automated device localisation [146]. Active tracking can furthermore be interleaved with imaging sequences and be used to automatically update the scan geometry and coordinates for the imaging sequence [157].

Standing waves along conducting cables, which approach the quarter wavelength of the RF excitation field in tissue ($\frac{\lambda_{tissue}}{4}$) are the primary source of device heating in the MRI environment [75]. This can be a potential safety hazard for active tracking [31, 33, 34] and temperature rises of more than 50 °C and sparks have been reported [35] for elongated conductive structures [32, 33]. The regulatory hurdles in this context are significant because RF safety throughout the procedure has to be guaranteed [36]. The International Electrotechnical Commission (IEC) issued the following limits for safe use of devices in human subjects [141], which are also accepted by the ASTM [36]: The maximum temperature

increase in normal scan mode is limited to $\Delta 0.5$ °C for the whole body and a maximum localised temperature of 39 °C for the torso.

Various methods such as quarter-wavelength coaxial chokes [158] or integration of transformers into the transmission line [159] have been proposed to eliminate resonant RF heating in active tracking catheters. These have shown to overcome the heating risks but would further increase challenges for the design and production of these, mainly single use, catheters. Hence, widespread use of active tracking in humans during iMRI is still limited due to the system complexity and design challenges [149] to overcome safety hazards and achieve the required mechanical properties (i.e. torque transmission and elasticity) for clinical devices.

Nevertheless, active tracking provides an accurate and reliable solution for clinical applications where the patient and cable connections do not come in contact e.g. for real-time position tracking of an ultrasound transducer during MRI-guided focused ultrasound surgery (MRgFUS) [160].

2.4.5.3 Wireless Resonant Markers

Inductively coupling fiducial markers [145], in the following termed wirelessly connected resonant circuits (wRC), provide an alternative positive contrast technique and wRCs are readily identifiable against the background with standard imaging pulse sequences [161]. wRCs are based on the principle of EM induction, where an electric circuit is tuned to resonate at the Larmor frequency, determined by the field strength of the imaging system (Equation 2.2). The circuit consists of a capacitive element with capacitance C, an inductive element with inductance L and a resistive element with resistance R. This circuit, contains two independent energy storage elements L and C and can therefore resonate. Both, the inductive and capacitive reactance, are frequency dependent and resonance occurs when both reactances cancel. Therefore, a wRC has to be designed and tuned according to Equation 2.19 to match the carrier frequency f_1 of the MRI system.

$$f_r = \frac{\omega_0}{2\pi} = \frac{1}{2\pi\sqrt{LC}} \tag{2.19}$$

The transmit coil of an MRI system produces an RF excitation pulse with carrier frequency f_1. This alternating field (B_1) induces a current in the inductor of the wRC via inductive coupling (see Figure 2.16). This generates a local magnetic flux and causes an intense excitation of the spins in the direct surroundings of the inductive element [145]. Hence, the local B_1 field is amplified and locally increased FAs are produced in close vicinity of the wRC.

A high quality factor $Q(f_r)$ of the wRC results in a significant amplification in central flux and even RF pulses with low FA can result in a substantial rotation of magnetisation in close vicinity of the inductive element [145]. The background, on the contrary, will give relatively little signal compared to the amplified signal [75]. The quality factor Q is a dimensionless parameter that can be used to describe the bandwidth of a resonator in relation to its resonance frequency [162]. Q is defined as 2π times the ratio of the energy that is stored divided by the energy that is lost in a single cycle [163]. The quality factor can also be calculated according to Equation 2.20 by measuring the cut-off frequencies f_L and f_H at -3 decibel (dB) and the resonance frequency f_r.

$$Q = \frac{f_r}{f_H - f_L} \tag{2.20}$$

Generally, wRCs are designed for a specific MRI scanner configuration (vertical or horizontal B_0 field axis) and field strength [164] due to their dependence on excitation frequency (see Equation 2.19) and orientation in regards to transmit and receive coil [75]. The orientation of a device containing a wRC is important in order to accomplish satisfactory coupling to the RF transmit and receive coil(s) (see Figure 2.16). Finding the right coil design is essential for a particular device and application.

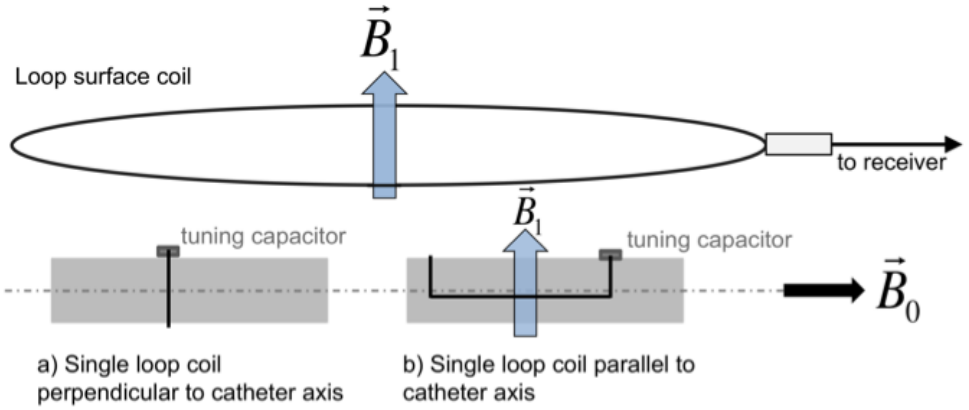

FIGURE 2.16: Schematics of inductive RF signal coupling between a single loop receive coil and two different coil configurations to be used as wRC on the tip of a catheter. Figure **(a)** illustrates a single loop coil in an orientation that results in poor signal coupling and Figure **(b)** a single loop coil in an orientation that that results in maximum signal coupling. During RF transmit mode (not shown), a wRC on the catheter locally amplifies the B_1 excitation field [145]. In RF receive mode, a wRC picks up the MR signal in its immediate vicinity, resulting in a B_1 field vector that inductively couples to the receive coil [75]. Note, this is a modification of Figure 1 found in [75].

Chapter 3

Novel Solutions for MRI Visualisation of Interventional Devices

This chapter has been partially published as:

- **M. A. Rube**, P. Seifert, B. Uihlein, D. Kakchingtabam, P. Andre, A. Melzer, "Novel MR-safe guidewire with passive Iron-Platinum alloy nanoparticles for MR-guided interventions", *in Proc Intl Soc Mag Reson Med 20*, (Melbourne, Australia), p. 4239, 2012.
- **M. A. Rube**, E. Immel, B. F. Cox, A. Melzer, "Towards interventional MRI: Semi-active device localization in phantom experiments and in a Thiel embalmed human cadaver model", *in Proc 26th Int Congr Comput Assist Radiol Surg*, (Pisa, Italy), p. 178, 2012.
- **M. A. Rube**, B. F. Cox, M. Gueorguieva, D. Kakchingtabam, P. Andre, A. Melzer, "Iron-Platinum alloy nanoparticles for guidewire and resonant markers for catheter localization during interventional MRI", *Biomed Tech*, vol. 57(S1), p. 4397, 2012.

Experimental contributions:
(i) B. F. Cox prepared and supervised the human cadaver experiments (the cadavers were embalmed and provided by CAHID). (ii) P. Seifert and B. Uihlein manufactured the guidewire prototypes. (iii) D. Kakchingtabam and P. Andre synthesised the FePt nanoparticles. (iv) M. Gueorguieva provided the code for computing the flip angle maps. (v) B. Cox, A. Melzer and J.G. Houston validated the devices from a clinical perspective.

3.1 Introduction

Endovascular interventions require sequential and combined use of guidewires and catheters, as well as device exchanges [122]. Due to the aforementioned safety and technology challenges (see Section 1.2), there is still a shortage of MRI-safe interventional instruments [27]. Thus, novel devices and materials are required to enable interventional procedures using MRI guidance. Endovascular interventions depend upon a distinct visualisation of catheters and guidewires with respect to the vessels and anatomy of interest. Moreover, it is important to be able to identify each device individually. This is the key reason why different device visualisation approaches were employed in the context of this thesis. It is proposed to use wRCs (Section 2.4.5.3) for catheter visualisation because no electrically conductive connection is required between the marker and the MRI system. This avoids the risk of RF induced heating and reduces system complexity in terms of production and eases procedure workflow [164]. Different optimised marker designs and configurations (single wRC, multiple wRCs or one wRC and passive susceptibility markers) were developed and adapted to the distal shape of a particular catheter or MRI-safe guidewires.

Phantom and Thiel soft-embalmed human cadaver experiments have been conducted to validate the capability of these novel guidewires and catheters for MRI-guided endovascular interventions.

3.2 Materials and Methods

The following sections describe the design of interventional devices such as guidewires and catheters including MRI visualisation methods and how these devices were examined *in vitro* and *ex vivo*.

3.2.1 Device Design

Various devices were developed or modified for iMRI and this section describes the devices in detail.

3.2.1.1 Design of MRI-Safe Guidewires

A polymer-based guidewire, specifically developed for MRI-guided interventions, was manufactured by EPFlex Feinwerktechnik GmbH (Dettingen/Erms, Germany) and refined in collaboration with our group[1]. This guidewire (Figure 3.1) consisted of a high strength fibre (para-aramid synthetic fibre (Kevlar®)) core, surrounded by a bending resistant high performance polymer (Polyether ether ketone (PEEK)) and a hydrophilic coating. The tip section was conically tapered by EPFlex to create an atraumatic tip. The guidewires were supplied with a "J"-shaped or straight tip, a diameter of 0.014" or 0.035" and a length of 150 cm or 180 cm. Guidewires with a diameter of 0.035" were used during interventions on major vessels (Chapter 5 and 6) and guidewires with a diameter of 0.014" were used in smaller branches i.e. during neurovascular interventions (see Chapter 7).

Superparamagnetic nanoparticles (nPs) were applied in distinct locations at the tip section (Figure 3.1c) for iMRI visualisation. The first nPs marker was positioned at the tip and additional markers were applied distally along the tip section. EPFlex then coated the radio-opaque tip section with a copolymer (Polyether Block Amide (PEBAX)) as illustrated in Figure 3.1.

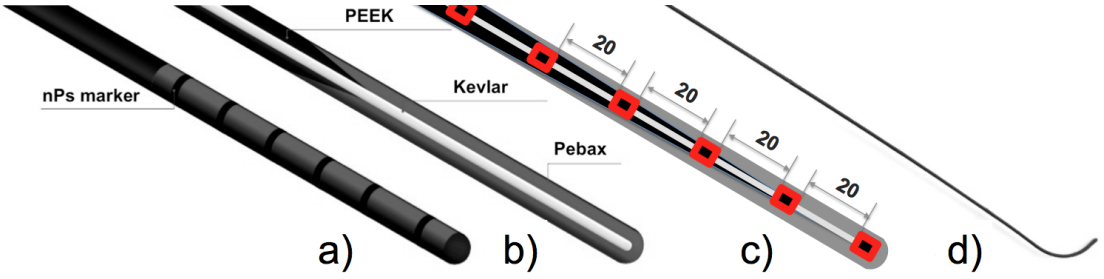

FIGURE 3.1: Illustration of the CE marked MRI-safe PEEK-based guidewire developed at EPFlex in collaboration with the author at IMSaT - **(a)** the hydrophilic coated surface of the guidewire, **(b)** cut through the guidewire illustrating the polymeric components, **(c)** schematic representation of the tip section with the nanoparticles (nPs) markers illustrated in red (spacing in mm) and **(d)** a photograph of the tip section with a "J"-shaped tip.

Two different nP types were selected and evaluated for passive iMRI visualisation. Firstly, commercially available superparamagnetic iron oxide (SPIO) nPs (Nano4imaging GmbH, Aachen, Germany) and secondly, superparamagnetic

[1]Guidewire samples were received from EPFlex during each development and production stage.

iron-platinum alloy (FePt) nPs in a polymeric matrix (FePt nPs). These FePt nPs were developed at the University of St. Andrews as strong T_2 MRI contrast agent with a large T_2 relaxivity (r_2) for biomedical applications [165]. In a static magnetic field B_0, superparamagnetic nPs are magnetised up to saturation magnetisation, while each particle distorts the local magnetic field depending on its magnetic susceptibility. Both employed nPs (FePt and SPIO) have a much stronger paramagnetism than i.e. Gd [26] leading to a magnetic dipole-dipole interaction between the nPs in such a manner that these are aligned following the field lines of B_0 [166] (see Section 2.4.5.1). Like other inhomogeneities in MRI, these nPs cause an acceleration of the dephasing process of protons (leading to a reduction in relaxation times T_2^*, T_2 and also T_1). This inhomogeneity effects extend over a volume many times larger than the actual particle [26]. Thus, very low concentrations are sufficient for passive visualisation in MRI.

Various FePt nPs concentrations (2.5, 5, 20 mg/mL) in a polymeric matrix were compared to commercially available SPIO nPs in order to discover the most suitable material and concentration for marking guidewires to be used in MRI-guided interventions. Thus, seven markers, each 10 μL FePt nPs and 3 mm in length, were distributed over the tip section using a micro pipette (Genex Beta 720080GN, Genex Labratories, Torquay, UK).

3.2.1.2 Design of MRI-Safe Catheters

A set of commercially available non-braided MRI-compatible catheters[2] (Table - 3.1) was prepared for MRI visualisation with wRCs. The wRCs were fabricated either in saddle (Figure 3.2b) or planar rectangular spiral (PRS) coil configuration (Figure 3.2c) using enamelled copper wire (2UEWF, Conrad, Hirschau, Germany) and connected to a non-magnetic surface mounted capacitor (VJ0402, Vishay Intertechnology, Inc., Malvern, PA, US). Each wRC was then tuned to 63.8 MHz or 123.5 MHz (the proton Larmor frequency at 1.5 T and 2.9 T[3], respectively) using a

[2] 4-F, 5-F, and where required 6-F catheters were selected because 4-F and 5-F are the most frequently used flush and selective catheter sizes [132].

[3] Note, that the field strength of the MRI scanner (Magnetom Trio, Siemens Healthcare, Erlangen, Germany) used for the experiments in this chapter was 2.9 T and not 3 T. However, for simplicity, the commonly reported (rounded) value 3 T will be used during this thesis.

spectrum analyser (HMS1000, HAMEG, Mainhausen, Germany), crimped around a catheter and coated with medical grade heat shrink tubing (Advanced Polymers, Salem, NH, US). It has previously been shown [75] that heat shrink tubing provides sufficient electrical insulation and limits tissue loading effects with associated degradation of the quality factor.

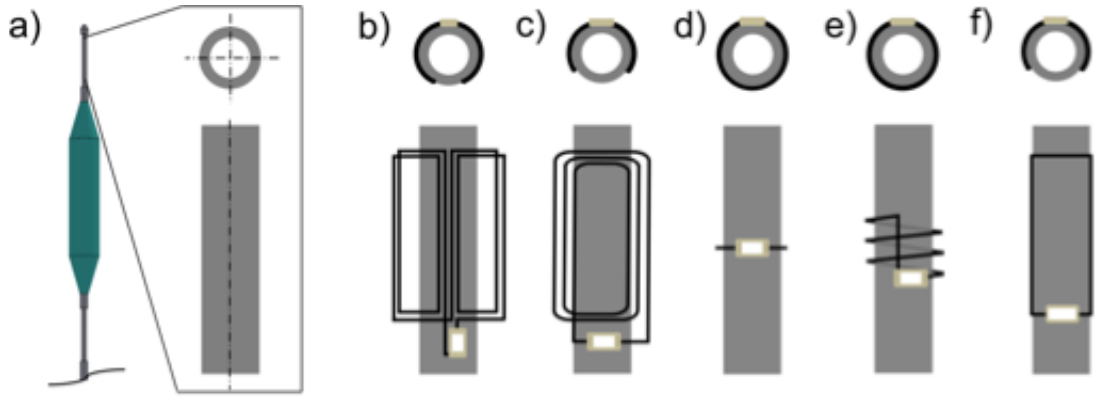

FIGURE 3.2: Schematics of various coil designs for wRCs. **(a)** Exemplary part drawing of a balloon (green) catheter with two grooves for attachment of two wRCs, **(b)** wRC with saddle coil, **(c)** wRC with planar rectangular spiral (PRS) coil, **(d)** wRC with single loop coil parallel to the catheter axis, **(e)** wRC with solenoid coil with pitch with the central axis parallel to the catheter axis and **(f)** wRC with single loop coil perpendicular to the catheter axis. Note, coil designs **(b)**, **(c)** and **(f)** (bottom row) are shown as planar coils and have to be crimped to the catheter (see top row) before the final coating is applied.

Depending on the head shape of a particular catheter different marker configurations were employed: Straight catheters were equipped with a single wRC on the tip (Figure 3.3a - e). Balloon catheters were equipped with either one or two wRC distal and/or proximal to the balloon (Figure 3.3f - j). Multiple markers were applied to selective catheters to visualise the profile and orientation of the tip section during MRI. Thus, the tip section was either marked with several wRCs (Figure 3.3n) or a single wRC on the tip and several FePt nPs [165] markers along the shaft (Figure 3.3l - m)). In contrast to all other catheters, one shaped catheter (C1 - Table 3.1) was prepared to be used at a field strength of 3 T. Furthermore, a custom made non-braided micro catheter (μC1 - Table 3.1) was prepared for small vessels i.e. during neurovascular interventions. The current wRC design is limited to devices with an outer diameter of 1 mm and above. Therefore, iron oxide (FeO) particles (Goodfellow Cambridge Ltd., Huntingdon, UK) were incorporated into

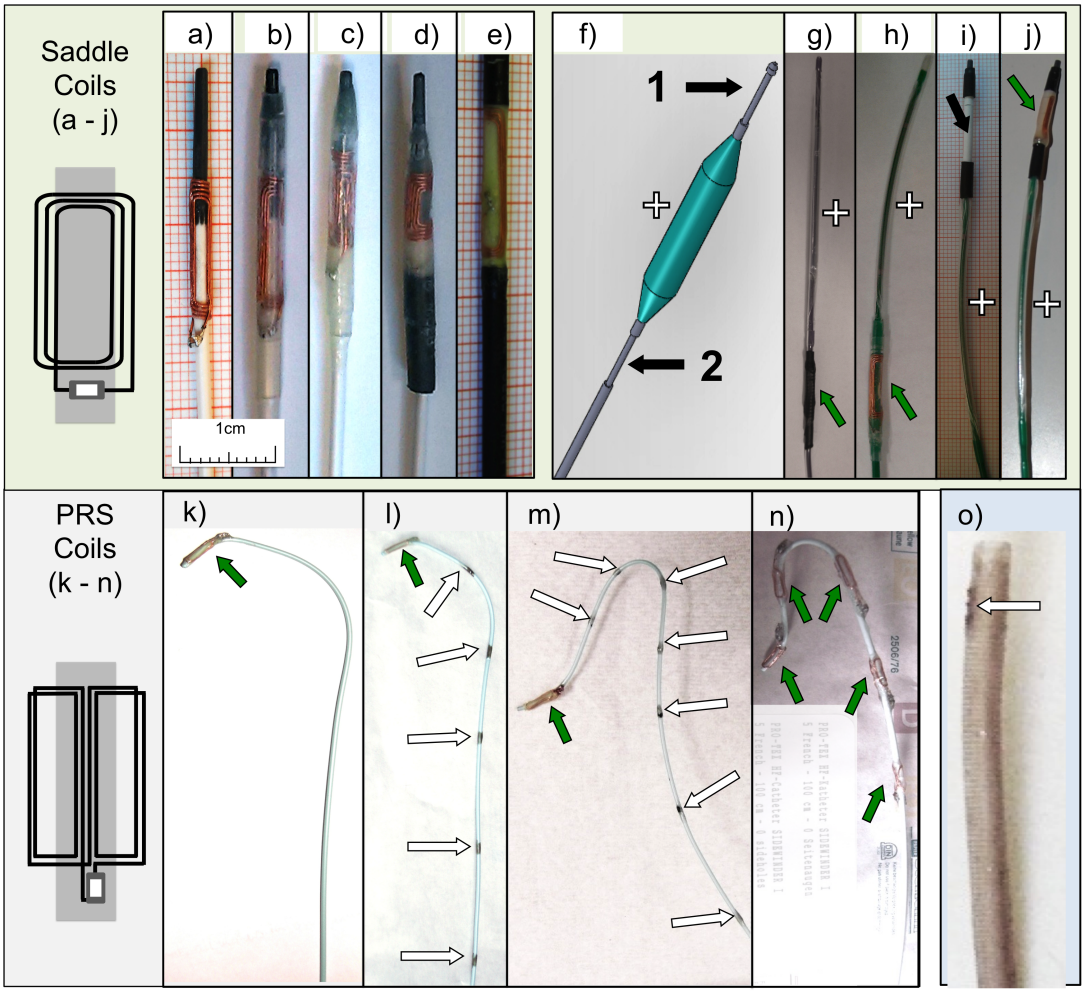

FIGURE 3.3: Photographs of catheters prepared for iMRI visualisation (for details see Table 3.1). The green arrows illustrate wRCs and the white arrows passive markers:

Straight catheters (a - e): **(a)** Catheter with one wRC (S1) before heat shrink tubing was applied in **(b)**, **(c)** catheter with one wRC (S2), **(d)** catheter with one wRC (S3) and **(e)** catheter coated over the whole length to avoid diameter changes.

Balloon catheters (f - j): **(f)** CAD drawing of a balloon catheter indicating the two locations (grooves) for wRCs (1: location behind the tip, 2: location behind the balloon indicated by '+'), **(g)** photographs of a catheter (B1) with a single wRC behind the balloon, **(h)** catheter (B2) with a single wRC behind the balloon, and **(i)** a customised balloon catheter (B3, same model as B2) with an extension to create space (black arrow) for a wRC **(j)** at the tip.

Shaped catheters (k - n): Cobra catheter (C1) with one wRC at the tip before **(k)** and after **(l)** the FePt nPs markers were applied. **(m)** Sidewinder II (SW2) with one wRC at the tip and 7 FePt nPs markers and **(n)** Sidewinder I (SW1) with five wRCs applied at the tip section and along the shaft.

Micro catheter (o): Tip of μC1 with FeO particles tip marker (white arrow).

the tip of this micro catheter. These FeO particles allow susceptibility-based visualisation, similar to what has been described in Sections 2.4.5.1 and 3.2.1.1 for guidewires.

3.2.2 MRI Setup and Protocol

All experiments, except the experiments to assess the catheter (C1 - Table 3.1) that was prepared for 3 T, were conducted at IMSaT in a clinical 1.5 T MRI scanner (Signa HDx, Software release 15.0M4A, GE Healthcare, Waukesha, WI, USA) (see Figure 3.4). Receive coils were selected for each device and study and are reported in the particular sections. When applicable, a novel interventional coil suite "DuoFlex" developed in collaboration with MR Instruments, Inc. (Minnetonka, MN, USA) and GE Healthcare (Waukesha, WI, USA) was used for imaging. The DuoFlex coil suite facilitates access for interventional procedures with different combinations of coil elements (4ch paddle elements [24 cm x 24 cm], 4ch paddle elements [10 cm x 10 cm], 1ch single loop element), which can be plugged into a connector box. The coil suite also supports a lightweight single loop element for interventions with a large opening and an exchangeable soft cover. This soft cover can be covered by sterile drapes and disposed of when contaminated.

The standard GE console and the product rtMRI platform (i/Drive Pro Plus, GE Healthcare, Waukesha, WI, USA) or RTHawk (Version 0.9.28, HeartVista, Inc., Palo Alto, CA, USA) were utilised. The 3T experiments were conducted at the Clinical Research Centre (NHS Tayside and University of Dundee, UK) using a clinical 3 T MRI scanner (Magnetom Trio, Software Release Syngo MR B15, Siemens Healthcare, Erlangen, Germany) with a 12ch head coil (Siemens Healthcare, Erlangen, Germany). A summary of the pulse sequences and parameters for the guidewire and catheter experiments are shown in Table 3.2 and Table 3.3, respectively.

3.2.3 In Vitro Experiments in Tissue Mimicking Phantoms

Basic bench testing was conducted in tissue mimicking phantoms to assess guidewire and catheter performance. If not otherwise stated, the phantoms or vessels of a

TABLE 3.1: Commercially available non-braided angiography catheters customised and prepared for iMRI visualisation.

Ref. #	**Type / ∅ / Length / Lumen / Balloon**	**wRCs: # / Location / Properties**[a]	**nPs Markers: # / Location / Properties**	**Max. ∅**
S1	Straight[b] / 5-F / 70 cm / 0.035" / -	1 / 5 mm from the tip, PRS coil: wire ∅: 0.2 mm, l = 15 mm, N = 5, C = 18 pF, $Q \approx 65$	-	7-F
S2	Straight[b] / 5-F / 70 cm / 0.035" / -	1 / 5 mm from the tip, PRS coil: wire ∅: 0.2 mm, l = 10 mm, N = 5, C = 29.2 pF, $Q \approx 49$	-	7-F
S3	Straight[b] / 5-F / 70 cm / 0.035" / -	1 / 5 mm from the tip, PRS coil: wire ∅: 0.3 mm, l = 8 mm, N = 5, C = 35.7 pF, $Q \approx 51$	-	8-F
B1	PTA Balloon[c] / 5-F / 75 cm / 0.035" / 10 mm x 4 cm	1 / 5 mm behind balloon, PRS coil: wire ∅: 0.3 mm, l = 15 mm, N = 5, C = 22 pF, $Q \approx 68$	-	7-F
B2	PTA Balloon[d] / 5-F / 75 cm / 0.035" / 10 mm x 4 cm	1 / 5 mm behind balloon, PRS coil: wire ∅: 0.3 mm, l = 15 mm, N = 5, C = 27 pF, $Q \approx 61$	-	7-F
B3	PTA Balloon[d] / 5-F / 75 cm / 0.035" / 10 mm x 4 cm	2 / (1) 5 mm from the tip, (2) 5 mm behind the balloon, saddle coil: wire ∅: 0.2 mm, l = 8 mm, N = 2, C_1 = 47 pF, C_2 = 54 pF, $Q_1 \approx 38$, $Q_2 \approx 30$	-	7-F
M1	Multipurpose (MPA)[e] / 6-F / 90 cm / 0.035" / -	1 / 2 mm from the tip, PRS coil: wire ∅: 0.3 mm, l = 10 mm, N = 5, C = 27 pF, $Q \approx 50$	1 / long marker along the tip section (13 cm) / 3 μL/cm of 1.25 g/mL FePt nPs	8-F
C1	Cobra[f] / 4-F / 65 cm / 0.035" / -	1 / 2 mm from the tip, saddle coil: wire ∅: 0.2 mm, l = 11 mm, N = 2, C = 16.9 pF, $Q \approx 28$, f_0 = 123.5 MHz	5 / increasingly spaced at 2 cm, 3 cm, 3 cm, 4 cm, 4 cm / each 7 μL of 1.25 g/mL FePt nPs, l = 5 mm	8-F
SW1	Sidewinder I[f] / 5-F / 100 cm / 0.035" / -	5 / equally spaced every 2 cm, saddle coils: wire ∅: 0.2 mm, l = 10 mm, N = 2, C = 50 - 54 pF, $Q \approx$ 30 - 37	-	8-F
SW2	Sidewinder II[f] / 4-F / 100 cm / 0.035" / -	1 / 5 mm from the tip, saddle coil: wire ∅: 0.2 mm, l = 11 mm, N = 2, C = 51.9 pF, $Q \approx 32$,	7 equally spaced every 2 cm / each 11 μL of 1.25 g/mL FePt nPs, l = 5 mm	7-F
μC1	Micro catheter[g] / 2.6-F / 150 cm / 0.035" / -	-	1 / at the tip - FeO particles (average size 1-6 μm) / L = 1 mm	2.7-F

[a]Design: wire ∅, length (l), number of windings (N), capacitance (C), quality factor (Q)
[b]Beacon Tip Royal Flush, Cook Inc., Bloomington, IN, US
[c]Workhorse II, AngioDynamics, Latham, NY, US
[d]Advance 35LP, Straight, Cook, Bloomington, IN, US
[e]MPA Soft-Vu, AngioDynamics, Latham, NY, US
[f]Pro-tex HF, Somatex, Teltow, Germany
[g]Penumbra, Inc., Alameda, CA, USA

(a) Photograph of the iMRI Setup

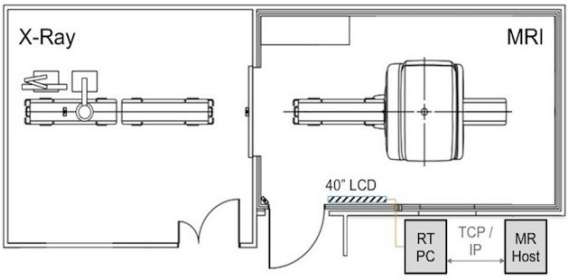

(b) Floor-plan of the iMRI Setup

FIGURE 3.4: Multi-modality setup at the Institute for Medical Science and Technology (IMSaT) in Dundee (first installation in the UK in 2009) - The left room contains a digital subtraction angiographic unit (OEC 9900 Elite, GE Healthcare Systems, Waukesha, WI, USA) and the right room is an RF shielded enclosure with a clinical 1.5 T MRI scanner (Signa HDxt, GE Healthcare, Waukesha, WI, USA). The rooms are interconnected with sliding doors (Imedco, Haegendorf, Switzerland), that shield RF and radiation and allow a patient transfer on a mobile table with radiolucent sliding table top (MR 1050 surgical suite, GE Healthcare and Maquet, Rastatt, Germany). To further assist interventions, a shielded 40" liquid crystal display (LCD) monitor (Multeos 401, NEC Corporation, Tokyo, Japan) was installed and connected to the scan console via optical fibre cables (M1-1000, Opticis, Sungnam City, Korea).

phantom were filled with 0.9% saline solution[4] in order to mimic the electrical properties of blood.

3.2.3.1 In Vitro Evaluation of Guidewires

To date, no dedicated standards for assessing MRI visualisation properties of guidewires are available. Hence, the current ASTM standard test method (F2119-07) for evaluation of MR image artefacts from passive implants [30] was adopted to assess the MRI visualisation properties of the PEEK-based guidewire. A plastic container (l = 16 cm, w = 13 cm, h = 14 cm) was filled with 0.9% saline solution and doped with Gd (1:500) to reduce T_1 relaxation and to keep TR during imaging at a reasonable level. The guidewire was then immersed in the phantom and positioned in an 8-channel (ch) brain coil (HD Braincoil, GE Healthcare, Waukesha, WI, USA) for MRI according to Table 3.2.

[4]The following ingredients were used: 9 g of sodium chloride (NaCl) dissolved in one litre of tap water. This resulted in the following relaxation times measured at 1.5 T and 20 °C: $T_1 \approx$ 1150 ms, $T_2 \approx$ 130 ms.

TABLE 3.2: Summary of the MRI parameters for the guidewire experiments

Parameter	**Diagnostic**				**rtMRI**	
	SE	*GRE*	*WMI bSSFP*	*FSPGR*	*FGRE*	*WMI edSSFP*
TE / TR [ms]	20 / 500	15 / 200	2.4 / 4.8	10 / 100	1.6 / 5.4	4.0 / 8.0
FOV [cm x cm]	25 x 25	25 x 25	20 x 20	40 x 40	40 x 40	40 x 40
Matrix	256 x 256	256 x 256	256 x 256	256 x 256	256 x 256	256 x 256
FA [°]	-	30	80	60	40	50
Slice thickness [mm]	3	3	13	3	4	5

Pairs of images (SE, GRE) were acquired both with and without guidewire in the phantom (as suggested in [30]). The DICOM images were processed and analysed with a commercially available software package (OsiriX Pro 1.04.010, Aycan, Wuerzburg, Germany). The susceptibility artefacts were assessed by computing the differences between guidewire and reference images. Marker sizes were measured according to Figure 3.5 in coronal and axial planes where the signal void of a marker showed a maximum diameter along the long axis **a** (in parallel to B_0). Additionally, rtMRI pulse sequences (FGRE, FSPGR) were selected to evaluate the visualisation performance for MRI-guided interventions.

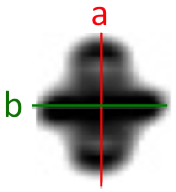

FIGURE 3.5: Measurement of the signal void induced by a passive susceptibility marker: **a** denotes the long axis (in parallel to B_0) and **b** the short axis (perpendicular to B_0). Note, **b** represents the size along the x-axis, which is equivalent along the y-axis due to radial symmetry [72, 151].

While passive markers generally result in signal voids as the means for detection (negative contrast) [154], it can be beneficial i.e. for localisation, if these can be visualised with positive contrast while the background signals are suppressed. This phenomenon is commonly known as white marker imaging [151] (WMI). Two different WMI techniques were implemented in this thesis for guidewire visualisation. Firstly, WMI based off-resonance excitation [73] (WMI bSSFP), whereby off-resonance excitation generates positive contrast of the susceptibility markers

TABLE 3.3: Summary of the MRI parameters for the catheter experiments

Parameter	1.5 T (GE)						3 T (Siemens)	
	Diagnostic					rtMRI	Diagnostic	rtMRI
	GRE	*FGRE*	*FIESTA*	*SPGR*	*FSE*	*RT FGRE*	*3D FLASH*	*RT FLASH*
TE / TR [ms]	15 / 500	4.0 / 7.7	1.1 / 3.7	3.7 / 8240	14 / 425	1.5 / 5.3	3.4 / 8.8	3.4 / 8.8
FOV [cm x cm]	32 x 32	25 x 25	25 x 25	20 x 20	40 x 40	40 x 40	17 x 19	20 x 20
Matrix	256 x 224	256 x 256	256 x 256	256 x 256	256 x 256	256 x 256	256 x 224	256 x 224
FA [°] / ETL	30	30	5 - 90	5 - 90	$ETL = 4$	20	14	12
Slice thickness [mm]	3	7	10	6	10	5	0.74	3

compared to their background [73]. Secondly, an echo-dephased steady state free precession sequence (WMI edFFSP) [72] was implemented, which can achieve complete background suppression while hyper intense signals in close vicinity of passive susceptibility markers are preserved [72]. Note, the imaging parameters are also presented in Table 3.2.

3.2.3.2 In Vitro Evaluation of Catheters

The modified catheters (Table - 3.1) were tested in plastic phantoms or arterial vessel replica models (left lower extremities (LE): L-F-S-Left-003 or head model: H+N-S-A-10, Elastrat, Geneva, Switzerland). Please note that all pulse sequences and parameters are summarised in Table 3.3. Preceding experiments [167] have demonstrated that quantitative predictions of the coupling properties and resulting signal enhancement of wRCs were found very challenging due to the aforementioned coil orientation (Figure 2.16) and imaging parameter dependence (Section 3.2.1.2). Therefore, a double angle method (DAM) [168] was implemented to evaluate the orientation dependence and the related coupling effects of wRC configurations to be used on catheters. Pairs of MR images (SPGR) with $FA_2 = 2 \cdot FA_1$ were acquired using an 8ch brain coil (HD Braincoil, GE Healthcare, Waukesha, WI, USA). FA maps were then computed using a commercially available software package (MATLAB 2009a, The Mathworks, Natick, MA, US) according to what has been proposed by Cunningham and colleagues [168].

Catheters with a Single wRC: Straight and balloon catheters (S1 - S3, B1, B2 - Table 3.1) with a single wRC were positioned in a plastic phantom (l = 18 cm, w = 10 cm, h = 10 cm). rtMRI (FGRE) was performed with the DuoFlex

interventional coil prototype (see page 51) using a 4ch 24 cm element combined with the single loop element with disposable cover.

Catheters with Multiple wRCs: Varying the excitation angle (FA) can affect the visualisation of wRCs as previously described by Quick *et al.* [75]. Thus, a balloon catheter (B2 - Table 3.1) with two wRCs, each with a different quality factor ($Q_1 \approx 37$, $Q_1 \approx 30$) was therefore inserted in the LE vessel model for MRI. The signals induced by each wRC in comparison to the background signals were then investigated (FIESTA) as a function of the FA using a commercially available software package (Osirix 32bit, version 5.5, Pixmeo Sarl, Geneva, Switzerland). The contrast-to-noise ratio (CNR) was determined by the signal intensity (SI) difference between wRC and background and normalised against the background noise [75].

To evaluate multiple wRCs for catheter shaft visualisation, a sidewinder catheter (SW1) equipped with five wRCs was positioned in a plastic phantom (l = 24 cm, w = 24 cm, h = 10 cm) and evaluated using rtMRI (RT FGRE).

Catheters with one wRC on the Tip and Passive Markers Along the Shaft: A sidewinder II catheter (SW2 - Table 3.1) was evaluated for iMRI at a field strength of 1.5 T *(i)*. Firstly, the susceptibility artefacts induced by the FePt nPs markers were measured (GRE) (according to [30]). Secondly, the catheter was navigated in the LE vessel model while rtMRI scans (RT FGRE) were obtained to assess the navigation properties. As mentioned in Section 3.2.1.2, one shaped catheter (C1 - Table 3.1) was also prepared to be used at a field strength of 3 T. Therefore, high spatial resolution (3D FLASH) and rtMRI (RT FLASH) of the catheter in a plastic phantom (l = 24 cm, w = 24 cm, h = 10 cm) was conducted in a 3 T MRI scanner *(ii)*.

Micro Catheter: The micro catheter (μC1 - Table 3.1) with a passive marker on the tip was evaluated for iMRI. The size of the susceptibility artefact was measured during MRI (GRE - Table 3.3) according to Figure 3.5. The catheter was then navigated in an arterial head model while rtMRI scans (RT FGRE -

Table 3.3 and edSSFP - Table 3.2) were obtained with the DuoFlex interventional coil prototype (see Section 3.2.2).

RF Induced Heating Experiments: RF induced heating was evaluated during MRI according to the ASTM protocol (F2182-09), originally developed for RF induced heating on or near passive implants [36]. To consider the worst-case scenario, the catheter (S1 - Table 3.1) equipped with the wRC providing the highest quality factor ($Q \approx 65$) was assessed. The temperature was recorded with gallium arsenide temperature sensors connected to a measurement unit (Fotemp4, Optocon AG, Dresden, Germany) via optical fibre cables. The measurement unit (temporal resolution: 4 seconds, overall measuring accuracy: $\pm$ 0.2 °C) was positioned outside of the Faraday cage and the optical fibre cables were fed through the wave-guides in order to connect the temperature probes. Three probes were then attached to the wRC (distal, medial, proximal) and one probe to the patient table to be used as reference. The wRC was positioned in a head-torso phantom (head: l = 27 cm, w = 15 cm, h = 9 cm / torso: l = 65 cm, w = 42 cm, h = 9 cm) filled with a tissue equivalent gel[5] to prevent heat convection. Fast spin echo [36] (FSE) imaging was performed in a 1.5 T MRI scanner (see Section 3.2.2) using the integrated body coil (transmit/receive). This sequence was prescribed for approximately 15 minutes and produced an averaged whole body SAR of 2 W/kg.

3.2.4 Ex Vivo Experiments in Thiel Embalmed Human Cadavers

All human cadavers used in the context of this thesis were donated according to standard procedures as set out in the Human Tissue (Scotland) Anatomy Act 2006, and the Thiel Advisory Committee (University of Dundee, UK) has approved all procedures involving human cadavers. The cadavers were embalmed according to the Thiel soft-fix embalming method as currently in use at the Centre for Anatomy

[5]Ingredients according to [36]: H_20, 1.32 g/L NaCl, 10 g/L poly-acrylic acid partial sodium salt (PAA) (Sigma Aldrich Corp., Saint Louis, Missouri, USA), electrical conductivity: $\sigma = 0.47$ S/m $\pm$ 10% at $f = 63.8$ MHz

and Human Identification (CAHID) in Dundee [169]. Two Thiel soft-embalmed human cadavers (female, approximated age: 60 - 85, approximated weight: 65 - 85 kg) were prepared in the angiography suite and then transferred to the MRI suite (Figure 3.4). Vascular access was established with 12-F introducer sheaths (Cook Medical, Bloomington, IN, USA) placed into the right femoral vein and left femoral artery. Please note, the large diameter sheaths were required to partially block off the vessels for subsequent perfusion experiments. The vessels were then flushed with Thiel moistening solution before the abdomen of a cadaver was positioned in an 8ch body array coil (FullFOV, GE Healthcare, Waukesha, WI, USA).

3.2.4.1 Ex Vivo Evaluation of Guidewires

According to the results of the preceding phantom experiments the marker solvent with 20 mg/mL FePt nPs was chosen and employed for the cadaver experiments. The guidewires were inserted through the sheath and then navigated using rtMRI guidance (FGRE). Two experienced interventional radiologists evaluated overall guidewire visibility and mechanical performance (pushability, torque and gliding properties) during navigation to the target vessel segment (vena cava).

3.2.4.2 Ex Vivo Evaluation of Catheters

In the first cadaver, a straight catheter (S2 - Table 3.1) equipped with one wRC on the tip was inserted over a guidewire (Section 3.2.1.1) and positioned in the left common iliac artery. In the second cadaver a balloon catheter (B3 - Table 3.1) equipped with two wRCs was introduced over the MRI-compatible guidewire and positioned in the left common iliac artery while diagnostic (FSPGR) and rtMRI (FGRE) scans were obtained.

3.3 Results

The results for *in vitro* and *ex vivo* validation for the developed guidewires and catheters are presented in the following:

3.3.1 In Vitro Evaluation of Developed Devices

This section describes the results of the device validation in tissue mimicking phantoms. During these *in vitro* experiments, all devices with their applied markers showed no macroscopic evidence of fracture or kinking and remained patent.

3.3.1.1 In Vitro Evaluation of Guidewires

Figure 3.6 illustrates MR images of the guidewire containing FePt nPs (20 mg/mL) markers for visualisation. The signal voids were found dependent on various imaging parameters and the orientation in the scanner. The artefact size was found mainly dependent on the guidewire orientation in respect to B_0 and was increasing with TE. The long axis **a** of the susceptibility artefacts aligned with the field lines of B_0 (Figure 3.6). The measurements of the susceptibility artefacts resulting from the different nPs markers on the guidewires are summarised in Table 3.4. This table illustrates the induced artefact sizes during SE and GRE imaging according to the ASTM protocol (F2119-07) [30] and during FSPGR imaging optimised for subsequent cadaver experiments. Additionally, it was feasible to visualise the markers on the guidewire with positive contrast. This is demonstrated in Figure 3.6b. The markers were visualised with high SIs while background suppression was achieved using WMI (Figure 3.6).

3.3.1.2 In Vitro Evaluation of Catheters

Figure 3.7 illustrates FA maps, which were computed for different coil configurations to be used as wRC on catheters. Both coil designs showed areas in close vicinity of the wRC with significantly amplified FAs for all orientations but one. In this particular orientation the FA amplification effect was less pronounced. For the single loop coil the area of amplified FAs was minimal ($FA_{max} = 54°$) if the coil was contained in the transverse plane P_{xy} (see the image in the middle of Figure 3.7a). Saddle coils showed a weaker signal amplification if the main axis was orientated in parallel to the transverse plane P_{xy} (see the image in the middle of Figure 3.7b). However, this effect was less distinct for the saddle ($FA_{max} = 57°$) than for the loop coil.

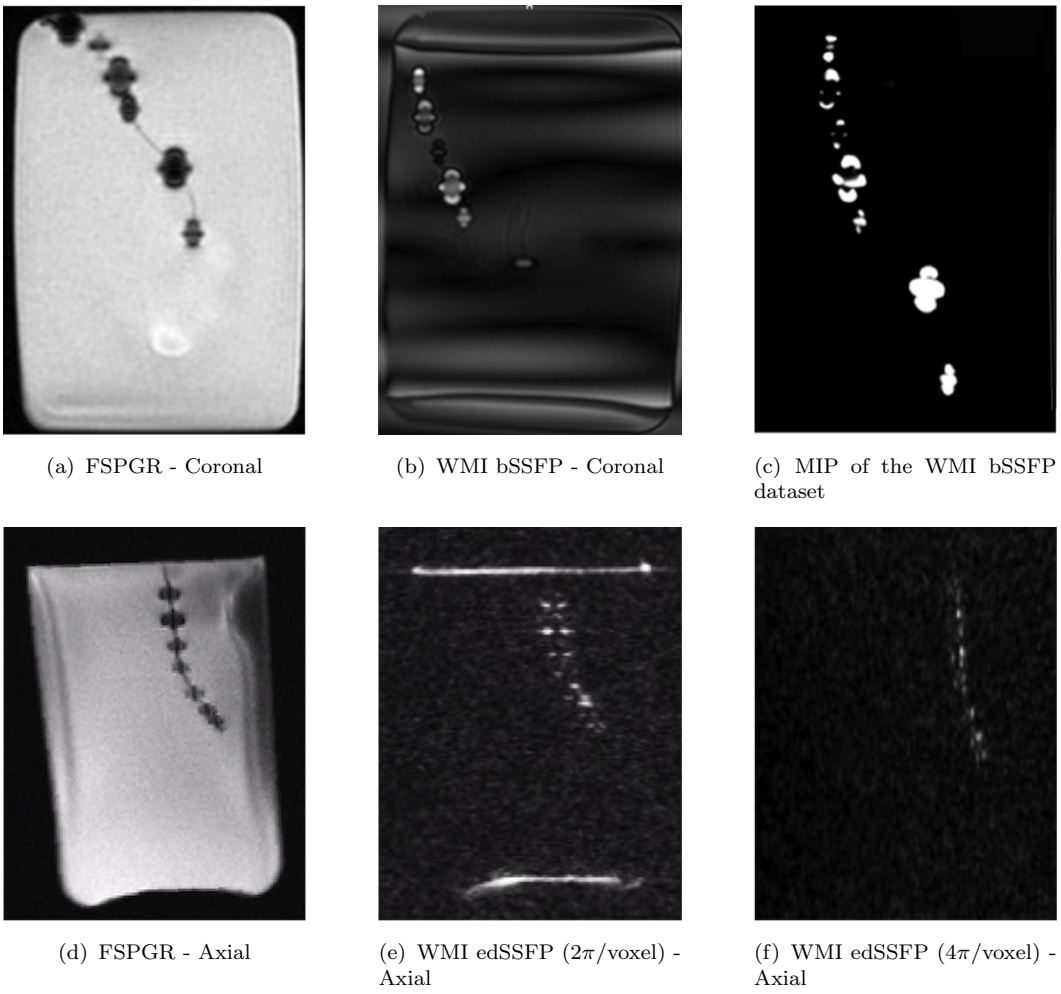

(a) FSPGR - Coronal

(b) WMI bSSFP - Coronal

(c) MIP of the WMI bSSFP dataset

(d) FSPGR - Axial

(e) WMI edSSFP (2π/voxel) - Axial

(f) WMI edSSFP (4π/voxel) - Axial

FIGURE 3.6: Visualisation of the MRI-safe guidewire prototype (FePt nPs (20 mg/mL) markers): Images were obtained with FSPGR in **(a)** and **(d)** and WMI bSSFP employing off-resonance excitation in **(b)**. Figure **(c)** shows a MIP of the WMI bSSFP dataset. Figures **(e)** and **(f)** were obtained with echo-dephased steady state free precession (WMI edSSFP) imaging resulting in incomplete background suppression in **(e)** (dephasing of 2π/voxel in the readout direction) and complete background suppression in **(f)** (dephasing of 4π/voxel in the readout direction). Note, the sequence parameters are summarised in Table 3.2.

Catheters with a Single wRC: Figure 3.8 illustrates straight (a - c) and balloon catheters (d, e) that were imaged in a phantom. The quality factor of each wRC significantly affected the signal characteristics in MRI. A locally increased SI was visible at the location of each wRC (Figure 3.8). Note, a comparative analysis of how different quality factors affect the signal amplification is described in the following paragraph.

TABLE 3.4: Measurements (according to Figure 3.5) of the induced susceptibility artefacts caused by nPs markers on the MRI-safe guidewire - The images (SE, GRE) were obtained according to the standard protocol [30] and with a pulse sequence optimised sequence for Thiel cadaver imaging (FSPGR). Note the sequence parameters are summarised in Table 3.2).

Pulse Sequence	**nPs**	**Concentration [mg/mL]**	**Size (a) [mm]**	**Size (b) [mm]**
SE	FePt	2.5	2 - 3	2 - 3
		5	2 - 4	2 - 3
		20	3 - 6	3 - 5
	SPIO	n/a	7 - 8	6 - 8
GRE	FePt	2.5	3 - 5	2 - 4
		5	4 - 7	4 - 6
		20	7 - 13	6 - 11
	SPIO	n/a	12 - 16	13 - 15
FSPGR	FePt	2.5	5 - 8	3 - 6
		5	6 - 9	4 - 8
		20	12 - 15	9 - 13
	SPIO	n/a	13 - 15	10 - 12

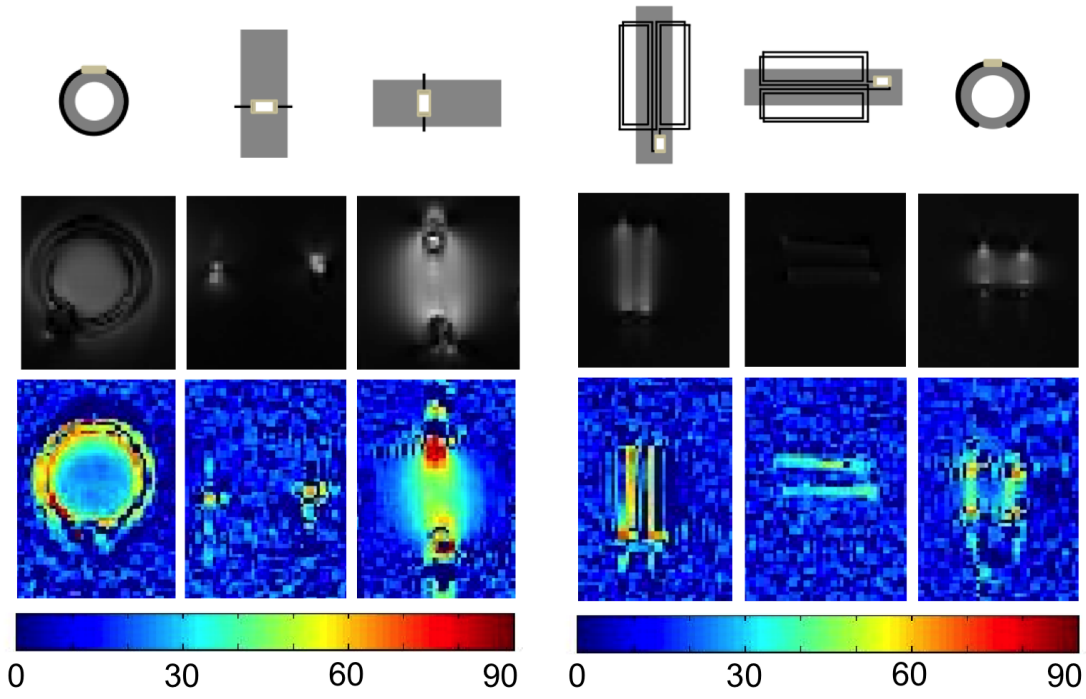

(a) Single Loop Coil (b) Saddle Coil

FIGURE 3.7: Colour coded FA maps of wRCs with different coil configurations - **(a)** Single loop coil (Figure 3.2f) and **(b)** saddle coil (Figure 3.2) configuration. The wRCs were positioned in three different orientations in regards to B_0. The orientation is illustrated above each FA map and the magnitude image (FA = $FA_1 = 10°$). Note, the main axis of B_0 (z-axis) is from bottom to top and the x-axis from left to right.

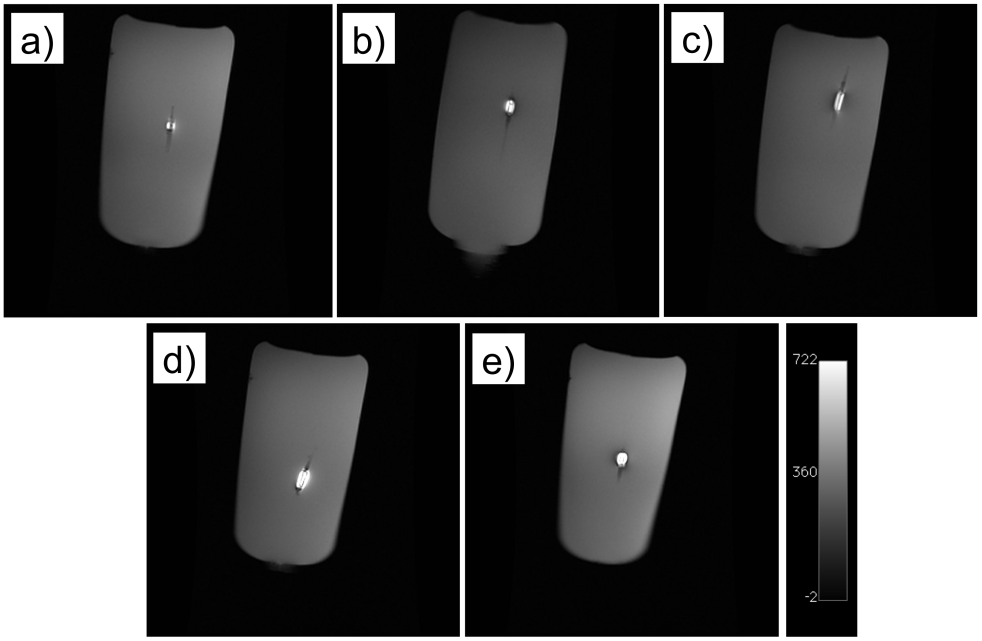

FIGURE 3.8: MR images (FGRE - Table 3.3, same window level) obtained for a phantom and various catheters (Table 3.1) equipped with a single wRC. Figures **(a - c)** show straight (**(a)**: S3, **(b)**:S2, **(c)**:S1) and Figures **(d - e)** show balloon catheters (**(d)**: B2, **(e)**:B1).

Catheters with Multiple wRCs: The quality factor of a wRC significantly affects the signal characteristics in MRI (see Section 2.4.5.3). The phantom experiments with the balloon catheter (Figure 3.9) demonstrate that during imaging with low FA ($\leq 5°$), signals were predominantly obtained from the two wRCs while signals from the background were suppressed. Similar to what has been reported by Quick and colleagues [75], imaging with intermediate FAs provided simultaneous wRC and anatomic visualisation, and high FAs provide solely anatomic visualisation.

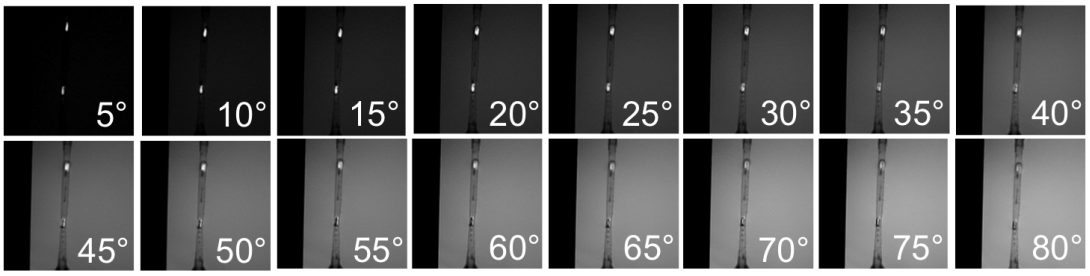

FIGURE 3.9: Two wRCs on a balloon catheter (B3 - Table 3.1) inserted in the arterial vessel phantom. MR images were obtained (FGRE - Table 3.3) while the FA was varied.

The wRC with higher quality factor ($Q_1 \approx 38$) resulted in an area with higher SIs in particular for low FAs with maximum SI and CNR at a FA of 10° (Figure 3.10). The wRC with the lower quality factor ($Q_2 \approx 30$) resulted in lower SIs (compared to the wRC with Q_1) with a maximum SI (Figure 3.10) and CNR if a FA of 15° was used. For intermediate FAs, the wRC and the background tissues were both visible. However, no signal increase (compared to the background) was obtained using high FAs (Q_2: CNR = 0 at FA = 48° and Q_1: CNR = 0 at FA = 73°).

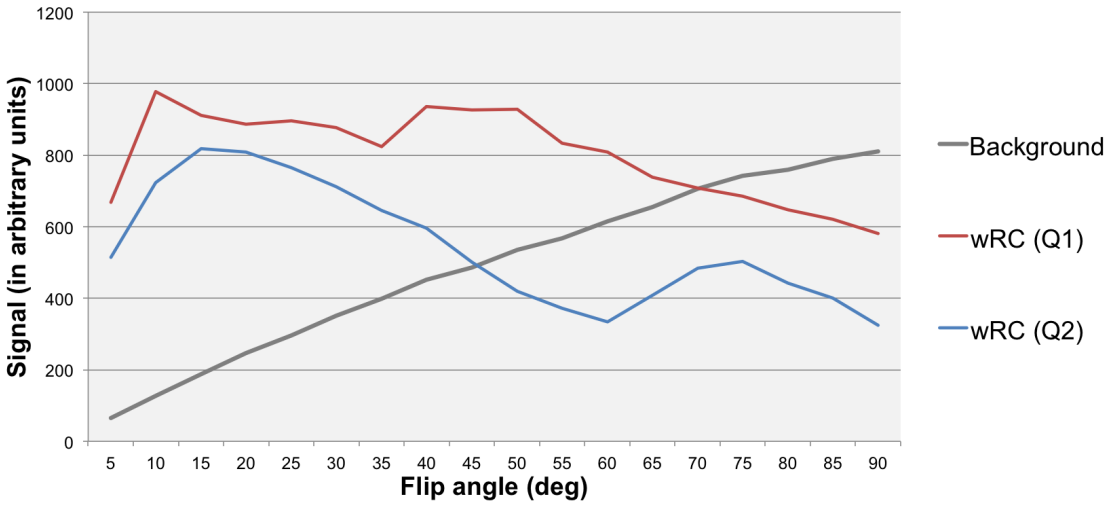

FIGURE 3.10: Investigation of wRC signal versus background signal as a function of the FA. The experiment was conducted with a FIESTA pulse sequence (Table 3.3), similar to what has been proposed in [75].

For shaped catheters it is important to visualise the head shape and orientation of the tip section. Figure 3.11 illustrates a MRI scan that shows the tip profile of a sidewinder catheter (SW1) with multiple wRCs. The catheter tip section, containing the wRCs, was visible over a length of 10 cm.

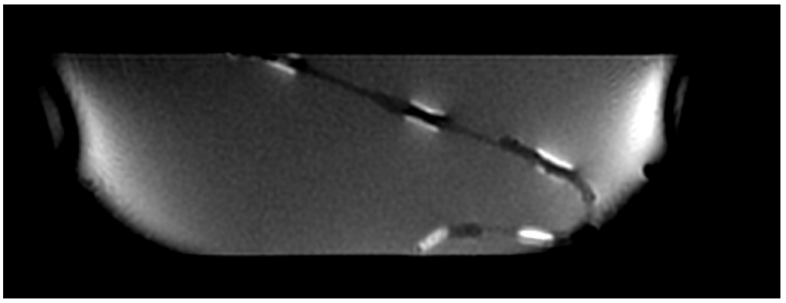

FIGURE 3.11: Sagittal MR image (FIESTA - Table 3.3) of a plastic phantom containing the sidewinder I catheter (SW1 - Table 3.1) equipped with five wRCs.

Catheters with one wRC on the Tip and Passive Markers Along the Shaft: An alternative approach to provide visualisation of the catheter shape and orientation is to employ a single wRC on the tip and susceptibility markers along the catheter shaft. This is shown in Figures 3.12, 3.13 and 3.14.

(i) Imaging experiments at 1.5 Tesla

The susceptibility artefacts caused by the FePt nPs exhibited 3 - 6 mm sized signal voids (axis a - see Figure 3.5) increasing with TE (Figure 3.12).

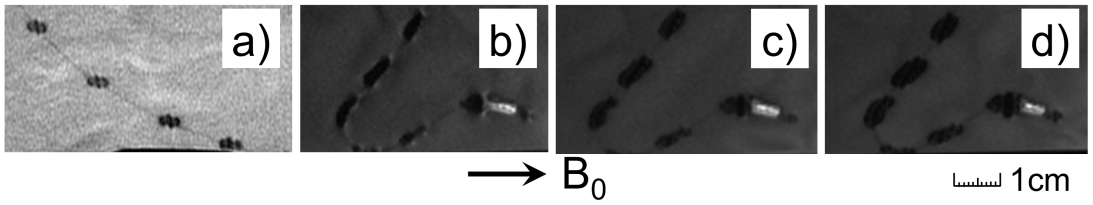

FIGURE 3.12: MR images (according to Table 3.3) of a sidewinder II catheter (SW2 - Table 3.1) with a wRC on the tip and FePt nPs markers along the shaft - Figure **(a)** was obtained (GRE) according to the ASTM protocol [30] with a guidewire (without markers) in place. Figures **(b - d)** were obtained with a rtMRI sequence (FGRE) and demonstrate how the artefact can be manipulated by varying TE (**(b)** TE = 2.5 ms, **(c)** TE = 5 ms, **(d)** TE = 10 ms).

Figure 3.13a illustrates catheter navigation into the superficial femoral artery while images were obtained in sagittal orientation. Figure 3.13 illustrates MR images, which were obtained in sagittal (a) or coronal orientation (b - e) while the same catheter was navigated into the lateral circumflex femoral artery. Note, only one FePt nPs marker was visible in Figure 3.13c) but none in b) and d) as these were not contained in the current rtMRI scan plane. It should also be noted that the susceptibility artefacts resulting from the FePt nPs markers affected the signal enhancement of a wRC if both markers were located close to each other. Figure 3.13e illustrates such a situation where the catheter was bent and one of the FePt nPs markers (white arrow) was positioned very close to the wRC on the tip (green arrow) and thereby reducing the signal enhancing effect of the wRC.

(ii) Imaging experiments at 3 Tesla

The susceptibility artefacts (Figure 3.14a) caused by the FePt nPs exhibited 7 - 11 mm (measured according to Figure 3.5) sized signal voids along axis a (same

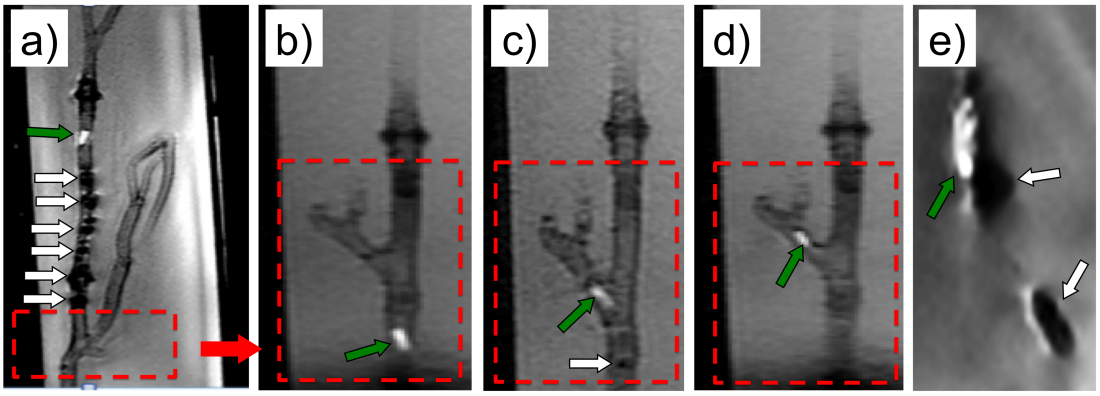

FIGURE 3.13: rtMRI scans (FGRE - Table 3.3) while a sidewinder II catheter (SW2 - Table 3.1) with wRC on the tip (green arrow) and seven FePt nPs markers (white arrows) along the shaft was navigated (downstream) in the LE vessel replica model - Figure **(a)** illustrates catheter navigation into the superficial femoral artery, Figures **(b - d)** (2x magnification) illustrate catheter navigation into the lateral circumflex femoral artery. Figure **(e)** (7x magnification) illustrates how a FePt nPs marker affected the signal enhancement effect of a wRC if both markers were positioned very close to each other.

imaging parameters as for the experiments at 1.5 T (Figure 3.12a). The wRC on the tip (Figure 3.14) showed high device to background contrast during imaging with low and intermediate FAs (FA $< 45°$: high CNR, FA $= 75°$: CNR $= 0$). The wRC (Figure 3.14, green arrow) on the cobra catheter (C1 - Table 3.1) was clearly visible while the passive susceptibility markers along the shaft were not detected in the MIP (Figure 3.14b).

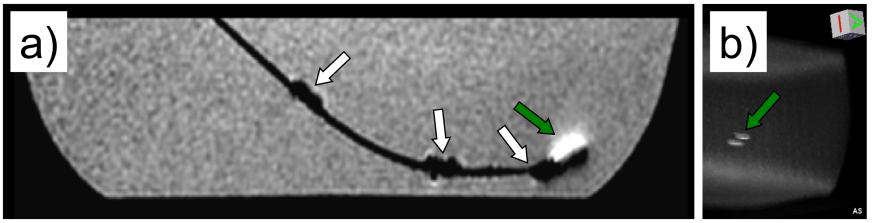

FIGURE 3.14: 3 T MRI (3D FSPGR - Table 3.3) of a phantom containing the cobra catheter (C1 - Table 3.1) equipped with single wRC at the tip (green arrow) and FePt nPs markers (white arrows) along the catheter shaft. Figure **(a)** illustrates a sagittal slice and **(b)** a MIP of the 3D dataset.

Micro Catheter: MR images of the micro catheter during navigation in an arterial vessel phantom are demonstrated in Figure 3.15. The FeO particle marker on the micro catheter (μC1 - Table 3.1) exhibited 14 - 16 mm sized signal voids

along the axis **a** and 11 - 13 mm along the axis **b** (measured according to Figure 3.5).

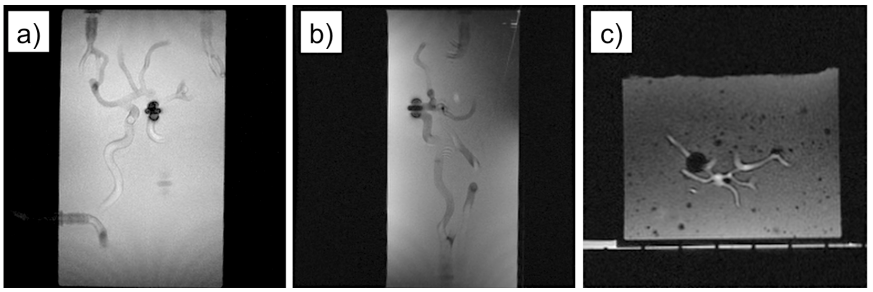

FIGURE 3.15: MR images (RT FGRE - Table 3.3) of the micro catheter (μC1 - Table 3.1) with a passive tip marker navigated in an arterial head phantom - Figure **(a)** illustrates a coronal, **(b)** a sagittal and **(c)** an axial scan (different catheter location). Note, air bubbles lead to susceptibility artefacts in the background due to the degrading gel (on the forth day of experiments) **(c)**.

Additionally, it was evaluated if the FeO marker on the micro catheter can be visualised with positive contrast while the background signals are suppressed (i.e. for localisation). Figure 3.16 demonstrates that WMI edSSFP imaging with dephasing of $4\pi/voxel$ in the readout direction resulted in complete suppression of background signals while hyper intense signals in close vicinity of the FeO marker were preserved.

RF Induced Heating Experiments for the wRC with the Highest Q: The maximum local temperature (measured at three locations of the wRC) did not exceed 0.6 °C during the entire RF induced temperature measurement [36]. Figure 3.17 shows four box plots that summarise the temperatures that were recorded during MRI (FSE - Table 3.3) with high SAR exposure (2W/kg) over a period of 15 minutes.

3.3.2 Ex Vivo Evaluation of Developed Devices

The following paragraphs describe the *ex vivo* validation of the guidewires and catheters that was performed using Thiel-Soft embalmed human cadavers.

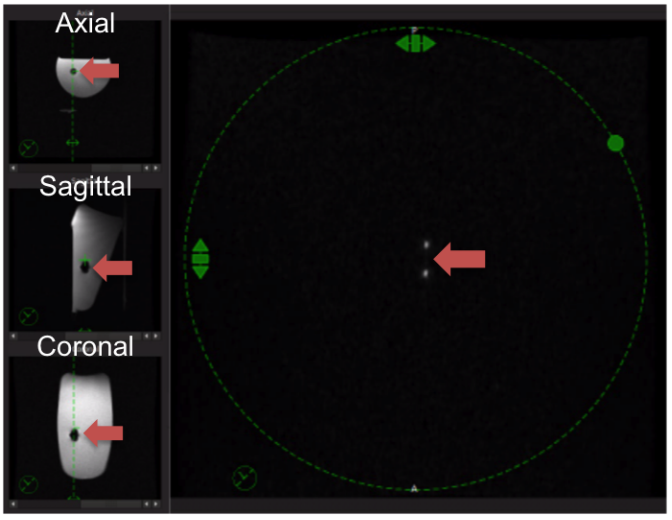

FIGURE 3.16: Complete background suppression was achieved with dephasing by 4π/voxel in the readout direction while exploiting positive contrast of a FeO marker on the micro catheter (μC1 - Table 3.1) using a dedicated edSSFP pulse sequence. The red arows indicate the FeO marker location in the FOV. The main image (right) shows one frame during rtMRI (WMI edSSFP - Table 3.2). The three scout images on the left (top to bottom - axial, sagittal, coronal) indicate the orientation of the current rtMRI scan plane.

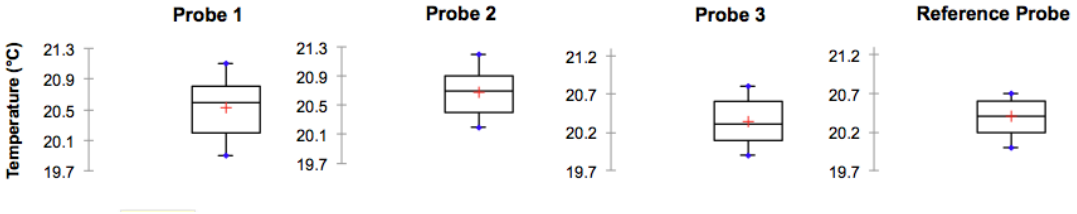

FIGURE 3.17: Box plots of the temperature measurements according to the ASTM protocol (F2182-09) [36]. Three temperature probes were attached to a wRC (probe 1: proximal, probe 2: distal and probe 3: medial) on the tip of a catheter (S1 - Table 3.1) and one probe was attached to the MR table outside of the bore and used as reference.

3.3.2.1 Ex Vivo Evaluation of the Guidewires

Two experienced interventional radiologists successfully navigated the guidewire from the femoral vein into the targeted vessel segment (vena cava) of both cadavers, solely using MRI-guidance (Figure 3.18a). Both radiologists rated the mechanical performance (pushability, torque and gliding properties) for this task comparable to standard guidewires used in X-Ray fluoroscopy. The susceptibility artefacts induced by the FePt nPs markers enabled distinct rtMRI visualisation of the guidewire (Figure 3.18a) with a mean marker size of 14 mm (axis **a**) and 12 mm

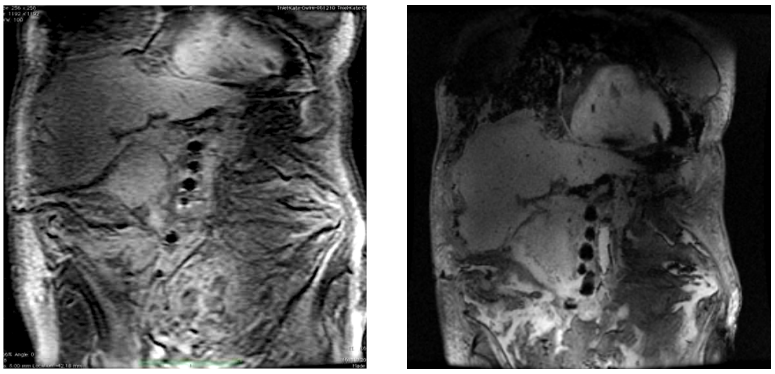

(a) Coronal RT FGRE (b) Coronal FSPGR

FIGURE 3.18: MR images (according to Table 3.2) of the guidewire navigated in the vena cava of a Thiel soft-embalmed human cadaver - Figure **(a)** shows a rtMRI scan (FGRE) and **(b)** a diagnostic FSPGR scans.

(axis **b**). The susceptibility artefacts aligned with the field lines of B_0. The FePt nPs markers showed ball-shaped rather than dipole - dipole shaped artefacts as during the idealised phantom experiments (see Figure 3.6).

3.3.2.2 Ex Vivo Evaluation of the Catheters

During our experiments, two different catheters, a straight (S2 - Table 3.1) (see Figure 3.19) and a balloon catheter (B3 - Table 3.1) were inserted and successfully navigated from the left femoral artery into the common left iliac artery of two Thiel soft-embalmed human cadavers (Figure 3.20). The wRCs on both catheters exhibited high device to background contrast during imaging with low and intermediate FAs (<45°). In the cadaver experiments the signal of each wRC was less intense as compared to the phantom experiments. However, the bright spot appeared similar in size and each wRCs (Figure 3.19 and 3.20) was visible during all steps of a procedure (manual scan plane adjustments). For the straight catheter, the area of increased SIs measured 9 - 11.5 mm along the main catheter axis and 4 - 6 mm perpendicular to the catheter axis. For both wRCs on the balloon catheter 10 - 12.5 mm and 6.5 - 8 mm were measured, respectively.

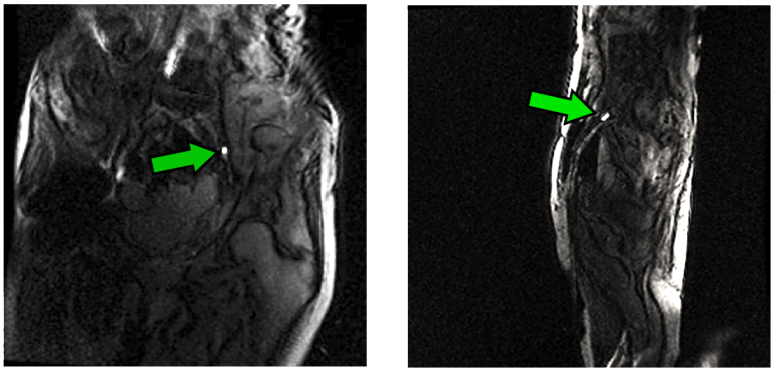

(a) Sagittal - rtMRI Scan (b) Coronal - rtMRI Scan

FIGURE 3.19: MR images (according to Table 3.3) of a straight catheter (S2 - Table 3.1) with single wRC (green arrow) positioned in the left common iliac of Thiel soft-embalmed human cadaver (transfemoral access) - Figure **(a)** shows a coronal and **(b)** a sagittal rtMRI scan (FGRE).

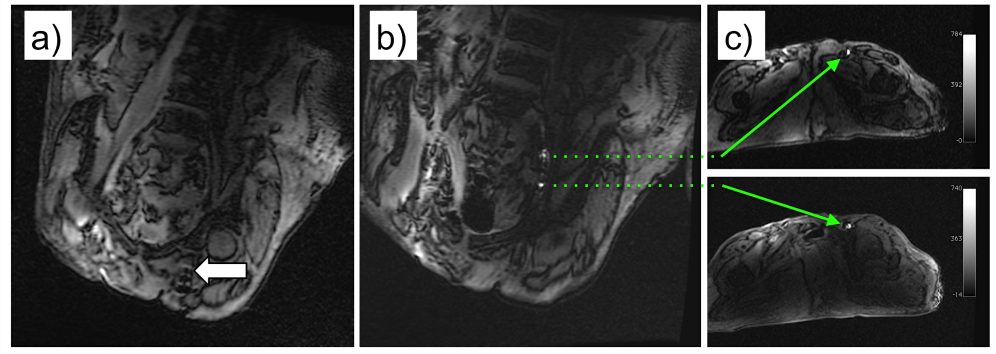

FIGURE 3.20: Balloon catheter (B3 - Table 3.1) with two wRCs navigated into the right common iliac artery of a Thiel soft-embalmed cadaver - The MR images were obtained (FSPGR - Table 3.3) during catheter navigation. Figure **(a)** shows the passive markers while the MRI-safe guidewire was advanced into the aorta, Figure **(b)** shows a coronal scan plane with both wRCs and **(c)** two axial scan planes that contain a wRC each (green arrows). Note, the significantly improved RF penetration resulting in a higher SNR during MRI as compared to the cadaver in Figure 3.19.

3.4 Discussion

Endovascular interventions require distinct visualisation of the shape and position of a device as well as its location in regards to the vessel wall [78]. Importantly, all device visualisation techniques that were employed in this chapter did not require a connection between the device and the MRI scanner, thereby simplifying instrument handling and avoiding elongated electrically conductive structures.

Such structures can potentially act as an RF antenna and thus accumulate energy, which constitutes a significant safety risk for the patient [32, 36] (see also Section 2.4.5). The main benefit of wRCs is that these markers are technically simpler compared to active tracking coils [146] and have the potential for integration into the commercial production of endovascular devices [164] as no physical wire connection to the MRI scanner is required. Susceptibility-based visualisation of devices is generally more difficult to depict on MRI as passive markers cause signal voids while wRCs cause signal intensity increases. However, the coil and capacitor dimensions, which are required to achieve a sufficient Q (greater than 15), limit the use of wRCs for devices with a small outer diameter (below 1 mm). At present, this restricts the use of this technology to guidewires with an outer diameter of 0.038" or less.

3.4.0.3 MRI-Safe Guidewire Design

The PEEK-based guidewire does not contain any metallic structures besides the nPs markers, which can be realised on micro metre scale. In addition, it has previously been demonstrated that no relevant heating could be detected during imaging with fast GRE-based sequences [134]. The phantom and cadaver experiments demonstrated that this guidewire enabled rtMRI-guided interventions while multiple contrast mechanisms (including WMI) can be achieved. The induced susceptibility artefacts, resulting from the FePt and SPIO nPs, have been optimised for experimental use but can be manipulated by changing imaging parameters (mainly TE) or the concentration and material of the nPs. iMRI pulse sequences, however, require high frame rates and therefore short TE and TR. Thus, the manipulation of the induced artefacts solely by changing imaging parameters is limited. The two lower FePt nPs concentrations (2.5 and 5 mg/mL) were found useful in idealised phantom conditions but generally hard to identify during the *ex vivo* experiments. The induced artefact size was too small in particular during imaging with very short TE. Hence, the passive marker solvent with 20 mg/mL FePt nPs or the SPIO nPs were found most useful for localizing guidewires during MRI-guided interventions.

Passive visualisation was found to be sufficient for guidewire navigation during all experiments in this chapter. However, in small vessels or next to air-filled cavities (which also result in signal voids), a more precise visualisation method (i.e. active tracking with multiple micro receive coils) could improve localisation and visualisation of the shape and orientation of a device, in particular in small branching vessels. A possible solution is to use WMI (see Figure 3.6) to localise the passive markers and then manually update the scan plane or overlay the marker locations i.e on a 3D MRA roadmap (similar to what has previously been proposed [27]). However, this would not allow automated tracking and be at the expense of significantly increased scanning time.

The FePt nPs were synthesised in-house, while the SPIO nPs were commercially available. It has been reported that these FePt nPs [165] provide a six-fold increase in FePt-based T_2 contrast properties compared to those of commercially available iron oxide nPs for clinical use. However, this had a minor impact for the application on guidewires, as both nPs marker (FePt and SPIO) can be realised on micro metre scale and therefore do not compromise the design of the guidewire. The radiologists furthermore considered the mechanical performance (i.e. torque, pushability, elasticity) similar, for the particular task, as commercially available guidewires for X-Ray fluoroscopy. However, further studies are required to fully assess the mechanical performance of this novel MRI-safe in particular during more challenging tasks and complex device manipulations.

3.4.0.4 MRI-Safe Catheter Design

As illustrated in Figure 3.7, the computed FA maps correspond well with existing literature [164] that loop coil (including single loop and PRS coils with an axis perpendicular to B_0) or saddle coil designs (Figure 3.7b) provide the best coupling properties for long and thin devices if the axis is mainly orientated in parallel to B_0. This is the case for most catheters that are designed for interventions in cylindrical bore magnets (horizontal B_0 field). Alternatively, it has previously been shown that this orientation dependence can be overcome i.e. by using two decoupled perpendicular coils [170, 171].

The results of this study also demonstrate that the shape and orientation of catheters can be visualised in MRI using either multiple wRCs or a wRC on the tip and passive markers such as FePt nPs along the shaft. The phantom experiments showed that combining FePt nPs and a wRC provided a suitable and reliable device localisation technique for both field strengths, 1.5 T and 3 T. Small wRCs that inductively couple to the MRI transmit and receive coils of MRI systems do not require elongated electrical conductors. The RF induced heating experiments according to the ASTM protocol [36] demonstrated that no significant heating (<0.6 °C) was detected for the catheter (S1 - Table 3.1) equipped with the wRC providing the highest quality factor ($Q \approx 65$). This protocol constitutes the worst-case scenario (for 1.5 T) while no blood flow cooling effects were considered. This maximum local temperature rise was found to be well within the limits for localised heating in human subjects [141].

A limitation of the catheters that were used in this study is that wRCs were applied to the surface of the catheters and therefore increased the outer diameter and stiffness of the device. This would necessitate arterial access of a larger calibre than would normally be performed and potentially limits the use of these catheters to interventions in larger vessels. Thus, passive visualisation was employed for micro catheters, which created additional challenges to differentiate between micro catheter and guidewires because both devices employed passive visualisation. Please note that the increased stiffness and outer diameter are temporary problems relating to manually fabricated wRCs. Recently, micro systems-based technologies for producing wRCs have been validated [172], which would allow for complete integration under the final coating of catheters. The experiments in this study demonstrate that the quality factor of a wRC significantly affected the signal characteristics in MRI in terms of locally increased SIs and CNR threshold. In this regard, micro system-based manufacturing technologies are currently evaluated[6] to understand if sufficient quality factors can be achieved for iMRI.

[6]M. Kaiser, M. Detert, M. A. Rube, A. El-Tahir, O. J. Elle, A. Melzer, B. Schmidt, G. H. Rose. "Resonant marker design and fabrication for device visualization during interventional magnetic resonance imaging". *Biomed Tech (Berl)* (accepted with revisions).

3.4.0.5 Thiel Soft-Embalmed Cadavers as Ex-Vivo Model

In the cadaver experiments the SNR was significantly poorer than in idealised *in vitro* conditions, which also affected the signal amplification of the wRCs (less intense but similar in size). However, it has previously been shown that MRI of Thiel soft-embalmed tissue is constrained and living organisms provide better RF penetration [67] (see also Section 1.3). It is foreseen that device visualisation and discrimination between device and surrounding tissues will improve in animal and patient studies. To further evaluate the device visualisation techniques, which were presented in this chapter, pre-clinical validation studies were conducted to assess the device performance for specific interventions *in vitro*, *ex vivo* and *in vivo* (large animal models). These studies are described in Chapters 6 and 7.

3.5 Concluding Remarks

In this chapter a number of interesting device visualisation strategies were demonstrated for interventional MRI. A major shortcoming for the past three decades in the field of MRI-guided endovascular interventions was the lack of MRI-safe guidewires with regulatory approval. Thus, the novel PEEK-based guidewire could enable many MRI-guided procedures in future. Despite the encouraging *in vitro* and *ex vivo* results, the author is aware that further design optimisations are required before the presented interventional devices can be used in a similar fashion as state of the art devices for X-Ray fluoroscopy. The next steps in research should involve a completely integrated design of wRCs into the device material or outer coating of the finished device. Future research should furthermore focus on a comprehensive assessment of the mechanical performance of the guidewires and catheters.

Chapter 4

Mobile Technology to Improve iMRI Workflow

Major parts of this chapter have been submitted for publication as:
M. A. Rube, A. B. Holbrook, B. F. Cox, R. Buciuc, A. Melzer, "Wireless mobile technology to improve workflow and feasibility of MRI-guided percutaneous interventions", *Int J Comput Assist Radiol Surg* [in press].

Experimental contributions:
(i) B. F. Cox prepared the Thiel-embalmed cadavers and gel phantoms for the experiments. (ii) A. B. Holbrook assisted in developing the front-end of the browser-based user interface (see also [173]). (iii) B. Cox, A. Melzer and R. Buciuc validated the developments from a clinical perspective.

4.1 Introduction

MRI provides true multi-planar imaging with arbitrary slice orientation and consequently allows aligning the scan plane interactively according to an instrument trajectory [105] to target challenging lesions. MRI can furthermore be utilised to characterise lesions before, after and during a procedure [24]. To date, most scanner manufacturers provide moderately interactive real-time User Interfaces (UI) that are adequate for diagnostic MRI or available as work in progress packages [43, 44] for off label use only. In addition a very limited number of display and input devices, such as tableside controls, are available. However, to date no intuitive scanner interaction has been achieved that accommodates dynamic changes to the scan acquisition that are frequently required during iMRI.

A substantial hurdle for MRI in the context of percutaneous interventions is the lack of a dedicated and adequate workflow [19] that i.e. omits the need for leaving the scan room during interventions for viewing images and communicating with the radiographer. High acoustic noise levels during scanner operation, ranging between 70 and 110 dB [20], add a substantial health and safety risk, in particular, for fast GRE-based sequences [20] that are frequently used for iMRI [24, 105] applications. Hence, noise protection is required and special solutions for audio communication [51] between interventionist, radiographer and patient. Guettler *et al.* proposed a wireless Bluetooth (BT)-based communication system that can be used during MRI scanner operation [52]. This concept was adopted for this study and extended for multi-user communication between physician, assisting staff and scanner operator using tablet personal computers (tablet PCs).

Wireless input devices such as tablet PCs are also promising candidates to be used at the patient side as interactive image display and for interactive MRI control. The display resolution of such tablet PCs is continuously improving such that modern tablet devices meet or exceed display resolution of desktop Liquid-Crystal Display (LCD) monitors in terms of dots per inch (DPI). The FDA has recently approved a tablet PC (iPad, Apple, Cupertino, CA, USA) and associated applications (apps) for radiologists to read diagnostic images (K123082). Recent studies have evaluated the image quality and diagnostic performance of tablet PCs

in comparison to diagnostic LCD monitors for emergency brain CT scans [174] and for mobile on-call radiology in CT and MRI studies [175]. Holbrook *et al.* have proposed to use a tablet device for controlling or monitoring of MRI-guided high intensity focused ultrasound (HIFU) procedures [176] and for collaborative iMRI [177].

The overall objective of this study was to improve percutaneous iMRI, through easy to use and inexpensive mobile tablet devices. The implementation consisted of selected wireless tablet PCs, a multi-user communication system and a platform independent web-based UI optimised for interactive iMRI. This setup was validated for iMRI during percutaneous biopsies on phantoms and Thiel soft-embalmed human cadavers employing the MRI-guided freehand approach [105].

4.2 Materials and Methods

This section describes the implementations, the setup and the modifications as well as their assessment in regards to MRI safety and performance *in vitro* and *ex vivo*.

4.2.1 Interventional MRI Setup and Modifications

The setup for validation is a dedicated imaging suite for MRI-guided interventions and surgery (see Figure 4.1) and consists of a clinical 1.5 T MRI scanner (Signa HDx, Software release 15.0M4A, GE Healthcare, Waukesha, WI, USA) connected to a surgical suite (1050, Maquet, Rastatt, Germany). In this study, the DuoFlex interventional coil prototype (see Section 3.2.2) was used with a 4ch 24 cm element combined with the single loop element with disposable cover (Figure 4.3).

Two-way data communication between the MRI scanner (MR Host) and an external Linux (Ubuntu 11.10 64bit) workstation (16-CPU, 32 GB memory, z820, Hewlett-Packard, Palo Alto, CA) (RT PC) was accomplished via Gigabit Ethernet (IEEE 802.3z). Next to the magnet, a 23-inch LCD monitor (SW2309W, Dell, Austin, TEX, USA) was installed on a flexible swivel arm. A second, shielded 40-inch LCD monitor (Multeos 401, NEC Corporation, Tokyo, Japan) was mounted

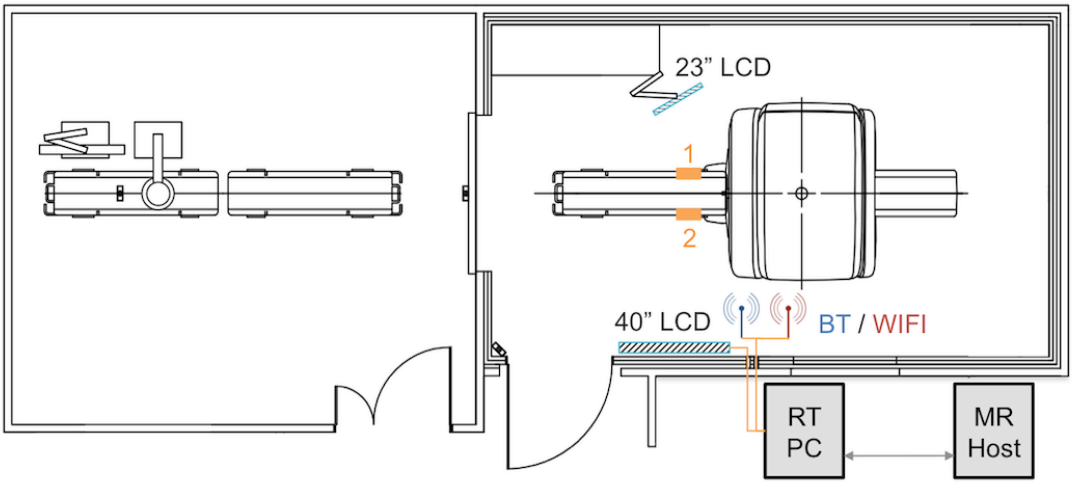

FIGURE 4.1: 2D floor plan with wireless control and communication setup - "1" and "2" represent the mounting positions of the tablet PC. The position can be changed according to the preference of the physician in terms performing interventions from the left or the right side of the patient table or on the other side of the bore. Please note that Figure 3.4 on page 53 illustrates the same facility without modifications.

to the opposite wall. The integrity of galvanic isolation between the MRI control room and scan room was retained by using optical fibre cables and optical-to-electrical as well as electrical-to-optical converters that keep RF noise outside of the Faraday cage. Both monitors were connected with an optical fibre cable (M1-1000, Opticis, Sungnam City, Korea) to the RT PC and used simultaneously to display the iMRI-UI. This allowed interventions to be performed from both sides of the patient table while either the interventionist or the assisting nurse monitored the 23 or 40-inch screen, respectively. A Wireless Local Area Network (WLAN) was implemented for wireless data transfer within the scan room as illustrated in Figure 4.1. The WLAN (2.4 GHz, IEEE 802.11) connection was established with a modified router (DIR615, D-Link, Taipei, Taiwan) where one antenna was positioned in the magnet room and the other one outside the Faraday cage providing the same local network Service Set Identifier (SSID) throughout both areas.

Interactive MRI pulse sequences with different contrast mechanisms were developed and implemented in the RTHawk [45] software framework (Version 0.9.28, HeartVista, Inc., Palo Alto, CA, USA). Three interactive MRI pulse sequences were implemented that allow different contrast weightings (T_1, T_2^*, T_2/T_1) for

lesion detection and can be switched and also be interleaved on the fly: A FSPGR providing rapid T_1-weighted imaging [86, 178], a bSSFP sequence providing T_2/T_1 contrast [95, 96], in particular useful for blood vessel visualisation employing high flip-angles [97] and a reversed fast steady state precession (PSIF) sequence providing fast T_2*-weighted imaging for iMRI [179].

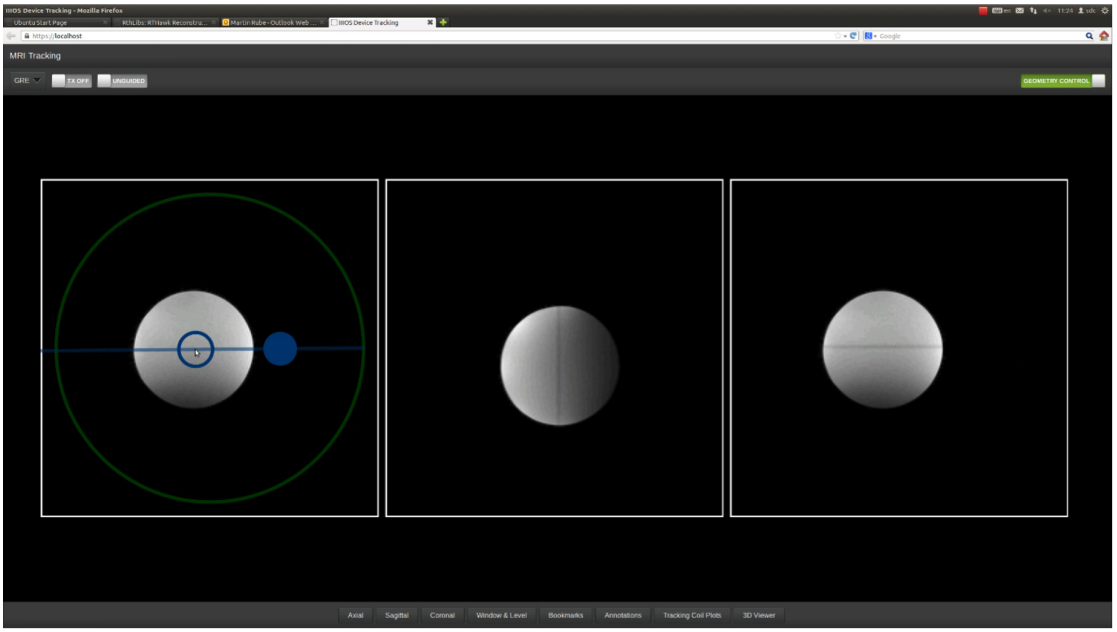

FIGURE 4.2: Screenshot of the web-based user interface for iMRI running on a workstation (Ubuntu 11.10) - Up to three real-time imaging planes can be selected that are frequently updated according to the user selected geometry, scan parameter and pulse sequence choice. MR images of a spherical phantom are shown exemplary that were obtained with a FSPGR sequence in an interleaved manner. The pulse sequence can be selected from dropdown list located on the top left corner of the screen under the browser address bar. The geometry control is activated for the left window and the scan plane selection can also be operated via a tablet PC using multi-touch gestures.

A dedicated multi-device iMRI-UI (Figure 4.2) was developed and integrated into RTHawk. This UI allows scanner interaction through an Internet browser, across multiple operating systems and platforms such as PCs, tablet PCs or mobile phones [173]. MRI controls were integrated into a backend developed in C++. These were then attached to a locally hosted node.js server hosting the UI over a secure sockets layer (SSL), using a mongoDB database for authentication. The interface was developed exclusively with Hyper Text Markup Language (HTML), Cascading Style Sheets (CSS), and JavaScript, using the following open source libraries: Enyo 2.0 for the interface, Flot.js for plotting, and Three.js for HTML5

canvas and webGL rendering. The iMRI-UI was employed for image display and interactive scan and parameter control and it was designed to image up to three independent slices. The user was able to select and interleave different pulse sequences. The UI also supported 3D volume rendering of scan planes and included a thermometry module that has been described elsewhere [173]. A Virtual Network Computing (VNC) connection was established between the MRI scanner running a VNC server and the MRI input device running a VNC client application to compare the developed iMRI-UI to the standard real-time interface (GE i/Drive Pro Plus, GE Healthcare, Waukesha, WI), which is provided by the scanner manufacturer. The implemented web interface was also tested on various computers and mobile devices with different Internet browsers: Mozilla Firefox (Ubuntu 11.10, OSX Snow Leopard), Google Chrome (Ubuntu 11.10, OSX Snow Leopard, MS Windows 7), and Apple Safari (OSX Snow Leopard) and Mobile Safari.

Two mobile tablet PCs have been selected (iPad 1 and 3, Apple, Cupertino, US) with a 9.7 inch (diagonal) multi-touch display and a resolution of 1024 x 768 and 2048 x 1536 pixels, respectively. Each tablet PC was inserted into a plastic cover to simulate sterile equipment and mounted to a customised MRI-safe intravascular pole (GE Healthcare, Waukesha, WI, USA) with modified car mounts for tablet PCs (Matek Trading Co., Ltd, Hanoi, Vietnam). Two-way communication between the scanner operator, the operating physician, and the assisting nurse was established using Voice-over-Internet-Protocol (VoIP) technology and wireless mobile BT headsets (Calisto B70, Plantronics, Santa Cruz, CA, USA) integrated into modified earmuffs (RS Components Ltd, Corby, UK). Two-way communication was also established with two tablet PCs in the scan room and a PC in the control room using a VoIP software application (Skype, Luxembourg City, Luxemburg).

4.2.2 Acceptance Testing

Primary interactions between the MR system and the additional components in the MRI scan room were evaluated with the test method proposed by ASTM. The magnetically induced displacement force was assessed according to the standard

test method (ASTM F2052-06) [129] for measurement of magnetically induced displacement force on medical devices in the MRI environment. Each device was suspended from a string attached to the 0° indicator on the intravascular pole to measure the deflection angle α. The displacement force F_m can be calculated [129] based on the deflection angle, the mass m of the device, and the gravitational factor g according to Equation 4.1.

$$F_m = m \cdot g \; tan(\alpha) \tag{4.1}$$

Moreover, potential RF interference was evaluated on a phantom with a coherent noise test (GRE, TE / TR= 13 / 32 ms, FOV = 20 cm x 20 cm, Matrix = 512 x 256, FA = 10°, Slice thickness = 5 mm, Bandwidth = 122.7 Hz/pixel) with an 8ch HD brain coil as well as a white pixel test (SE EPI, TE / TR = 36.1 / 6000 ms, FOV = 9.9 cm x 9.9 cm, Matrix = 128 x 64, Slice thickness = 10 mm, Bandwidth = 3906.25 Hz/pixel) employing the integrated body coil. Both tests were available from the service browser on the MRI scanner to evaluate image quality.

4.2.3 Techniques for MRI-Guided Interventions

An experienced interventional radiologist (10 years experience - "expert") and one physician in training (no interventional experience - "novice") performed all procedures. A carbon fibre composite puncture needle with Nitinol mandrin (21G / 150 mm, Radimed, Bochum, Germany) was used during MRI-guided needle punctures. Tissue samples (in case of artificial targets) were obtained for verification with an MRI-safe biopsy needle (MR Biopsy-Handy, 16G, 15cm, Somatex, Teltow, Germany). Passive, susceptibility-based visualisation (see Section 2.4.5.1) of the needles [22, 29] was applied for needle guidance.

Initially, a planning dataset with high spatial resolution (FSPGR, TE / TR = 10 / 80 ms, FA = 60°, FOV = 25 cm x 25 cm, Matrix = 384 x 384, Slice thickness = 2 mm) was acquired and the target and skin entry points were selected. The target point was defined as a sphere (⌀ = 8 mm). The patient table was then moved out of the bore and the physical entry point was marked on the skin/surface

by calculating the distance offset (in x and z direction) from the laser crosshair. A small incision was then performed using a non-ferro magnetic disposable titanium scalpel (# 11 blade) at the entry point and the needle was positioned.

The physician then requested the scanner operator to remotely move the patient table back into the MRI scanner while the physician kept his finger at the skin entry point to mark-up the location on the subsequent MRI images. The FSPGR rtMRI acquisition was then initiated on request of the physician and two perpendicular scan planes were setup containing both the entry and target point. Once the physician was satisfied with the location of the skin entry point and scan plane orientation, the needle was inserted under rtMRI guidance. During rtMRI the physician was able to adjust the pulse sequence (bSSFP, FSPGR, PSIF), geometry and parameters via the tablet PC or communicate the adjustments to the scanner operator. The physician terminated rtMRI via the tablet PC once the needle was positioned in the lesion. A second high-resolution dataset (the same sequence and parameters as during planning) was then acquired with the needle still in place to verify the needle position. Note, the imaging pulse sequences and parameters were optimised for MRI of Thiel soft-embalmed cadavers [67].

An intervention was rated successful if the needle tip was positioned within the predefined target region and clearly identified on multiple rtMRI planes and in the high-resolution dataset. In the case of targeting Gd-doped target, visual checks were additionally conducted to ensure that the desired targeting was achieved. The root-mean-square (RMS) 3D error was calculated based on the high-resolution dataset for the discrepancy between the actual needle tip and the target point position (3D coordinates of the planned target point).

4.2.4 In Vitro Evaluation in Tissue Mimicking Phantoms

The *in vitro* experiments were conducted in a muscle tissue-mimicking, ballistic gelatine phantom with 10% w/w gelatine powder (G8-500, Fisher Scientific, Hampton, NH, USA) [180]. A range of targets (⌀ 20 mm), mimicking lesions and consisting of gelatine, agar (A360-500, Fisher Scientific, Hampton, NH, USA), fat and food colouring (Dr. Oetker, Bielefeld, Germany) for visual confirmation were

positioned within the gelatine matrix. A layer of boiled spaghetti (Buitoni, Sansepolcro, Italy) in gelatine was added to the phantom to mimic blood vessels that should be avoided during targeting.

Each physician performed ten double (trajectory lengths ranged from 80 - 160 mm) and ten single oblique interventions (trajectory lengths ranged from 100 - 160 mm). The times for needle targeting and the total intervention were recorded.

4.2.5 Ex Vivo Evaluation in Thiel Embalmed Human Cadavers

The human cadavers used in this study were donated according to standard procedures as set out in the Human Tissue (Scotland) Act 2006 and the Thiel Advisory Committee (University of Dundee, UK) has approved all procedures in this study. Three Thiel soft-embalmed cadavers (sex: 1 female and 2 male, age: 50 - 75 years, weight: 65 - 80 kg) were prepared in the angio suite (the room on the left side in Figure 4.1) and then transferred to the MRI suite (Figure 4.3). The peripheral cannulation and tumour phantom implant was performed through a pre-existing median laparotomy. Gd-doped targets (agar/fat, $\varnothing = 25$ mm) were implanted to mimic liver lesions that appear bright in T_1-weighted images for targeting. Alternatively target choice was predetermined during the procedure planning stages on a MRI distinctive area within the liver parenchyma (one cadaver). An MRI compatible anaesthetic ventilator (ventiPAC, PneuPAC Ltd., Luton, UK) was used for mechanical ventilation (Inspiration time $T_I = 2$ s, Expiration time $T_E = 4$ s, and tidal volume $V_T = 750$ ml) with tracheal intubation to simulate hepatic motion throughout the procedure. The expert and the novice performed four double oblique interventions (trajectory lengths ranged from 60 - 120 mm) in each human cadaver.

4.3 Results

The findings of the acceptance testing as well as the *in vitro* and *ex vivo* validation are presented in this section.

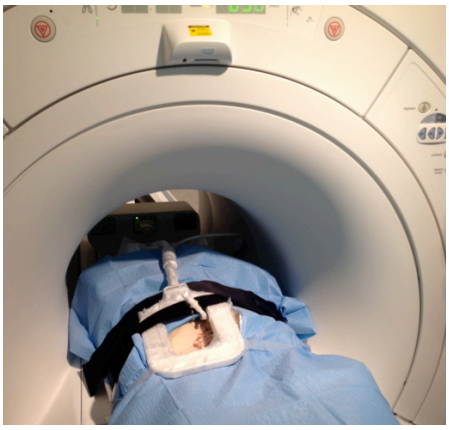

FIGURE 4.3: Photograph of a Thiel soft-embalmed human cadaver positioned in front of the MRI scanner. The single loop element with disposable cover was positioned anterior for easy percutaneous access to the liver while the 4ch 24cm element of the DuoFlex interventional coil was positioned posterior. The black strap was used for compression of the chest to improve hepatic access.

4.3.1 Acceptance Testing

According to the standard test method (ASTM F2052-06) [129], a mean deflection angle (α) of 34° was measured for the employed tablet PC and a mean deflection angle of 29° while attached to the custom made holder. Furthermore a mean deflection angle of 42° was measured for the BT headset and a mean deflection angle of 6° was measured while the BT headset was incorporated in the ear defenders. This results in a magnetically induced deflection force $F_m = 4.90$ N for the tablet device ($F_m = 5.59$ N for the tablet PC attached to the holder) and $F_m = 0.16$ N for the BT headset ($F_m = 0.24$ N for the BT headset incorporated in the ear defenders). No displacement force was present for the custom made holder itself or the ear defenders without the BT headset, even if positioned in the bore. No displacement force was present for the tablet PC at a distance greater or equal to 50 cm (4-10 mT) from the end of the bore.

It was verified that the tablet devices (Figure 4.4) that were used in this study can be operated with gloves while covered in drape as illustrated in Figure 4.4c. Audio communication via VoIP was possible throughout all interventions with a stable BT connection. However, during scanner operation the acoustic noise level was high, which led to imperfect sound quality, which was still rated suitable for communication. No degraded image quality or RF interference could

be detected on any MR image, the white pixel, or on the coherent noise test while the devices were set up in the scan room and the WLAN connection was established. The WLAN supplied by the modified router provided a stable and fast connection, facilitating rapid image update rates without noticeable delay for the rtMRI feed into the scan room. Using the VNC connection provided a feasible connection with the scanner manufacturers UI but the performing physicians rated the latency (ranging between 0.2 - 1.3 seconds) between actual image acquisition and display not acceptable for interventions. On the contrary, the node.js server showed no noticeable lags or time delays serving the MR images to the clients (Figure 4.4c). Multiple connections were established (i.e. via multiple browsers on one PC and across several tablet devices), all able to access and visualise the data individually as desired, or controlling or monitoring the procedure via the iMRI-UI as allowed by each user's login permissions.

4.3.2 In Vitro Studies in Tissue Mimicking Phantoms

All phantom biopsies (n = 40) were technically successful (the needle tip was positioned within the predefined target region). The mean 3D RMS error between the planned target point and the needle tip was 2.8 ± 1.0 mm, with further details given in Table 4.1. The mean targeting time was 5 minutes and 21 seconds and the mean procedure time was 15 minutes and 46 seconds (range 10 - 19 minutes) for the expert. The mean targeting time was 6 minutes and 35 seconds and the mean procedure time was 17 minutes and 31 seconds (range 12 - 22 minutes) for the novice.

The in-room interactive tablet PCs provided the operator with images in near real-time and the ability to self-select important parameters or switch between pulse sequences on the fly (one click on the touch screen and no delay). Parameter control and slice repositioning from inside the scan room was achieved, facilitating fast navigation to the puncture target. The close proximity of the touch device allowed for zooming (Figure 4.4c and d) and precise target acquisition during simulated interventions. The interventional workflow for a freehand needle biopsy illustrated in Figure 4.5.

TABLE 4.1: Needle Targeting Accuracy

User	**Total**	**3D RMS error (mm)**
In Vitro - Single Oblique		
Expert	n = 10	1.5 (± 0.5)
Novice	n = 10	2.5 (± 0.6)
In Vitro - Double Oblique		
Expert	n = 10	2.5 (± 0.8)
Novice	n =10	4.0 (± 1.2)
In Vitro - All		
All Paths	n = 40	2.8 (± 1.0)
Ex Vivo - Double Oblique		
Expert	n = 12	2.9 (± 0.8)
Novice	n = 12	4.1 (± 0.9)

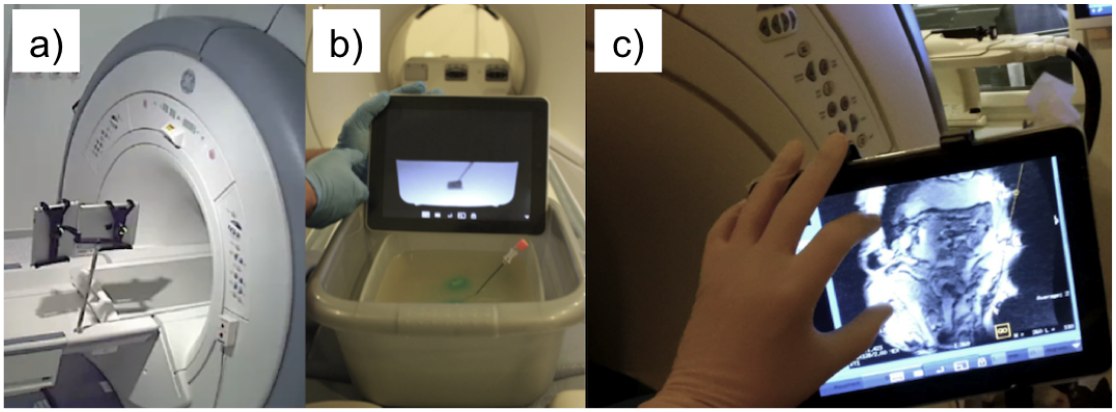

FIGURE 4.4: Wireless scanner interaction from within the magnet room with a tablet PC. The multi-touch mobile tablet PCs were mounted on an MRI compatible intravascular pole **(a)**, whereas, one tablet was used to display the iMRI-UI while the other tablet was used for communication in combination with BT headsets. A successful needle puncture in the phantom is demonstrated **(b)**. The physician (wearing gloves) was also able to zoom into relevant anatomical areas on the tablet PC. This is illustrated during a needle biopsy in a Thiel soft-embalmed human cadaver in Figure **(c)**.

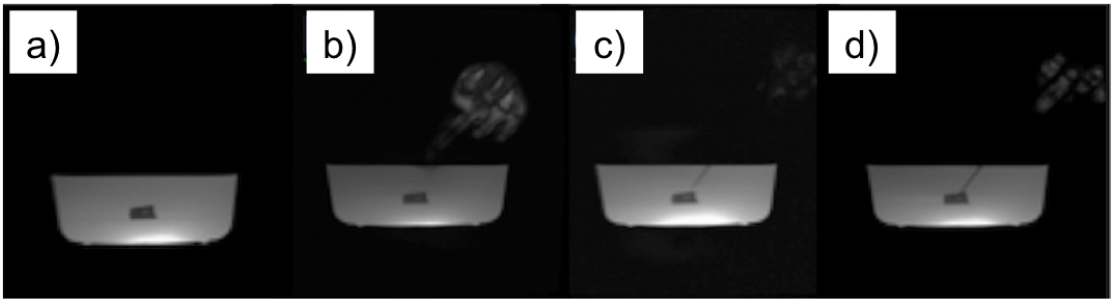

FIGURE 4.5: Simplified needle biopsy for a single oblique trajectory using the freehand approach and near real-time MRI guidance (FSPGR, TE/TR = 4.0 / 8.3 ms, Matrix = 256 x 256, FOV = 33 cm x 33 cm, FA = 60°, Slice thickness = 7 mm). The target lesion is shown in Figure **(a)**. The needle entry point was identified **(b)** by finger pointing and the real-time scan plane was then updated to contain the skin entry and target point. The needle was then advanced towards the intended target **(c)** and the lesion punctured **(d)**.

4.3.3 Ex Vivo Studies in Thiel Embalmed Human Cadavers

All cadaver biopsies (n = 24) were technically successful (needle tip was positioned within the predefined target region) under simulated free breathing conditions. The mean RMS 3D error between the planned target point and the needle tip was 2.9 ± 0.8 mm for the expert and 4.1 ± 0.9 mm for the novice, with further details given in Table 4.1.

The variations between individual cadavers (surgical history, post mortem training procedures, the shelf time, pre-existing or artificial lesions) were found to be significant. Detailed recording of procedure times (ranging from 20 - 55 minutes) was abandoned for the Thiel soft-embalmed cadaver experiments due to the influence of confounding variations and problems, which are not present in living patients. These included trapped air (green arrow in Figure 4.6e) in the abdominal cavity, decreased liver dimensions due to dehydration, varying quality of preserved tissues, and pre-existing damage due to previous training events. Note, the substantial difference in image quality between Figures 4.6 and 4.7 along with the absence of air in the cadaver in Figure 4.7.

A screenshot of a successful needle puncture with a double oblique trajectory is shown in Figure 4.6 and Figure 4.7. The screenshot of the iMRI-UI (Figure 4.6d) contains three near real-time MR images that were frequently updated with

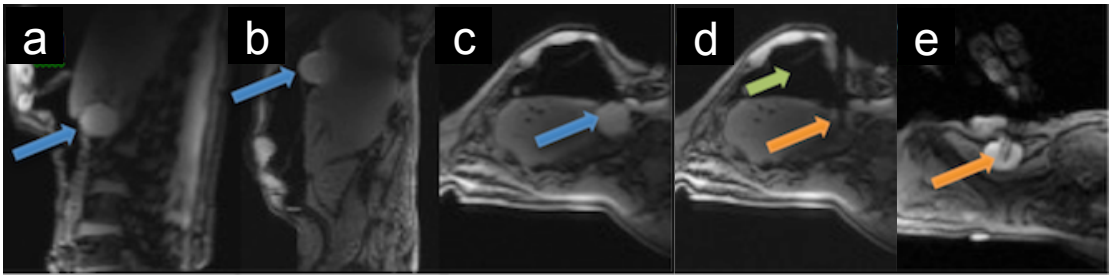

FIGURE 4.6: MRI-guided liver biopsy in a Thiel soft-embalmed human cadaver performed with the freehand technique and under simulated free-breathing conditions. The implanted targets (blue arrows) are shown in the planning images **(a - c)** acquired with a diagnostic FSPGR that was optimised for Thiel cadaver imaging (FSPGR, TE / TR = 1.8 / 70 ms, FA = 60°, Matrix = 256 x 256, FOV = 30 cm x 30 cm, Slice thickness = 5 mm, NEX = 2). The planning images in Figures (**a** and **b** represent sagittal images and **(c)** an axial oblique image. A deep target was successfully punctured with the biopsy gun during near real-time MRI in an axial oblique plane **(d)** and a shallow target was punctured in an axial plane **(e)**. The orange arrow indicates the needle tip that can be detected (signal void). Note, targeting was constrained because of trapped air (green arrow) in the abdominal cavity of this particular cadaver. Also note, most vessels and organs (including the liver) in Thiel soft-embalmed cadavers are collapsed due to the absence of perfusion and tissue dehydration. Additionally, it should be noted that the cadavers were used in previous training procedures, which affected usability in particular due to preformed incisions and trapped air.

a T_1-weighted pulse sequence in three different slice orientations. The needle was advanced during continuous MRI with a temporal resolution of 1 frame per second. A correct needle placement was then confirmed with a high spatial resolution dataset (Figure 4.8). Trapped air (green arrow in Figure 4.6e) in the abdominal cavity of the cadaver, decreased liver dimensions (compared to a liver in a living human) and a short needle that was required for the 60 cm bore diameter constrained the choice of potential needle paths.

4.4 Discussion

A substantial hurdle for MRI-guided percutaneous interventions is the lack of a dedicated and efficient workflow [19] that is required for effective procedures in the complex MR environment. In this chapter a wireless system for communication and interactive remote control of a clinical whole body MRI scanner was therefore developed and validated to facilitate iMRI. The magnetically induced deflection

FIGURE 4.7: Screenshot acquired on the tablet PC during needle placement with interactive rtMRI guidance (FSPGR, TE / TR = 2.8 / 6.6 ms, FA = 60°, Matrix = 256 x 256, FOV = 30 cm x 30 cm, Slice thickness = 8). An axial oblique plane (left) and a sagittal oblique plane were updated in an interleaved manner for targeting a predefined and existing target area with double oblique needle trajectory.

FIGURE 4.8: Verification of correct needle placements (coronal, axial, sagittal) in the target (dark) area of the liver a Thiel soft-embalmed cadaver (FSPGR, TE / TR = 3.1 / 70 ms, FA = 60°, Matrix = 384 x 224, FOV = 36 cm x 36 cm, Slice thickness = 4 mm, NEX = 4). The blue arrow indicates the needle (signal void).

angle was measured to be less than 45° for all components, which means the deflection force induced by the field of the 1.5 T MRI scanner was less than the force on the device due to gravity [129]. While these results are a good indication for MRI safety, the test method for magnetically induced displacement force alone is not sufficient for ultimately determining the device safety in the MRI environment and further testing may be required before clinical application [129] and regulatory approval.

4.4.1 Interventional MRI Workflow

Challenging but important technical tasks during MRI-guided needle interventions are selecting the correct MRI scan planes and maintaining an appropriate angulation during needle placement [105]. Slice re-alignments typically require significant intra-procedure communication [19] and time. The close proximity of the touch screen improved the scanner interaction considerably both during phantom and cadaver experiments.

To use a VNC connection for remote control of the MRI scanner is attractive because this connection can give multiple users access to centralised resources, in this case the MRI scanner host PC, through conventional or consumer devices [181]. However, the presented results demonstrate that the latency for the imaging feed was unacceptable for iMRI. In comparison to this setup, the standard commercially available real-time UI that was available on our scanner (i/Drive Plus, GE Healthcare, Waukesha, WI, USA) provided only limited features and can only be used with a single pulse sequence (FGRE - RF spoiled or unspoiled) and one interactive imaging plane at a time. The proposed browser-based iMRI-UI allowed flexible and intuitive scan plane adjustments in real-time. Different contrast mechanisms (T_1, T_2, T_2/T_1) can interactively be selected on the fly and also be interleaved. The availability of various contrast mechanisms is in particular useful where a sequence with only a single contrast weighting may not simultaneously generate contrast among tumours, lesions and normal soft tissues, which compromises lesion assessment and MRI guidance [179].

In the course of a procedure, the device trajectory, the pulse sequence and scan parameters could be adjusted dynamically. This decreased needle passage, which is associated with trauma and bleeding and also results in workflow interruptions [19, 105]. It should be noted that the three planes were a design choice based on user feedback and not a capability limitation.

The two interventional radiologists concluded that the described setup resembles a suitable hybrid approach combining the workflow from CT with real-time needle guidance capability that they are familiar with from ultrasound while MRI provides superior soft tissue. The proposed image guidance arrangements were also found satisfactory in terms of decreasing interruptions i.e. caused by moving clinical staff in and out of the scan room, moving the patient in and out of the bore as well as scan interruptions for sequence and parameter updates. The established multi-user communication with a wireless setup that can potentially be produced at a low cost (the cost of the additional components was approximately US$ 3000), clearly improved our iMRI workflow compared to previous experiments. This benefit, however, has to be quantified in further studies. Additional acoustic or digital noise filtering could also enhance the communication [52].

Controlling an MRI scanner and guiding interventional procedures from a web browser presents many interesting solutions for device integration. The web-based model allows easy access to data and the experimental controls, whether on a tablet in the magnet room, a desktop in the control room, or a device potentially anywhere. This could enable an intuitive and collaborative multi-user approach for MRI-guided interventions, and facilitate educational demonstrations or collaborative treatment planning. In theory, MRI-guided interventions including thermal treatments could be assisted, guided and monitored remotely. However, with increasing distance and network traffic, compared to a local network, the latency between transmitter and receiver would also increase and compromise procedure safety.

4.4.2 In Vitro and Ex Vivo Studies

All experiments in this study were performed in a closed bore MRI scanner with 60 cm bore diameter. This limited the selection of individual cadavers and the choice of needle trajectories and achievable target depth because only short needles could be used in the narrow bore. A short and wide bore scanner could significantly improve patient access and device placements [19, 24, 105, 182]. It should be noted that the proposed scanner control via mobile tablet PCs in combination with auto-land marking [183] could furthermore facilitate interventions on the other side of the bore where patients might be more accessible (no patient table mount) but generally no MRI controls are located (i.e. current wide bore MRI scanners).

Targeting accuracy is essential for image-guided interventions and an in-plane error of 5 mm is acceptable in most clinical situations according to Rothgang and colleagues [19]. The 3D RMS error was found to be below this value in the phantom and the cadaver experiments performed by the expert and novice. Our targeting accuracy results (Table 4.1) are equivalent to the targeting errors that have previously been reported (Stattaus *et al.* [182] - *in vivo*: 3.4 mm median lateral deviation, Fischer *et al.* [131] - 5.2 mm mean in-plane error, Rothgang *et al.* [19] - *in vitro / in vivo*: 1.8 mm / 2.9 mean targeting error in all directions) for MRI-guided percutaneous interventions employing the freehand technique. The mean puncture times (novice: 6 minutes and 35 seconds / expert: 5 minutes and 21 seconds) and mean procedure times (novice: 17 minutes and 31 seconds / expert: 15 minutes and 46 seconds) are reasonable in comparison to what previous freehand liver biopsy studies have reported (Stattaus *et al.* [182] - *in vivo*: 19 minutes mean puncture time, Das *et al.* [104] - in vivo: 20 - 25 minutes mean intervention time, Fischbach *et al.* [25] - *in vivo*: 18 minutes mean intervention time).

The variation between individual cadavers, i.e. time of death to embalming, the shelf time (which affects the MRI properties [67]), the surgical history (causing air trapped within the abdominal and thoracic cavities, displaced and shrunken liver, lack of blood supply and unusual liver motion), and whether or not pre-existing (one cadaver) or artificial lesions were employed, influenced procedure times. Due to the influence of these cadaver specific variations, which are not

found during clinical procedures, detailed recording of procedure times was not applied during the Thiel soft-embalmed cadaver experiments. Further experience with the cadaver model, vascular re-perfusion [61] and adaptation of technique should solve most of these problems in the future so that the benefit of the real human anatomy [61] can be fully explored for the development and training of iMRI procedures.

4.5 Concluding Remarks

MRI has unique potential for guiding percutaneous interventions specifically for procedures that cannot be performed safely or satisfactorily using other guidance modalities due to lack of tissue contrast, imaging interference (e.g. ribs or air filled bowel during ultrasound), vascular imaging [24] or ionising radiation, which is most relevant e.g. for young patients [59, 119]. The presented components and techniques can improve the workflow of percutaneous interventions using MRI guidance by providing interactive, versatile and intuitive MRI acquisition control at the patient table as well as scanner operator - physician - assistant communication. Future research should involve acoustic or digital noise filtering for audio communication, a full MRI safety assessment of all incorporated components, integration of optimised fast pulse sequences into the web UI and a protocol for pre-clinical trials (i.e. using large animals). It should be noted that the methods presented in this chapter were designed for percutaneous needle interventions but can be translated with limited effort to other MRI-guided applications. A final word of caution is warranted in reproducing the described setup and each solution and component should be tested individually on site and approved by the local MRI safety authorities.

Chapter 5

Wireless Tracking of Interventional Devices

This chapter is based upon:
M. A. Rube, A. B. Holbrook, B. F. Cox, J. G. Houston, A. Melzer, "Wireless MR tracking of interventional devices using phase-field dithering and projection reconstruction", *Magn Reson Imaging* [Epub ahead of print]; doi:10.1016/j.mri.2014.03.007

Experimental contributions:
(i) B. F. Cox prepared the phantoms, the flow pump and prepared and supervised the human cadaver experiments (the cadavers were embalmed and provided by CAHID). (ii) A. B. Holbrook contributed to implement the reconstruction. (iii) B. Cox, A. Melzer and J. G. Houston validated the developments from a clinical perspective.

5.1 Introduction

During iMRI, operator/physician interaction is required for acquiring and displaying images according to the position and orientation of the interventional device. This is particularly important for endovascular procedures, where blood flow and respiratory motion are present during device manipulation. Interactions with the MRI system, in terms of device localisation and change of acquisition parameters, are challenging [157] in comparison to conventional X-Ray guided procedures and represent a major hurdle for an efficient workflow [19, 184].

Safe, reliable, and easy to use tracking and visualisation of moving devices are key elements for successful clinical implementation of iMRI [6]. Over the past decades, several device visualisation and tracking methods have been developed for iMRI as outlined in Section 2.4.5. This chapter presents an application of MR-tracking, based on the well-known method introduced by Dumoulin and colleagues [146], which was dramatically improved in his publication in 2010 [185] in which phase-field dithering was added to the tracking pulse sequence. Phase-dithering removed issues encountered when working with situations where signal dephasing occurs due to pulsatile flow, issues resulting from the proximity of imaging coils (i.e. B_1 effects), as well as due to complex susceptibility artefacts.

In contrast to the aforementioned MR-tracking sequence by Dumoulin *et al.*, this tracking implementation was applied to wRCs that inductively couple [145] to the surface receiver coils of an MRI system (see Section 2.4.5.3). Device tracking based on wRCs presents a promising solution for iMRI because no electrically conductive connection between the device tip and the MRI scanner is required. This avoids the risk of RF induced tissue heating [31, 33, 35, 186] and reduces system complexity in terms of engineering and procedure workflow. This MR tip-tracking sequence was also interleaved with various fast, user-selectable pulse sequences that generated different contrast mechanisms with potentially different temporal resolutions. Each imaging sequence received a frequent geometry update from the tracking kernel. The coil position was also mapped to a pre-acquired 3D angiographic roadmap.

This work serves as a feasibility study of wireless device tracking to be used

during iMRI and was demonstrated on a clinical 1.5 T MRI scanner by means of arterial flow phantom and Thiel soft-embalmed human cadaver [62, 67, 169] experiments.

5.2 Theory

As described in Section 2.4.5.3, wRCs are based on the principle of electromagnetic induction, where an electric circuit is tuned to resonate at the proton Larmor frequency (f_0) of the imaging system according to Equation 2.19. It has been proposed [145, 187] to use a small object containing a solution with very short T_1 within the coil of the wRC to enhance the signal amplification effect. However, this is not applicable for the described purposes, as endovascular procedures are performed according to Seldinger [122], whereby catheters are placed over a guidewire, and essentially no MR signal-carrying lumen can be used to contribute to the signal amplification.

Weiss *et al.* [188] suggested using low FA RF excitation pulses and projection readouts to localise a wRC during iMRI. This concept was adopted and integrated into a dedicated non-imaging MR pulse sequence proposed by Dumoulin and colleagues [185]. This pulse sequence had been originally developed for improved active catheter tracking in low SNR conditions and for active tracking of micro coils that were inductively coupled to the receive coil.

The proposed tracking pulse sequence (Figure 5.1) employs non spatially-selective or weakly spatially-selective RF excitation pulses with very low FA. MR signal is detected in the presence of a frequency-encoding gradient applied along all three axes (G_x, G_y, G_z) while intentionally no phase-encoding gradient pulse is present. This 1D projection sequence is repeated four times while the gradient polarities are alternated in a Hadamard modulated readout (HR) scheme [146] to compensate for off-resonance effects. The position (X,Y,Z) of the wRC with respect to the applied magnetic field gradient pulse is determined by FFT (see Section 2.2.4) and is computed according to Equation 5.1 by finding the peak position (P_i) for each of the four excitations as previously described by Dumoulin and colleagues [146].

$$
\begin{aligned}
X &= -P_1 + P_2 + P_3 - P_4 \\
Y &= -P_1 + P_2 - P_3 + P_4 \\
Z &= -P_1 - P_2 + P_3 + P_4
\end{aligned}
\tag{5.1}
$$

Phase-dithering is employed to improve the peak-to-noise ratio (PNR), similar to the method that has been described in [185]. Therefore, additional dephasing magnetic field gradient pulses (illustrated as (A) in Figure 5.1a) are applied orthogonal to the subsequent frequency encoding gradient pulses to suppress background signals while preserving the intensified signal around the wRC. A magnetic field gradient applied perpendicular to the frequency encoding direction causes dephasing of the tissue signal and leads to a reduction of overall background signal. Ideally, a one-cycle (2π radians) dephasing gradient is applied across the excited slab, resulting in complete background cancellation [189, 190]. The same dephasing gradient does not affect the signal of the wRC significantly, because the coil is relatively small (less than 15 mm) compared to the excited background tissue slab [190], thus the enhanced signal caused by the wRC is preserved.

The direction and amplitude of an efficient dephasing gradient is highly dependent [185] on the object within the FOV and the orientation of the wRC in regards to the RF transmission coil. To avoid imperfect dephasing, a series of readouts with N different dephasing gradient directions is acquired. The candidate with the highest PNR for each HR is then selected automatically. The dephasing gradient direction (Figure 5.1b) is chosen to be always in a plane (P) that is perpendicular to the direction of the frequency encoding gradient pulse. An arbitrary choice has to be made for the first direction [185] because an infinite number of orthogonal directions exist. The dephasing gradient is then rotated by $2\pi/N$ for each sequential acquisition [185]. This implementation requires N x 4 repetitions to compute the most accurate position of the wRC. Spoiling gradients are applied at the end of each repetition to dephase the magnetization, and thus (for low FA excitations) reduce phase coherences.

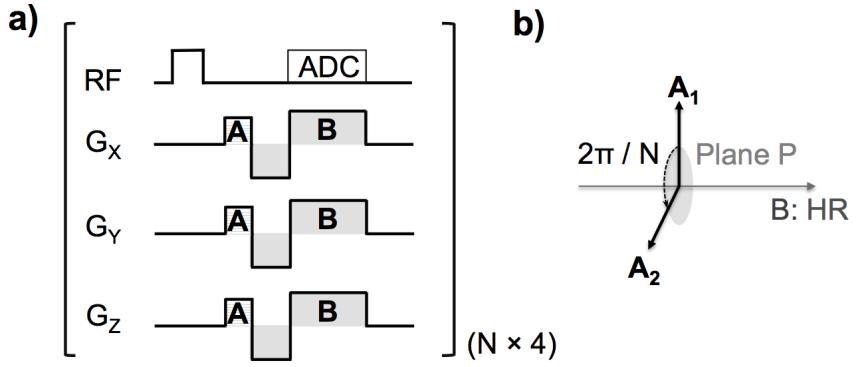

FIGURE 5.1: Pulse Sequence diagram for detecting the position of the wRC - **(a)** A weakly selective RF excitation pulse with very low FA excites all spins within the active slab. The spins in the close vicinity of the wRC experience an amplified FA because a current is induced within the coil of the wRC. The frequency encoding gradient pulse (B) is multiplexed with a Hadamard scheme as described by Dumoulin *et al.* [146]. Before the frequency encoding readout a phase-field dithering (A) is applied [185]. The direction of the dephasing gradient (A) is chosen to be in a plane P perpendicular to the direction of the frequency encoding gradient pulse (B) as indicated in **(b)**. An arbitrary choice is made for the first direction and the gradient direction is then rotated in the plane P by $2\pi/N$ for the next repetition. This tracking scheme requires N repetitions for the different dephasing directions multiplied by the four different Hadamard multiplexed frequency encoding gradient pulse directions. The polarity $[G_x, G_y, G_z]$ of the gradient (B) for the four readouts is $B1 = [+,+,+]$, $B2 = [-,-,+]$, $B3 = [-,+,-]$, $B4 = [+,-,+]$.

5.3 Materials and Methods

This section describes the implementation of the MR-tracking and the imaging pulse sequences in detail. In addition, the iMRI, the phantom and cadaver setup and protocols are outlined.

5.3.1 Tracking Pulse Sequence

The tracking pulse sequence diagram is shown in Figure 5.1. The HR scheme provides three dimensions of positional information within four excitations. Therefore, this tracking implementation requires four times the number of different dephasing gradient directions (N x 4 x TR) to compute the most accurate position of the wRC.

It should be noted, that ideally the coil of the wRC should have had all dimensions matching the readout resolution. This would have resulted in a very

sharp peak in the presence of magnetic field gradients and hence spatially very accurate tracking results. However, for the described (non-ideal) wRC designs (see Figure 3.3 and Section 3.4.0.4) it was essential to use the centre of mass for the peak detection algorithm and not the maximum signal intensity value, as the broad peak represents a relatively large area of spins with amplified FA in close vicinity of the wRC.

The tracking sequence was implemented with standard multiple receiver imaging coils and no limitation of receiver channels. Therefore, the PNR was taken into account for each coil element. The coil element with the highest PNR (for a given phase-field dithering direction) was selected because this represents the coil element that inductively couples best to the wRC. The catheter tip position was then computed in the MRI coordinate system after a gradient warp correction for gradient non-linearities. The tracking pulse sequence parameters were used as follows: TE/TR = 1.52/2.18 ms, FA = 0.3°, FOV = 48 cm along the readout direction, Isotropic tracking resolution = 1.8 mm, Slice thickness = 300 mm.

5.3.2 Interleaved Imaging Pulse Sequences

The tracking sequence was interleaved with one or more user-selectable rapid imaging sequences in a closed loop manner. This is illustrated in Figure 5.2. Generally the tracking pulse sequence can be interleaved with any imaging pulse sequence that accepts a position update from the tracking sequence and does not interfere with its low FA excitation. For instance, remaining magnetisation has to be eliminated before a subsequent tracking cycle. The position of the tip of the interventional device was detected by the tracking sequence and then used to automatically adjust the scan plane of the following imaging slice. Spoiling gradients were applied at the end of the imaging sequence to dephase the magnetisation, and thus reduce phase coherences before a subsequent low FA excitation was employed in the tracking sequence.

Three different imaging sequences were implemented that received a scan plane update from the tracking sequence. First, a bSSFP sequence using a Cartesian k-space data acquisition scheme and generating T_2/T_1 contrast [95, 96] was

FIGURE 5.2: The block diagram of the interleaved tracking and imaging pulse sequence with automated scan plane updates. The wRC position is determined by the tracking kernel, which then automatically emits a coordinate update. The imaging sequence receives this new coordinate and geometry update and is executed after a steady state stabilisation interval. The imaging sequence can be repeated for a number of user selected exclusive runs before it receives a new coordinate update. Finally, spoiling gradients are applied to reduce phase coherences before a subsequent low FA excitation.

TABLE 5.1: MRI pulse sequences and parameters for the tracking study

Parameter	**Diagnostic MRI**	**Interactive rtMRI**		
	2D SPGR TOF	*bSSFP*	*FSPGR*	*spGRE*
TE / TR [ms]	2.3 / 18.0	2.5 / 5.0	2.8 / 5.6	3.5 / 20.4
FOV [cm x cm]	20 x 20	30 x 30	30 x 30	24 x 24
Matrix / Resolution	256 x 256	320 x 192	256 x 128	0.9 mm
FA [°]	30	70	30	70
Slice thickness [mm]	2 / 20% gap	7	7	8

realised. Second, a FSPGR sequence with Cartesian k-space acquisition scheme generating high spatial resolution and T_1 contrast [191] was integrated. Third, a GRE-based sequence with spiral k-space data acquisition scheme (spGRE) was designed to achieve a high temporal resolution. Therefore, five 10.65 ms spiral readouts were used to cover k-space for a FOV of 24 cm to achieve an in-plane resolution of 0.9 mm and a temporal resolution of 10 frames per second (fps) for the spGRE sequence. The operator was able to select each imaging sequence through the control console on the fly. All imaging parameters for the tracking study are summarised in Table 5.1.

Figure 5.2 illustrates how each imaging sequence received a coordinate and geometry update and was executed after a steady state stabilisation interval. As previously proposed [192], a non-linear ramp-up with eight consecutive RF pulses ($\beta = 3$) was used to transfer the initial longitudinal magnetisation toward its steady state prior to bSSFP data acquisition. Alternatively, a stabilisation interval (similar to what has been described in Figure 2.12) employing 40 dummy

repetitions [193] was used prior to FSPGR data acquisition. The catheter tip position was also used in a previously acquired static 3D MRA roadmap for catheter guidance. As proof of principle a bright blood ToF [194] sequence (2D SPGR ToF) was integrated into the iMRI interface producing a 2D stack of non-contrast enhanced MRA (nonCE-MRA) images.

5.3.3 Real-Time MRI Implementation

All experiments in this study were performed in the iMRI suite at IMSaT, which was described in Section 3.2.2, and with the modifications that were outlined in Section 4.2 (except the browser-based iMRI UI that was designed for percutaneous interventions). All MRI experiments were conducted in the 1.5 T MRI scanner (Signa HDx, Software Release 15.0M4A, GE Healthcare, Waukesha, WI, USA) with the DuoFlex coil prototype (see Section 3.2.2) consisting of a single loop element with disposable cover (posterior) and a 4ch 24 cm element (anterior).

All pulse sequences were designed in a graphical pulse sequence environment (SpinBench, Version 1.3.2, HeartVista, Inc., Palo Alto, CA, USA) and implemented in RTHawk [45] (RTHawk, Version 0.9.28, HeartVista, Inc., Palo Alto, CA, USA), running on the external workstation. A real-time visualisation application [57] (Vurtigo, Version 2-1b, Sunnybrook Health Sciences Centre, Toronto, Canada) embedded in RTHawk, was used to render the tip position, the current scan plane, and optionally a 3D MRA dataset. This allowed the operating physician to view the real-time catheter tip position connected to the rtMRI scan plane and also to monitor the catheter movement overlaid to a MIP of the nonCE-MRA dataset. The performance of the tracking kernel for reliable detection of the catheter was optimised and evaluated by moving a straight catheter (S1 - Table 3.1) through the imaging volume along known reference points.

5.3.4 In Vitro Experiments in Perfused Arterial Phantoms

In vitro experiments (20 repetitions) were conducted by two experienced interventional radiologists in an arterial vessel phantom consisting of an above the knee

lower extremities (LE), an abdominal and a thoracic module (L-F-S-Left-003, A-S-N-001, T-R-N-020, Elastrat, Geneva, Switzerland). The phantom was connected to a modified heart lung machine (HL-30, Maquet, Rastatt, Germany) and perfused with 0.9% saline solution to mimic the electrical and relaxation properties of blood ($T_1 \approx 1150$ ms, $T_2 \approx 130$ ms at 1.5 T and 20 °C). The pump was positioned outside the scan room and set to a flow rate of 4.8 L/min, a heart rate of 85 beats per minute and a systolic/diastolic pressure of approximately 130 / 70 mmHg.

The containers of the vessel phantom were backfilled with a 10% gelatinous solution to mimic muscle tissue ($T_1 \approx 846$ ms, $T_2 \approx 51$ ms at 1.5 T and 20 °C). Vascular access was established with a 12-F introducer sheath (Check-Flo, Cook Inc., Bloomington, IN, US) in the right femoral LE. A straight (S1 - Table 3.1) and a balloon catheter (B1 - Table 3.1) were inserted over a 0.035" MRI-safe polymer guidewire (Section 3.2.1.1). The balloon catheter was inflated with a 1:100 Gd-DOTA (Dotarem; Guerbet, RoissyCDG Cedex, France) doped solution to allow positioning verification and to monitor the dilatation process.

FIGURE 5.3: Balloon angioplasty performed in a clinical whole body 1.5 T MRI scanner (Signa HDx, GE Healthcare, Waukesha, WI, USA). The catheter was manipulated in front of the bore while the catheter was tracked and the scan plane updated and displayed accordingly. The pictures were taken from three wireless IP cameras (M1031W, Axis, Lund, Sweden) that were installed in the scan room. All three images were acquired at the same point in time on **(a)** the left camera, **(b)** the right camera and **(c)** the camera behind the bore with a 10x zoom lens. The interventional radiologist was able to monitor the procedure on a 40" in-room monitor NEC (Multeos 401, NEC Corporation, Tokyo, Japan) and adjust the scan acquisition on demand or with a wireless input device as described in Chapter 4 (not shown on the photographs).

5.3.5 Ex Vivo Experiments in Thiel Embalmed Human Cadavers

The human cadavers used in this study were donated according to standard procedures as set out in the Human Tissue (Scotland) Anatomy Act 2006, and the Thiel Advisory Committee (University of Dundee, UK) has approved all procedures in this study involving human cadavers. Three Thiel soft-embalmed cadavers (sex: 2 male and 1 female, age: 50 - 70 years, weight: 65 - 80 kg) were prepared in the angio-suite and then each cadaver was transferred to the MRI for the experiments (the setup is illustrated in Figure 3.4). Vascular access was established with a 12-F introducer sheath (Check-Flo, Cook Inc., Bloomington, IN, US) in the left femoral artery. The femoral artery was then flushed with 0.9% saline solution to mimic the electrical properties of blood.

Two experienced interventional radiologists evaluated the proposed methods by navigating the straight catheter over the MRI-safe guidewire into the femoral artery. No 3D roadmap was acquired for the cadaver experiments due to the absence of perfusion (at the time of experiments, venous return was not be established in the Thiel cadaver model and extravasation permitted perfusion of longer vascular segments).

5.4 Results

All catheters with wRCs remained functional throughout the flow phantom and cadaver experiments. The wRCs resulted in an increase in mechanical stiffness and an outer diameter of 2.4 mm (7-F) of both catheters. This prohibited their use in vessels with an inner diameter of 3 mm or less.

5.4.1 In Vitro Evaluation in Perfused Arterial Phantoms

Figure 5.4 illustrates the signal after FFT for four different receive coil channels. Each coil element was receiving MR signals during a tracking cycle with phase-field dithering (N = 3) while the straight catheter was navigated through the phantom. The coil element with the highest PNR averaged over the 4 HR is plotted in Figure

5.5 (same phase-field dithering cycle as in Figure 5.4), which was automatically selected by the peak detection algorithm. Without phase-field dithering, catheter positions were not adequately resolved due to high background noise.

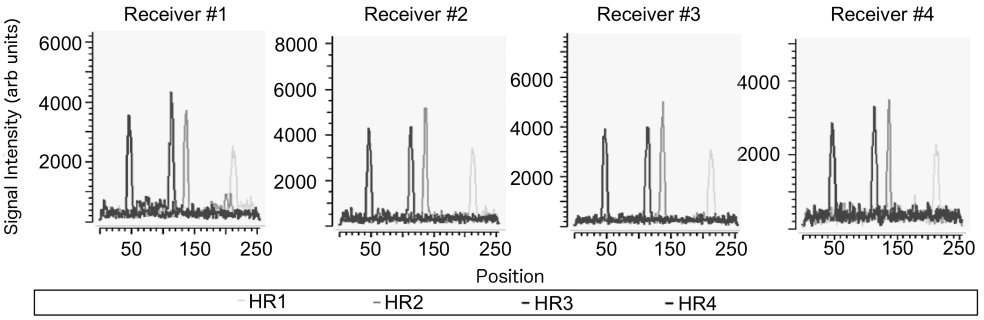

FIGURE 5.4: Signal plots post fast Fourier transform (FFT) while each of the four plus one different coil channels were receiving MR-tracking signals during a tracking cycle with phase-field dithering (N = 3). The catheter coil peaks in the four Hadamard modulated readouts (HR) can be distinguished from the background noise for each coil element. The catheter position was computed from the coil element with the highest peak-to-noise ratio (PNR) averaged over the 4 HR. This coil element is displayed separately in Figure 5.5. The pulse sequence then emitted a new geometry if the PNR was above a user-defined threshold. The PNR was found to exceed a value of 15 along all readout directions (data not shown) during catheter navigation in the perfused phantom.

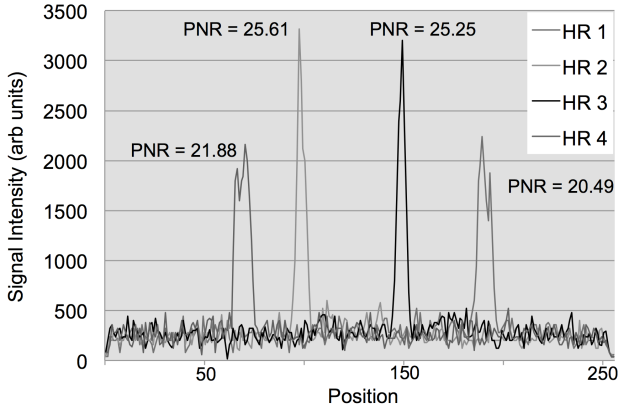

FIGURE 5.5: MR-tracking signals post fast Fourier transformation (FFT) from a phase-field dithering cycle (N = 3) using the 5-French straight catheter in the perfused arterial phantom. The plot displays the coil element with the highest peak-to-noise ratio (PNR) averaged over the 4 Hadamard modulated readouts (HR). The catheter coil peaks / locations in the four HR can be distinguished from the background noise. Note, if the wRC and the MR environment were ideal, each HR would have shown a single narrow peak.

An area with enhanced FA was clearly visible at the tip of the catheter, once the wRC was located in the imaging slice, after a coordinate update (Figure 5.7a and b). The tracking kernel provided up to 38 catheter position updates per second. The tracking sequence delivered very low SAR compared to standard imaging pulse sequences because of the low FA excitation.

Distance errors were measured as the difference between the tracking position and the centre of gravity of the catheter tip (X_c, Y_c, Z_c) as displayed in Figure 5.6a. The centre of gravity is depicted as sphere in Figure 5.6a. All tracking points were found to be inside the area of enhanced signal resulting from the wRC on the catheter tip. The statistical summary for the distance error is displayed in Figure 5.6b. The volume root mean square (RMS) distance error was 2.81 mm, the mean distance error in 3D was 2.49 mm and the standard deviation was 1.31 mm.

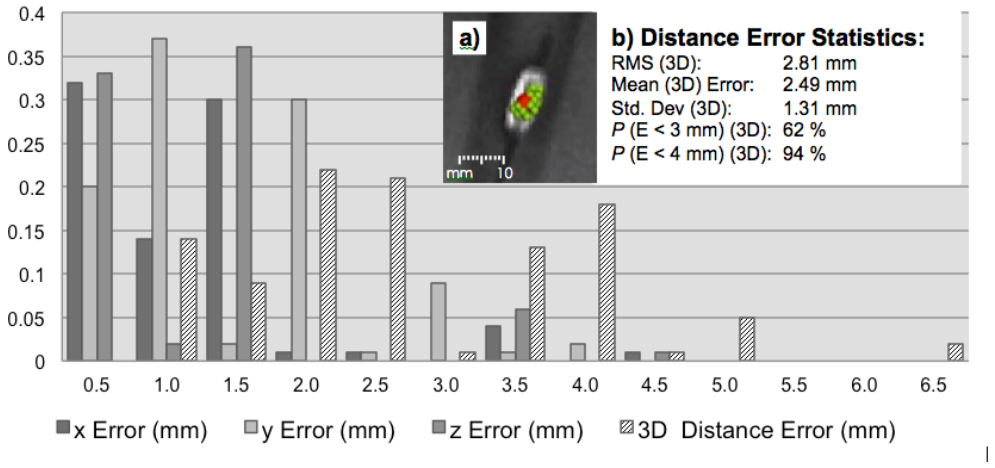

FIGURE 5.6: Distance errors (mm) represented as a frequency histogram - The error (E) represents the distance between the tracking position and the centre of gravity of the wRC on the catheter (X_c, Y_c, Z_c). The centre of gravity is indicated as red sphere in **(a)**. The green points in **(a)** show the tracking point history (n = 1000) for one fixed catheter position in the vessel phantom. The statistical summary for the distance error is displayed in **(b)**. As demonstrated in the graph, all points were found to be inside the area with enhanced signal intensity caused by the wRC on the catheter tip

Two interventional radiologists concluded that both catheters could be steered through the target vasculature with adequate visualisation of the catheter tip in addition to the surrounding anatomy (Figure 5.7). The small FA of the tracking excitation followed by spoiling and a steady state preparation interval did not noticeably affect the quality of the rtMRI images. The imaging pulse sequences

received a frequent geometry update from the tracking kernel and the coil position was also mapped to a pre-acquired 3D roadmap. Figure 5.7 illustrates the ability to switch between different sequences during a procedure with each sequence tailored to the particular task at hand. The tracking position was stable while navigating through the femoral artery, iliac artery (Figure 5.7b) and the aorta. The position remained adequate during balloon inflation in the right iliac artery (Figure 5.7c). The operator was able to switch back and forth between different pulse sequences (one mouse click, no time delay) while each sequence was receiving an adequate coordinate update.

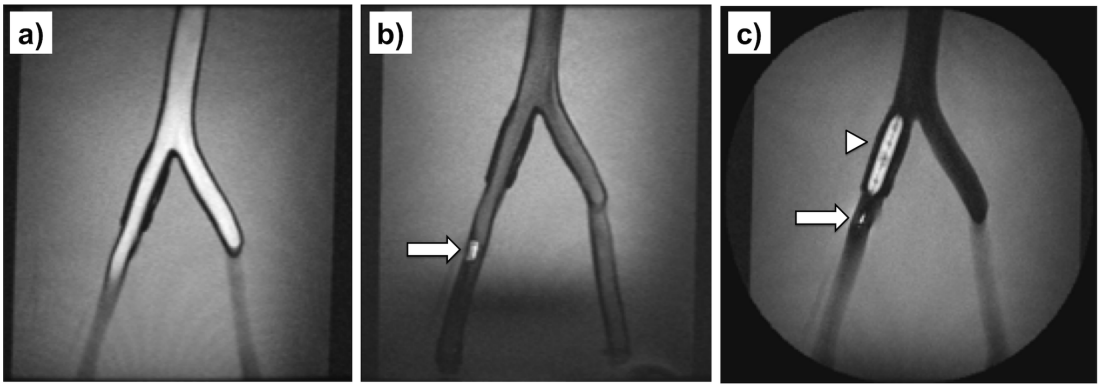

FIGURE 5.7: MRI-guided balloon angioplasty of the right iliac artery in the perfused arterial phantom. The rtMRI sequence received a tracking update from the tracking pulse sequence and the pulse sequence and parameters were switched on the fly over the user interface - bright blood imaging **(a)** with bSSFP (TE/TR = 2.5/5.0 ms, FA = 70°, FOV = 30 cm, Matrix 256 x 256, Slice thickness = 2.5 mm). The straight catheter (wRC is illustrated as arrow) was advanced **(b)** while the FA is reduced in the bSSFP to FA = 30°. The catheter was then exchanged with a balloon (wRC is illustrated as arrow) catheter and inflated **(c)** with a 1:100 Gadolinium doped solution and once the catheter was in position, a balloon inflation (arrowhead) was performed using FSPGR imaging (TE/TR = 2.8/7.0 ms, FA = 70°, FOV = 30 cm, Matrix 256 x 256, Slice thickness = 7 mm).

A 2D spGRE plane was fused to a 3D nonCE-MRA roadmap (Figure 5.8a). Then a catheter was inserted and advanced while the imaging plane was continuously re-aligned to the updated tracking position of the catheter (Figure 5.8b). A 2D view of a FSPGR sequence while the slice was updated to the current catheter position (red sphere pointed out by arrow) is demonstrated in Figure 5.8c. The catheter position was also mapped to the roadmap (Figure 5.8b) according to the preference of the physician and was optionally used to realign the scan plane to

the current catheter position. Figures 5.8d and e demonstrate how the catheter was moved inside the 3D roadmap while the 2D spGRE scan plane (arrowhead) was automatically realigned to the current catheter position (red sphere pointed out by arrow).

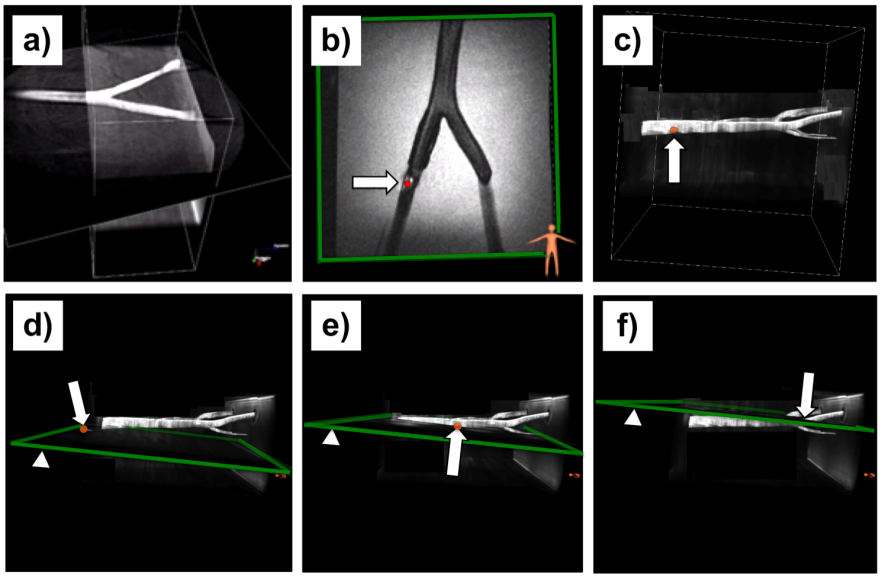

FIGURE 5.8: Wireless device tracking in 2D and 3D. Figure **(a)** A (2D) spGRE plane was fused to a short section of a previously acquired maximum intensity projection (MIP) of a non-contrast-enhanced MR 3D angiogram while no device was present. Note the image, obtained with the spGRE (TE / TR = 3.5 / 20.4 ms, FA = 30°, FOV = 24 cm, 5 interleaves, Slice thickness = 8 mm) and a frame rate of 10 images per second, shows a black area right before the aortic bifurcation due to the present turbulence. The catheter was inserted and the tracking position was rendered to the dataset. Then the imaging plane **(b)** was automatically re-aligned based on the tracking position of the wRC (red sphere pointed out by arrow). According to the preference of the interventional radiologist, the tracking position of the wRC was rendered to a previously acquired MIP of a non-contrast-enhanced MR angiogram (3D) while the scan 2D plane was not updated **(c)**. Images **(d - e)** demonstrate how the catheter was moved inside the roadmap while the 2D spGRE (TE / TR = 3.5 / 20.4 ms, FA = 7°, FOV = 24 cm, 5 interleaves, Slice thickness = 8 mm) scan plane (arrowhead) was automatically realigned to the current catheter position.

5.4.2 Ex Vivo Evaluation in Thiel Embalmed Human Cadavers

During *ex vivo* experiments, two interventional radiologists successfully inserted and navigated the straight catheter (5-F) through the femoral artery of three

Thiel soft embalmed cadavers. Figure 5.9 illustrates the signal after FFT for four different receive coil channels, similar to what was described for the phantom experiments. Each coil element was receiving MR-tracking signals during a tracking cycle with phase-field dithering (N = 3). The PNR was calculated for each HR and is displayed in Figure 5.9 above each peak. During catheter navigation and continuous movement the PNR was found to exceed a value of 10 along all readout directions (data not shown). The sequence parameters required optimisation for the Thiel embalmed human cadaver. Hence, a FA of 1.5° and smoothing of the curve were applied to improve the PNR.

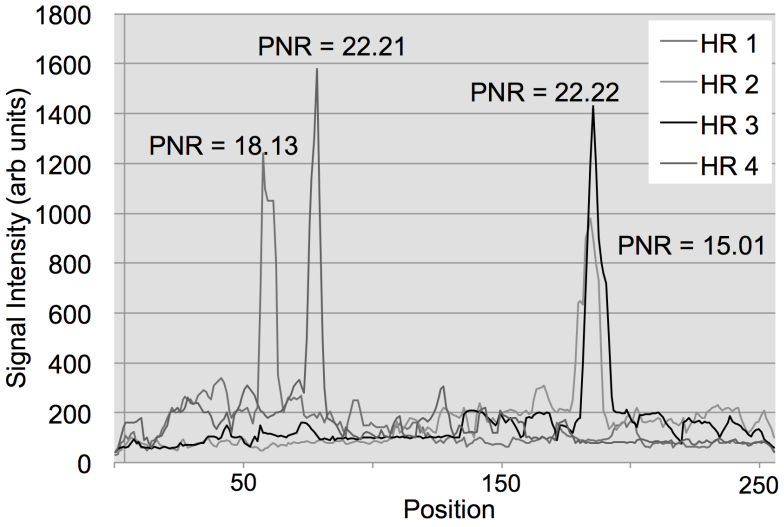

FIGURE 5.9: MR-tracking signals post fast Fourier transformation (FFT) from a phase-field dithering cycle (N = 3) while the 5-French straight catheter was positioned in the femoral artery of a Thiel soft-embalmed human cadaver. The plot displays the coil element with the highest peak-to-noise ratio (PNR) averaged over the 4 Hadamard modulated readouts (HR). The catheter coil peaks / locations in the four HR can be distinguished from the background noise. Note, smoothing of the curve and a FA of 1.5° were applied to improve the PNR for the tracking pulse sequence for the cadaver experiments.

During catheter navigation an area with enhanced FA was clearly visible (Figure 5.10) at the tip of the catheter after a coordinate update was received and executed. Figure 5.10 illustrates interactive switching between different pulse sequences during the catheterisation of the femoral artery of a Thiel soft embalmed cadaver. This was enabled on request of the operating physician, depending on his preference of high spatial or temporal resolution. Figure 5.10e illustrates the

tracking positions that were found for 1000 repetitions of the tracking pulse sequence with phase-field dithering (N = 3) while the catheter was maintained in the same position.

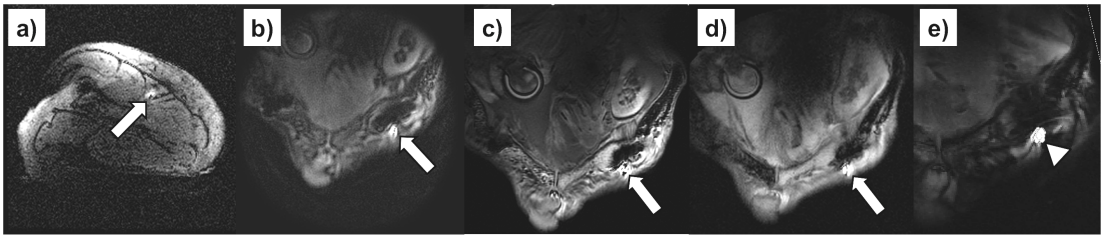

FIGURE 5.10: MRI-guided catheter navigation in the left femoral artery of a Thiel soft embalmed human cadaver. The arrow indicates the wRC that appears very bright compared to the background tissue. An axial FGRE (TE/TR = 5/11.8 ms, FA = 20°, FOV = 21 cm, Matrix 256 x 256, Slice thickness = 5 mm) localiser slice **(a)** that contains the wRC is displayed. The rtMRI sequence received a tracking update from the tracking pulse sequence and the pulse sequence and parameters were switched on the fly with the user interface. Images obtained with **(b)** a FSPGR sequence (TE/TR = 2.8/7.0 ms, FA = 70°, FOV = 25 cm, Matrix 256 x 256, Slice thickness = 7 mm), **(c)** a bSSFP sequence (TE/TR = 2.5/5.0 ms, FA = 70°, FOV = 30 cm, Matrix 256 x 256, Slice thickness = 2.5 mm) and **(d)** a spGRE sequence (TE / TR = 3.5 / 20.4 ms, FA = 30°, FOV = 24 cm, 16 interleaves, Slice thickness = 8 mm). On the right **(e)** the history of 1000 tracking points (arrowhead) for a fixed catheter position was overlaid on a magnitude image of the cadaver.

5.5 Discussion

A wireless tracking sequence employing phase-field dithering and projection reconstruction was developed and interleaved with various user-selectable fast pulse sequences to facilitate cardiovascular interventions in clinical whole body MRI scanners. RTHawk is a flexible research real time MRI software framework [45] and allows generating new pulse sequences and dynamically changing major aspects of data acquisition such as gradient waveforms, excitations and scan planes on the fly. A dedicated real-time visualization application for guiding interventions called Vurtigo [57], developed at the Sunnybrook Health Sciences Centre and embedded in RTHawk, was used to render the tip tracking position, the current

scan plane, and optionally a 3D MRA dataset. The proposed tracking and imaging methods do not require hardware modifications of the MRI scanner setup and address the key issue of robust MR tracking.

On the other hand, active tracking based on physically connected micro coils mounted at catheter distal ends has widely been used [34, 103, 146, 185, 195] and provides an excellent, reliable and very robust form of MR tracking. However, these micro receive coils of the catheter have to be connected to the MRI system in a similar fashion as imaging coils. This constitutes significant design challenges [149], potential cable loops [196] and the risk of instrument heating [31–33] leading to increased cost of producing these catheters (see also Section 2.4.5.2). The proposed technique is based on small resonant circuits that inductively couple to the MRI transmit and receive coils and does not utilise long electrical conductors [75] and did not show significant heating (less than 0.6°C) during RF induced heating experiments, which were described in Section 3.3.1.2.

Phase-dithering, similar as described by Dumoulin *et al.* for active tracking [185], has significantly improved the tracking accuracy and the peaks in the MR tracking were adequately resolved. The accuracy of the proposed tracking method was found to be similar to methods that were proposed for active catheter tracking and cited an overall accuracy in the range of +/- 2 - 4 mm [195, 197, 198]. Similarly, the time that was required for a positional update was approximately 26 ms, which is comparable to active tracking methods ranging between 20 ms [185] and 24 ms [34]. Further improvement for this tracking pulse sequence is possible by averaging over multiple tracking cycles, at the expense of increased scanning time. The results of the phantom and cadaver experiments successfully demonstrate that fast and reliable detection of wRCs is feasible and may successfully be employed for iMRI applications. The PNR of the cadaver experiments (Figure 5.9) was lower compared to the idealised phantom experiments (Figure 5.5). However, MR imaging of Thiel soft-embalmed cadavers is constrained [67] and constitutes the worst case as living organisms provide better RF penetration [67] and it is foreseen that imaging and tracking will improve in animal and patient studies.

Additionally, it would be desirable for complex catheter shapes and challenging vascular navigation to obtain more than one tracking position on catheters to determine the tip orientation in particular where the tip can fold on itself (i.e. create a loop of the shaft near the tip), which cannot be detected with a single coil. Therefore, it was proposed to use multiple independent micro receive coils for active catheter tracking [34, 57, 146]. In the presented implementation, if more than one wRC is used, multiple signals would couple to the receive coils resulting in multiple peaks per projection readout. These peaks would correspond to a range of possible 3D position candidates after computation of the Hadamard encoded readouts. To overcome this problem, an algorithm for fast 3D localisation of several wRCs has been proposed [187] and applied in prostate biopsies (using three wRCs containing a MR signal-carrying lumen each). This method [187] could potentially also be adapted for MR tracking of multiple wRCs on catheters (SW1 - Table 3.1) employing phase-field dithering, which has to be investigated in further studies.

Another interesting approach to address this problem is to combine a single wRC on the tip of the catheter and passive susceptibility markers along the shaft (SW2 or M1 - Table 3.1). These catheters could also be used with this tip tracking implementation (no modifications required) while the wRC on the tip is used for position tracking (and scan plane updates) and the passive markers for catheter shaft visualisation.

The presented implementations offer reliable catheter tip localisation and scan position updates in combination with the ability to switch between high- and low-resolution as well as different contrast mechanisms. Despite the fact that the results with bSSFP or FSPGR imaging were obtained with approximately one fps, higher frame rates could easily be achieved by utilizing parallel imaging [39, 40] or other acceleration techniques while not affecting the tracking robustness. The presented spGRE achieved frame rates up to ten fps and was found useful for imaging of dynamic processes e.g. for blood flow proximal and distal to an occluded vessel pre and post treatment. Higher frame rates utilizing spGRE may be possible; however this would compromise image quality. While the 2D display was

the preferred guidance method, the operating interventional radiologists rated the real-time tip tracking position displayed in the 3D roadmap very useful, particularly during the initial steps of an intervention. This was also preferred when exact positioning under rtMRI guidance was not essential or in anatomical structures with complex vasculature that could not be imaged within a single 2D plane. The tracking position displayed in the roadmap can be particularly useful when low SAR exposure is a key requirement.

In this study, two different (straight/balloon) catheters were used to demonstrate fast sequence and device interchange ability during a procedure. However, a major hurdle to clinical evaluation is the integration of wRCs with a sufficient quality factor into the catheter design [164, 167, 199]. Ideally, the coil design (see Figure 3.3a) should have had all dimensions matching the readout resolution but with current manufacturing technologies, we were not able to achieve a sufficient Q for the given catheter dimensions. Alternatively, a higher Q could have been achieved by increasing the diameter of the copper wire. However, this was discarded because a larger outer diameter would necessitate arterial access of a larger caliber and limits the use to interventions in larger vessels only. As already discussed in Section 3.4.0.4, the stiffness and increased outer diameter is a temporary problem of manually wound wRCs and recently micro systems based technologies for production of wRCs have been validated [164, 200, 201]. In the future, these optimised and miniaturised wRCs, will enhance the tracking accuracy and alleviate negative catheter changes (e.g. increased diameter, stiffness and glide). However, these manufacturing technologies have to be evaluated to understand if sufficient quality factors [164, 167, 199] can be achieved for MR-tracking.

5.6 Concluding Remarks

A feasible concept for fast and robust wireless device tracking was presented that is not limited to catheters and can in principle be used on any device (e.g. a guidewire or cannula) with a wRC. The wireless tracking can be combined with various pulse sequences and does not require any changes to the MRI scanner hardware. This implementation reduces complexity, minimises user interaction

with the MRI system and provides the interventional radiologist with a flexible and intuitive tool to perform interventions under rtMRI guidance. Future research should aim to fully integrate wRCs into the device material and to enable tracking of multiple catheter positions, which is a requirement for complex endovascular navigation. Alternatively, the concept from Chapter 3 could be augmented and one wRC could be used for catheter tip tracking and passive markers for visualisation of the catheter profile.

Chapter 6

Applications to Specific Interventions: Pre-clinical Iliac Angioplasty

Major parts of this chapter have been submitted for publication as:
M. A. Rube, F. Fernandez-Guttierez, B. F. Cox, J. G. Houston, R. D. White, H. McLeod, M. Fatahi, A. Melzer, "Preclinical Feasibility of a Technology Framework for MRI-guided Iliac Angioplasty", *Int J Comput Assist Radiol Surg* [in press].

Experimental contributions:
(i) B. F. Cox prepared the phantoms and the flow pump. (ii) F. Fernandez-Guttierez provided the interventional workflow design and recorded all procedure times. (iii) B. F. Cox, R. D. White, and J. G. Houston performed the clinical part (intervention) during the phantom experiments. (iv) M. Fatahi and H. McLeod assisted during the experiments (i.e. as study nurse). (v) A. Theissen assisted with the ethical approval and also prepared and supervised the animal experiments. (vi) A. Melzer and S. Zangos prepared the ethical approval and performed the interventions during the animal experiments.

6.1 Rational for Cardiovascular iMRI

Cardiovascular applications of iMRI have substantial clinical potential but face a number of challenges before clinical routine implementation [120]. As outlined in Chapter 1 (page 3) there are still several tasks that have not been fully addressed in the past: Real-time guidance; interactive MRI remote control; in-room communication; safe, robust and versatile device visualisation and tracking as well as workflow optimisation and training. As a consequence, MRI has not gained an important role for guiding interventions with broad clinical acceptance [59] and is primarily limited to research centres [19].

The objective of this chapter was to validate an improved framework of technologies to address these obstacles and to validate safe, fast and efficient solely MRI-guided angioplasty of the iliac arteries *in vitro* (perfused vascular phantom) and *in vivo* (porcine model).

6.2 Materials and Methods

This section describes the materials and methods for this angioplasty study and includes many cross-references to related content described elsewhere in this thesis as the devices and the technologies have been introduced in the preceding chapters.

6.2.1 Interventional Devices

The devices for this study were selected according to MRI compatibility and were modified or developed in-house as described in Chapter 3. Passive markers (SPIO nPs) were employed for guidewire visualisation (see Section 3.2.1.1) and wRCs were used for catheter visualisation (see Section 3.2.1.2).

6.2.1.1 Guidewires

For X-Ray-guided interventions, commercially available 0.035” guidewires (Standard Glidewire, Terumo, Somerset, NJ, USA) were used. For MRI-guided interventions, MRI-safe guidewires were used with SPIO nPs markers incorporated into the tip material, as described in Section 3.2.1.1.

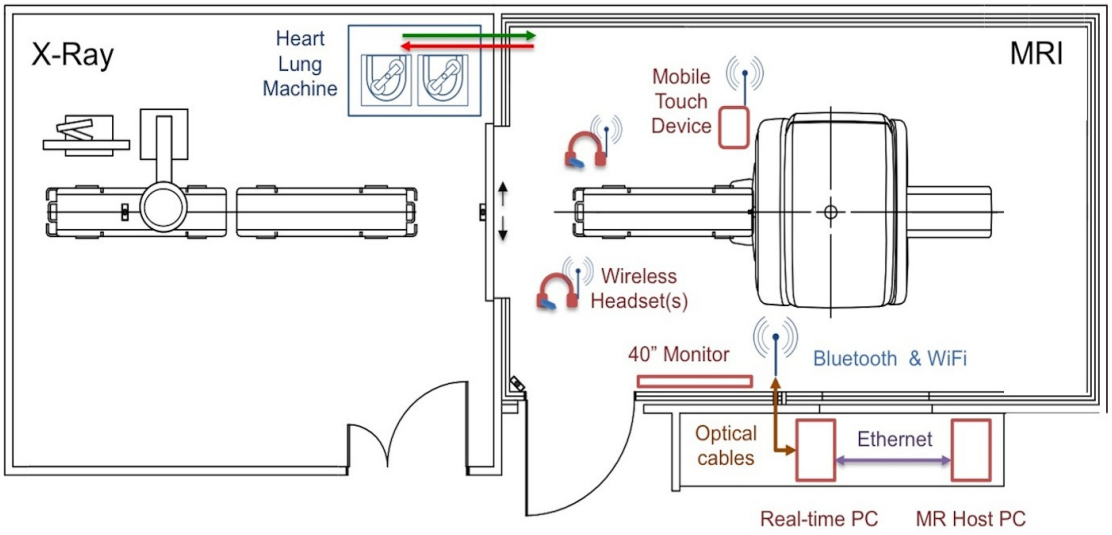

FIGURE 6.1: Multi-modality setup at IMSaT including modifications for rtMRI image display, in-room MRI remote control, communication and the heart-lung machine (HL-30, Maquet, Rastatt, Germany) for vascular perfusion. Note, a photograph of the initial setup without modifications is displayed in Figure 3.4.

6.2.1.2 Catheters

The following catheters were used for the MRI-guided interventions: 5-F straight catheters (S1, S2, S3 - Table 3.1), a 5-F MPA catheter (M1 - Table 3.1) and 5-F PTA balloon catheters (B1, B2 - Table 3.1). For X-Ray-guided interventions, the same (commercially available) type and manufacturer were used without wRCs.

6.2.2 In Vitro Studies in Perfused Arterial Phantoms

All experiments were conducted at the Institute for Medical Science and Technology, Dundee, UK, in a multi-modality setup (Figure 6.1) consisting of a digital subtraction angiographic (DSA) unit (OEC 9900 Elite, software release 7.0.31, GE Healthcare, Waukesha, WI, USA) and a 1.5 T MRI unit (Signa HDx, software release 15.0M4A, GE Healthcare, Waukesha, WI, USA). The units were located in two adjoining rooms, interconnected with shielded sliding doors that allow patient transfer between the units on a mobile table with radiolucent sliding table top (MR 1050 surgical suite, GE Healthcare and Maquet, Rastatt, Germany).

6.2.2.1 MRI Remote Control and Communication

A wireless inroom operator control system based on a mobile tablet device (iPad 1, Apple, Cupertino, CA, USA) was implemented to provide the vast majority of control in the procedure room (see Figure 6.2). The main components of the setup were described in Section 4.2. A tablet PC, mounted on a modified MRI-safe intravenous (IV) fluid-holder pole, enabled the physician to interact directly with the MRI scanner and/or the rtMRI system (RTHawk, Version 0.9.28, HeartVista, Inc., Los Altos, CA, USA). Communication between the tablet PC and Linux workstation was established via VNC. This setup allowed the physician and operator to make real-time changes to the scan sequence parameters to follow the manipulation of devices on the fly. A second tablet PC (iPad 3, Apple, Cupertino, CA, USA) provided wireless audiovisual communication, which has been described in Section 4.2. Each tablet device was inserted into a plastic cover to simulate sterile conditions, while the physician was still able to operate the touch screen with latex gloves.

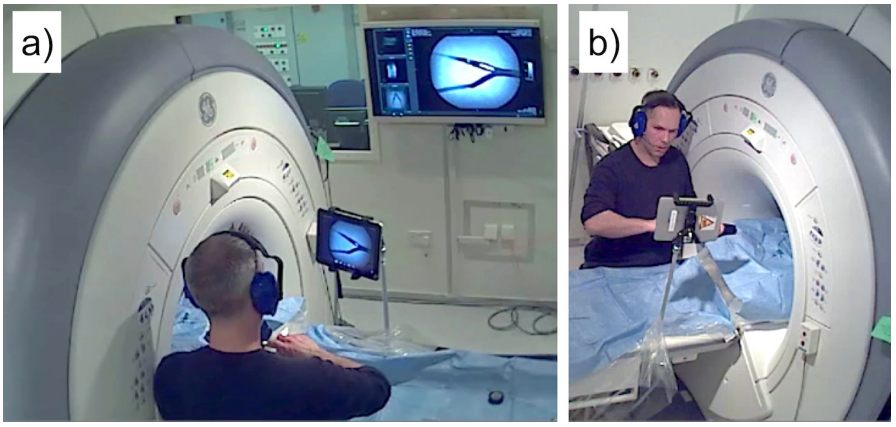

FIGURE 6.2: In-room iMRI display and control setup - Photographs taken during a MRI-guided iliac angioplasty procedure demonstrating the in-room iMRI display and control setup. The pictures were taken from two wireless IP cameras (M1031W, Axis, Lund, Sweden) that were installed in the scanner room. These IP cameras are designed to deliver live video through the WLAN (see Section 4.3.2) to a web browser or recording application. The picture **(a)** was acquired from the back and picture **(b)** from the front. The mobile tablet PC was mounted on an IV pole. The screen of the tablet shows the same rtMRI scene as the 40" in-room monitor. Note, the physician was able to zoom into the region of interest on the touchscreen **(a)**.

6.2.2.2 Experimental Phantoms

In vitro experiments were conducted on an arterial vessel phantom consisting of linked femoral, abdominal and thoracic modules (L-F-S-Left-003, A-S-N-001, T-R-N-020, Elastrat, Geneva, Switzerland). A neonatal blood pressure cuff (SoftCheck Neonatals, Statcorp Medical, Jacksonville, FL, USA) was secured to the right common iliac artery (with electrical tape and rubber sheet). The pressure cuff (arrowhead in Figure 6.3) was inflated with water to occlude the artery. The resistance was optimised in order to allow passive deflation with angioplasty balloon expansion.

The phantoms were placed in the supine position on the MRI-safe sliding tabletop. A heart-lung machine (HL-30, Maquet, Rastatt, Germany) was then connected to the arterial model. One HL-30 D150 pump was customised to work with a single roller head in order to mimic (pulsatile) physiologic flow. The model was connected to the pump as demonstrated in Figure 6.3. Inflow was connected to the models cardiac chamber (arrow) and outflow was achieved with dual upper (neck and arm) and lower (everywhere else) systems. System pressure was controlled using a non-operational D150 pump occlusion knob on the lower system outflow tube in order to mimic systolic / diastolic pressures. The master arterial flow pump was set to a flow rate of approximately 5.5 litres per minute, a heart rate of 85 - 95 BPM and a blood pressure of approximately 130 / 70 mmHg. Vascular access was established with a 12-F introducer sheath (Check-Flo, Cook Inc., Bloomington, IN, USA) (indicated by a '+' in Figure 6.3), inserted into the right femoral artery. All vessels, tubing and the pump reservoir were filled with 0.9% saline solution to mimic the electrical properties of blood. Furthermore, each container of the vessel phantom modules was backfilled with a 10% gelatinous solution to improve the MRI vascular visualisation (for details about tissue mimicking materials see Section 3.2.3). The heart-lung machine was positioned in the X-Ray angiography suite (see Figure 6.1) to prevent interference with the MRI system. For MRI experiments, however, the phantom was connected to the vessel model via tubing (see Figures 6.1 and 6.3), passing the Faraday cage through the waveguides. Silicon tubing (PT 12.7x3.2, Silex, Bordon, UK), with an inner diameter

of 16 mm and length of 5 m, was utilised for the inflow as well as the outflow, for both the X-Ray and MRI experiments.

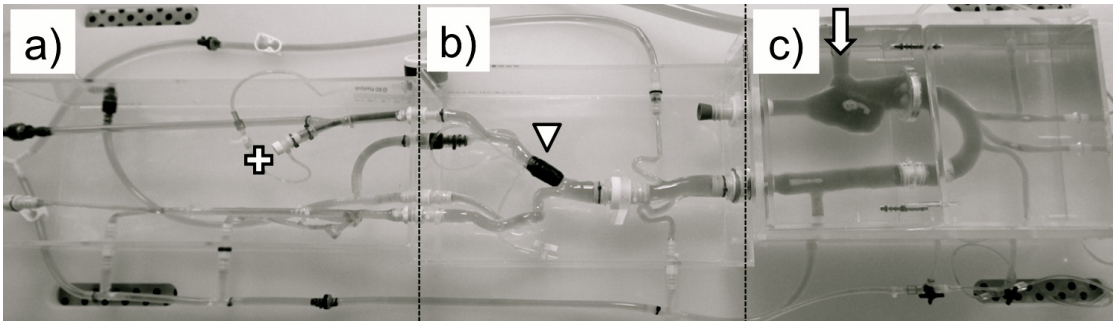

FIGURE 6.3: Arterial phantom setup for cardiovascular iMRI - the vessels were perfused with food colouring for optimised visualisation and demonstration: The model consisted of three connected modules: a leg model **(a)** - full left leg and a simplified right leg, an abdominal model **(b)** and a rigid thoracic phantom **(c)** (L-F-S-Left-003, A-S-N-001, T-R-N-020, Elastrat, Geneva, Switzerland). The master arterial pump of the heart lung machine (HL-30, Maquet, Rastatt, Germany) was connected to cardiac chamber of the thoracic phantom and the arrow indicates the inflow. The '+' indicates the 12-F introducer sheath for vascular access and the arrowhead indicates the neonatal pressure cuff (SoftCheck Neonatals, Statcorp Medical, Jacksonville, FL, USA) that was attached to the right common iliac artery to mimic a stenosis.

6.2.2.3 Study Protocol

Percutaneous balloon angioplasty is a technique widely used to treat iliac artery stenosis or occlusion. In this study, two trained interventional radiologists (one consultant and one final year trainee (SpR / Registrar)) and one physician in training performed 39 procedures in 6 sessions. A detailed analysis of the equivalent workflow from the X-Ray angiography suite was conducted[1] and applied. All procedures were performed according to the protocol described in Figure 6.4 and the time for each step was recorded. The clinical protocol employed for X-Ray-guided common iliac angioplasty is displayed in Figure 6.4a. With increasing experience the DSA protocol was adapted to the MRI environment and the steps were adjusted to the final MRI protocol, which is demonstrated in Figure 6.4b. At the beginning of each session, a set of X-Ray-guided procedures was performed as

[1]Please note, the workflow analysis was not scope of this thesis but will be published in the associated Ph.D thesis "Workflow analysis, modelling and simulation for improving conventional and MRI-guided vascular interventions" by F. Fernandez-Gutierrez.

a reference for the subsequent experiments. Each person in the room was wearing lead aprons for radiation protection. The phantom was then transferred into the MRI room. During MRI-guided interventions, a trained MRI technologist or researcher operated the scanner. In addition the physician, who had visual and audio contact with the operator, was able to make the required adjustments with the tablet PC.

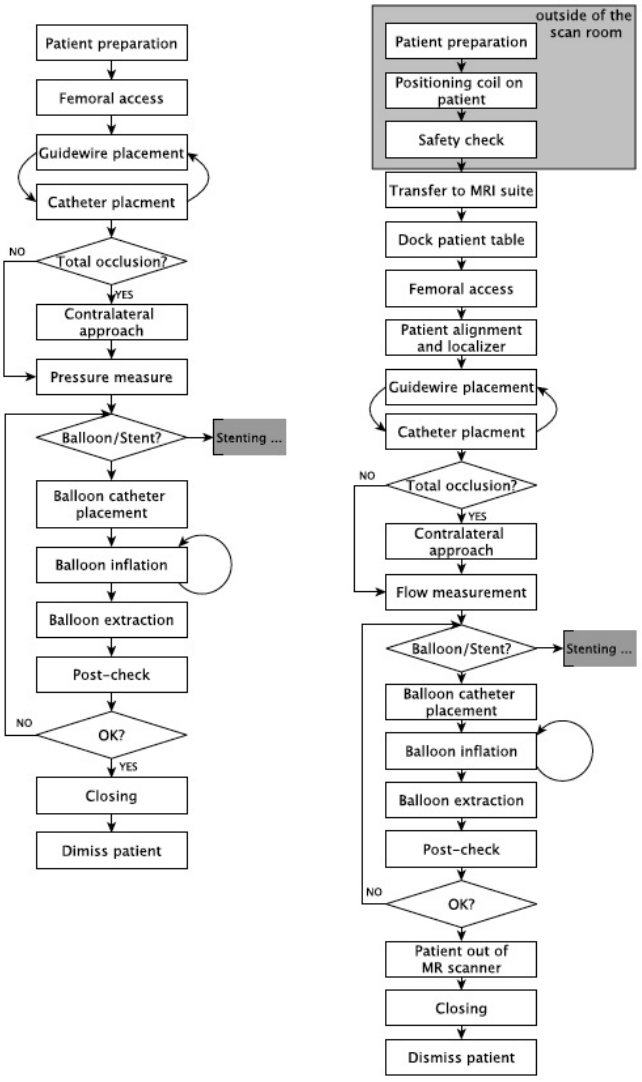

(a) X-Ray Protocol (b) MRI Protocol

FIGURE 6.4: Flow diagram of the common iliac angioplasty protocol - **(a)** Standard protocol applied in the interventional radiology department of the local hospital (Ninewells Hospital, Dundee, UK) for X-Ray-guided balloon angioplasties and **(b)** the adapted protocol for MRI guided-interventions. Note, stenting was not considered in the current study.

X-Ray Imaging: X-Ray-guided common iliac angioplasty procedures were performed using the OEC 9900 C-Arm (GE Healthcare, Waukesha, WI, USA) according to the standard protocol applied in the interventional radiology department of the local hospital (Ninewells Hospital, Dundee, UK), at which the two interventional radiologists worked (see Figure 6.4a). X-Ray contrast agent (Omnipaque, GE Healthcare, Princeton, NJ, USA) diluted in 0.9% saline solution (50:50) was injected into the balloon catheter for visualisation and to verify correct placement. After the balloon catheter was removed, a straight catheter was inserted and DSA was performed with a bolus of contrast agent to evaluate the results.

MR Imaging: All MR images were obtained with the DuoFlex coil suite (see Section 3.2.2).. For this study, a 4ch 24 cm element was used, which was positioned posteriorly and a single loop element with disposable cover, which was positioned anteriorly. The imaging parameters are summarised in Tables 6.1 and 6.2 and were acquired without breath hold or cardiac triggering. After the pre-interventional diagnostic scan sequence, an interactive rtMRI sequence was used during device manipulation. During the intervention, diagnostic images were only acquired on request of the physician. At first the interventions were performed using the product rtMRI protocol and later on with the developed rtMRI protocol, both with communication between operator and physician.

MR Imaging - Product Protocol

Diagnostic imaging, based on high-resolution FSPGR and ToF MRA, was performed for pre-interventional assessment and procedure planning. During the intervention, interactive FGRE or FSPGR images were acquired using the product rtMRI interface (i/Drive Pro Plus, GE Healthcare, Waukesha, WI, USA). For visualisation of the expanded endovascular balloon, a 0.9% saline solution doped (1:100) with a Gd-based MRI contrast agent (Magnevist, Beyer-Schering Pharma AG, Berlin, Germany) was injected into the catheter. This enabled us to depict the balloon in a T_1-weighted FSPGR sequence. After the procedure, a high-resolution FSPGR and a ToF MRA sequence were acquired to verify the technical success, while the guidewire was kept in place. All pulse sequences and imaging parameters

TABLE 6.1: Summary of the MR imaging parameters for the product protocol

Parameter	**Diagnostic MRI**		**Interactive rtMRI**	
	FSPGR	*2D ToF*	*FGRE*	*FSPGR*
TE / TR [ms]	2.0 / 4.5	2.6 / 7.5	1.7 / 4.8	1.8 / 5.9
FOV [cm x cm]	40 x 40	35 x 35	40 x 40	40 x 40
Matrix	256 x 256	320 x 192	256 x 128	256 x 128
FA [°]	70	70	30	70
Slice thickness [mm]	7	7	7	7

are displayed in Table 6.1.

MR Imaging - Research Protocol

All pulse sequences for the research protocol were developed and inplemented in RTHawk [45] (Version 0.9.28, HeartVista, Inc., Los Altos, CA, USA). The following sequences were implemented: A high-resolution FSPGR for diagnostic imaging, a real-time flow analysis (rtFLOW) with bipolar velocity-encoding gradients and a spiral k-space acquisition scheme for pre-interventional assessment, procedure planning and stenosis assessment. In consensus with the interventional radiologists, we increased the spatial resolution for the sequences with a Cartesian readout scheme and reduced the k-space coverage in the phase encoding direction (ky = 62%) and employed zero filling [202] (see Section 2.4 on page 32) to decrease scan time.

During an intervention the operation physician was able to switch on the fly between various pulse sequences including the rtFLOW sequence: A bSSFP sequence with either Cartesian or spiral readout scheme was used for bright blood visualisation, a FGRE (Cartesian) sequence for guidewire and catheter visualisation; and a (T_1-weighted) FSPGR (Cartesian) sequence for visualisation of the inflated balloon. The 0.9% saline solution doped with Gd-based contrast agent, which was used for injection into the balloon catheter was the same as used with the product protocol. The FA was varied (15 - 60°) depending on which device would be advanced and anatomical location examined. It was set to 30° or lower for catheter visualisation and to 60° for T_1-weighting for visualisation of the inflated balloon catheter. At the end of each procedure the outcome was assessed,

TABLE 6.2: Summary of the MR imaging parameters for the research protocol

Parameter	**Diagnostic MRI**		**Interactive rtMRI**			
	FSPGR	*Spiral bSSFP (MRA)*	*rtFLOW*	*bSSFP*	*Spiral bSSFP*	*FGRE*
TE / TR [ms]	2.0 / 4.5	3.5 / 21.5	4.9 / 23.5	4.8 / 6.9	3.5 / 20.0	3.0 / 7.4
FOV [cm]	40	24	24	40	40	24
Matrix or Resolution	256 x 256	1.76 mm	1.76 mm	256 x 256	1.76	256 x 256
FA [°]	70	70	30	70	70	≤30 / 60
Slice thickness [mm]	3	7	5	5	7	5
Interleaves	-	16	5	-	6	-

with a similar protocol as during the planning stage, with flow analysis in the target section and high-resolution diagnostic imaging. All employed pulse sequences and imaging parameters are reported in Table 6.2.

6.2.3 In Vivo Validation in a Porcine Model

Animal experiments in living pigs were performed in the department of diagnostic and interventional radiology in the Goethe University hospital in Frankfurt, Germany. The protocol[2] for animal experiments was approved by the local Institutional Review Board (IRB). Three living pigs (40 - 50 kg) were prepared at the animal laboratory and transferred to the imaging facility with manual ventilation (Ambu bag, Glostrup, Denmark). All imaging and procedures were performed under general anaesthesia. Following substances were injected intravascular: Heparing 5000 (2.5 ml), Propophol (20ml/st 2% solution) and Phentanyl (0.5 μm/ml every 30 min). Vascular access was established with 12-F introducer sheaths (Check-Flo, Cook Inc., Bloomington, IN, US), which were inserted into the left and right femoral artery. The pigs were also monitored via standard ECG (heart bit frequency) and detection of blood oxygenation and CO_2 level using an MRI compatible mobile monitoring device (SpO2 Invivo, Cambridge, MA, USA). The animals were sacrificed at the end of the study.

[2]This protocol consisted of a series of experiments, all to be performed in each individual animal if no complications occurred. Following experiments were part of the protocol: (i) General device visualisation and navigation, (ii) percutaneous transluminal angioplasties of the iliac arteries or veins, common carotid arteries or veins, (iii) stenting of the iliac or common carotid arteries, (iv) deployment of implants including inferior vena cava filters, patent foramen ovale occluders and heart valves.

MRI (no cardiac triggering) was performed in a short and wide bore 1.5T MRI scanner (Magnetom Espree, Software Version: Syngo MR B17, Siemens Healthcare, Erlangen, Germany) (see Figure 6.5) using the 8ch body matrix coil combined with eight elements of the integrated spine matrix coil. All MR images were displayed on a 18.1" in-room console (Conraq / Siemens, Erlangen, Germany). During MRI-guided procedures, the X-Ray system was still available for preparation, backup or emergencies.

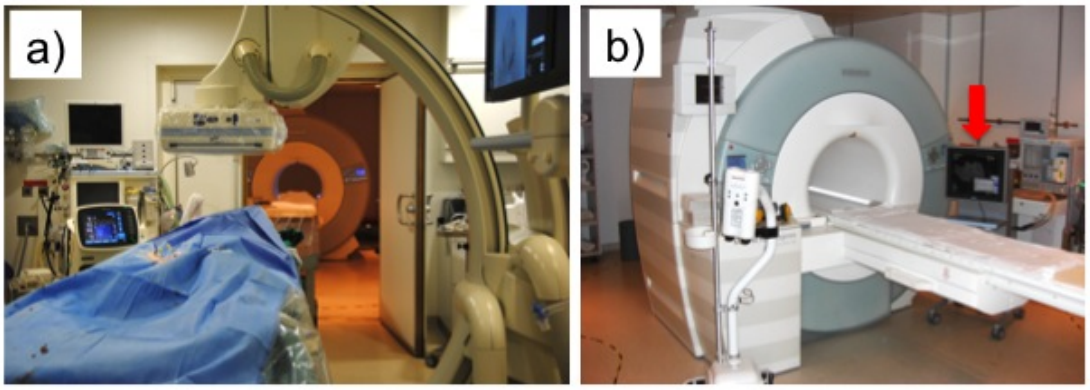

FIGURE 6.5: Multi-modality setup at the department of diagnostic and interventional radiology in the Goethe University hospital in Frankfurt, Germany. The right room **(a)** contains a digital subtraction angiographic unit (Axiom Artis dTA, Siemens, Erlangen, Germany) and the left room **(b)** is an RF shielded enclosure with a clinical short and wide bore 1.5T MRI scanner (Magnetom Espree, Siemens Healthcare, Erlangen, Germany). The rooms are interconnected with sliding doors, that shield RF and radiation and allow a patient transfer. The red arrow in Figure **(b)** illustrates the in-room console (Conraq / Siemens, Erlangen, Germany) for rtMRI display.

No major modifications to the MRI setup or adding research pulse sequences were allowed because this imaging facility was in a clinical centre. However, a Wireless Personal Area Network (WPAN) based on Bluetooth was established using an optical fibre USB cable (M2-100, Opticis, Sungnam City, Korea) and a USB WLAN dongle (Belkin, Playa Vista, CA, USA) for in-room audio communication with a mobile tablet device (iPad 3, Apple, Cupertino, CA, USA) and a wireless headset (Calisto B70, Plantronics, Santa Cruz, CA, USA). Moreover, a second optical fibre cable was fed through the waveguides and connected to the MRI scanner host PC to be able to adjust the rtMRI acquisition from within the magnet room. Therefore, a wireless optical mouse (M185, Logitech, Morges,

TABLE 6.3: Summary of the MR imaging parameters for the animal experiments

Parameter	**Diagnostic MRI**		**Interactive rtMRI**	
	HASTE	*Radial VIBE*	*Radial true-FISP*	*Radial FLASH*
TE / TR [ms]	86 / 900	1.6 / 22.4	1.9 / 3.8	1.9 / 3.8
FOV [cm]	33 x 45	35 x 35	35.6 x 35.6	25.5 x 25.5
Matrix	256 x 192	160 x 160	240 x 240	240 x 240
FA [°]	-	40	20	20
Slice thickness [mm]	5	7	8	8
Radial Views	-	995	500	505

Switzerland) was modified (the standard AA batteries were replaced commercially available Lithium-ion battery packs in a plastic housing) and sealed.

6.2.3.1 Study Protocol

In this study, one trained interventional radiologist (certified board member with more than 10 years experience) performed 6 procedures in 3 sessions while a researcher operated the MRI scanner. All procedures were performed according to the protocol described in Figure 6.4b (Section 6.2.2.3). Additionally, each device was positioned in the aorta to perform a second balloon angioplasty for demonstration purposes. A pre-interventional 3D planning sequence (radial VIBE [3] [203]) for enhanced vessel visualisation without contrast material was acquired along with a half Fourier acquisition single shot SE (HASTE) acquisition. Then interactive rtMRI was performed with an RF spoiled or a trueFISP radial sequence [204, 205] providing an image update rate of 384 ms. All MR pulse sequences and imaging parameters are summarised in Table 6.3. For visualisation of the expanded endovascular balloon, a saline solution doped with a Gd-based MRI contrast agent (MAGNEVIST, Schering AG, Berlin, Germany) was injected into the catheter. This enabled depicting the balloon during rtMRI.

[3] The conventional (non-radial) volumetric interpolated breath-hold examination (VIBE) is a T_1-weighted 3D FLASH sequence with fat-selective RF pre-pulses and partial k-space acquisition.

6.3 Results

This section describes the detailed findings of the *in vitro* and *in vivo* common iliac angioplasty studies.

6.3.1 In Vitro Studies in Perfused Arterial Phantoms

A total of 39 common iliac angioplasty procedures were performed in the perfused vascular phantom. Nine X-Ray-guided procedures were used as references for the 30 procedures that were successfully and solely performed using MRI guidance. In the present study, guidewire positioning was feasible, as was selective catheterisation of the common iliac artery, with the proposed visualisation techniques. Over-the-wire positioning of the catheters was possible, as were consecutive balloon angioplasties after removal of the guidewire (n = 39 out of 39). The average procedure times and the range per operating physician are shown in Figure 6.6.

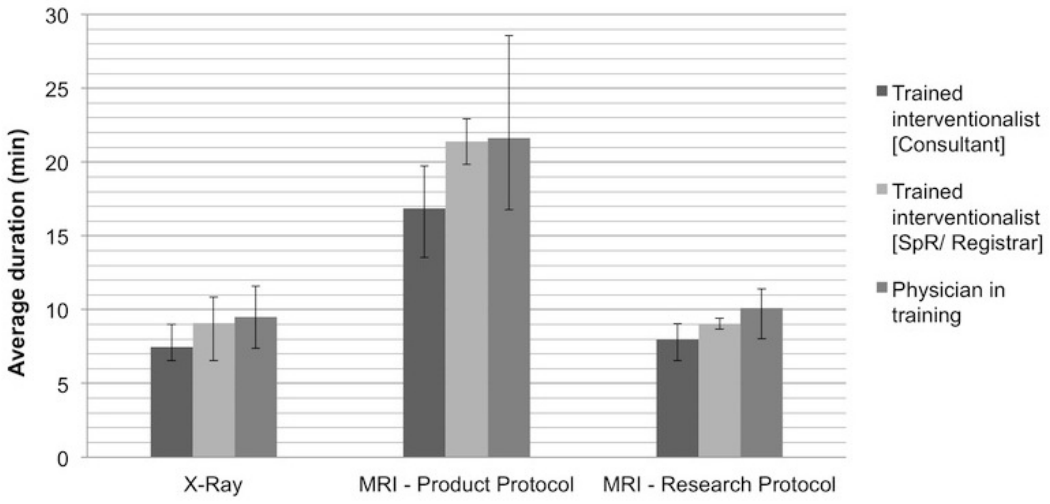

FIGURE 6.6: Average procedure times and range (illustrated as bars) for common iliac angioplasty categorised by setup and protocol. The vertical axis displays the average time in minutes, from the first localiser until the phantom was taken off the MRI patient table. The three columns separate the operating physicians. The first set of columns shows the mean time for the X-Ray-guided procedure that were performed as reference. Each physician performed three independent X-Ray-guided iliac angioplasties. The second and third set of columns show the MRI-guided interventions. The second set of columns shows the average procedure time for the product protocol (n = 5 per physician) and the last set of columns shows the MRI-guided iliac angioplasties performed with the developed research protocol (n = 5 per physician).

6.3.1.1 X-Ray - Guided Interventions

The mean procedure time (see Figure 6.6) for all X-Ray guided interventions (n = 9) was 8 minutes and 42 seconds (ranging from 6 minutes and 32 seconds to 10 minutes and 51 seconds). The accumulated average X-Ray radiation dose for all three procedures per radiologist was: 0.131 $mGym^2$ (trained interventional radiologist consultant level); 0.147 $mGym^2$ (trained interventional radiologist - SpR/Registrar); and 0.139 $mGym^2$ (physician in training).

6.3.1.2 MRI - Guided Interventions

During guidewire positioning in the aorta, the rtMRI FGRE sequence was used with a FA of 30° for improved visualisation of the passive markers. During catheter insertion, the resonant coil led to high local signal increase during interactive FGRE imaging with a FA of 15°. This allowed for fast placement of the catheter in the targeted vessel segment. Signal enhancements during imaging with low FAs were more pronounced than with equivalent sequences with higher FAs. Figure 6.7 demonstrates device navigation during various steps of the balloon angioplasty with the standard GE console (Figure 6.7a) and the product rtMRI interface (i/Drive Pro Plus, GE Healthcare, Waukesha, WI, USA) (Figure 6.7b - d) and Figure 6.8 shows the steps using the advanced research protocol. Figure 6.7a shows a MIP of a 2D ToF MRA obtained in axial slice orientation without any device present. Figure 6.7b displays the tip section of the MRI-safe guidewire (the arrow illustrates the guidewire tip) positioned in the abdominal aorta. The wRC (arrowhead) on the straight catheter can be identified in Figure 6.7c as a white spot high up in the right common iliac artery. Figure 6.7d displays the inflated balloon (indicated by a '+') (1:100 Gd-doped saline solution) that had been placed just above the common iliac artery and required re-positioning.

Figure 6.8a shows the guidewire, visualised with the passive markers (the arrow illustrates the passive marker on the guidewire tip), which had been advanced through the iliac arteries and positioned in the abdominal aorta during imaging with the advanced research protocol. The image also shows a turbulent flow pattern secondary to the connector distal to the renal arteries. Figure 6.8b shows

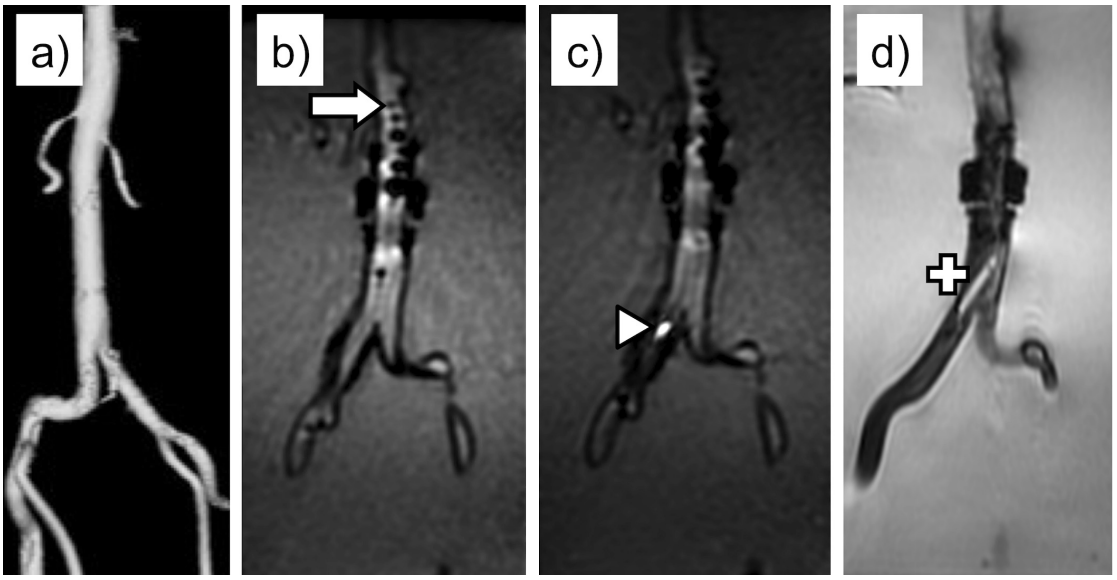

FIGURE 6.7: MR images of the devices positioned in the common iliac artery obtained with the product rtMRI interface (i/Drive Pro Plus, GE Healthcare, Waukesha, WI, USA) - **(a)** Pre-interventional MIP of the 2D ToF MRA showing the abdominal aorta and the iliac arteries without any device present, **(b)** shows the tip section of the MRI-safe guidewire (the arrow indicates the tip) that was positioned in the aorta, **(c)** the white spot (arrowhead) at the level beginning of the iliac arteries shows is the wRC on the straight catheter, **(d)** inflated balloon ('+') catheter (with 1:100 Gd-doped saline solution) that was moved just above the common iliac artery and required re-positioning.

the wRC (arrowhead) on the straight catheter, advanced over the guidewire and positioned at the level of the simulated stenosis in the common iliac artery.

Figure 6.8c shows a high FA image with the expanded Gd-filled balloon ('+') catheter at the stenosed section of the common iliac artery. The signal enhancement of the wRC on the balloon catheter allowed for fast positioning of the balloon catheter in the target area. Inflating the balloon with a Gd-doped saline solution and changing the FA to 60° to achieve T_1-weighting enabled good intra-arterial balloon position verification. Figure 6.8d shows a MIP of a 2D ToF MRA after the stenosis has been treated. A drastic decrease in velocity (peak velocities of 20 - 25 cm/s pre-treatment and 10 - 12 cm/s post-treatment) was observed with the rtFLOW assessment after treatment of the stenosis, as illustrated in Figure 6.9.

The catheters and guidewires along with their applied markers showed no macroscopic evidence of fracture or kinking and the catheters remained patent. The operators and physicians agreed that the catheter and guidewire position in the MR images was identified easily and reliably on all occasions (n = 30 out of

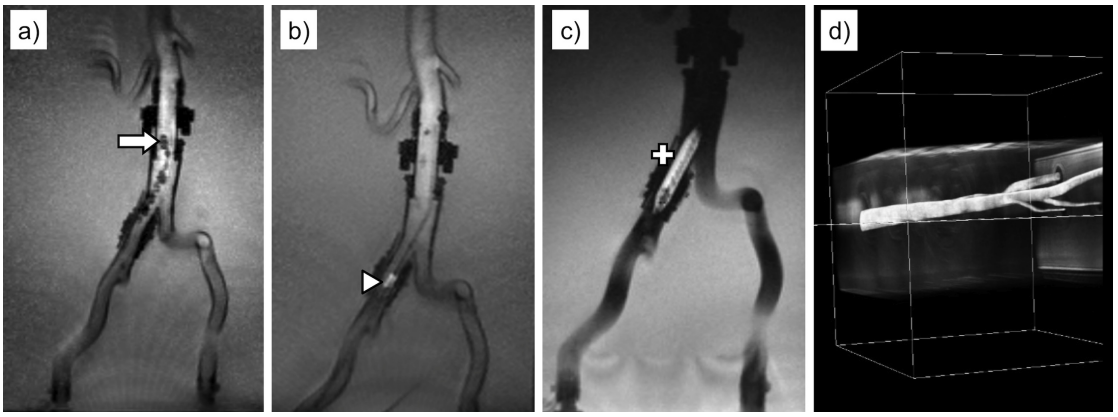

FIGURE 6.8: MR images of device placements in the common iliac artery obtained with the developed real-time interface and customised interventional protocol - image **(a)** shows the tip section of the MRI-safe guidewire (the arrow indicates the tip) with the susceptibility artefacts of each distinct passive marker. Image **(b)** displays the straight catheter with the resonant tip marker (arrowhead) at the level of the iliac arteries. On image **(c)** the inflated balloon catheter ('+') with 1:100 Gd-doped saline solution, positioned in the right common iliac artery, can be depicted. Image **(d)** demonstrates a post-interventional MIP of a 2D ToF MRA with treated stenosis in the right common iliac artery.

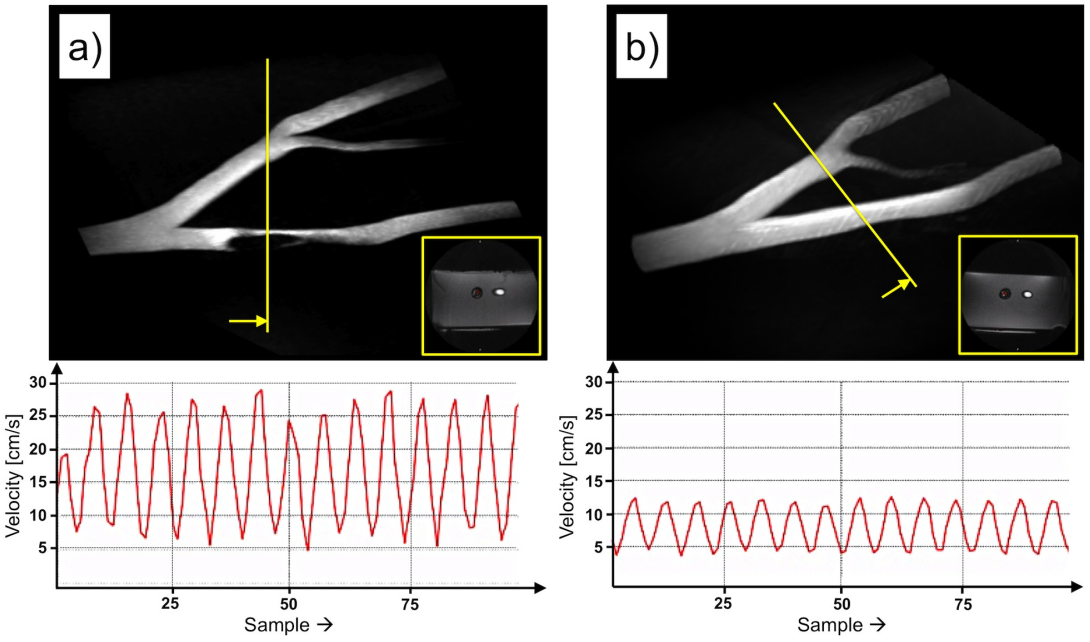

FIGURE 6.9: Flow/velocity examination performed in real-time and at various segments of the common iliac artery. The flow study at the level of the stenosis is shown exemplarily before **(a)** and after the stenosis treatment **(b)**. The arrows in the MIP dataset (2D ToF) indicate the orientation of the flow-encoded axial images that are shown in the frame in the lower right corner of both MIP datasets. The flow patterns below the two MIP datasets are also obtained with real-time phase contrast (rtFLOW) MRI and demonstrate the velocity profile averaged over a ROI, which was positioned within the vessel segment of interest (ROI not shown for simplicity).

30). The averaged procedure time per radiologist and the range (illustrated as bars) are presented in Figure 6.6. The mean procedure time for all MRI-guided interventions with the product protocol (n = 5 per radiologist) was 19 minutes and 58 seconds (range 13 minutes and 32 seconds to 28 minutes and 34 seconds). The mean procedure time with the research protocol (n = 5 per radiologist) was 9 minutes 2 seconds (range 6 minutes and 33 seconds to 11 minutes and 23 seconds) with the research protocol (n = 5 per radiologist). Moreover, the physicians rated the ergonomics for endovascular device placement during MRI scanning as being tolerable.

6.3.2 In Vivo Validation in a Porcine Model

All *in vivo* procedures were successfully performed using MRI guidance. Over the guidewire positioning of straight and balloon catheters was possible, as were the consecutive balloon angioplasties after removal of the guidewire. The catheters and guidewires along with their applied markers showed no macroscopic evidence of fracture or kinking and the catheters remained patent. A successful balloon angioplasty of the right common iliac artery is demonstrated in Figure 6.10. The mean procedure time for the balloon angioplasties of the right common iliac artery was 25 minutes and 42 seconds.

Figure 6.11 shows a balloon angioplasty while the balloon catheter was moved into the aorta with a radial FLASH sequence. Each wRC led to locally increased signal intensities in particular during interactive rtMRI with low FA. This allowed for fast placement of the catheter in the targeted vessel segment (iliac artery - Figure 6.10 and aorta - Figure 6.11). Imaging with a FA of 20° allowed satisfactory visualisation of the guidewire (iliac artery - Figure 6.10a and aorta - Figure 6.10b), the wRC (iliac artery - Figure 6.10c - e) and aorta - Figure 6.11) and also the balloon, which was inflated with 1:100 Gd-doped saline solution (iliac artery - Figure 6.10d and e and aorta - Figure 6.11c - e). The operator and physician agreed that the catheter position in the MR images was identified easily and reliably on all occasions (n = 6 out of 6). Guidewire visualisation was more difficult and time consuming compared to the phantom experiments due to enclosed air and other

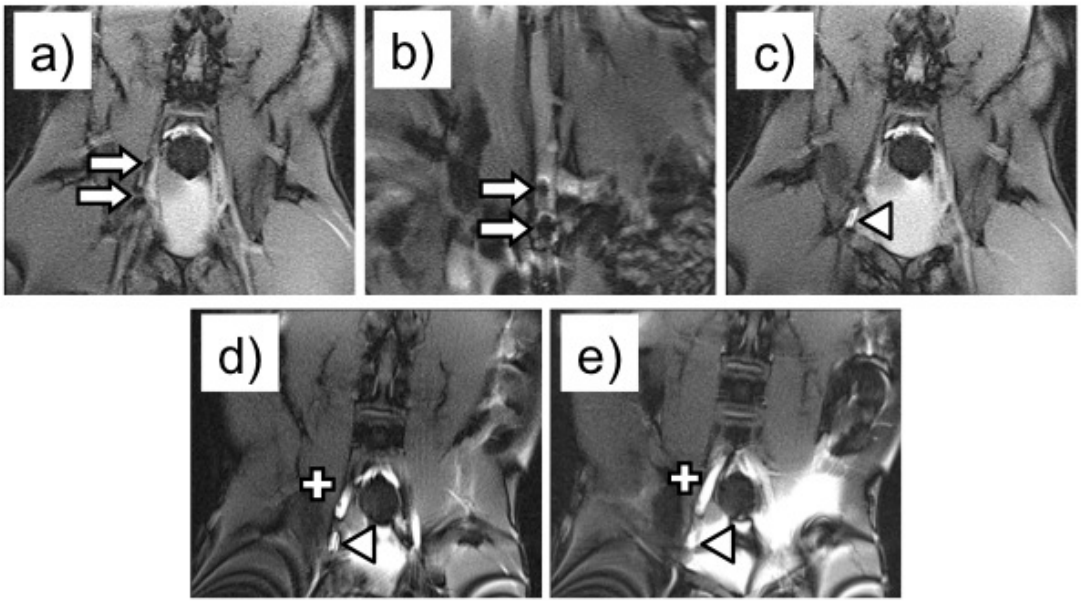

FIGURE 6.10: MR images obtained with an interactive radial FLASH sequence illustrating device placements in the aorta of a pig - Figure **(a)** shows the tip section of the MRI-safe guidewire with the susceptibility artefacts of each distinct passive marker (arrow). Figure **(b)** shows the tip section of the MRI-safe guidewire positioned in the aorta. Image **(c)** displays the balloon catheter with wRC (arrowhead) at the level of the iliac arteries. Figures **(d)** and **(e)** show two images during balloon inflation ('+') with 1:100 Gd-doped saline solution, while the catheter was positioned in the right common iliac artery. Note, severe banding artefacts close to the end of the receive coil and susceptibility artefacts occurred during imaging with the interactive radial trueFISP sequence.

susceptibility artefacts in the abdomen of the pigs (in particular during imaging with the trueFISP sequence).

6.4 Discussion

Although MRI has been previously used for guiding and monitoring a variety of interventions, most cardiovascular studies focus on challenging procedures including stenting [123], cardiac electrophysiology mapping during catheterisation [56, 57] and heart valve repairs and replacements [58]. However, it is also important to ensure familiarity with conventional endovascular procedures using MRI guidance before approaching more complex cardiovascular techniques. This work demonstrates the pre-clinical feasibility and efficiency of common endovascular interventions (such as balloon angioplasty of the common iliac artery) using MRI

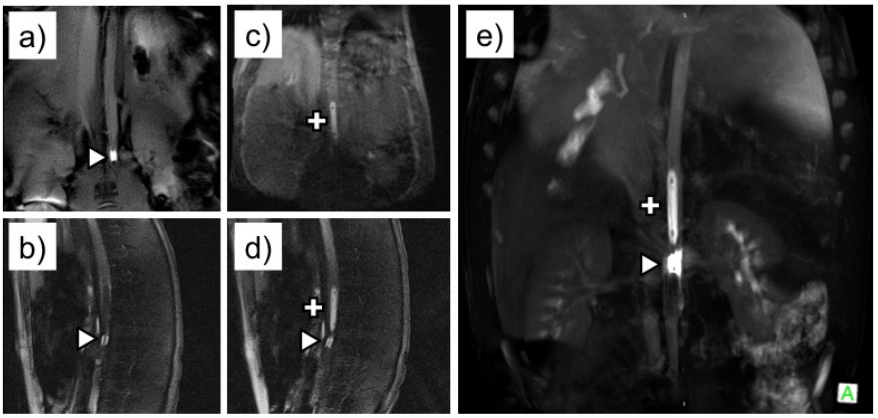

FIGURE 6.11: MR images obtained with an interactive radial FLASH sequence during device navigation in the aorta of a pig - Figures **(a)** (coronal) and **(b)** (sagittal) show the wRC on the balloon catheter (arrowhead). Figures **(c)** (coronal) and **(b)** (sagittal) show the inflated (1:100 Gd-doped saline solution) balloon ('+') with wRC (arrowhead). Figure **(e)** is a MIP of a MRA dataset obtained with a Radial VIBE sequence. Note, the two signal voids within the balloon ('+') in **(e)** are susceptibility artefacts caused by the X-Ray markers, which are generally invisible if the balloon is deflated.

guidance. A combination of optimised workflow, suitable technologies for communication, in-room visualisation and remote control of the MRI scanner, and safe and readily visualised endovascular devices, enabled satisfactory and effective interventions. This may be a first step towards standardisation to facilitate training of MRI-guided techniques.

6.4.1 Interventional Devices

Endovascular interventions require iterative use of guidewires and catheters, as well as device exchanges with one or the other in place. Both device visualisation techniques employed in this study did not require a connection between the device and the MRI scanner, thereby simplifying instrument handling as well as avoiding unintended RF coupling effects. For this study, non-braided angiographic catheters (see Chapter 3) were selected, which are MRI-safe but have little torque and limited navigation characteristics. This was not an issue for balloon angioplasty of the common iliac artery (phantom and animal model) or the aorta (animal model) but could be problematic for more challenging interventions. The passive markers on the guidewire were found to be sufficient for device navigation during all

interventions performed in the current study. However, the animal experiments demonstrated that in small vessels and next to air-filled cavities (which also give signal voids), a more versatile contrast method would improve device localisation. During MRI-guided interventions, the MRI-safe guidewire was considered satisfactory for the outlined tasks, with a similar performance to commercially available guidewires for X-Ray fluoroscopy, as validated by the interventional radiologists. Further studies are needed to fully assess the mechanical performance of this new MRI-safe guidewire.

6.4.2 iMRI Setup

The limited patient access in closed-bore magnets provides a significant challenge for MRI-guided interventions, particularly if the physician has to reach into the iso-centre of the MRI scanner e.g. for needle insertion [19, 24]. For endovascular interventions, however, the access site is mainly via the common femoral artery and only the treatment area is positioned in the centre of the bore. This allows the physician to be situated in front of the MRI scanner while inserting endovascular devices (see Figure 6.2). In this study, all physicians agreed that this position was tolerable throughout the procedures and the scanner display and control within arm reach was considered to be useful as demonstrated in the phantom experiments. Moreover, the ergonomic component and access to the patient was significantly improved by using longer introducer sheaths and a short and wide bore MRI scanner for the animal experiments. However, a detailed study is required to evaluate these modifications as well as long-term ergonomic effects.

Another hurdle to be overcome is the need to simplify receive coil positioning while a sterile iMRI environment is maintained. The interventional coil prototype facilitated fast and reliable coil positioning during the phantom experiments while enabling suitable quality interventional imaging for a relatively large FOV. Imaging and positioning of standard imaging coils, such as an 8ch body array coil (animal experiments), was found to be time-consuming and could also prove challenging in terms of maintaining sterility around the puncture site. This problem has been addressed with a new interventional coil design (DuoFlex Coil Suite - see Section

3.2.2) that employs an exchangeable soft cover, which can be covered by sterile drapes and disposed of after a procedure.

6.4.3 Protocol and Workflow

Clinical MRI-guided endovascular procedures require suitable patient access within the scanner, a good compromise between high-speed imaging, spatial resolution and image quality, as well as intuitive interaction with the scanner. In this study, all scan plane adjustments were performed manually i.e. to follow an interventional device that was moved out of the current scan plane. In Chapter 5, a concept for robust wireless tracking of catheters equipped with wRC was proposed. Integrating this concept into the proposed framework could further improve and simplify the interventional workflow, which needs to be quantitatively assessed in further studies.

6.4.3.1 In Vitro Studies

MRI-guided common iliac angioplasty procedures were conducted and assessed with a newly developed iMRI framework regarding time and efficacy. In this context, a product platform (i/Drive Pro Plus, GE Healthcare, Waukesha, USA) with CE mark and FDA approval was compared to a research rtMRI platform (RTHawk, HeartVista Inc., Palo Alto, CA, USA), approved only for investigative use and not to be used with patients.

The integration of mobile touchscreen tablet devices and wireless communication was investigated as part of the interventional workflow. This enabled the radiologist to have control of the MRI scanner at the procedural table (see Figure 6.2). This obviated the need for scan interruptions or verbal and gestural commands to the MR technician, which were found to be a major challenge in preceding experiments. The use of a research platform enabled us to design a specific protocol and interface tailored to MRI-guided endovascular interventions. This tailored rtMRI interface, in combination with the mobile touchscreen device, led to a significant decrease in both complexity and the need for technician-driven scan adjustments. Furthermore, the ability to select the rtFLOW visualisation on

the fly (similar to Doppler ultrasound) was considered to be useful for pre- and post-interventional assessment.

These implementations improved the interventional workflow and also reduced the required mean patient table time to 9 minutes and 2 seconds, which is comparable to the X-Ray guided interventions (8 minutes and 42 seconds) that were performed according to the protocol from the local hospital. The length of time taken to perform the MRI-guided procedures was reduced (minimum procedure time: 6 minutes and 33 seconds) as our experience with the setup increased. Further experience and training with this developed framework of technologies could potentially lead to shorter procedure times in future [59]. MRI-guided procedures were also successful with the commercially available rtMRI interface. However, workflow interruptions, caused by e.g. stopping the scanner, offline adjustments to pulse sequence parameters and re-starting the scan acquisition, resulted in delays and the mean procedure time was more than double (19 minutes and 58 seconds) than either the X-Ray-guided or MRI-guided procedures with the research protocol.

6.4.3.2 In Vivo Studies

MRI-guided common iliac angioplasty procedures were conducted in three pigs using an open and short bore scanner. Because this imaging facility was in a clinical centre, no major or permanent modifications to the MRI setup our pulse sequences were allowed. MRI-guided procedures were also successful with this setup demonstrating the feasibility of MRI-guided angioplasty *in vivo*. However, the workflow and procedure times (mean: 25 minutes and 42 seconds) were influenced by more challenging device localisation, a compromised protocol (limited availability of suitable rtMRI pulse sequences), numerous manual scan plane adjustments, which were found more time consuming than the phantom experiments (vasculature around the iliac arteries cannot be scanned in a single plane) and the need for offline adjustments to the pulse sequence.

6.5 Conclusions

In conclusion, the results of this study illustrate that endovascular interventions such as common iliac angioplasty, solely with MRI, are experimentally feasible with this novel framework of technologies (real-time guidance, interactive MRI remote control, in-room communication and device visualisation). Dedicated equipment designed for interventions and streamlined workflow improved the procedural efficacy. Developing an interactive protocol allowed switching between pulse sequences without interruption of imaging. This provided real-time device manipulation and instant evaluation of technical procedural success, along with adjustments to the treatment protocol on the fly. Accordingly, with this protocol the implications and response of the treatment to the downstream vasculature can also be evaluated. In particular the rtFLOW visualisation was found to be helpful for pre- and post-interventional assessment. Although the initial *in vitro* results (partially verified *in vivo*) are encouraging, this novel framework was applied in idealised phantom conditions only and needs to be repeated *in vivo*. The next research steps should validate the rtFLOW measurement accuracy and compare it to Doppler ultrasound and laser Doppler flowmetry. Future work is planned to investigate the entire framework of technologies including wireless device tracking in further animal studies before the translation into clinical studies.

Chapter 7

Applications to Specific Interventions: Pre-clinical Endovascular Recanalisation in Acute Ischemic Stroke

Experimental contributions:
(i) B. F. Cox prepared the phantoms, the flow pump and the human cadaver experiments (the cadavers were embalmed and provided by CAHID). (ii) B. F. Cox and R. Buciuc performed the clinical part (intervention) of the *in vitro* and *ex vivo* experiments. (iii) A. Theissen prepared and supervised the *in vivo* experiments. (vi) R. Buciuc, A. Melzer and S. Zangos performed the clinical part (intervention) of the *in vivo* experiments.

7.1 Motivation

Stroke remains the third most common cause of death in the industrialized nations and the single most common cause of serious long-term disability [206, 207]. The time period after stroke onset is very critical because acute ischemic stroke is treatable and a significant portion of threatened brain is potentially salvageable [207] with immediate treatment. Advances in imaging technology [207] and reperfusion therapy have improved the clinical management of acute stroke patients. Patient management is largely dependent on the time period after stroke onset [208]; within the three-hour window intravenous (IV) thrombolysis [208–210] and within the six-hour window intra-arterial (IA) thrombolytic therapy are clinically effective options [208, 211]. Despite the fact that randomised clinical trials have suggested both treatment options to be beneficial for acute stroke [209, 210, 212, 213] only a small patient group receives IV (<10%) [76] and IA thrombolytic therapy [78].

Endovascular treatment has emerged as a key option for patients who either have a contraindication to thrombolytics, are beyond the time window or incomplete recanalisation has been achieved with thrombolysis treatment [207]. Moreover, endovascular therapy is increasingly used after administration of IV thrombolytics in patients with moderate-to-severe acute ischemic stroke [76]. The major drawback of endovascular treatment, is the delay in initiating treatment [76] in consequence of preparation, patient handling and transfer times between imaging modalities [207].

Although the Interventional Management of Stroke (IMS) pilot trials (IMS I and II) have demonstrated [214, 215] that IV thrombolysis followed by IA thrombolysis therapy may be more effective than IV thrombolytic therapy alone [216], the recent phase 3 trial (IMS III) was stopped early because no significant clinical benefit of endovascular therapy after IV thrombolysis could be shown [58]. The pilot trials (IMS I and II) demonstrate a direct link between clinical outcome and time from stroke onset to revascularization [76, 217, 218]. The IMS III investigators concluded that a delay in initiating treatment (30 minute) compared to IMS I could be a key reason for the lack of clinical benefit in the IMS III trial and recommended that future trials should attempt to minimize delays to the initiation

of endovascular therapy [76].

Over the past decade, MRI has gained a significant impact on imaging of stroke [219] and in many hospitals has become an integral part of early stroke diagnosis and assessment of affected brain tissues. Diffusion-weighted imaging (DWI) can rapidly detect ischemic brain lesions, and perfusion-weighted imaging (PWI) can identify blood flow abnormalities [220] and the penumbra at risk. MRA can identify vessel occlusion [219], detect chronic, small brain haemorrhages and may predict patients that respond unfavourably to thrombolytic therapies [220].

Diagnosis and treatment in the same modality could also reduce patient handling, streamline the procedure workflow and save crucial time that is required for the transfer between diagnostic and treatment facilities [78]. Early MRI scans may provide significant advantages (compared to CT) for identification of patients who are likely to benefit from thrombolytic therapy, even beyond 3 hours after stroke onset [220]. Using MRI for diagnosis and also treatment could accommodate imaging and assessment of arterial and venous blood flow [221], the state of vessel walls [42], brain diffusion and perfusion, tissue metabolism, tissue cell death and brain function. MRI avoids ionising radiation and nephrotoxic and allergenic iodine-based contrast media [77] and is the only imaging modality that can visualise the blood vessels and the state of the brain parenchyma. Thus, iMRI could facilitate critical decision making during a procedure as the viability of brain tissues can be evaluated and tissues at risk for irreversible infarction can be detected [78].

This work serves as a pre-clinical study of MRI-guided endovascular mechanical thrombolysis (clot retrieval) and was demonstrated by means of MRI-guided vascular phantom and Thiel soft-embalmed human cadaver experiments. To validate the developed devices for mechanical clot retrieval and the applied MRI visualization *in vivo*, preliminary experiments were conducted in a porcine model. All *in vivo* procedures were performed in one animal, which was also used for the experiments described in Chapter 6. However, the arterial route of blood supply to the brain differs between species and also between mammals. For instance in ox, sheep and also pig the proximal segment of the internal carotid artery is absent. Instead, branches of the internal maxillary and/or the external carotid artery feed

into an arterial rete (a complex of arteries and veins located very close to each other) [222]. A major drawback of the porcine model is the arterial rete, which prevents catheterisation of the intracerebral arteries [60].

As alternative, the carotid arterial territory was selected for catheterisation *in vivo*, which is also significantly associated with ischemic stroke [223].

7.2 Materials and Methods

The following subsections describe the materials and methods for this study and include cross-references to related content described elsewhere in this thesis as many of the methods have been introduced in the preceding chapters.

7.2.1 Interventional Devices

MRI-safe guidewires (see Section 3.2.1.1) with a length of 180 cm and a diameter of 0.035" and custom made micro guidewires (EPFlex, Dettingen/Erms, Germany) with a length of 150 cm and a diameter of 0.014" were used for this study. A conventional non-braided 5-F MPA catheter (M1 - Table 3.1) was prepared for the initial steps of the procedure. Subsequently a custom made non-braided 2.6-F micro catheter (μC1 - Table 3.1) was employed for navigation. In addition, the first prototypes of the EPFlex 3-F Basketriever where used as clot retriever.

7.2.2 In Vitro Studies in Perfused Arterial Phantoms

In vitro experiments were conducted in an arterial vessel phantom consisting of a linked femoral, an abdominal, a thoracic and a head and intracranial module (L-F-S-Left-003, A-S-N-001, T-R-N-020, H+N-S-A-10, Elastrat Sarl, Geneva, Switzerland). Artificial blood clots made of fibrin sealant (TISSEEL, Baxter Healthcare, Deerfield, IL, USA) were inserted into the M1 and M2 segments of the middle cerebral artery (MCA). For the first series of experiments (n = 3) a clot was inserted into the left MCA (M1), for the second series of experiments (n = 3) into the right MCA (M1) and for the third for series of experiments (n = 3) into the

left MCA (M2). The phantoms were connected to the Maquet heart lung machine (see Section 6.2.2.2) and positioned in the supine position on the MR safe sliding table top. Pump perfusion parameters were set to a flowrate of 5.5 litres per minute, which translated into a heart rate of 110 beats per minute and the systolic/diastolic pressure was maintained at approximately 120/80 mmHg.

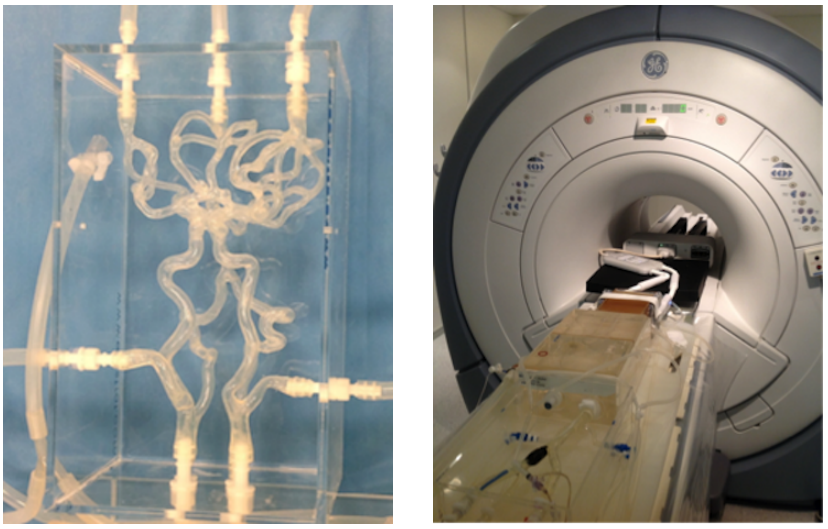

(a) Intracranial module (b) Linked arterial phantom

FIGURE 7.1: Photographs of the phantom-setup for the MRI-guided endovascular mechanical thrombolysis experiments - Figure **(a)** shows the intracranial module of the phantom (without gel) and **(b)** shows the linked arterial phantoms in front of the 1.5T MRI scanner.

7.2.2.1 Imaging Protocol and Workflow

The setup for MRI-guided interventions has already been described in Section 6.2.2.1. The vascular phantom studies were conducted with the DuoFlex interventional coil suite (see Section 3.2.2 for details) consisting of a single loop element with disposable cover (posterior) and a 4ch paddle element (anterior). All rtMRI implementations were developed in RTHawk in conjunction with the embedded Vurtigo plugin (see Sections 5.3 and 6.2). Wireless device tracking and a dedicated UI were used for this study as outlined in Chapter 5. The device position was therefore rendered to the current 2D rtMRI scan plane and/or a 3D MRA roadmap. The following paragraphs describe the modifications compared to the preceding chapters:

TABLE 7.1: MRI parameters for the in vitro and ex vivo MRI-guided endovascular mechanical thrombolysis experiments

Parameter	**Diagnostic MRA**	**Interactive rtMRI**		
	3D SPGR ToF	*FSPGR*	*FGRE*	*spGRE*
TE / TR [ms]	2.8 / 23	2.0 / 4.5	2.82 / 7.04	3.5 / 20.4
FOV [cm x cm]	16 x 16	24 x 24	24 x 24	24 x 24
Matrix or Resolution	320 x 224	256 x 256	256 x 256	1.76 mm
FA [°]	20	14	60	30
Slice thickness [mm]	1.4	6	10	8
Interleaves	-	-	-	16

Non-braided customised 8-F vascular sheaths (Penumbra, Inc., Alameda, CA, USA) were placed in the target carotid arteries via femoral access (see Figure 7.1) using rtMRI guidance. Automated device tracking was only performed with the MPA catheter until the internal carotid artery was reached then the catheter was exchanged over the 0.035" guidewire to the micro catheter. The micro catheter was used for upstream navigation in combination with either the 0.035" or 0.014" guidewire. All pulse sequences and imaging parameters are summarized in Table 7.1. An intervention was rated successful once the devices were navigated into the targeted vessel segment and mechanical blood clot removal was verified with 3D ToF MRA. Another major differences was that a much smaller FOV (compared to the preceding chapters) was required to accommodate experiments with the cranial model.

7.2.3 Ex Vivo Studies in Thiel Embalmed Human Cadavers

Initially, a series of T_2-weighted baseline scans (FSE, TE/TR = 103.9 / 3000 ms, ETL = 16, FOV = 22 cm x 17.6 cm, Matrix 256 x 192, Slice thickness = 3 mm) was acquired to investigate if the brain of an individual cadaver was still suitable for interventional procedures and MRI. If a cadaver was rated suitable, the cadaver was prepared in the angio suite in the supine position and then transferred to the MRI suite (similar setup as in Figure 6.1). Percutaneous vascular access

was established bilaterally with a 12-F introducer sheath (Check-Flo, Cook Inc., Bloomington, IN, US), which was inserted in each femoral artery.

Initially, perfusion experiments were performed with the same pump setup as described for the phantom experiments. However, MRA revealed that perfusion resulted in significant extravasation and perfusion with the pump was abandoned. To mimic perfusion for MRA, 10 ml Gd-doped solution (1:100) were slowly injected through the vascular sheath in the carotid artery. This allowed for 3D roadmaps of the vascular tree that were used in the subsequent rtMRI-guided interventions. Then the same protocol as outlined for the phantom experiments (Section 7.2.2.1) was followed, except that no artificial blood clots were deployed because substances with human or animal origin (contained in fibrin sealant) were explicitly excluded in the approved cadaver protocol. Device navigation in front of the bore was evaluated in three different sets of experiments: Left MCA (M1) (n = 3), right MCA (M1) (n = 3) and right MCA (M2) (n = 3). An intervention was rated successful once the devices were navigated into the targeted vessel segment (n = 10).

7.2.4 Preliminary In Vivo Validation in a Porcine Model

The animal experiments in this study were scope of the approved animal protocol described in Chapter 6 (see Section 6.2.3 for details). All experiments were performed under general anesthesia by an experienced neuro-interventional radiologist (board certified in general diagnostic radiology and neuroradiology) in a short and wide bore 1.5 T scanner (Magnetom Espree, Siemens Healthcare, Erlangen, Germany) similar to what has been outlined in Section 6.2.3. To reduce animal use, one of the pigs (50 kg) that was used in the iliac angioplasty experiments described in Chapter 6, was also used for this study. The pig was prepared for iMRI and positioned (supine) on the MRI table. The 12-F introducer sheath (Check-Flo, Cook Inc., Bloomington, IN, US) was maintained in the right femoral artery for percutaneous vascular access. The same scan protocol (Table 6.3) as for the *in vivo* angioplasty experiments of the iliac artery, (see Section 6.2.3.1) was applied to balloon angioplasty of the right common carotid artery (n = 2).

An intervention was rated successful once the devices were navigated into the targeted vessel segment and correct balloon dilatation was verified with a high spatial resolution 3D radial VIBE dataset (see Table 6.3 for details).

7.3 Results

The following subsections describe the findings of the *in vitro*, *ex vivo* and *in vivo* experiments of this pre-clinical pilot study of MRI-guided endovascular mechanical thrombolysis.

7.3.1 In Vitro Studies in Perfused Arterial Phantoms

Artificial blood clots were successfully removed in three series of *in vitro* experiments (1. left MCA (M1) (n = 3/3), 2. right MCA (M1) (n = 3/3), 3. left MCA (M2) (n = 3/3)) by an experienced interventional neuro-radiologist and within 15 minutes. The workflow of a blood clot removal at the left MCA (M1) is demonstrated in Figures 7.2 and 7.3. It should be noted that the Basketriever were tested during initial phantom experiments but did not provide sufficient MRI visualisation, in particular for the expanded basket that was supposed to retrieve blood clots. Thus, all subsequent experiments were performed without Basketriever and artificial clots were removed with guidewire and catheter manipulation.

For the first series of experiments (n = 3), a 3D MRA dataset was obtained and used as 3D roadmap (see Figures 7.2a and b). A perfusion defect ('+') was clearly visible in the left MCA due to the artificial blood clot in the M1 segment. The same 3D roadmap was subsequently used for device navigation. This is illustrated in Figure 7.2c where a 2D rtMRI plane was rendered to the MIP dataset. The position of the tip of the MPA catheter (arrow) was computed by the tracking implementation and rendered to the 3D roadmap. This is shown in Figure 7.2c. Automated tracking of the MPA catheter tip was feasible until the vessel diameter of the internal carotid artery (C4 segment) prohibited the catheter with wRC to pass and an exchange to the micro catheter (μC1 - Table 3.1) was required.

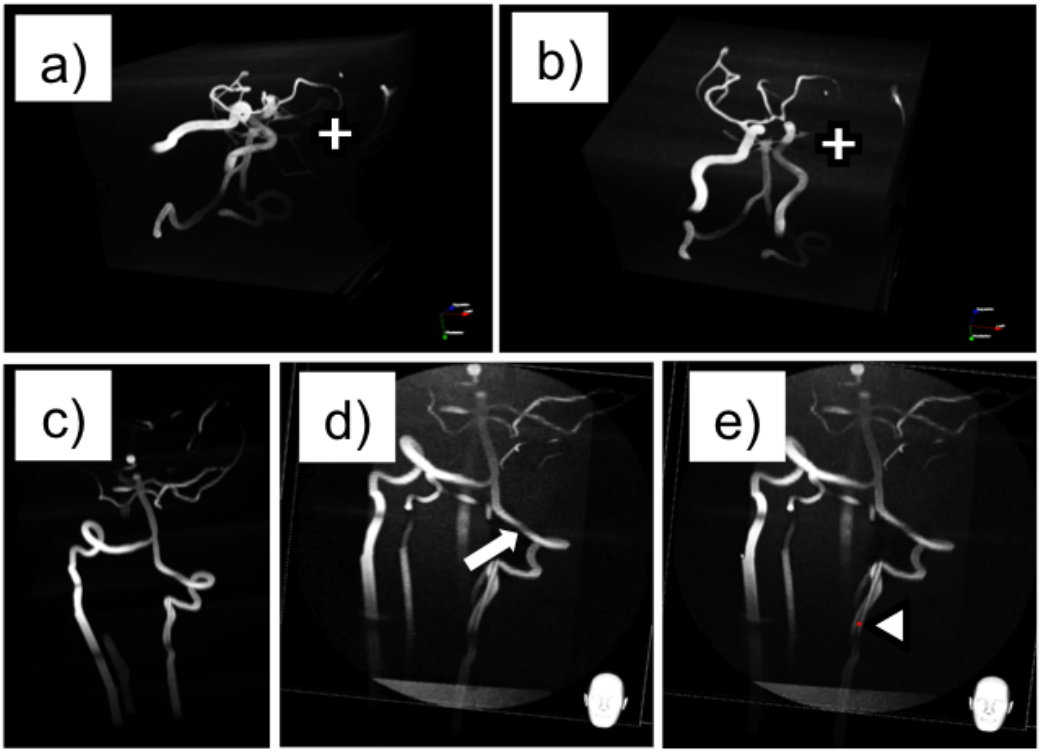

FIGURE 7.2: Device navigation in an intra-cranial arterial vessel replica model prior to treatment of an occlusion caused by an artificial blood clot in the M1 segment of the left MCA: A 3D ToF MRA dataset was acquired **(a)** as first step and the MIP was then used as 3D roadmap (Figures **(a)** - **(c)**). The '+' indicates the lack of perfusion due to the artificial blood clot in the left MCA (M1). As second step, a 2D rtMRI plane (FSPGR - Table 7.1) was rendered to the roadmap **(d)** while the guidewire was inserted (arrow). As third step, the MPA catheter was navigated while the rtMRI and the tracking pulse sequences were interleaved **(e)**. The red sphere (arrowhead) indicates the catheter tip tracking position that was computed by the wireless tracking pulse sequence.

Figure 7.3 demonstrates how the guidewire (the white arrow indicates the tip) and the micro catheter (the green arrow indicates the tip) were advanced into the left MCA (M1) in order to remove the blood clot using rtMRI guidance. The scan plane was then manually adjusted further upstream as per request of the operating physician. Alternatively the physician was able to request that the 2D rtMRI plane was fused to the 3D roadmap, tilted according to his preference and the opacity adjusted to accommodate device navigation (Figure 7.3d and e). The second and third series of experiments were successfully performed similar to what was outlined for the first set of experiments in Figures 7.2 and 7.3.

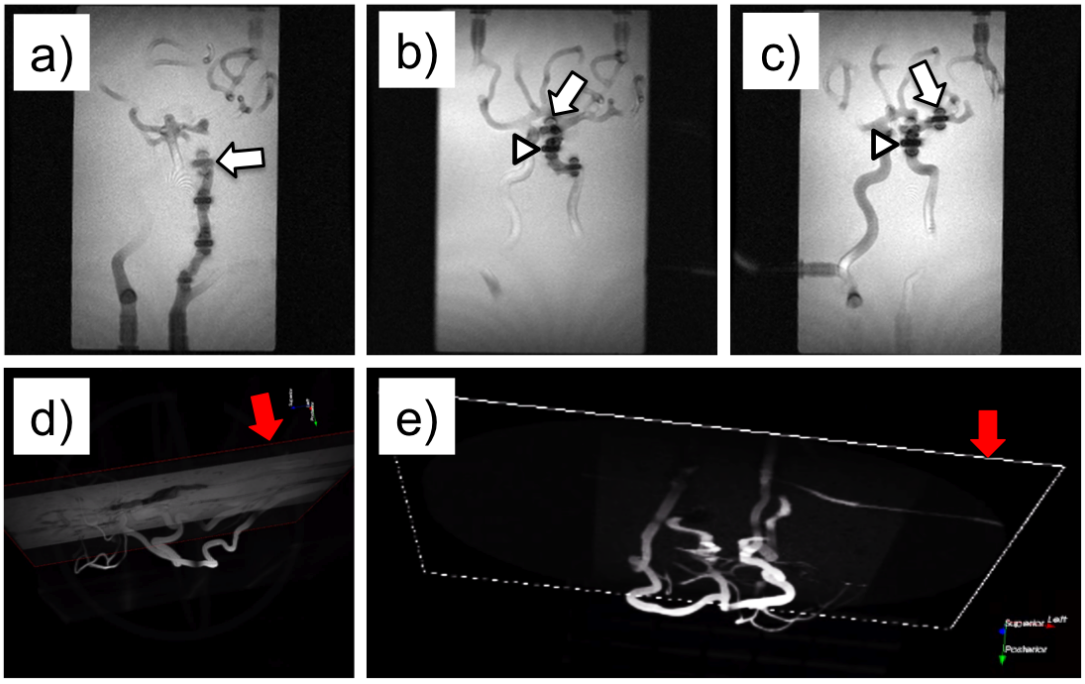

FIGURE 7.3: Micro catheter navigation in the intra-cranial model - Figures **(a - c)** show rtMRI (FGRE - Table 7.1) frames while the guidewire and micro catheter were advanced into the left MCA to manipulate and remove a blood clot in the M1 segment. The arrow indicates the tip of the guidewire and the arrowhead the tip of the micro catheter. The inteventional neuro-radiologist was also able to see a 2D rtMRI scan plane (red arrow) rendered to the 3D roadmap **(d)** of the arterial intracranial model while the opacity could be adjusted **(e)** on demand.

7.3.2 Ex Vivo Studies in Thiel Embalmed Human Cadavers

The initial T_2-weighted baseline brain scans (Figures 7.4a - c) revealed that two (one male and one female, age range 50 - 70, weight 65 - 85 kg) out of four cadavers were suitable for brain imaging and neurovascular interventions. Figure 7.4d illustrates a MIP (black and white inverted) roadmap, obtained with 3D MRA after a slow injection (0.5 mL/sec) of 10 ml Gd-doped solution (1:100). In one cadaver a pre-existing flow defect (most likely caused by trapped air) was discovered, which was employed as target for navigation. This flow defect in the left MCA (M1) (white arrow) can be perceived as significantly reduced perfusion/absence of Gd-doped fluid. The Gd-doped solution allowed a distinct visualisation of the neuro-vasculature (see Figure 7.5) during rtMRI. Device navigation (Figure

7.5) was successfully performed in three different sets of experiments (1. left MCA (M1) (n = 3/3), 2. right MCA (M1) (n = 3/3), 3. left MCA (M2) (n = 1/3)) by an experienced neuro-interventional radiologist and within 25 minutes. Automated device tracking was feasible until reaching the C4 segment of the internal carotid artery where the vessel diameter prohibited the MPA catheter to pass. The poor torque transition of the micro guidewire prototypes prevented (n = 2/3) to access the M2 segment of the left MCA.

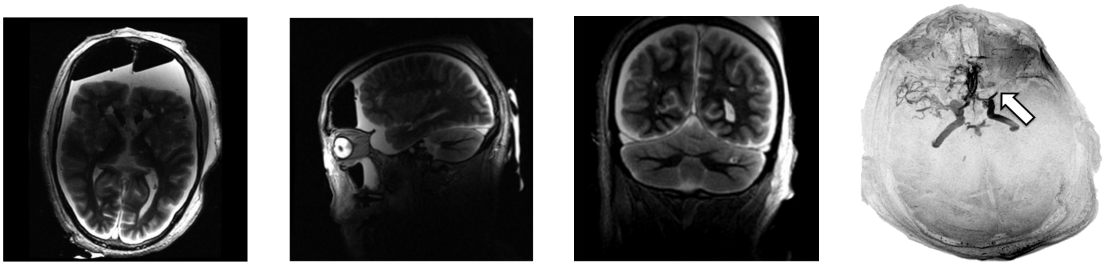

(a) Axial Baseline (b) Sagittal Baseline (c) Coronal Baseline (d) MIP - 3D ToF SPGR

FIGURE 7.4: MR images of a Thiel cadaver that was found suitable for iMRI T_2-weighted baseline scans (**(a)** axial, **(b)** sagittal, **(c)** coronal) to assess suitability of a cadaveric brain. Figure **(d)** shows a MIP (black and white inverted) of a 3D MRA dataset (Table 7.1). The white arrow illustrates the absence of Gd-doped fluid due to pre-existing flow defect (most likely due to trapped air) in the left MCA (M1). Note, the extensive amount of air and fluid in the intracranial space in Figures **(a)** and **(b)**.

7.3.3 Preliminary In Vivo Validation Experiments

Passive device visualisation enabled placement of the balloon catheter within 10 minutes after the first insertion of the guidewire at the femoral artery access site. Balloon dilatation of the right carotid artery was successfully performed (n = 2/2). Figure 7.6 illustrates sequential MR images (radial trueFISP) during device positioning of the guidewire (the white arrow illustrates the tip), the micro catheter (the arrowhead illustrates the tip) and the wRC on the balloon catheter (red arrow). The susceptibility artefact induced by the FeO marker allowed adequate localisation of the guidewire tip but was occasionally masking relevant anatomy, in particular during navigation into or close to small branches. Manual scan plane

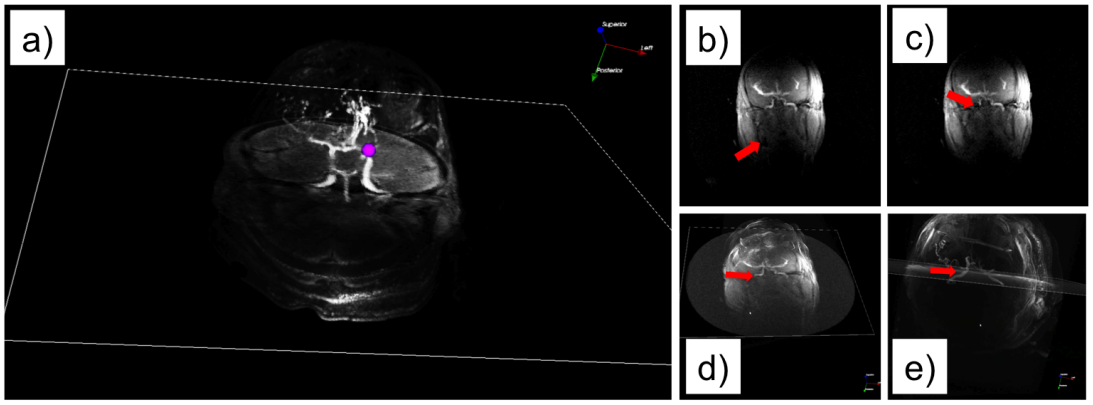

FIGURE 7.5: Device navigation in the brain of a Thiel soft-embalmed human cadaver - Figure **(a)** shows the tip tracking position (purple sphere) of the MPA catheter rendered to a 3D roadmap and 2D rtMRI (FSPGR - Table 7.1) scan plane while the MPA catheter with a wRC was navigated into the left internal carotid artery (C4 segment). Figures **(b - e)** illustrate the navigation of a micro guidewire into the right MCA with rtMRI guidance (FSPGR) while the 2D scan plane was rendered to a 3D roadmap **(d - e)**. The red arrows illustrate the tip of the micro guidewire.

adjustments, in order to locate devices in the current scan plane, were found feasible but generally time consuming (compared to automated tracking), in particular for the micro guidewires.

Once the balloon catheter was adequately positioned, the pulse sequence was stopped and a radial FLASH was initiated to monitor the balloon dilatation process (inflation with 1:100 Gd-doped saline solution). Figure 7.7 illustrates sequential images during the inflation process in the right common carotid artery. The position of the inflated balloon was then verified and evaluated with a 3D radial VIBE sequence (Figure 7.8).

7.4 Discussion

Generally, it is important that imaging methods are selected based on the condition of the patient, the anatomical regions and structures involved, the time since stroke onset, the logistical constraints of using one or the other modality, and the capability of a facility to perform advanced therapy such as IA thrombolysis [207]. Possible limitations of iMRI-guided stroke therapy include a restricted access to the patient and that MRI scans are more challenging to obtain (as compared to

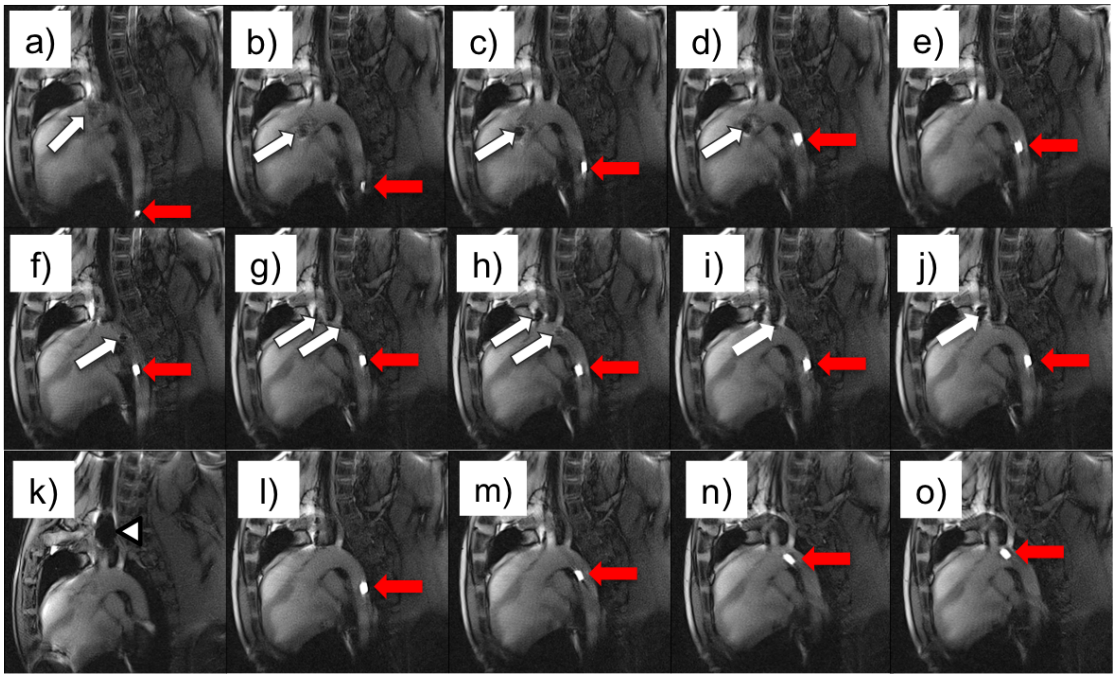

FIGURE 7.6: *in vivo* imaging during device navigation using rtMRI guidance (radial trueFISP - Table 6.3) to position a balloon in the right common carotid artery for angioplasty - Figures **(a - e)** illustrate how the balloon catheter (wRC pointed out by red arrows) was initially advanced in combination with the guidewire (markers pointed out by white arrows). Figures **(f - j)** illustrate how the guidewire was advanced and positioned distally to the right carotid artery. Figure **(k)** shows the tip marker of the micro catheter (arrowhead) that was advanced over the guidewire and placed into the carotid artery (balloon catheter has been withdrawn). The guidewire was then advanced into the carotid artery and the micro catheter exchanged to the balloon catheter in Figure **(l)**. Figures **(m - o)** illustrate how the balloon catheter was advanced and positioned for subsequent balloon dilatation (see Figure 7.7).

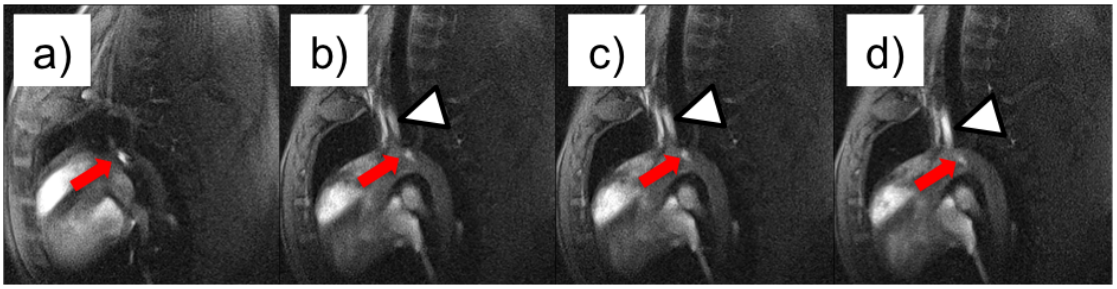

FIGURE 7.7: In vivo rtMRI (radial FLASH - Table 6.3) during balloon inflation (arrowhead shows balloon filled with 1:100 Gd-doped saline solution) in the right common carotid artery of a pig. The red arrow indicates the wRC behind the balloon.

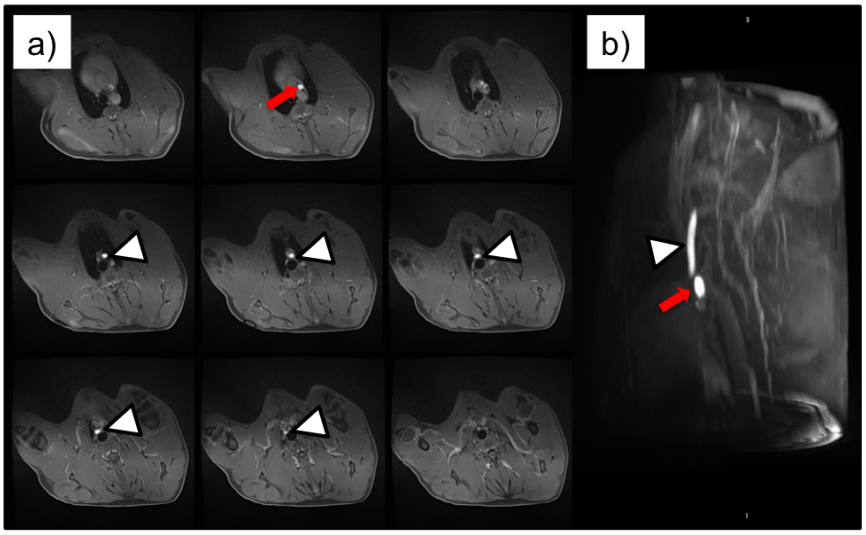

FIGURE 7.8: Assessment of an in vivo balloon dilatation in the right carotid artery. Figure **(a)** shows the images obtained with a 3D radial VIBE (Table 6.3) slice by slice in axial orientation. Figure **(b)** shows a MIP of the 3D dataset. Red arrows indicate the wRC on the balloon catheter and white arrowheads show the inflated balloon (with 1:100 Gd-doped saline solution).

i.e. CT), in particular in acutely ill or uncooperative patients [220]. Additionally, contraindications to MRI (such as ferromagnetic foreign bodies [224] and passive or active implants [22, 225]) are challenging to identify in the acute stroke setting [220] and can exclude a significant population of patients. Other drawbacks related to MRI are the increased scan time that is required for both diagnostic (compared to CT) and interventional (compared to X-Ray fluoroscopy) imaging, the need for MRI-safe equipment (including anaesthesia equipment) and the learning curve to perform these procedures.

This chapter presents a pre-clinical pilot trial to evaluate the feasibility of MRI-guided mechanical clot retrieval. These *in vitro* experiments demonstrate that recanalisation of occluded vessel segments (M1, M2) of the MCA, were feasible and practical using the developed framework of technologies and interventional devices. This was also validated by means of *ex vivo* experiments using Thiel soft-embalmed human cadavers. The initial *ex vivo* experiments were performed with pulsatile flow (driven by a heart lung machine) because perfusion is a prerequisite for achieving vessel patency for guidewire movement and visualization. To the authors' knowledge, this is the first report that brain reperfusion has been

established in a Thiel soft-fixed cadaver. However, this artificial perfusion of cadaveric brains resulted in considerable extravasation and thus loss of discernible brain structure. Thus, optimizations of the perfusion setup and the protocol are required for future studies. In addition, *in vivo* experiments were conducted in a porcine model to further validate the developed devices and their visualization in order to assess their future potential for MRI-guided mechanical clot retrieval *in vivo*. The preliminary *in vivo* results of balloon angioplasties of the carotid artery are encouraging but it is expected that significant additional research is required before MRI becomes a feasible imaging modality for guiding endovascular interventions in acute ischemic stroke.

One inherent limitation that has to be acknowledged in the context of this study is that it was not possible to deploy artificial blood clots in the *ex vivo* and *in vivo* models prior to the experiments. A suitable material to mimic blood clots that does not contain substances of animal or human origin has to be identified for future investigations. Other limitations of the current study are that only a smaller number of experiments were performed, in particular in the animal study. It should also be noted that domestic pigs are frequently used as *in vivo* models for interventional research due to the numerous similarities between human and porcine anatomy and physiology [60, 78] but have significant drawbacks for intracranial endovascular interventions. Most important, the arterial rete prevents catheterisation of the intracerebral arteries [60]. It is necessary that limitations related to the *in vivo* model will be addressed in further studies in order to fully assess the potential of MRI-guided stroke treatment. Nevertheless, it was the ambition of this study to set the stage for future investigations of acute ischemic stroke treatment using MRI guidance.

7.4.1 Interventional Devices

The small inner diameters of the intracerebral arteries in combination with the requirement to select MRI safe materials constitute a significant challenge for the design and production of interventional devices. The presented micro guidewires and catheters enabled device navigation into the M1 and M2 vessel segments of the

MCA without macroscopic device breakages. However, further device optimisations (similar to what has been described in Section 3.4.0.4) and advanced material processing technologies are required, in particular to improve the mechanical and handling properties of the micro guidewires and the MRI visualisation of the Basketrievers (clot retrievers) for future experiments. Furthermore, the amount of FeO particles has to be adjusted in order to optimize the size of the susceptibility artefact at the tip of the microcatheter in order to avoid masking of delicate anatomical structures. One drawback of the presented devices is that guidewires and micro catheter were both prepared with passive markers, which makes unambiguous device identification challenging.

7.4.2 Device Tracking and Navigation

Automated device tracking simplified device navigation in the phantom and cadaver experiments, in particular during the initial stages of an intervention (between access site and carotid arteries). However, the wRC applied to the device surface permitted catheter navigation in vessel segments with a diameter of 2.5 mm or less. Device exchange to a micro catheter and manual scan plane alignments were required above the C4 segment of the internal carotid artery. Manual scan plane alignments were found feasible but caused significant delays and hampered an efficient iMRI workflow. Thus, a miniaturized wRC design is highly desirable (see also Section 3.4.0.4) to allow wireless device tracking while being able to access smaller branches.

7.5 Conclusions

In conclusion, the results of this study demonstrate that rtMRI-guided endovascular recanalization of the MCA were feasible *in vitro* and *ex vivo*, indicating that the presented devices and methods (real-time guidance, interactive MRI remote control, in-room communication, device tracking and visualisation) have future potential to decrease delays in initiating endovascular stroke treatment. The devices were furthermore validated *in vivo* by means of balloon angioplasties of the

carotid artery in a porcine model. Unique features of MRI for stroke therapy are the detection of hemorrhages, occlusions of large vessels, irreversibly brain injuries and areas that are viable but under-perfused [207], which support critical intra-procedural decision making during the course of an intervention and be superior to X-Ray at revealing potential complications of a given intervention [78]. An additional benefit is the predictive value of MRI post reperfusion, not only for complications but also for recovery [226]. However, device optimizations and tracking of instruments with a smaller diameter along with further *in vivo* studies using suitable materials to mimic blood clots are required before clinical evaluation. Furthermore it is essential that the potential clinical workflow and the time benefit of MRI-guided endovascular recanalisation are investigated in future studies.

Chapter 8

Summary and Outlook

8.1 Summary

Despite considerable research efforts over the past decades, many interventional applications of MRI such as local injections, tumour ablations, solid tumour biopsies and endovascular procedures have not gained sufficient momentum to enter routine clinical practice. The main objective of the research presented in this thesis was to develop a set of tools to address a number of the remaining challenges in the field of iMRI, specifically for percutaneous and endovascular procedures. This work proposes novel solutions for device visualisation and tracking, real-time guidance, interactive remote control and communication for iMRI. Overall, the presented work allows a conclusion that common endovascular interventions (balloon angioplasty of the common iliac and carotid artery and also clot retrieval of the MCA) and percutaneous interventions such as biopsies are experimentally feasible solely using MRI guidance.

The key contributions from the preceding results chapters to the field of iMRI are summarized in the following:

Device Visualisation and Tracking

In this thesis a set of catheters and a polymer-based guidewire were developed, optimised and validated. To the authors knowledge this is the only MRI-safe guidewire to date with regulatory clearance in Europe (CE mark in October 2012), which is thought to be a milestone for enabling MRI-guided endovascular interventions. This work also demonstrated that interventional devices could be visualized in MRI using wRCs and passive susceptibility markers without compromising patient safety due to RF induced heating. MRI visualisation of the profile and orientation of devices was achieved with multiple wRCs or a combination of wRCs and passive susceptibility markers. The key problem of wireless device tracking was addressed and successfully tested by interventionalists during procedures on *in vitro* and *ex vivo* models. This tracking solution provides a feedback loop and copes with device exchanges, which is crucial for catheter-based procedures.

Real-time Guidance and MRI Remote Control

Dynamic closed-loop control of image acquisition and in-room display was realised for iMRI. A dedicated web-browser based UI was developed, which provides the operating physician the ability to adjust the scan acquisition via wireless consumer devices such as tablet computers at the patient table allowing changes between different pulse sequences, each tailored to the particular step of an intervention. A specialized UI has been developed for interactive scanner control during endovascular and percutaneous needle interventions, which showed to improve the workflow for iliac angioplasties and liver core biopsies, respectively.

Communication

High acoustic noise levels during MRI scanner operation require the staff and patient in the scan room to wear noise protection and special solutions for audio communication were therefore developed and successfully tested for iMRI. Tablet computers in conjunction with Bluetooth-based headsets were adopted for scanner operator - physician - assistant communication in conjunction with MRI remote control. These developments enabled multi-user communication in the MRI scan room and the results support an improved iMRI workflow for percutaneous and endovascular interventions compared to previous experiments.

Workflow and Pre-clinical Validation

A substantial hurdle for performing interventions in the complex MR environment is the lack of dedicated and efficient workflow. The devices and methods, described in this thesis have been shown to overcome many of the present limitations and were investigated for MRI-guided interventions as an alternative strategy to the conventional interventional image guidance methods such as X-Ray fluoroscopy. In the final part of this thesis, two pre-clinical projects were carried out to validate the developed framework of technologies (dedicated iMRI soft- and hardware along with a novel protocol) for common endovascular interventions *in vitro*, *ex vivo* and *in vivo*. Firstly, the framework was applied to balloon angioplasties of the

iliac arteries. The experimental results demonstrated that these interventions are feasible in a reasonable time, which was comparable to X-Ray fluoroscopy-guided procedures and significantly faster than with the standard MRI user interface provided by the scanner manufacturer. Secondly, the described methods were applied to recanalisation in acute ischemic stroke and it was demonstrated that MRI-guided recanalisation in simulated clotted arteries (middle cerebral artery, carotid artery) setting were experimentally feasible using the described framework of technologies.

8.2 Open Issues and Future Work

Research in the field of iMRI is an active area and the results presented in this thesis have contributed to a number of the key hurdles for enabling MRI-guided procedures. However, many methods require additional investigations and numerous problems still remain to be solved before translation from small experimental trials to clinical procedures.

Device Visualisation, Tracking and MRI Remote Control

An essential step for translation into the clinical setting is that it must be shown that devices are safe and effective for the intended use and the regulatory hurdles in this context are high (Class III in Europe for minimally invasive devices in direct contact with the central circulatory system [227]). Although the presented results are encouraging, to date the only device with regulatory approval (in Europe) presented in this thesis is the guidewire. Design optimizations of the catheter markers are required before the presented interventional devices can be used in a similar fashion as state of the art devices for X-Ray fluoroscopy. The next steps in research should involve a completely integrated design of wRCs. Collaboration has been established with the University of Magdeburg to investigate if micro systems-based technologies could provide a viable solution for integrated wRCs, which can also be used for wireless device tracking. Moreover, the presented tracking implementation was found to be satisfactory for balloon angioplasties of

the iliac artery *in vitro* and *ex vivo* but further studies are required to evaluate if a single tracking coil and thus position is sufficient for more complex navigation and catheter profiles before animal trials and clinical application. Future research should focus on a pulse sequence and a tracking algorithm, which locates multiple resonant markers that inductively couple to the receive coil.

Communication and Real-time Guidance

One important feature, which has not been investigated in this thesis, is communication with the patient during scanner operation. Future research should be attributed to establishing selective communication between patient, physician, assisting staff and scanner operator. A complete MRI safety assessment (according to ASTM) of all components that have been modified and added to the MRI scan room (to enable communication and remote control) is another open issue. This assessment would also allow a conclusion if further controls should be implemented for mitigation of the residual risks i.e. by adding RF shields or by improving the fixation means of the tablet devices. Another interesting solution to overcome the high acoustic noise and resulting communication problems during MRI scanner operation has recently been proposed by Grodzki *et al.* [228, 229]. The researchers developed a quiet 3D pulse sequence that requires very limited gradient activity by combining single point imaging (centre of k-space) with radial projection imaging (outer k-space) and can be used with standard imaging hardware. It is anticipated that inaudible pulse sequences will in future also attract strong interest in the interventional and surgical community. Future work should investigate if these pulse sequences can also be adopted for 2D imaging with high frame rates and achieve sufficient FOV coverage to be suitable for interventional applications.

Workflow and Pre-clinical Validation

In addition, some limitations of the presented framework of technologies (imaging and tracking pulse sequences implemented in RTHawk, web-browser based UI, tablet PCs and multi-user communication) are worth noting. First, only parts

of the setup could be validated *in vivo* (tablet PCs and multi-user communication) due to compatibility issues (RTHawk is currently compatible with GE MRI scanners only) and only a clinical scanner (Siemens) was available for *in vivo* experiments. Second, the presented work provides limited quantitative data on the evaluation of the real-time phase contrast (rtFLOW) implementation. It should be noted, that no clinical evaluation (diagnostic only) could be performed because the RTHawk application and related software are currently not approved for clinical use. Further investigations should validate the rtFLOW and compare the measurement accuracy and waveforms to Doppler Ultrasound or laser Doppler flowmetry and correlate the measurements with *in vivo* data. Work is on-going to investigate the safety of critical parts of the presented framework of technologies along with further bridging studies in animal models to prepare a clinical study. Another inherent limitation worth noting is that the experiments for clot retrieval of occluded cerebral arteries were performed *in vitro* and *ex vivo* with a small number of repetitions only. Although the cadaver experiments are encouraging, blood clot removals require further investigation in future *in vivo* studies.

It should be noted that it is thought to be unlikely that MRI will replace conventional imaging modalities for the majority of interventions (except procedures that solely depend on unique MRI features such as real-time thermometry). However, it is expected that with further research iMRI could become an alternative interventional image guidance method for paediatric or pregnant patients and in procedures with long intervention times where radiation dose accumulates. One of the largest hurdles to overcome is the limited access to the patient, which is a related to current magnet designs required for full body scanners with a field strength of 1.5 T or higher. This remains a particular challenge for percutaneous needle interventions where the physician has to advance the needle (close to the iso-centre of the magnet) and simultaneously monitor the needle progress on a screen.

8.3 Potential Directions of Future Research

This final subsection describes certain potential future areas of iMRI research to augment the work presented in this thesis.

Real-time Guidance and MRI Remote Control

Controlling an MRI scanner and guiding interventional procedures from a web browser presents many interesting solutions for device integration, educational demonstrations or collaborative treatment planning and monitoring. In addition, the presented developments could open the door for using the same user interface across multiple platforms and MRI scanner manufacturers, which should be investigated in future collaborative studies. One potential application how the presented methods could be applied to multimodality-guided interventions is currently investigated in collaboration with a group at the University of St. Andrews, UK. This research project focuses on combining macro scale MRI with micro scale optical imaging technologies, which have recently emerged as key tools for biomedical applications. Promising candidates for intra-operative assessment include optical coherence tomography, which provides sub millimetre precision [230] and Raman spectroscopy, which can detect molecular changes [231] and discriminate between normal and abnormal tissue and in real-time. In this project the developed mobile device and web technologies are applied to MRI-guided optical biopsies using an MRI compatible and disposable fibre-based Raman probe[1]. The iMRI technologies presented in this thesis are used to monitor and access the UI of the Raman spectroscopy software in conjunction with the iMRI UI on the monitor and the tablet PCs in the MRI scan room.

wRC-Based Tracking for Robotic Assisted Interventions

MRI-compatible robotic assistance system such as the Innomotion (Innomedic, Herxheim, Germany) robotic arm, which has received the CE mark in 2005 [116]

[1]Initial results of this research will be presented as: Ashok PC, Praveen BB, Rube MA, Cox BF, Melzer A, Dholakia K. Development of a fibre based Raman probe compatible with interventional Magnetic Resonance Imaging. Proceedings of SPIE Photonics West 2014, BiOS Technical Conference, San Francisco, CA, USA

or the Symbis robot, which is currently under development by IMRIS (Winnipeg, Manitoba, Canada), have substantial potential for MRI-guided interventions because they overcome the challenges that are related to the limited patient access. Device tracking will play an essential role in the context of robotic assisted interventions and surgical procedures using MRI guidance. For instance, the Innomotion system currently employs passive markers and a post-processing algorithm to locate the position of the application module. This static position information is then used to move the robot without further MR-based tracking. However, a significant limitation of this robotic system is that there is no feedback loop between MRI scanner and the robotic system. As a result the patient has to be moved out of the bore and the needle is inserted in front of the scanner, which is a major source of motion related targeting errors.

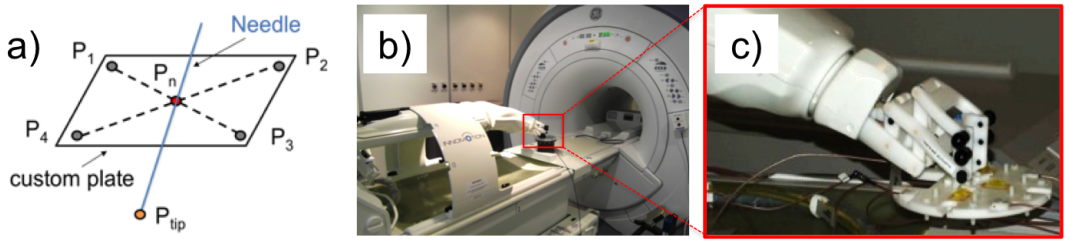

FIGURE 8.1: Conceptual drawing for combined active and wireless instrument tip tracking during robotic assisted interventions using MRI guidance - Figure **(a)** shows a schematic drawing (not to scale) of a robotic applicator module for tracking. The tip of an instrument (a needle is shown exemplary) equipped with a wRC can be tracked (P_{tip}) according to the method that was described in Chapter 5. The points P_1; P_2; P_3 and P_4 can be obtained with active tracking. Figure **(b)** shows how this could in theory be applied to the Innomotion robot located at IMSaT using a custom applicator module (red). This applicator module[2] with micro coils for active tracking is enlarged in Figure **(c)**.

One aspect of future research in the robotic field is to combine two device-tracking methods, active tracking and the method proposed in Chapter 5. Integrating active tracking of robotic arms[2] or applicator modules and wireless tracking of a wRC on the tip of a straight instrument (i.e. a cannula) could enable MRI-guided interventions with a continuous feedback loop. The main advantage of this concept is that the patient and active tracking cables do not come into contact,

[2]The results of this research will be published as: Xiao X, Huang Z, Rube MA, Melzer A. Investigation of active tracking for robotic arm assisted MRgFUS. *Int J Med Robot Comput Assist Surg* (Accepted with Revisions)

which prevents RF induced heating. A conceptual applicator module for this combined tracking approach is illustrated in Figure 8.1. Active tracking according to [185] can be used to calculate the location of the tracking coils that are attached to the tracking applicator module. In addition the wireless device tracking method can be used to track a wRC on the tip of the instrument (P_{tip}). The point P_n on the instrument trajectory (a needle is shown exemplary) can then be obtained indirectly by computing the coordinates P_1, P_2, P_3 and P_4. The point (P_n) is then calculated as intersection of the two lines between the points $P_1 - P_3$ and the points $P_2 - P_4$. Both pulse sequences can be interleaved (with a temporal resolution of $2x4xTRxN$, where N is the number of phase-field k directions) and can also be interleaved with imaging pulse sequences similar to what has been described in Chapter 5.

Appendix A

Publications Arising From This Thesis

Patent Applications

M. A. Rube, A. Melzer; GB 1310081.3, Patent pending

Articles in Peer-Reviewed Journals

I. Karakitsios, M. Bobeica, T. Saliev, **M. A. Rube**, A. Melzer A. "Thermometry during MR-guided focused ultrasound in a preclinical model based on Thiel embalmed tissue". *Minim Invasive Ther Allied Technol* vol. 23, no. 1, pp 120-6, 2014.

M. Wolska-Krawczyk, **M. A. Rube**, E. Immel, A. Melzer, A. Buecker. "Heating and safety of a new MR compatible guidewire prototype versus standard nitinol guidewire". *Radiol Phys Technol*, vol. 7, no. 1, pp 95-101, 2014.

M. A. Rube, A. B. Holbrook, B. F. Cox, J. G. Houston, A. Melzer. "Wireless tracking of interventional devices using phase-field dithering and projection reconstruction". *Magn Reson Imaging* [Epub ahead of print]; doi:10.1016/j.mri.2014.03.007

M. A. Rube, F. Fernandez-Gutierrez, B. F. Cox, J. G. Houston, R. D. White, H. McLeod, M. Fatahi, A. Melzer. "Preclinical feasibility of a technology framework for MRI-guided iliac angioplasty". *Int J Comput Assist Radiol Surg* (in press)

M. A. Rube, A. B. Holbrook, B. F. Cox, R. Buciuc, A. Melzer. "Wireless mobile technology to improve workflow and feasibility of MR-guided percutaneous interventions". *Int J Comput Assist Radiol Surg* (in press)

M. Kaiser, M. Detert, **M. A. Rube**, A. El-Tahir, O. J. Elle, A. Melzer, B. Schmidt, G. H. Rose. "Resonant marker design and fabrication for device visualization during interventional magnetic resonance imaging". *Biomed Tech (Berl)* (Accepted with Revisions)

X. Xiao, Z. Huang, **M. A. Rube**, A. Melzer. "Investigation of active tracking for robotic arm assisted magnetic resonance guided focused ultrasound ablation". *Int J Med Robot Comput Assist Surg* (Accepted with Revisions)

F. Fernandez-Gutierrez, S. Martinez, **M. A. Rube**, B. F. Cox, M. Fatahi, K. Scott-Brown, J. G. Houston, H. McLeod, R. White, K. French, M. Gueorguieva, E. Immel, A. Melzer. "Comparative ergonomic workflow and user experience analysis of MRI versus fluoroscopy guided vascular interventions: an iliac angioplasty case study". *Int J Comput Assist Radiol Surg* (under review)

P. C. Ashok, B. B. Parveen, **M. A. Rube**, K. French, A. Melzer, K. Dholakia. "Magnetic Resonance Imaging Compatible Fiber Raman Probe for Interventional Procedures". *PLoS ONE* (under review)

Conference Proceedings

M. A. Rube, P. Samraj, E. Immel, P. Andre, A. Melzer A, "MRI visible FePt-nanoparticles for catheter localization in 1.5T", *Proceedings of the 10th Scientific UK Radiology Congress (UKRC), Manchester, UK, 2011*

M. A. Rube, P. Samraj, E. Immel, D. Kakchingtabam, P. Andre, A. Melzer, "Combination of MRI visible iron-platinum (FePt) nanoparticles and resonant markers for catheter localization and guidance in 1.5T MRI", *Proceedings of the 26th Scientific Meeting of Cardiovascular and Interventional Radiological Society of Europe (CIRSE), Munich, Germany, 2011*

R. J. Toomey, E. Immel, M. Gueorguieva, J. G. Houston, **M. A. Rube**, R. Eisma, A. Melzer, "Angiography of multiple vascular segments in a soft-embalmed cadaver model", *Proceedings of the 26th Scientific Meeting of Cardiovascular and Interventional Radiological Society of Europe (CIRSE), Munich, Germany, 2011*

M. A. Rube, E. Immel, R. Toomey, M. Wolska-Krawczyk, A. Melzer, "Semi-active resonant markers for interventional device localization in phantom experiments and in a Thiel embalmed cadaver model in 1.5T real-time MR imaging", *Proceedings of the 23rd Scientific Meeting of the Society for Medical Innovation and Technology (SMIT) (Oral presentation), Tel Aviv, Israel, 2011*

M. Wolska-Krawczyk, **M. A. Rube**, E. Immel, R. J. Toomey, F. Fernadez-Guiterrez, A. Buecker, A. Melzer, "Prototype of MR compatible guidewire versus nitinol based guidewire in a saline filled phantom. A comparison of RF heating in 1,5 T MR scanner", *Proceedings of the 23rd Scientific Meeting of the Society for Medical Innovation and Technology (SMIT), Tel Aviv, Israel, 2011*

M. Wolska-Krawczyk, **M. A. Rube**, E. Immel, R. Toomey, F. Fernadez-Guiterrez, A. Buecker, A. Melzer, "Measurements of excessive heating by resonating RF waves of nitinol based guidewire in a saline filled phantom and in a vessel of a Thiel embalmed human cadaver with artificial induced saline flow in 1.5 Tesla MR scanner", *Proceedings of the 23rd Scientific Meeting of the Society for Medical Innovation and Technology (SMIT), Tel Aviv, Israel, 2011*

D. Gourevich, O. Dogadkin, R. Malik, A. Volovyk A., B. Gerold, D. Xu, Y. Vachutinsky, F. Arditti, L. Wang, P. Prentice, Y. Medan, J. Gnaim, S. Cochran, A. Melzer, **M. A. Rube**, "An in-vitro study of increased drug uptake with MRI-guided focused ultrasound surgery", *Proceedings of the 28th Scientific Meeting of the European Society for Magnetic Resonance in Medicine and Biology (ESMRMB), Leipzig, Germany, 2011*

A. Volovyk, S. Eljamel, T. Saliev, R. Eisma, Y. Medan, **M. A. Rube**, A. Melzer, "Thiel embalmed cadavers as a model for transcranial MRgFUS", *Proceedings of the 28th Scientific Meeting of the European Society for Magnetic Resonance in Medicine and Biology (ESMRMB), Leipzig, Germany, 2011*

M. A. Rube, E. Immel, S. J. Gandy, D. Kakchingtabam, P. Andre, P. Samraj, J. G. Houston, A. Melzer, "Combined MRI visible iron-platinum (FePt) nanoparticles and a resonant tip marker for device localization and guidance in 1.5T and 3T MRI", *Proceedings of the 97th Scientific Meeting of the Radiological Society of North America (RSNA) (Oral presentation), Chicago, USA, 2011*

M. A. Rube, E. Kokkalis, E. Immel, M. Gueorguieva, A. Melzer, "Training and testing environment for MR-guided vascular interventions", *Proceedings of the 20th Scientific Meeting of the International Society of Magnetic Resonance Imaging in Medicine, Melbourne (ISMRM), Australia, 2012*

M. A. Rube, P. Seifert, B. Uihlein, D. Kakchingtabam, P. Andre, A. Melzer, "Novel MR-safe guidewire with passive iron-platinum alloy nanoparticles for MR-guided interventions", *Proceedings of the 20th Scientifice Meeting of the International Society of Magnetic Resonance Imaging in Medicine (ISMRM), Melbourne, Australia, 2012*

M. A. Rube, E. Immel, B. F. Cox, A. Melzer. "Towards interventional MRI: Semi-active device localization in phantom experiments and in a Thiel embalmed human cadaver model", *Proceedings of Computer Assisted Radiology and Surgery (CARS) (Oral Presentation), Pisa, Italy, 2012*

M. A. Rube, B. F. Cox, M. Gueorguieva, D. Kakchingtabam, P. Andre, A. Melzer. "Iron-platinum alloy nanoparticles for guidewire and resonant markers for catheter localization during interventional MRI". *Proceedings of the 46th Annual Conference of the Deutsche Gesellschaft fuer Biomedizinische Technik (BMT) (Oral presentation) , Jena, Germany, 2012*

B. F. Cox, H. McLeod, **M. A. Rube**, S. Vinnicombe, A. B. Holbrook, R. Eisma, T. Saliev, I. Karakitsios, A. Melzer, "MR real-time tracking of hepatic motion during respiration in a Thiel soft-fix cadaver", *Proceedings of the 46th Annual Conference of the Deutsche Gesellschaft fuer Biomedizinische Technik (BMT) (Oral presentation), Jena, Germany, 2012*

M. A. Rube, P. Seifert, D. Kakchingtabam, P. Andre, A. Melzer, "Novel MR-safe guidewire with passive iron-platinum alloy nanoparticles for cardiovascular interventional MRI", *Proceedings of the 27th Scientific Meeting of Cardiovascular and Interventional Radiological Society of Europe (CIRSE), Lissabon, Portugal, 2012*

M. A. Rube, B. F. Cox, A. B. Holbrook, L. Melzer, A. Melzer, "Interventional magnetic resonance imaging with an in-room interactive touch device", *Proceedings of the 5th Image Guided Therapy Workshop by the National Center for Image Guided Therapy (NCIGT), Boston, MA, USA, 2012*

M. Pendleton, B. F. Cox, T. Saliev, **M. A. Rube**, H. McLeod, A. Melzer, "Imaging of vessel patency in Thiel embalmed liver", *Proceedings of the 5th Image Guided Therapy Workshop by the National Center for Image Guided Therapy (NCIGT), Boston, MA, USA, 2012*

A. B. Holbrook, **M. A. Rube**, A. Melzer, K. Butts-Pauly, "Interventional MRI from the internet browser", *9th Interventional MRI Symposium (IMRI), Boston, MA, USA, 2012*

B. F. Cox, H. McLeod H, **M. A. Rube**, S. Vinnicombe, A. B. Holbrook, R. Eisma, T. Saliev, I. Karakitsios, A. Melzer, "MR real-time tracking of hepatic motion during respiration in a Thiel soft-fix cadaver", *9th Interventional MRI Symposium (IRMI), Boston, USA, 2012*

B. F. Cox, H. McLeod H, **M. A. Rube**, S. Vinnicombe, A. B. Holbrook, R. Eisma, T. Saliev, I. Karakitsios, A. Melzer, "MR tracking of hepatic movement during artificial respiration in a Thiel soft-fix cadaver", *Proceedings of the 98th Scientific Meeting of the Radiological Society of North America (RSNA), Chicago, USA, 2012*

M. A. Rube, A. B. Holbrook, B. F. Cox, L. Melzer, M. Lenhardt, A. Melzer. "Wireless remote control and in-room communication for MRI-guided interventions using mobile touch devices". *Proceedings of Computer Assisted Radiology and Surgery (CARS) (Oral Presentation), Heidelberg, Germany, 2013*

F. Fernandez-Gutierrez, M. Santiago, **M. A. Rube**, B. F. Cox, M. Fatahi, K. C. Scott-Brown, J. G. Houston, H. Mcleod, R. D. White, K. French, M. Gueorguieva, E. Immel, A. Melzer. "An operational comparison of MRI and X-Ray for vascular interventions. Case of study: Task and user experience analysis for iliac angioplasty". *Proceedings of the 25th Scientific Meeting of the Society for Medical Innovation and Technology, Baden-Baden, Germany, 2013*

Bibliography

[1] A. Cuschieri, *Operative Manual of Endoscopic Surgery.* New York, LLC: Springer-Verlag, July 1992.

[2] M. J. Mack, "Minimally invasive and robotic surgery.," *JAMA*, vol. 285, pp. 568–72, Feb. 2001.

[3] M. O. Schurr, A. Melzer, P. Dautzenberg, B. Neisius, R. Trapp, and G. Buess, "Development of steerable instruments for minimal invasive surgery in modular conception.," *Acta Chir Belg*, vol. 93, no. 3, pp. 73–7, 1993.

[4] M. Bock and F. K. Wacker, "MR-guided intravascular interventions: techniques and applications.," *J Magn Reson Imaging*, vol. 27, pp. 326–38, Feb. 2008.

[5] W. C. Röntgen, "Über eine neue Art von Strahlen," *Ann Phys*, vol. 300, no. 1, pp. 1–11, 1898.

[6] A. Melzer, E. Immel, R. Toomey, and F. Fernandez-Gutierrez, "MR-guided interventions and surgery," in *Springer Handb Med Technol* (R. Kramme, K.-P. Hoffmann, and R. S. Pozos, eds.), ch. 25, pp. 477–501, Springer Berlin Heidelberg, 2011.

[7] P. C. Lauterbur, "Image formation by induced local interactions: Examples employing nuclear magnetic resonance," *Nature*, vol. 242, pp. 190–1, 1973.

[8] M. A. Bernstein, K. E. King, and X. J. Zhou, *Handbook of MRI pulse sequences.* Elsevier Academic Press, 2004.

[9] W. M. Gedroyc, "Interventional magnetic resonance imaging.," *BJU Int*, vol. 86, pp. 174–80, July 2000.

[10] B. R. Rosen, J. W. Belliveau, J. M. Vevea, and T. J. Brady, "Perfusion imaging with NMR contrast agents," *Magn Reson Med*, vol. 14, no. 2, pp. 249–65, 1990.

[11] D. G. Taylor and M. C. Bushell, "The spatial mapping of translational diffusion coefficients by the NMR imaging technique," *Phys Med Biol*, vol. 30, p. 345, 1985.

[12] D. L. Parker, V. Smith, P. Sheldon, L. E. Crooks, and L. Fussell, "Temperature distribution measurements in two-dimensional NMR imaging," *Med Phys*, vol. 10, no. 3, pp. 321–5, 1983.

[13] H. H. Quick and M. E. Ladd, "MR imaging of the vessel wall," *Eur Radiol*, vol. 12, pp. 889–900, 2002.

[14] J. Barral, *In vivo Magnetic Resonance Imaging.* Ph.d. dissertation, Stanford University, CA, USA, 2010.

[15] F. A. Jolesz, P. R. Morrison, S. J. Koran, R. J. Kelley, S. G. Hushek, R. W. Newman, M. P. Fried, A. Melzer, R. M. Seibel, and H. Jalahej, "Compatible instrumentation for intraoperative MRI: expanding resources.," *J Magn Reson Imaging*, vol. 8, no. 1, pp. 8–11, 1998.

[16] A. Melzer, A. M. Schmidt, K. Kipfmüller, M. Deliing, D. Stöckel, D. H. Grönemeyer, and R. M. M. Seibel, "Prerequisites for magnetic resonance image-guided interventions and endoscopic surgery," *Minim Invasive Ther Allied Technol*, vol. 5, pp. 255–62, Jan. 1996.

[17] A. B. Holbrook, *Real time magnetic resonance imaging guided high intensity focused ultrasound in the free-breathing liver*. Ph.d. dissertation, Stanford University, CA, USA, 2011.

[18] P. Mueller, D. Stark, F. Simeone, S. Saini, R. Butch, R. R. Edelman, J. Wittenberg, and Ferrucci JT, "MR-guided aspiration biopsy: needle design and clinical trials.," *Radiology*, vol. 161, pp. 605–9, 1986.

[19] E. Rothgang, W. D. Gilson, F. Wacker, J. Hornegger, C. H. Lorenz, and C. R. Weiss, "Rapid freehand MR-guided percutaneous needle interventions: An image-based approach to improve workflow and feasibility.," *J Magn Reson Imaging*, vol. 37, pp. 1202–12, May 2013.

[20] M. McJury and F. G. Shellock, "Auditory noise associated with MR procedures: a review.," *J Magn Reson Imaging*, vol. 12, pp. 37–45, July 2000.

[21] G. Schaefers and A. Melzer, "Testing methods for MR safety and compatibility of medical devices.," *Minim Invasive Ther Allied Technol*, vol. 15, pp. 71–5, Jan. 2006.

[22] A. Melzer, S. Michitsch, S. Konak, G. Schaefers, and T. Bertsch, "Nitinol in magnetic resonance imaging.," *Minim Invasive Ther Allied Technol*, vol. 13, pp. 261–71, Aug. 2004.

[23] S. Kos, R. Huegli, G. M. Bongartz, A. L. Jacob, and D. Bilecen, "MR-guided endovascular interventions: a comprehensive review on techniques and applications.," *Eur Radiol*, vol. 18, pp. 645–57, Apr. 2008.

[24] C. R. Weiss, S. G. Nour, and J. S. Lewin, "MR-guided biopsy: a review of current techniques and applications.," *J Magn Reson Imaging*, vol. 27, pp. 311–25, Feb. 2008.

[25] F. Fischbach, J. Bunke, M. Thormann, G. Gaffke, K. Jungnickel, J. Smink, and J. Ricke, "MR-guided freehand biopsy of liver lesions with fast continuous imaging using a 1.0-T open MRI scanner: experience in 50 patients.," *Cardiovasc Intervent Radiol*, vol. 34, pp. 188–92, Feb. 2011.

[26] D. W. McRobbie, E. A. Moore, M. J. Graves, and M. R. Prince, *MRI: From picture to proton*, vol. 232. Cambridge: Cambridge University Press, second ed., Aug. 2007.

[27] R. Mekle, E. Hofmann, K. Scheffler, and D. Bilecen, "A polymer-based MR-compatible guidewire: a study to explore new prospects for interventional peripheral magnetic resonance angiography (ipMRA).," *J Magn Reson Imaging*, vol. 23, pp. 145–55, Feb. 2006.

[28] Z. T. H. Tse, H. Elhawary, C. A. F. Montesinos, M. Rea, I. Young, and M. Lamperth, "Testing MR image artifacts generated by engineering materials," *Magn Reson Eng*, vol. 39B, pp. 109–17, Apr. 2011.

[29] M. E. Ladd, P. Erhart, J. F. Debatin, B. J. Romanowski, P. Boesiger, and G. C. McKinnon, "Biopsy needle susceptibility artifacts.," *Magn Reson Med*, vol. 36, pp. 646–51, Oct. 1996.

[30] ASTM International, "F2119-07: Standard test method for evaluation of MR image artifacts from passive implants," 2007.

[31] M. E. Ladd, H. H. Quick, P. Boesiger, and G. C. Mckinnon, "RF heating of actively visualized catheters and guidewires," in *Proc Intl Soc Mag Reson Med 6*, (Sydney, Australia), p. 473, 1998.

[32] M. K. Konings, L. W. Bartels, H. F. Smits, and C. J. Bakker, "Heating around intravascular guidewires by resonating RF waves.," *J Magn Reson Imaging*, vol. 12, pp. 79–85, July 2000.

[33] W. R. Nitz, A. Oppelt, W. Renz, C. Manke, M. Lenhart, and J. Link, "On the heating of linear conductive structures as guide wires and catheters in interventional MRI," *J Magn Reson Imaging*, vol. 13, pp. 105–14, 2001.

[34] M. Bock, S. Müller, S. Zuehlsdorff, P. Speier, C. Fink, P. Hallscheidt, R. Umathum, and W. Semmler, "Active catheter tracking using parallel MRI and real-time image reconstruction.," *Magn Reson Med*, vol. 55, pp. 1454–9, June 2006.

[35] A. Buecker, "Safety of MRI-guided vascular interventions.," *Minim Invasive Ther Allied Technol*, vol. 15, pp. 65–70, Jan. 2006.

[36] ASTM International, "F2182-09: Standard test method for measurement of radio frequency induced heating on or near passive implants during magnetic resonance imaging," 2010.

[37] M. Lustig, D. Donoho, J. Santos, and J. Pauly, "Compressed sensing MRI," *IEEE Signal Process Mag*, vol. 25, pp. 72–82, Mar. 2008.

[38] W. R. Nitz, "Fast and ultrafast non-echo-planar MR imaging techniques.," *Eur Radiol*, vol. 12, pp. 2866–82, Dec. 2002.

[39] K. P. Pruessmann, M. Weiger, M. B. Scheidegger, and P. Boesiger, "SENSE: Sensitivity encoding for fast MRI," *Magn Reson Med*, vol. 42, pp. 952–62, 1999.

[40] D. K. Sodickson and W. J. Manning, "Simultaneous acquisition of spatial harmonics (SMASH): Fast imaging with radiofrequency coil arrays," *Magn Reson Med*, vol. 38, pp. 591–603, Oct. 1997.

[41] M. Guttman, C. Ozturk, A. N. Raval, V. K. Raman, A. J. Dick, R. DeSilva, P. Karmarkar, R. J. Lederman, and E. R. McVeigh, "Interventional cardiovascular procedures guided by real-time MR imaging: an interactive interface using multiple slices, adaptive projection modes and live 3D renderings.," *J Magn Reson Imaging*, vol. 26, pp. 1429–35, Dec. 2007.

[42] S. R. Yutzy and J. L. Duerk, "Pulse sequences and system interfaces for interventional and real-time MRI.," *J Magn Reson Imaging*, vol. 27, pp. 267–75, Feb. 2008.

[43] C. H. Lorenz, K. J. Kirchberg, S. Zuehlsdorff, P. Speier, M. Caylus, W. Borys, T. Moeller, and M. A. Guttman, "Interactive Frontend (IFE): A platform for graphical MR scanner control and scan automation," in *Proc Intl Soc Mag Reson Med 13*, vol. 12, (Miami, FL, USA), p. 2170, 2005.

[44] J. Smink, M. Hakkinen, R. Holthuizen, S. Krueger, M. Ries, Y. Berber, C. Moonen, M. Kohler, and E. Vahala, "eXTernal Control (XTC): a flexible, real-time, low-latency, bi-directional scanner interface," in *Proc Intl Soc Mag Reson Med 20*, p. 1755, 2011.

[45] J. M. Santos, G. a. Wright, and J. M. Pauly, "Flexible real-time magnetic resonance imaging framework," in *Conf Proc IEEE Eng Med Biol Soc*, vol. 2, (San Francisco, CA, USA), pp. 1048–51, Jan. 2004.

[46] P. Chadwick, "Assessment of electromagnetic fields around magnetic resonance imaging (MRI) equipment. UK Health and Safety Executive RR570.," tech. rep., 2007.

[47] M. Capstick, D. McRobbie, J. Hand, A. Christ, S. Kuhn, K. Hansson Mild, and E. Al., "An investigation into occupational exposure to electro-magnetic fields for personnel working with and around medical magnetic resonance imaging. Report on Project VT/2007/017 of the European Commission Employment, Social Affairs and Equal Opportunities DG," tech. rep., 2008.

[48] D. W. McRobbie, "Occupational exposure in MRI.," *Br J Radiol*, vol. 85, pp. 293–312, Apr. 2012.

[49] S. F. Keevil and D. J. Lomas, "The European Union physical agents (electromagnetic fields) directive: an update for the MRI community.," *Br J Radiol*, vol. 86, p. 20130492, Dec. 2013.

[50] M. Bock, R. Umathum, S. Zuehlsdorff, S. Volz, C. Fink, P. Hallscheidt, H. Zimmermann, W. Nitz, and W. Semmler, "Interventional magnetic resonance imaging: an alternative to image guidance with ionising radiation.," *Radiat Prot Dosim*, vol. 117, pp. 74–8, Jan. 2005.

[51] K. Ratnayaka, A. Z. Faranesh, M. A. Guttman, O. Kocaturk, C. E. Saikus, and R. J. Lederman, "Interventional cardiovascular magnetic resonance: still tantalizing.," *J Cardiovasc Magn Reson*, vol. 10, pp. 62–85, Jan. 2008.

[52] F. V. Guettler, J. C. Rump, and U. Teichgraeber, "MR-compatible wireless communication system for the interventional open high-field MRI," in *Proc Intl Soc Mag Reson Med 17*, (Honolulu, HI, USA), p. 2576, 2009.

[53] M. McJury, A. Blug, C. Joerger, B. Condon, and D. Wyper, "Acoustic noise levels during MRI scanning at 1.5T," *BJR*, vol. 67, pp. 413–5, 1994.

[54] M. A. Rube, A. B. Holbrook, B. F. Cox, L. Melzer, L. Moritz, and A. Melzer, "Interventional Radiology," *Int J Comput Assist Radiol Surg*, vol. 8(S1), pp. 5–11, May 2013.

[55] D. L. Kraitchman, W. D. Gilson, and C. H. Lorenz, "Stem cell therapy: MRI guidance and monitoring.," *J Magn Reson Imaging*, vol. 27, pp. 299–310, Feb. 2008.

[56] E. J. Schmidt, R. P. Mallozzi, A. Thiagalingam, G. Holmvang, A. D'Avila, R. Guhde, R. Darrow, G. S. Slavin, M. M. Fung, J. Dando, L. Foley, C. L. Dumoulin, and V. Y. Reddy, "Electroanatomic mapping and radiofrequency ablation of porcine left atria and atrioventricular nodes using magnetic resonance catheter tracking.," *Circ Arrhythm Electrophysiol*, vol. 2, pp. 695–704, Dec. 2009.

[57] P. E. Radau, S. Pintilie, R. Flor, L. Biswas, S. O. Oduneye, V. Ramanan, K. A. Anderson, and G. A. Wright, "VURTIGO : Visualization platform for teal-time , MRI-guided cardiac electroanatomic mapping," in *STACOM* (O. Camara, E. Konukoglu, M. Pop, K. Rhode, M. Sermesant, and A. Young, eds.), (Toronto, Canada), pp. 244–53, Springer-Verlag, Berlin Heidelberg, 2011.

[58] A. Melzer, K. Horvath, M. Guttman, M. Li, E. Immel, R. Lederman, J. Spilner, C. Lorenz, and E. Mcveigh, "MR-guided trans apical delivery of a self expanding heart valve prosthesis equipped with a resonant circuit," in *Proc Intl Soc Mag Reson Med 14*, (Seattle, Washington), p. 270, 2006.

[59] R. Hoffmann, C. Thomas, H. Rempp, D. Schmidt, P. L. Pereira, C. D. Claussen, and S. Clasen, "Performing MR-guided biopsies in clinical routine: factors that influence accuracy and procedure time.," *Eur Radiol*, vol. 22, pp. 663–71, Mar. 2012.

[60] R. F. Dondelinger, M. P. Ghysels, D. Brisbois, E. Donkers, F. R. Snaps, J. Saunders, and J. Devie, "Relevant radiological anatomy of the pig as a training model in interventional radiology," *Eur Radiol*, vol. 8, no. 7, pp. 1254–73, 1998.

[61] B. F. Cox, R. Eisma, M. A. Rube, M. Gueorguieva, H. McLeod, E. Immel, and A. Melzer, "Developing Thiel soft-fix cadavers as a suitable model for iMRI training and research," in *Proc 9th Inteventional MRI Symp*, (Boston, MA, USA), p. 103, 2012.

[62] W. Thiel, "Eine Arterienmasse zur Nachinjektion bei der Konservierung ganzer Leichen. [An arterial substance for subsequent injection during the preservation of the whole corpse]," *Ann Anat*, vol. 174, pp. 197–200, 1992.

[63] B. Prasad Rai, B. Tang, R. Eisma, R. W. Soames, H. Wen, and G. Nabi, "A qualitative assessment of human cadavers embalmed by Thiel's method used in laparoscopic training for renal resection.," *Anat Sci Educ*, vol. 5, no. 3, pp. 182–6, 2012.

[64] A. Bregy, A. Alfieri, S. Demertzis, P. Mordasini, A. K. Jetzer, D. Kuhlen, T. Schaffner, R. Dacey, H.-J. Steiger, and M. Reinert, "Automated end-to-side anastomosis to the middle cerebral artery: a feasibility study.," *J Neurosurg*, vol. 108, pp. 567–74, Mar. 2008.

[65] F. Hölzle, E.-P. Franz, J. Lehmbrock, S. Weihe, C. Teistra, H. Deppe, and K.-D. Wolff, "Thiel embalming technique: a valuable method for teaching oral surgery and implantology.," *Clin Implant Dent Relat Res*, vol. 14, pp. 121–6, Mar. 2012.

[66] G. McLeod, R. Eisma, A. Schwab, G. Corner, R. Soames, and S. Cochran, "An evaluation of Thiel-embalmed cadavers for ultrasound-based regional anaesthesia training and research," *Ultrasound*, vol. 18, pp. 125–9, July 2010.

[67] M. J. Gueorguieva, D. T. B. Yeo, R. Eisma, and A. Melzer, "MRI of Thiel-embalmed human cadavers," *J Magn Reson Imaging*, vol. 39, no. 3, pp. 576–83, 2014.

[68] R. Eisma, S. Mahendran, S. Majumdar, D. Smith, and R. W. Soames, "A comparison of Thiel and formalin embalmed cadavers for thyroid surgery training.," *Surgeon*, vol. 9, pp. 142–6, June 2011.

[69] M. Pendleton, B. F. Cox, T. Saliev, M. A. Rube, H. McLeod, and A. Melzer, "Imaging of vessel patency in Thiel embalmed liver," in *Fifth Image Guid Ther Work*, (Boston, MA, USA), p. 10, 2012.

[70] K. C. Wright, "Working with laboratory animals: general principles and practical considerations," *J Vasc Interv Radiol*, vol. 8, no. 3, pp. 363–373, 1997.

[71] P. Dunleavy, *Authoring a Ph.D.: How to plan, draft, write and finish a doctoral thesis Or dissertation*. Palgrave MacMillan, 2003.

[72] S. Patil, O. Bieri, and K. Scheffler, "Echo-dephased steady state free precession," *Magn Reson Mater Phys Biol Med*, pp. 277–85, 2009.

[73] J.-H. Seppenwoolde, R. O. Engberink, A. V. D. Toorn, E. L. Blezer, and C. J. Bakker, "Selective MRI of magnetically labeled cells a comparative evaluation of positive contrast techniques," in *Proc Intl Soc Mag Reson Med 14*, p. 360, 2006.

[74] S. Patil, *Passive tracking and system interfaces for interventional MRI*. Ph.d. dissertation, Universität Basel, Switzerland, Basel, 2009.

[75] H. H. Quick, M. O. Zenge, H. Kuehl, G. Kaiser, S. Aker, S. Massing, S. Bosk, and M. E. Ladd, "Interventional magnetic resonance angiography with no strings attached: wireless active catheter visualization," *Magn Reson Med*, vol. 53, pp. 446–55, Feb. 2005.

[76] J. P. Broderick, Y. Y. Palesch, A. M. Demchuk, S. D. Yeatts, P. Khatri, M. D. Hill, E. C. Jauch, T. G. Jovin, B. Yan, F. L. Silver, R. von Kummer, C. a. Molina, B. M. Demaerschalk, R. Budzik, W. M. Clark, O. O. Zaidat, T. W. Malisch, M. Goyal, W. J. Schonewille, M. Mazighi, S. T. Engelter, C. Anderson, J. Spilker, J. Carrozzella, K. J. Ryckborst, L. S. Janis, R. H. Martin, L. D. Foster, and T. a. Tomsick, "Endovascular therapy after intravenous t-PA versus t-PA alone for stroke.," *N Engl J Med*, vol. 368, pp. 893–903, Mar. 2013.

[77] A. L. Bartorelli and G. Marenzi, "Contrast-induced nephropathy.," *J Interv Cardiol*, vol. 21, pp. 74–85, Mar. 2008.

[78] L. Feng, C. L. Dumoulin, S. Dashnaw, R. D. Darrow, R. L. Delapaz, P. L. Bishop, and J. Pile-Spellman, "Feasibility of stent placement in carotid arteries with real-time MR imaging guidance in pigs.," *Radiology*, vol. 234, pp. 558–62, Feb. 2005.

[79] M. T. Vlaardingerbroek and J. A. Den Boer, *Magnetic resonance imaging - theory and practice*. Berlin, Heidelberg, New York: Springer-Verlag, 3 ed., 2003.

[80] C. Cohen-Tannoudji, B. Diu, and F. Laloë, *Quantum mechanics*. Wiley-VCH, volume 2 ed., 1991.

[81] J. Schenck, "The role of magnetic susceptibility in magnetic resonance imaging: MRI magnetic compatibility of the first and second kinds," *Med Phys*, vol. 23, no. 6, pp. 815–850, 1996.

[82] James Clerk Maxwell, *Treatise on electricity and magnetism*. Oxford: Clarendon Press, 1873.

[83] A. Kumar, D. Welti, and R. R. Ernst, "NMR Fourier zeugmatography," *J Magn Reson*, vol. 18, pp. 69–83, Apr. 1975.

[84] B. J. W. Cooley and J. W. Tukey, "An algorithm for the machine calculation of complex Fourier series," *Math Comput*, vol. 19, no. 90, pp. 297–301, 1965.

[85] E. Hahn, "Spin Echoes," *Phys Rev*, vol. 80, pp. 580–94, Nov. 1950.

[86] A. Haase, J. Frahm, D. Matthaei, W. Hänike, and K. D. Merboldt, "FLASH Imaging. Rapid NMR Imaging Using Low Flip-Angle Pulses," *J Magn Reson*, vol. 67, no. 2, pp. 258–66, 1986.

[87] E. Spouse and W. M. Gedroyc, "MRI of the claustrophobic patient: interventionally configured magnets.," *Br J Radiol*, vol. 73, pp. 146–51, Feb. 2000.

[88] S. W. Gould, G. Lamb, D. Lomax, W. Gedroyc, and a. Darzi, "Interventional MR-guided excisional biopsy of breast lesions.," *J Magn Reson Imaging*, vol. 8, no. 1, pp. 26–30, 1998.

[89] A. Savnik, H. Malmskov, H. Thomsen, T. Bretlau, L. Bjerglund Graff, H. Nielsen, B. Danneskiold-Samsø e, J. Boesen, and H. Bliddal, "MRI of the arthritic small joints: comparison of extremity MRI (0.2 T) vs high-field MRI (1.5 T)," *Eur Radiol*, vol. 11, pp. 1030–38, May 2001.

[90] S. Zangos, K. Eichler, K. Engelmann, M. Ahmed, S. Dettmer, C. Herzog, W. Pegios, a. Wetter, T. Lehnert, M. G. Mack, and T. J. Vogl, "MR-guided transgluteal biopsies with an open low-field system in patients with clinically suspected prostate cancer: technique and preliminary results.," *Eur Radiol*, vol. 15, pp. 174–82, Jan. 2005.

[91] S. Zangos, T. Vetter, F. Huebner, M. Tuwari, F. Mayer, K. Eichler, M.-L. Hansmann, a. Wetter, C. Herzog, and T. J. Vogl, "MR-guided biopsies with a newly designed cordless coil in an open low-field system: initial findings.," *Eur Radiol*, vol. 16, pp. 2044–50, Sept. 2006.

[92] L. W. Bartels and C. J. G. Bakker, "Endovascular interventional magnetic resonance imaging.," *Phys Med Biol*, vol. 48, pp. R37–64, July 2003.

[93] C. M. Kramer, J. Barkhausen, S. D. Flamm, R. J. Kim, and E. Nagel, "Standardized cardiovascular magnetic resonance (CMR) protocols 2013 update.," *J Cardiovasc Magn Reson*, vol. 15, p. 91, Oct. 2013.

[94] D. T. Boll, J. S. Lewin, J. L. Duerk, A. J. Aschoff, and E. M. Merkle, "Comparison of MR imaging sequences for liver and head and neck interventions: is there a single optimal sequence for all purposes?," *Acad Radiol*, vol. 11, pp. 506–15, May 2004.

[95] A. Oppelt, R. Graumann, H. Barfuß, H. Fischer, W. Hartl, and W. Schajor, "FISP: eine neue schnelle pulssequenz für die kernspintomographie," *Electromedica*, vol. 54, pp. 15–8, 1986.

[96] M. Deimling and O. Heid, "Magnetization prepared true FISP imaging," in *Proc Intl Soc Mag Reson Med 2*, (San Francisco, CA, USA), p. 495, 1994.

[97] J. L. Duerk, J. S. Lewin, M. Wendt, and C. Petersilge, "Remember true FISP? A high SNR, near 1-second imaging method for T2-like contrast in interventional MRI at .2 T," *J Magn Reson Imaging*, vol. 8, no. 1, pp. 203–8, 1998.

[98] J. L. Duerk, J. S. Lewin, and D. H. Wu, "Application of keyhole imaging to interventional MRI: A simulation study to predict sequence requirements," *J Magn Reson Imaging*, vol. 6, pp. 9178–24, 1996.

[99] T. B. Parrish and X. Hu, "Hybrid technique for dynamic imaging.," *Magn Reson Med*, vol. 44, pp. 51–5, July 2000.

[100] M. a. Bernstein, S. B. Fain, and S. J. Riederer, "Effect of windowing and zero-filled reconstruction of MRI data on spatial resolution and acquisition strategy.," *J Magn Reson Imaging*, vol. 14, pp. 270–80, Oct. 2001.

[101] M. von Siebenthal, G. Székely, U. Gamper, P. Boesiger, A. Lomax, and P. Cattin, "4D MR imaging of respiratory organ motion and its variability.," *Phys Med Biol*, vol. 52, pp. 1547–64, Mar. 2007.

[102] B. Kiefer, J. Grassner, and R. Hausman, "Image acquisition in a second with half Fourier acquisition single-shot turbo spin-echo," *J Magn Reson Imaging*, vol. 4, no. Suppl. P, pp. 86–7, 1994.

[103] H. Zimmermann, S. Müller, B. Gutmann, H. Bardenheuer, A. Melzer, R. Umathum, W. Nitz, W. Semmler, and M. Bock, "Targeted-HASTE imaging with automated device tracking for MR-guided needle interventions in closed-bore MR systems.," *Magn Reson Med*, vol. 56, pp. 481–8, Sept. 2006.

[104] C. J. Das, A. H. Goenka, and D. N. Srivastava, "MR-guided abdominal biopsy using a 1.5-Tesla closed system: a feasibility study," *Abdom Imaging*, vol. 35, pp. 218–23, 2009.

[105] M. Moche, R. Trampel, T. Kahn, and H. Busse, "Navigation concepts for MR image-guided interventions," *J Magn Reson Imaging*, vol. 27, pp. 276–91, Feb. 2008.

[106] M. Bock and F. Wacker, "Interventional MR imaging," in *Clin Blood Pool MR Imaging* (T. Leiner, M. Goyen, M. Rohrer, and S. Schönberg, eds.), ch. 19, pp. 207–18, Heidelberg: Springer Medizin Verlag, 2008.

[107] R. Matsumoto, K. Oshio, and F. A. Jolesz, "Monitoring of laser and freezinginduced ablation in the liver with T1-weighted MR imaging," *J Magn Reson Imaging*, vol. 2, no. 5, pp. 555–62, 1992.

[108] T. J. Vogl, N. Weinhold, P. Müller, C. Phillip, A. Roggan, M. Mack, J. Balzer, H. Eichstädt, G. Blumhardt, H. Lobeck, and R. Felix, "Early clinical experiences with MR-guided laser-induced thermotherapy (LITT) of liver metastases in preoperative care," *Roefo*, vol. 164, no. 5, pp. 413–21, 1996.

[109] S. Gould, N. Vaughan, W. Gedroyc, G. Lamb, R. Goldin, and A. Darzi, "Monitoring of interstitial laser thermotherapy with heat-sensitive colour subtraction magnetic resonance imaging: Calibration with absolute tissue temperature and correlation with predicted lesion size," *Lasers Med Sci*, vol. 14, pp. 250–6, Dec. 1999.

[110] D. S. Lu, S. Sinha, J. Lucas, K. Farahani, R. Lufkin, and K. Lewin, "MR-guided percutaneous ethanol ablation of liver tissue in a 0.2-T open MR system: preliminary study in porcine model.," *J Magn Reson Imaging*, vol. 7, no. 2, pp. 303–8, 1997.

[111] S. Zangos, K. Eichler, a. Wetter, T. Lehnert, R. Hammerstingl, T. Diebold, P. Reichel, C. Herzog, M.-L. Hansmann, M. G. Mack, and T. J. Vogl, "MR-guided biopsies of lesions in the retroperitoneal space: technique and results.," *Eur Radiol*, vol. 16, pp. 307–12, Feb. 2006.

[112] P. Law, W. M. Gedroyc, and L. Regan, "Magnetic resonance-guided percutaneous laser ablation of uterine fibroids.," *J Magn Reson Imaging*, vol. 12, pp. 565–70, Oct. 2000.

[113] E. Dick, R. Joarder, M. de Jode, S. Taylor-Robinson, H. Thomas, G. Foster, and W. Gedroyc, "MR-guided laser thermal ablation of primary and secondary liver tumours," *Clin Radiol*, vol. 58, pp. 112–120, Feb. 2003.

[114] J. Stattaus, S. Maderwald, H. a. Baba, G. Gerken, J. Barkhausen, M. Forsting, and M. E. Ladd, "MR-guided liver biopsy within a short, wide-bore 1.5 Tesla MR system.," *Eur Radiol*, vol. 18, pp. 2865–73, Dec. 2008.

[115] S. Zangos, C. Herzog, K. Eichler, R. Hammerstingl, A. Lukoschek, S. Guthmann, B. Gutmann, U. J. Schoepf, P. Costello, and T. J. Vogl, "MR-compatible assistance system for punction in a high-field system," *Eur Radiol*, vol. 17, pp. 1118–24, 2007.

[116] A. Melzer, B. Gutmann, T. Remmele, R. Wolf, A. Lukoscheck, M. Bock, H. Bardenheuer, and H. Fischer, "INNOMOTION for percutaneous image-guided interventions: Principles

and evaluation of this MR- and CT-compatible robotic system.," *IEEE Eng Med Biol Mag*, vol. 27, no. 3, pp. 66–73, 2008.

[117] M. G. Schouten, J. G. R. Bomers, D. Yakar, H. Huisman, E. Rothgang, D. Bosboom, T. W. J. Scheenen, S. Misra, and J. J. Fütterer, "Evaluation of a robotic technique for transrectal MRI-guided prostate biopsies.," *Eur Radiol*, vol. 22, pp. 476–83, Feb. 2012.

[118] C. J. Martin, "A review of radiology staff doses and dose monitoring requirements.," *Radiat Prot Dosim*, vol. 136, pp. 140–57, Sept. 2009.

[119] J. D. Mathews, a. V. Forsythe, Z. Brady, M. W. Butler, S. K. Goergen, G. B. Byrnes, G. G. Giles, a. B. Wallace, P. R. Anderson, T. a. Guiver, P. McGale, T. M. Cain, J. G. Dowty, a. C. Bickerstaffe, and S. C. Darby, "Cancer risk in 680 000 people exposed to computed tomography scans in childhood or adolescence: data linkage study of 11 million Australians," *BMJ*, vol. 346:f2360, May 2013.

[120] S. G. Hushek, A. J. Martin, M. Steckner, E. Bosak, J. Debbins, and W. Kucharzyk, "MR systems for MRI-guided interventions," *J Magn Reson Imaging*, vol. 27, pp. 253–266, Mar. 2008.

[121] R. Wyttenbach, A. Gallino, M. Alerci, F. Mahler, L. Cozzi, M. Di Valentino, J. J. Badimon, V. Fuster, and R. Corti, "Effects of percutaneous transluminal angioplasty and endovascular brachytherapy on vascular remodeling of human femoropopliteal artery by noninvasive magnetic resonance imaging.," *Circulation*, vol. 110, pp. 1156–61, Aug. 2004.

[122] S. I. Seldinger, "Catheter replacement of the needle in percutaneous arteriography: A new technique," *Acta Radiol [Old Ser*, vol. 39, pp. 368–76, May 1953.

[123] R. Razavi, D. Hill, S. Keevil, M. Miquel, V. Muthurangu, S.Hegde, K. Rhode, M. Barnett, J. van Vaals, D. Hawkes, and E. Baker, "Cardiac catheterisation guided by MRI in children and adults with congenital heart disease," *Lancet*, vol. 362, pp. 1877–82, 2003.

[124] E. Immel and A. Melzer, "Improvement of the MR imaging behavior of vascular implants.," *Minim Invasive Ther Allied Technol*, vol. 15, pp. 85–92, Jan. 2006.

[125] N. A. Kraemer, E. Immel, H. C. W. Donker, C. Ocklenburg, and R. W. Guenther, "Evaluation of an active vena cava filter for mr imaging in a swine model," *Radiology*, vol. 258, no. 2, pp. 446–54, 2011.

[126] A. Bücker, J. M. Neuerburg, G. Adam, A. Glowinski, J. J. van Vaals, and R. W. Günther, "MR-guided coil embolisation of renal arteries in an animal model," *Roefo*, vol. 175, pp. 271–4, Feb. 2003.

[127] F. G. Shellock, T. O. Woods, and J. V. Crues, "MR labeling information for implants and devices: explanation of terminology.," *Radiology*, vol. 253, pp. 26–30, Oct. 2009.

[128] ASTM International, "F2213-06: Standard test method for measurement of magnetically induced torque on medical devices in the magnetic resonance environment," 2006.

[129] ASTM International, "F2052-06: Standard test method for measurement of magnetically induced displacement force on medical devices in the magnetic resonance environment," 2006.

[130] I. S. Organization, "ISO/TS 10974:2012. Requirements for the safety and compatibility of magnetic resonance imaging for patients with an active implantable medical device," 2012.

[131] G. S. Fischer, A. Deguet, C. Csoma, R. H. Taylor, L. Fayad, J. A. Carrino, S. J. Zinreich, and G. Fichtinger, "MRI image overlay: application to arthrography needle insertion.," *Comput Aided Surg*, vol. 12, pp. 2–14, Jan. 2007.

[132] S. K. Neequaye, R. Aggarwal, I. Van Herzeele, A. Darzi, and N. J. Cheshire, *Endovascular skills training and assessment*, vol. 46. Informa Healthcare, Nov. 2007.

[133] M. E. Ladd, M. G. G. Zirnrnerrnann, H. H. Quick, M. S. J. F. Debatin, P. Boesiger, G. K. V. Schulthess, and G. C. Mckinnon, "Active MR visualization of a vascular guidewire in vivo," *J Magn Reson Imaging*, vol. 8, pp. 220–5, 1998.

[134] M. Wolska-Krawczyk, M. A. Rube, E. Immel, A. Melzer, and A. Buecker, "Heating and safety of a new MR-compatible guidewire prototype versus a standard nitinol guidewire.," *Radiol Phys Technol*, vol. 7, pp. 95–101, Jan. 2014.

[135] S. Kos, R. Huegli, E. Hofmann, H. H. Quick, H. Kuehl, S. Aker, G. M. Kaiser, P. J. a. Borm, A. L. Jacob, and D. Bilecen, "MR-compatible polyetheretherketone-based guide wire assisting MR-guided stenting of iliac and supraaortic arteries in swine: feasibility study.," *Minim Invasive Ther Allied Technol*, vol. 18, pp. 181–8, Jan. 2009.

[136] N. A. Krämer, S. Krüger, S. Schmitz, M. Linssen, H. Schade, S. Weiss, E. Spüntrup, R. W. Günther, A. Bücker, and G. A. Krombach, "Preclinical evaluation of a novel fiber compound MR Gguidewire in vivo," *Invest Radiol*, vol. 44, no. 7, pp. 390–397, 2009.

[137] A. Tzifa, G. a. Krombach, N. Krämer, S. Krüger, A. Schütte, M. von Walter, T. Schaeffter, S. Qureshi, T. Krasemann, E. Rosenthal, C. a. Schwartz, G. Varma, A. Buhl, A. Kohlmeier, A. Bücker, R. W. Günther, and R. Razavi, "Magnetic resonance-guided cardiac interventions using magnetic resonance-compatible devices: a preclinical study and first-in-man congenital interventions.," *Circ Cardiovasc Interv*, vol. 3, pp. 585–92, Dec. 2010.

[138] M. A. Rube, P. Seifert, U. Bernhard, D. Kakchingtabam, P. Andre, and A. Melzer, "Novel MR-safe guidewire with passive Iron-Platinum alloy nanoparticles for MR-guided interventions," in *Proc Intl Soc Mag Reson Med 20*, (Melbourne), p. 4239, 2012.

[139] O. Kocaturk, A. H. Kim, C. E. Saikus, M. a. Guttman, A. Z. Faranesh, C. Ozturk, and R. J. Lederman, "Active two-channel 0.035" guidewire for interventional cardiovascular MRI.," *J Magn Reson Imaging*, vol. 30, pp. 461–5, Aug. 2009.

[140] M. Sonmez, C. E. Saikus, J. a. Bell, D. N. Franson, M. Halabi, A. Z. Faranesh, C. Ozturk, R. J. Lederman, and O. Kocaturk, "MRI active guidewire with an embedded temperature probe and providing a distinct tip signal to enhance clinical safety.," *J Cardiovasc Magn Reson*, vol. 14, p. 38, Jan. 2012.

[141] International Electrotechnical Commission (IEC), "IEC 60601-2-33 Ed. 3.0 B: Medical electrical equipment - Part 2-33: - Part 2-33: Particular requirements for the basic safety and essential performance of magnetic resonance equipment for medical diagnosis," 2010.

[142] D. Rubin, A. Ratner, and S. Young, "Magnetic susceptibility effects and their application in the developement of new ferromagnetic catheters for magnetic resonance imaging," *Invest Radiol*, vol. 12, no. 25, pp. 1325–32, 1990.

[143] C. J. Bakker, R. M. Hoogeveen, J. Weber, J. J. van Vaals, M. a. Viergever, and W. P. Mali, "Visualization of dedicated catheters using fast scanning techniques with potential for MR-guided vascular interventions.," *Magn Reson Med*, vol. 36, pp. 816–20, Dec. 1996.

[144] O. Unal, F. R. Korosec, R. Frayne, C. M. Strother, and C. A. Mistretta, "A rapid 2D time-resolved variable-ratek-space sampling MR technique for passive catheter tracking during endovascular procedures," *Magn Reson Med*, vol. 40, pp. 356–362, Sept. 1998.

[145] M. Burl, G. a. Coutts, and I. R. Young, "Tuned fiducial markers to identify body locations with minimal perturbation of tissue magnetization.," *Magn Reson Med*, vol. 36, pp. 491–3, Sept. 1996.

[146] C. L. Dumoulin, S. P. Souza, and R. D. Darrow, "Real-time position monitoring of invasive devices using magnetic resonance.," *Magn Reson Med*, vol. 29, pp. 411–5, Mar. 1993.

[147] O. Unal, J. Li, W. Cheng, H. Yu, and C. M. Strother, "MR-visible coatings for endovascular device visualization.," *J Magn Reson Imaging*, vol. 23, pp. 763–9, May 2006.

[148] M. A. Rube, P. Samraj, E. Immel, P. Andre, and A. Melzer, "MRI visible FePt - nanoparticles for catheter localization in 1.5T," in *Proc 10th Sci Meet United Kingdom Radiol Congr*, (Manchester, UK), 2011.

[149] S. Patil, O. Bieri, P. Jhooti, and K. Scheffler, "Automatic slice positioning (ASP) for passive real-time tracking of interventional devices using projection-reconstruction imaging with echo-dephasing (PRIDE).," *Magn Reson Med*, vol. 62, pp. 935–42, Oct. 2009.

[150] T. Leiner, M. Goyen, M. Rohrer, and S. Schönberg, *Clinical bloodpool MR imaging*. Heidelberg: Springer Medizin Verlag, 2008.

[151] J.-H. Seppenwoolde, M. a. Viergever, and C. J. G. Bakker, "Passive tracking exploiting local signal conservation: the white marker phenomenon.," *Magn Reson Med*, vol. 50, pp. 784–90, Oct. 2003.

[152] D. A. Yablonskiy and E. M. Haacke, "Theory of NMR signal behavior in magnetically inhomogeneous tissues: The static dephasing regime," *Magn Reson Med*, vol. 32, pp. 749–763, Dec. 1994.

[153] J. M. Peeters, J.-H. Seppenwoolde, L. W. Bartels, and C. J. G. Bakker, "Development and testing of passive tracking markers for different field strengths and tracking speeds.," *Phys Med Biol*, vol. 51, pp. N127–37, Mar. 2006.

[154] C. H. Cunningham, T. Arai, P. C. Yang, M. V. McConnell, J. M. Pauly, and S. M. Conolly, "Positive contrast magnetic resonance imaging of cells labeled with magnetic nanoparticles.," *Magn Reson Med*, vol. 53, pp. 999–1005, May 2005.

[155] M. Stuber, W. D. Gilson, M. Schär, D. a. Kedziorek, L. V. Hofmann, S. Shah, E.-J. Vonken, J. W. M. Bulte, and D. L. Kraitchman, "Positive contrast visualization of iron oxide-labeled stem cells using inversion-recovery with ON-resonant water suppression (IRON).," *Magn Reson Med*, vol. 58, pp. 1072–7, Nov. 2007.

[156] J.-H. Seppenwoolde, K. L. Vincken, and C. J. G. Bakker, "White-marker imaging–separating magnetic susceptibility effects from partial volume effects.," *Magn Reson Med*, vol. 58, pp. 605–9, Sept. 2007.

[157] M. Bock, S. Volz, S. Zühlsdorff, R. Umathum, C. Fink, P. Hallscheidt, and W. Semmler, "MR-guided intravascular procedures: real-time parameter control and automated slice positioning with active tracking coils.," *J Magn Reson Imaging*, vol. 19, pp. 580–9, May 2004.

[158] M. E. Ladd and H. H. Quick, "Reduction of resonant RF heating in intravascular catheters using coaxial chokes.," *Magn Reson Med*, vol. 43, pp. 615–9, Apr. 2000.

[159] S. Weiss, P. Vernickel, T. Schaeffter, V. Schulz, and B. Gleich, "Transmission line for improved RF safety of interventional devices.," *Magn Reson Med*, vol. 54, pp. 182–9, July 2005.

[160] A. B. Holbrook, P. Ghanouni, J. M. Santos, Y. Medan, and K. B. Pauly, "In vivo MR acoustic radiation force imaging in the porcine liver," *Med Phys*, vol. 38, no. 9, pp. 5081–9, 2011.

[161] A. Melzer and M. Busch, "MR imaging method and medical device for use in method," 2005.

[162] M. Tooley, *Electronic circuits - fundamentals & applications*. Routledge, third edit ed., 2006.

[163] J. S. McLean, "A re-examination of the fundamental limits on the radiation Q of electrically small antennas," *IEEE Trans Antennas Propag*, vol. 44, p. 672, May 1996.

[164] M. Kaiser, M. Detert, M. A. Rube, A. Eldirdiri, O. J. Elle, A. Melzer, B. Schmidt, and G. Rose, "Resonant marker design and fabrication techniques for device visualization during interventional magnetic resonance imaging," *Biomed Tech*, p. [in review], 2013.

[165] S. Chen, L. Wang, S. L. Duce, S. Brown, S. Lee, A. Melzer, S. A. Cuschieri, and P. Andre, "Engineered biocompatible nanoparticles for in vivo imaging applications," *J Am Chem Soc*, vol. 132, no. 16, pp. 15022–15029, 2010.

[166] M. Hofmann-Rechenberg, B. Amtenbrink, and H. Hofmann, "Superparamagnetic nanoparticles for biomedical applications," in *Nanostructured Mater Biomed Appl* (M. C. Tan, ed.), vol. 65, ch. 5, pp. 119–49, Transworld Research Network, May 2009.

[167] M. A. Rube, B. F. Cox, M. Gueorguieva, D. Kakchingtabam, P. Andre, and A. Melzer, "Iron-Platinum alloy nanoparticles for guidewire and resonant markers for catheter localization during interventional MRI.," *Biomed Tech*, vol. 57, p. 4397, Aug. 2012.

[168] C. H. Cunningham, J. M. Pauly, and K. S. Nayak, "Saturated double-angle method for rapid B1+ mapping.," *Magn Reson Med*, vol. 55, pp. 1326–33, June 2006.

[169] R. Eisma, C. Lamb, and R. W. Soames, "From formalin to thiel embalming: What changes? One anatomy department's experiences.," *Clin Anat*, vol. 26, pp. 564–71, July 2013.

[170] S. Weiss, T. Kuehne, and M. Zenge, "Switchable resonant fiducial marker for safe instrument localisation at all marker orientations," in *Proc Intl Soc Mag Reson Med 10*, vol. 544, p. 22335, 2002.

[171] T. Kuehne, R. Fahrig, and K. Butts, "Pair of resonant fiducial markers for localization of endovascular catheters at all catheter orientations.," *J Magn Reson Imaging*, vol. 17, pp. 620–624, May 2003.

[172] J. Krug, K. Will, and G. Rose, "Simulation and experimental validation of resonant electric markers used for medical device tracking in magnetic resonance imaging.," in *IEEE Eng Med Biol Soc*, vol. 2010, (Buenos Aires, Argentina), pp. 1878–81, Jan. 2010.

[173] A. B. Holbrook, M. A. Rube, A. Melzer, and K. Butts Pauly, "Interventional MRI from the Internet Browser," in *Proc 9th Inteventional MRI Symp* (T. Kapur, F. A. Jolesz, J. Lewin, and T. Kahn, eds.), (Boston, MA, USA), p. 114, 2012.

[174] P. Mc Laughlin, S. O. Neill, N. Fanning, A. M. Mc Garrigle, O. J. O. Connor, G. Wyse, and M. M. Maher, "Emergency CT brain: preliminary interpretation with a tablet device: image quality and diagnostic performance of the Apple iPad," *Emerg Radiol*, vol. 19, pp. 127–33, Dec. 2011.

[175] S. John, A. C. C. Poh, T. C. C. Lim, E. H. Y. Chan, and L. R. Chong, "The iPad tablet computer for mobile on-call radiology diagnosis? Auditing discrepancy in CT and MRI reporting," *J Digit Imaging*, vol. 25, pp. 628–34, Oct. 2012.

[176] A. B. Holbrook, R. D. Watkins, and K. B. Pauly, "Interactive interventional applications for the MRI scan room," in *Proc Intl Soc Mag Reson Med 20*, (Melbourne, Australia), p. 2954, 2012.

[177] A. B. Holbrook and K. Butts Pauly, "Collaborative MRI for improving patient throughput," in *Proc Intl Soc Mag Reson Med 20*, (Melbourne, Australia), p. 2956, 2012.

[178] Y. Zur, M. L. Wood, and L. J. Neuringer, "Spoiling of transverse magnetization in steady-state sequences," *Magn Reson Med*, vol. 21, pp. 251–263, Oct. 1991.

[179] Y. C. Chung, E. M. Merkle, J. S. Lewin, J. R. Shonk, and J. L. Duerk, "Fast T2-weighted imaging by PSIF at 0.2 T for interventional MRI.," *Magn Reson Med*, vol. 42, pp. 335–44, Aug. 1999.

[180] J. Jussila, "Preparing ballistic gelatine–review and proposal for a standard method," *Forensic Sci Int*, vol. 141, pp. 91–8, May 2004.

[181] T. Richardson, Q. Stafford-Fraser, K. Wood, and A. Hopper, "Virtual network computing," *IEEE Internet Comput*, vol. 2, no. 1, pp. 33–8, 1998.

[182] J. Stattaus, S. Maderwald, M. Forsting, J. Barkhausen, and M. E. Ladd, "MR-Guided core biopsy with MR fluoroscopy using a short, wide-bore 1.5-Tesla scanner: Feasibility and initial results," *J Magn Reson Imaging*, vol. 27, pp. 1181–7, 2008.

[183] I. Hancu, K. Park, and R. Darrow, "A landmark-free MRI scanner concept," in *Proc Intl Soc Mag Reson Med 20*, (Melbourne, Australia), p. 2744, 2012.

[184] F. Fernández-Gutiérrez, I. Barnett, B. Taylor, G. Houston, and A. Melzer, "Framework for detailed workflow analysis and modelling for simulation of multi-modal image-guided interventions," *J Enterp Inf Manag*, vol. 26, no. 1, pp. 75–90, 2013.

[185] C. L. Dumoulin, R. P. Mallozzi, R. D. Darrow, and E. J. Schmidt, "Phase-field dithering for active catheter tracking.," *Magn Reson Med*, vol. 63, pp. 1398–403, May 2010.

[186] W. R. Nitz, G. Brinker, D. Diehl, and G. Frese, "Specific absorption rate as a poor indicator of magnetic resonance-related implant heating.," *Invest Radiol*, vol. 40, pp. 773–6, Dec. 2005.

[187] D. Brujic, F. Galassi, M. Rea, and M. Ristic, "A novel algorithm for fast 3D localisation of N fiducial markers from 1D projections," in *Proc Intl Soc Mag Reson Med 20*, p. 2946, 2012.

[188] S. Weiss, T. Schaeffter, K. M. Luedeke, C. Leussler, D. Holz, K. Nehrke, V. Rasche, and R. Sinkus, "Catheter localization using a resonant fiducial marker during interactive MR fluoroscopy," in *Proc Intl Soc Mag Reson Med 7*, (Philadelphia, PA, USA), p. 1954, 1999.

[189] W. T. Dixon, L. N. Du, D. D. Faul, M. Gado, and S. Rossnick, "Projection angiograms of blood labeled by adiabatic fast passage," *Magn Reson Med*, vol. 3, pp. 454–462, June 1986.

[190] J. N. Draper, M. L. Lauzon, and R. Frayne, "Passive catheter visualization in magnetic resonance guided endovascular therapy using multicycle projection dephasers," *J Magn Reson Imaging*, vol. 24, pp. 160–7, 2006.

[191] A. Haase, J. Frahm, K. Merboldt, and W. Hanicke, "Direct FLASH MR imaging of magnetic field inhomogeneities by gradient compensation," *Magn Reson Med*, vol. 6, pp. 474–480, 1988.

[192] P. Le Roux, "Simplified model and stabilization of SSFP sequences," *J Magn Reson*, vol. 163, pp. 23–37, July 2003.

[193] R. F. Busse and S. J. Riederer, "Steady-state preparation for spoiled gradient echo imaging.," *Magn Reson Med*, vol. 45, pp. 653–61, Apr. 2001.

[194] D. G. Nishimura, "Time-of-flight MR angiography.," *Magn Reson Med*, vol. 14, pp. 194–201, May 1990.

[195] T. Wech, S. M. Shea, L. Pan, J. Barbot, K. Vij, C. H. Lorenz, and S. Patil, "Measurement accuracy of different active tracking sequences for interventional MRI," in *Proc Intl Soc Mag Reson Med 19*, vol. 19, (Montreal, Quebec, Canada), p. 1753, 2011.

[196] M. F. Dempsey, B. Condon, and D. M. Hadley, "Investigation of the factors responsible for burns during MRI.," *J Magn Reson Imaging*, vol. 13, pp. 627–31, Apr. 2001.

[197] D. Leung, J. F. Debatin, S. Wildermuth, G. C. Mckinnon, D. J. Holtz, C. L. Dumoulin, R. D. Darrow, E. Hofmann, and G. K. von Schulthess, "Intravascular MR tracking catheter preliminary experimental evaluation," *AJR Am J Roentgenol*, vol. 164, pp. 1265–1270, 1995.

[198] C. M. Hillenbrand, D. R. Elgort, E. Y. Wong, A. Reykowski, F. K. Wacker, J. S. Lewin, and J. L. Duerk, "Active device tracking and high-resolution intravascular MRI using a novel catheter-based, opposed-solenoid phased array coil.," *Magn Reson Med*, vol. 51, pp. 668–75, Apr. 2004.

[199] H. H. Quick, H. Kuehl, G. Kaiser, S. Bosk, J. F. Debatin, and M. E. Ladd, "Inductively coupled stent antennas in MRI.," *Magn Reson Med*, vol. 48, pp. 781–90, Nov. 2002.

[200] M. Detert, S. Friesecke, M. Deckert, G. Rose, B. Schmidt, and M. Kaiser, "Using the hot embossing technology for the realization of microtechnical structures in medical imaging," *Biomed Tech*, vol. 57, pp. 599–602, Aug. 2012.

[201] M. Kaiser, M. Detert, B. Schmidt, and G. Rose, "Technology Matrix: Production technologies of miniature instrument resonance markers for visualization under MRI,," in *Congr MedTech Pharma*, (Nuremberg, Germany), 2012.

[202] Y. P. Du, D. L. Parker, W. L. Davis, and G. Cao, "Reduction of partial-volume artifacts with zero-filled interpolation in three-dimensional MR angiography," *J Magn Reson Imaging*, vol. 4, pp. 733–41, Sept. 1994.

[203] H. Chandarana, A. B. Rosenkrantz, R. P. Lim, D. Kim, D. I. Mossa, K. Arhakis, B. Kiefer, T. K. Block, and V. S. Lee, "Radial k-space sampling for 3D fat-suppressed contrast-enhanced imaging of the liver during free breathing," in *Proc Intl Soc Mag Reson Med 19*, vol. 15, p. 2942, 2011.

[204] K. T. Block, M. Uecker, and J. Frahm, "Undersampled radial MRI with multiple coils. Iterative image reconstruction using a total variation constraint.," *Magn Reson Med*, vol. 57, pp. 1086–98, June 2007.

[205] S. Zhang, K. T. Block, and J. Frahm, "Magnetic resonance imaging in real time: advances using radial FLASH.," *J Magn Reson Imaging*, vol. 31, pp. 101–9, Jan. 2010.

[206] T. Brott and J. Bogousslavsky, "Treatment of acute ischemic stroke," *N Engl J Med*, vol. 343, pp. 710–22, Sept. 2000.

[207] R. G. González, J. A. Hirsch, W. Koroshetz, M. H. Lev, and P. W. Schaefer, *Acute Ischemic Stroke*. Berlin/Heidelberg: Springer-Verlag, 2006.

[208] E. C. Jauch, J. L. Saver, H. P. Adams, A. Bruno, J. J. B. Connors, B. M. Demaerschalk, P. Khatri, P. W. McMullan, A. I. Qureshi, K. Rosenfield, P. a. Scott, D. R. Summers, D. Z. Wang, M. Wintermark, and H. Yonas, "Guidelines for the early management of patients with acute ischemic stroke: a guideline for healthcare professionals from the American Heart Association/American Stroke Association.," *Stroke*, vol. 44, pp. 870–947, Mar. 2013.

[209] W. Hacke, "Intravenous thrombolysis with recombinant tissue plasminogen activator for acute hemispheric stroke," *JAMA*, vol. 274, p. 1017, Oct. 1995.

[210] W. Hacke, M. Kaste, C. Fieschi, R. von Kummer, A. Davalos, D. Meier, V. Larrue, E. Bluhmki, S. Davis, G. Donnan, D. Schneider, E. Diez-Tejedor, and P. Trouillas, "Randomised double-blind placebo-controlled trial of thrombolytic therapy with intravenous alteplase in acute ischaemic stroke (ECASS II)," *Lancet*, vol. 352, pp. 1245–1251, Oct. 1998.

[211] A. Furlan, R. Higashida, L. Wechsler, M. Gent, H. Rowley, C. Kase, M. Pessin, A. Ahuja, F. Callahan, W. M. Clark, F. Silver, and F. Rivera, "Intra-arterial prourokinase for acute ischemic stroke," *JAMA*, vol. 282, pp. 2003–11, Dec. 1999.

[212] S. T. S. Troke and S. T. G. Roup, "Tissue plasminogen activator for acute ischemic stroke," *N Engl J Med*, vol. 333, no. 24, pp. 1581–7, 1995.

[213] P. P. Ng, R. T. Higashida, S. P. Cullen, R. Malek, C. F. Dowd, and V. V. Halbach, "Intraarterial thrombolysis trials in acute ischemic stroke," *J Vasc Interv Radiol*, vol. 15, pp. S77–S85, Jan. 2004.

[214] G. Avenue, "The interventional management of stroke (IMS) II study.," *Stroke*, vol. 38, pp. 2127–35, July 2007.

[215] P. Khatri, T. Abruzzo, S. D. Yeatts, C. Nichols, J. P. Broderick, and T. a. Tomsick, "Good clinical outcome after ischemic stroke with successful revascularization is time-dependent.," *Neurology*, vol. 73, pp. 1066–72, Sept. 2009.

[216] P. Khatri, M. D. Hill, Y. Y. Palesch, J. Spilker, E. C. Jauch, J. A. Carrozzella, A. M. Demchuk, R. Martin, P. Mauldin, C. Dillon, K. J. Ryckborst, S. Janis, T. A. Tomsick, and J. P. Broderick, "Clinical trial protocols methodology of the interventional management of stroke III trial," *Int J Stroke Vol*, vol. 3, no. May, pp. 130–7, 2008.

[217] J. P. Broderick and P. M. Meyers, "Acute stroke therapy at the crossroads.," *JAMA*, vol. 306, pp. 2026–8, Nov. 2011.

[218] T. Tomsick, J. Broderick, J. Carrozella, P. Khatri, M. Hill, Y. Palesch, and J. Khoury, "Revascularization results in the Interventional Management of Stroke II trial.," *AJNR Am J Neuroradiol*, vol. 29, pp. 582–7, Mar. 2008.

[219] P. D. Schellinger, J. B. Fiebach, O. Jansen, P. a. Ringleb, a. Mohr, T. Steiner, S. Heiland, S. Schwab, O. Pohlers, H. Ryssel, B. Orakcioglu, K. Sartor, and W. Hacke, "Stroke magnetic resonance imaging within 6 hours after onset of hyperacute cerebral ischemia.," *Ann Neurol*, vol. 49, pp. 460–9, Apr. 2001.

[220] G. W. Albers, "Expanding the window for thrombolytic therapy in acute stroke: The potential role of acute MRI for patient selection," *Stroke*, vol. 30, pp. 2230–2237, Oct. 1999.

[221] P. R. Moran, "A flow velocity zeugmatographic interface for NMR imaging in humans.," *Magn Reson Imaging*, vol. 1, pp. 197–203, 1982.

[222] L. A. Gillan, "Blood supply to brains of ungulates with and without a rete mirabile caroticum.," *J Comp Neurol*, vol. 153, pp. 275–90, Feb. 1974.

[223] M. Wintermark, S. Arora, E. Tong, E. Vittinghoff, B. C. Lau, J. D. Chien, W. P. Dillon, and D. Saloner, "Carotid plaque computed tomography imaging in stroke and nonstroke patients.," *Ann Neurol*, vol. 64, pp. 149–57, Aug. 2008.

[224] J. F. Schenck, "Safety of strong, static magnetic fields.," *J Magn Reson Imaging*, vol. 12, pp. 2–19, July 2000.

[225] T. O. Woods, "Standards for medical devices in MRI: present and future.," *J Magn Reson Imaging*, vol. 26, pp. 1186–9, Nov. 2007.

[226] G. W. Albers, V. N. Thijs, L. Wechsler, S. Kemp, G. Schlaug, E. Skalabrin, R. Bammer, W. Kakuda, M. G. Lansberg, A. Shuaib, W. Coplin, S. Hamilton, M. Moseley, and M. P. Marks, "Magnetic resonance imaging profiles predict clinical response to early reperfusion: the diffusion and perfusion imaging evaluation for understanding stroke evolution (DEFUSE) study.," *Ann Neurol*, vol. 60, pp. 508–17, Nov. 2006.

[227] E. C. DG, "MEDDEV 2. 4/1 Rev. 9," 2010.

[228] D. M. Grodzki, P. M. Jakob, and B. Heismann, "Ultrashort echo time imaging using pointwise encoding time reduction with radial acquisition (PETRA).," *Magn Reson Med*, vol. 67, pp. 510–8, Feb. 2012.

[229] D. M. Grodzki and B. Heismann, "Quiet T1-weighted head scanning using PETRA," in *Proc Intl Soc Mag Reson Med 21*, vol. 21, (Salt Lake City, UT, USA), p. 456, 2013.

[230] C.-P. Liang, "Concurrent multiscale imaging with magnetic resonance imaging and optical coherence tomography," *J Biomed Opt*, vol. 18, p. 046015, Apr. 2013.

[231] Z. Movasaghi, S. Rehman, and I. U. Rehman, "Raman spectroscopy of biological tissues," *Appl Spectrosc Rev*, vol. 42, pp. 493–541, Sept. 2007.